

Towards the Uncertainty Quantification of Fractured Karst Systems

Reactive Transport and Fracture Networks: Where Numerical Modeling Meets Outcrop Observations

de Hoop, S.

DOI

[10.4233/uuid:37464633-9480-4726-9034-f55f9f6e1b16](https://doi.org/10.4233/uuid:37464633-9480-4726-9034-f55f9f6e1b16)

Publication date

2022

Document Version

Final published version

Citation (APA)

de Hoop, S. (2022). *Towards the Uncertainty Quantification of Fractured Karst Systems: Reactive Transport and Fracture Networks: Where Numerical Modeling Meets Outcrop Observations*. [Dissertation (TU Delft), Delft University of Technology]. <https://doi.org/10.4233/uuid:37464633-9480-4726-9034-f55f9f6e1b16>

Important note

To cite this publication, please use the final published version (if applicable).
Please check the document version above.

Copyright

Other than for strictly personal use, it is not permitted to download, forward or distribute the text or part of it, without the consent of the author(s) and/or copyright holder(s), unless the work is under an open content license such as Creative Commons.

Takedown policy

Please contact us and provide details if you believe this document breaches copyrights.
We will remove access to the work immediately and investigate your claim.

The background of the entire page is a complex, interconnected network of thin, white lines on a solid blue background. These lines represent fractures in a karst system, forming a dense, irregular web of polygons of various sizes and shapes. The overall appearance is that of a fractured rock surface or a subsurface flow network.

TOWARDS THE UNCERTAINTY QUANTIFICATION OF FRACTURED KARST SYSTEMS

REACTIVE TRANSPORT AND FRACTURE NETWORKS: WHERE
NUMERICAL MODELING MEETS OUTCROP OBSERVATIONS

Stephan de Hoop

Propositions

accompanying the dissertation

Towards the Uncertainty Quantification of Fractured Karst Systems

by

Stephan de Hoop

1. There is little sense in generating a model on a scale of orders of magnitude smaller than the scale of our available data. [Chapter 3 of this thesis]
2. Even though the natural caves observed in outcrops are formed via several complex processes, the interplay of advective, diffusive, and reactive mass transfer, expressed with Damköhler and Péclet number, do cover some of the encountered cave geometries. [Chapter 4 of this thesis]
3. The effectiveness of Adaptive Mesh Refinement strategies heavily depends on the solved physical process, and the heuristic coarsening criteria. [Chapter 5 of this thesis]
4. Collections of reservoir models often exhibit a significant degree of redundancy and allow for selecting a subset of representative models which reasonably accurately describe the behavior of the complete set of models. [Chapter 6 of this thesis]
5. The importance of understanding logic, statistics, and how media and the internet operate cannot be understated. It should be taught to children as early as possible.
6. Life is meaningless on a cosmic scale; however, this does not imply that our human life is meaningless altogether.
7. Given infinite time, anyone can master any subject; never stop learning and never give up.
8. Admitting you are wrong is a sign of strength; changing your opinion in light of new evidence is at the heart of science and something we should aim for in our daily lives.
9. As a society, we should remove the stigma of failure; we should strive for it, since how can we ever honestly know ourselves if we haven't failed?
10. Model Synthesis or Wave Function Collapse algorithm might be an interesting alternative to Multiple-Point Statistics for generating geological reservoir models.

These propositions are regarded as opposable and defensible, and have been approved as such by the promoters dr. D.V. Voskov, prof. dr. G. Bertotti, and dr. A. Barnhoorn.

Stellingen

bij het proefschrift

Op Weg Naar de Onzekerheidskwantificering van Gebroken Karst-Systemen

door

Stephan de Hoop

1. Het heeft weinig zin om een model te genereren op een schaal van ordes van grootte kleiner dan de schaal van onze beschikbare gegevens. [Hoofdstuk 3 van dit proefschrift]
2. Hoewel de natuurlijke grotten die in ontsluitingen worden waargenomen, worden gevormd via verschillende complexe processen, dekt het samenspel van advectieve, diffuse en reactieve massaoverdracht, uitgedrukt met het Damköhler- en Péclet-getal, enkele van de aangetroffen grotgeometrieën. [Hoofdstuk 4 van dit proefschrift]
3. De effectiviteit van Adaptive Mesh Refinement-strategieën hangt sterk af van het opgeloste fysieke proces en de heuristische verruwingscriteria. [Hoofdstuk 5 van dit proefschrift]
4. Verzamelingen van reservoirmodellen vertonen vaak een aanzienlijke mate van redundantie en maken het mogelijk een subset van representatieve modellen te selecteren die redelijk nauwkeurig het gedrag van de volledige set modellen beschrijven. [Hoofdstuk 6 van dit proefschrift]
5. Het belang van het begrijpen van logica, statistieken en hoe media en internet werken, kan niet worden onderschat. Het moet zo vroeg mogelijk aan kinderen worden geleerd.
6. Het leven is zinloos op kosmische schaal; dit betekent echter niet dat ons menselijk leven helemaal zinloos is.
7. Met oneindige tijd kan iedereen elk onderwerp beheersen; stop nooit met leren en geef nooit op.
8. Toegeven dat je ongelijk hebt, is een teken van kracht; je mening veranderen in het licht van nieuw bewijs is de kern van de wetenschap en iets waar we in ons dagelijks leven naar moeten streven.
9. Als samenleving moeten we het stigma van mislukking wegnemen; we moeten ernaar streven, want hoe kunnen we onszelf ooit eerlijk kennen als we niet hebben gefaald?
10. Modelsynthese of golf functie-instortingsalgoritme kan een interessant alternatief zijn voor meerpuntsstatistieken voor het genereren van geologische reservoirmodellen.

These propositions are regarded as opposable and defendable, and have been approved as such by the promotors dr. D.V. Voskov, prof. dr. G. Bertotti, and dr. A. Barnhoorn.

TOWARDS THE UNCERTAINTY QUANTIFICATION OF FRACTURED KARST SYSTEMS

**REACTIVE TRANSPORT AND FRACTURE NETWORKS: WHERE
NUMERICAL MODELING MEETS OUTCROP OBSERVATIONS**

Proefschrift

ter verkrijging van de graad van doctor
aan de Technische Universiteit Delft,
op gezag van de Rector Magnificus prof. dr. ir. T.H.J.J. van der Hagen,
voorzitter van het College voor Promoties,
in het openbaar te verdedigen op
donderdag, 3 november, 2022, om 10:00 uur

door

Stephan DE HOOP

Master of Science in Petroleum Engineering and Geosciences,
Technische Universiteit Delft, Nederland,
geboren te Apeldoorn, Nederland.

Dit proefschrift is goedgekeurd door de promotors.

Samenstelling promotiecommissie bestaat uit:

Rector Magnificus	voorzitter
Dr. D. V. Voskov	Technische Universiteit Delft, promotor
Prof. dr. G. Bertotti	Technische Universiteit Delft, promotor
Dr. A. Barnhoorn	Technische Universiteit Delft, promotor

Onafhankelijke leden:

Prof. dr. ir. D.M.J. Smeulders	Technische Universiteit Eindhoven
Prof. dr. D. Tartakovsky	Stanford University
Prof. dr. D. Koehn	Friedrich-Alexander-Universität Erlangen-Nürnberg
Prof. dr. S. Geiger	Technische Universiteit Delft
Prof. dr. ir. P.L.J. Zitha	Technische Universiteit Delft, reservelid



Keywords: reactive transport, multiphase flow, operator-based linearization, fracture networks, karst, uncertainty quantification

Printed by: ProefschriftMaken

Front & Back: Initial design by Timothy Baars and final design by Richard de Hoop. Fracture network modified from Houben et al., 2017.

Copyright © 2022 by S. de Hoop

ISBN 978-94-6469-044-6

An electronic version of this dissertation is available at
<http://repository.tudelft.nl/>.

Life can only be understood backwards; but it must be lived forwards.

Søren Kierkegaard

Without music, life would be a mistake.

Friedrich Nietzsche

If a lion could speak, we could not understand him.

Ludwig Wittgenstein

“I wish it need not have happened in my time,” said Frodo. “So do I,” said Gandalf, “and so do all who live to see such times. But that is not for them to decide. All we have to decide is what to do with the time that is given us.”

John Ronald Reuel Tolkien

CONTENTS

Summary	xi
Samenvatting	xiii
List of Figures	xv
List of Tables	xix
1 Introduction	1
1.1 Societal relevance	1
1.2 Natural Fracture Networks	2
1.3 Conceptual and Quantitative Karst Models	3
1.3.1 Epigenic vs. Hypogenic karst.	3
1.3.2 Conceptual hypogenic models.	4
1.3.3 Quantitative hypogenic models	6
1.4 Thesis objectives	7
1.5 Thesis outline	8
2 Methodology	9
2.1 Governing equations in continuous form	9
2.2 Phase behavior of compositional system	11
2.3 Porosity treatment	12
2.4 Fluid and Rock Description	14
2.5 Discretization	14
2.5.1 Discrete Fracture Model (DFM)	15
2.5.2 Transmissibility Multiplier	16
2.6 Operator-Based Linearization (OBL)	18
3 Advanced DFM Modeling	21
3.1 Introduction	22
3.2 Materials and Methods	25
3.2.1 Fracture network input data	25
3.2.2 Graph theory.	26
3.2.3 The topology and geometry of fracture networks.	27
3.2.4 Preprocessing algorithm	29
3.2.5 Governing equations.	34
3.2.6 Numerical solution	35
3.3 Results	35
3.3.1 Static performance of the preprocessing framework	36
3.3.2 Dynamic performance of preprocessing framework	41
3.3.3 Numerical performance high enthalpy.	48

3.4	Discussion	49
3.4.1	Topology	49
3.4.2	Fluid flow	50
3.4.3	Application and recommendations	51
3.5	Conclusion	51
3.6	Acknowledgements	52
3.7	Appendix: various algorithms for DFN preprocessing	53
4	Karst: Where Real-World Observations Meet Reactive Transport	57
4.1	Introduction	58
4.2	LiDAR data acquisition	59
4.2.1	Brief background on area of two expeditions.	59
4.2.2	ZEB Revo (RT) and SLAM	61
4.2.3	Data post-processing	62
4.3	LiDAR shape analysis	63
4.3.1	Example of visible speleogenetic features in LiDAR data	63
4.3.2	Extract skeleton	64
4.3.3	Extract sub-cloud, projection and curve fitting.	64
4.3.4	Results	64
4.4	Chemical modeling	69
4.4.1	Chemical reactions	69
4.4.2	Examples	71
4.4.3	Treatment of reactions in reactive transport simulations.	72
4.4.4	Fracture network preprocessing	73
4.5	Results reactive transport modeling.	74
4.5.1	Influence Damköhler and Péclet	74
4.5.2	Influence boundary conditions and resolution.	76
4.5.3	Presence of fractures	79
4.6	Conclusions.	80
4.7	Acknowledgements	82
5	Adaptive Mesh Refinement	83
5.1	Introduction	84
5.2	Methodology	85
5.2.1	Connectivity list	86
5.3	Multi-level grid generation	87
5.3.1	Cell aggregation	87
5.3.2	Transmissibility and upscaling.	92
5.4	Dynamic adaptivity framework	94
5.5	Applications for Geothermal Reservoirs.	96
5.5.1	Case 1: Homogeneous model	97
5.5.2	Case 2: Sugar-cube shale model	99
5.5.3	Case 3: Fluvial heterogeneous model	101
5.5.4	Case 4: Reactive transport	104

5.6	Discussion	108
5.7	Conclusions.	109
5.8	Acknowledgements	110
5.9	Appendix	110
6	Uncertainty Quantification for Fractured Reservoirs	113
6.1	Introduction	114
6.2	Method and theory	115
6.2.1	Generation fracture networks	115
6.2.2	Uncertainty quantification framework	117
6.3	Results	118
6.3.1	Fracture generation results.	119
6.3.2	Fracture pre-processing results	119
6.3.3	Uncertainty Quantification results	122
6.4	Conclusions.	124
6.5	Acknowledgements	125
7	Conclusion	127
7.1	Advanced meshing capabilities	127
7.2	Reactive transport framework and link with outcrop observations	128
7.3	Adaptive mesh refinement	128
7.4	Uncertainty quantification	128
	Acknowledgements	129
A	Benchmark	151
A.1	Introduction and context of the proposal	151
A.2	Benchmark scenarios	152
A.2.1	1D homogeneous domain	152
A.2.2	2D Heterogeneous domain	154
A.3	Expected output	157
A.3.1	1D homogeneous domain	157
A.3.2	2D heterogeneous domain	158
	Curriculum Vitae	161
	List of Publications	163

SUMMARY

Society relies on large amounts of energy to progress and allow for a high standard of living. The recent severe climate changes require advance technologies related to cleaner energy resources. One such technology beneficial for accelerating this current energy transition is geothermal energy. This type of energy often found in fractured and karstified carbonate aquifers. It is vital to understand the reservoir properties and reduce the risks of such subsurface-related activities. This thesis attempts to better understand the complex fractured carbonate reservoirs and improve the numerical simulation capabilities towards large-scale uncertainty quantification.

In Chapter 2 all the relevant mathematical equations used in this work are introduced. These equations are all discretized within the Delft Advanced Research Terra Simulator (DARTS) platform, developed at the Delft University of Technology. The resulting nonlinear system of equations is then linearized using the Operator-Based Linearization technique. The main advantage of this modeling approach is fast and straightforward partial derivatives. The porosity treatment when dissolving the rock matrix is also described in Chapter 2.

Chapter 3 shows the advance DFM capabilities and introduces a preprocessing strategy to handle complex (natural) fracture networks with variable fracture apertures. The preprocessing framework results in a fully conformal, uniformly distributed grid for realistic 2D fracture networks at a required level of precision. The simplified geometry and topology of the resulting network are compared with input (i.e., unchanged) data to evaluate the preprocessing influence. The simplified topology directly improves meshing results and, consequently, the accuracy and efficiency of numerical simulation.

Chapter 4 provides some background on the acquired LiDAR data sets and post-processing techniques that extract and analyze the internal geometry of the caves. Very regular and consistent cave passages are observed in the shape analysis. This chapter also investigates dissolution in a fracture network and varies several parameters to investigate the instigated patterns in different hydraulic and chemical regimes. Finally, these numerical simulation results are compared with the patterns observed in the LiDAR data.

Chapter 5 describes the AMR implementation in DARTS. Classical multi-scale problems arrive naturally from geoscience applications. Most effort has been put into solving the pressure equation with multi-scale methods. However, improving the transport solution can be pretty significant for the performance of the simulation, especially in complex applications related to thermal-compositional flow. The use of an Adaptive Mesh Refinement enables the grid to adapt dynamically during the simulation, which facilitates the efficient use of computational resources. The approach uses a multi-level connection list and can be applied to fully unstructured grids. The adaptivity of the grid in the developed framework is based on a hierarchical connectivity list. The performance

of the proposed approach is illustrated for several challenging geothermal applications of practical interest.

Chapter 6 describes a fast and robust scheme for uncertainty quantification (UQ) in fractured reservoirs. This is achieved by creating a simplified representation of the fracture network while preserving the main characteristics of the high-fidelity model. Information at different scales is included in the UQ workflow, which reduces the computational time while converging to the high-fidelity full ensemble statistics. The pre-processing algorithm allows for a hierarchical representation of the fracture network, which is utilized in the reduced UQ methodology. The reduced UQ workflow uses the coarser representation of the fracture networks to partition/rank the high-fidelity parameter space. Then a small subset of high-fidelity models is chosen to represent the full ensemble statistics. As a result of this, the computational time of the UQ is reduced by two/three orders of magnitude while converging to similar statistics as the high-fidelity complete ensemble statistics.

SAMENVATTING

De samenleving is afhankelijk van grote hoeveelheden energie om vooruitgang te boeken en een hoge levensstandaard mogelijk te maken. De recente ernstige klimaatveranderingen vereisen geavanceerde technologieën met betrekking tot schonere energiebronnen. Een dergelijke technologie die gunstig is voor het versnellen van deze huidige energietransitie, is geothermische energie. Dit type energie wordt vaak aangetroffen in gebroken en gekarstificeerde carbonaatwatervoerende lagen. Het is van vitaal belang om de eigenschappen van het reservoir te begrijpen en de risico's van dergelijke ondergrondse activiteiten te verminderen. Dit proefschrift probeert de complexe gefractuurde carbonaatreservoirs beter te begrijpen en de numerieke simulatiemogelijkheden voor grootschalige onzekerheidskwantificering te verbeteren.

In Hoofdstuk 2 worden alle relevante wiskundige vergelijkingen geïntroduceerd die in dit werk worden gebruikt. Deze vergelijkingen worden allemaal gediscretiseerd binnen het Delft Advanced Research Terra Simulator (DARTS) platform, ontwikkeld aan de TU Delft. Het resulterende niet-lineaire systeem van vergelijkingen wordt vervolgens gelineariseerd met behulp van de Operator-Based Linearization-techniek (OBL). Het belangrijkste voordeel van deze modelleringsaanpak is snelle en ongecompliceerde partiële afgeleiden. De porositeitsbehandeling bij het oplossen van de gesteentematrix wordt ook beschreven in Hoofdstuk 2.

Hoofdstuk 3 toont de geavanceerde DFM-mogelijkheden en introduceert een preprocessingstrategie om complexe (natuurlijke) breuknetwerken met variabele breukopeningen te verwerken. Het preprocessing-raamwerk resulteert in een volledig conform, uniform verdeeld raster voor realistische 2D-breuknetwerken met een vereist precisieniveau. De vereenvoudigde geometrie en topologie van het resulterende netwerk worden vergeleken met invoergegevens (d.w.z. ongewijzigde) om de invloed van de voorbereiding te evalueren. De vereenvoudigde topologie verbetert direct de meshing-resultaten en bijgevolg de nauwkeurigheid en efficiëntie van numerieke simulatie.

Hoofdstuk 4 geeft wat achtergrondinformatie over de verkregen LiDAR-gegevenssets en nabewerkingstechnieken die de interne geometrie van de grotten extraheren en analyseren. In de vormanalyse worden zeer regelmatige en consistente grot passages waargenomen. Dit hoofdstuk onderzoekt ook het oplossen in een breuknetwerk en varieert verschillende parameters om de geïnitieerde patronen in verschillende hydraulische en chemische regimes te onderzoeken. Ten slotte worden deze numerieke simulatiereultaten vergeleken met de patronen die zijn waargenomen in de LiDAR-gegevens.

Hoofdstuk 5 beschrijft de AMR-implementatie in DARTS. Klassieke meerschallige problemen komen natuurlijk voort uit geowetenschappelijke toepassingen. De meeste moeite is gedaan om de drukvergelijking op te lossen met multischaalmethoden. Het verbeteren van de transportoplossing kan echter behoorlijk belangrijk zijn voor de prestaties van de simulatie, vooral in complexe toepassingen die verband houden met thermische-compositionele stroming. Het gebruik van een Adaptive Mesh Refinement stelt het ras-

ter in staat zich dynamisch aan te passen tijdens de simulatie, wat een efficiënt gebruik van computationele middelen mogelijk maakt. De aanpak maakt gebruik van een verbindingslijst met meerdere niveaus en kan worden toegepast op volledig ongestructureerde netten. De adaptiviteit van het raster in het ontwikkelde raamwerk is gebaseerd op een hiërarchische connectiviteitslijst. De prestaties van de voorgestelde aanpak worden geïllustreerd voor verschillende uitdagende geothermische toepassingen van praktisch belang.

Hoofdstuk 6 beschrijft een snel en robuust schema voor onzekerheidskwantificering (UQ) in gebroken reservoirs. Dit wordt bereikt door een vereenvoudigde weergave van het breuknetwerk te creëren met behoud van de belangrijkste kenmerken van het high-fidelity-model. Informatie op verschillende schalen is opgenomen in de UQ-workflow, waardoor de rekentijd wordt verkort en tegelijkertijd wordt geconverteerd naar de high-fidelity volledige ensemble-statistieken. Het voorbewerkingsalgoritme zorgt voor een hiërarchische weergave van het breuknetwerk, dat wordt gebruikt in de gereduceerde UQ-methodologie. De verminderde UQ-workflow gebruikt de grovere weergave van de breuknetwerken om de high-fidelity parameter ruimte te partitioneren/rangschikken. Vervolgens wordt een kleine subset van high-fidelity-modellen gekozen om de volledige ensemble-statistieken weer te geven. Als resultaat hiervan wordt de rekentijd van de UQ verminderd met twee/drie orden van grootte, terwijl het convergeert naar vergelijkbare statistieken als de high-fidelity complete ensemble-statistieken.

LIST OF FIGURES

1.1	Current and future primary energy demand.	2
1.2	Overview conceptual models	5
1.3	Dissolution mechanisms	6
2.1	Total porosity treatment	12
2.2	DFM illustration	15
3.1	Fracture modeling workflow	23
3.2	Variable aperture model	26
3.3	Fracture topology	28
3.4	Preprocessing workflow	29
3.5	Fracture aperture correction types	34
3.6	Sub-graph aperture correction	35
3.7	Changes in fracture network characteristics	37
3.8	Angle distribution as function of cleaning accuracy	38
3.9	Fracture network topology after preprocessing	38
3.10	Detailed view of the fracture network topology of the Whitby network	39
3.11	Comparison of meshing results after preprocessing	40
3.12	Control volume size distribution as a function of preprocessing accuracy for the Whitby network	41
3.13	Mesh element quality distribution as a function of preprocessing accuracy for the Whitby network.	42
3.14	Temperature distribution as a function of preprocessing and meshing accuracy for the optimal strategy after 3150 [days] (Whitby network).	43
3.15	Temperature distribution as a function of preprocessing and meshing accuracy for the optimal strategy after 3150 [days] (Brejoes network).	44
3.16	Water saturation distribution as a function of preprocessing and meshing accuracy for the optimal strategy after 150 [days] (Brejoes network).	44
3.17	Temperature profile at the production well for several levels of preprocessing	46
3.18	Single phase steady-state simulation of a high-permeable matrix and low permeable fractures	47
3.19	Single phase traces simulation on variable aperture model	48
4.1	Geological map of the São Francisco Craton in NE Brazil	60
4.2	Overview of the location of the studied caves.	61
4.3	LiDAR data acquisition and comparison with photo	62
4.4	Example of visible speleogenetic features on LiDAR survey	63
4.5	Extraction of sub-point cloud and projection onto plane	65

4.6	Results shape analysis Lapa de Bode	66
4.7	Height and width distribution Lapa de Bode	67
4.8	Different cave geometries and scales observed during the fieldwork	68
4.9	3D Fluid-flow results in parametrized cave	69
4.10	Top view of Torrinha cave (regular spacing cave passages)	74
4.11	Comparison between equilibrium and kinetic chemistry	75
4.12	Different types of wormholes	76
4.13	Initial permeability fields	77
4.14	Effect of boundary conditions on porosity map	78
4.15	Convergence wormholes for single well mesh refinement	79
4.16	PVBT numerical convergence curves for a single well	79
4.17	Dissolution in fracture network with variable aperture	80
4.18	Dissolution in fracture network when varying dispersive forces	81
4.19	Dissolution in fracture network by varying the discretization accuracy	81
5.1	Example of grid indexing	87
5.2	Multi-level grid construction	88
5.3	Simple unstructured grid partitioning	90
5.4	Unstructured grid partitioning results	90
5.5	4x4 Cartesian grid showing cell aggregation, resulting in four coarse grid cells.	90
5.6	Mutli-level hierarchical grid indexing	94
5.7	2-level hierarchical adaptive grid example	95
5.8	Schematic representation of the prolongation and restriction for the example in figure 5.7.	96
5.9	Model setup for homogeneous unstructured grid partitioning	98
5.10	Temperature solution homogeneous model	98
5.11	Error of AMR solution on homogeneous model	99
5.12	Percentage of elements used during simulation in AMR for homogeneous unstructured model	99
5.13	Hierarchical grid for shale blocks	100
5.14	Temperature solution for shale blocks	101
5.15	Error of AMR solution for shale blocks model	101
5.16	Percentage of elements used during simulation in AMR for shale blocks model	102
5.17	Unstructured hierarchical grid for fluvial reservoir with low net-to-gross	102
5.18	Temperature solution for fluvial low net-to-gross reservoir	103
5.19	Error of AMR solution for fluvial low net-to-gross model w.r.t. fine-scale	103
5.20	Percentage of elements used during simulation in AMR for fluvial low net-to-gross model	104
5.21	Hierarchical grid used for carbonate dissolution model	105
5.22	Solid composition for carbonate dissolution model	106
5.23	Error of AMR solution for carbonate dissolution model	107
5.24	Percentage of elements used during simulation in AMR for carbonate dissolution model model	108

6.1	Synthetic example of MDS and purpose of clustering	118
6.2	Three examples of the fracture networks with different connectivity, generated using the algorithm in section Generation fracture networks.	119
6.3	Meshing result before and after preprocessing	120
6.4	Hierarchical flow-response as a function of preprocessing accuracy	120
6.5	Flow response of the ensemble of fracture networks for each coarsening level.	121
6.6	Quantiles of energy production for each ensemble scale	121
6.7	Changes to fracture network as a function of preprocessing accuracy	122
6.8	Connectivity of ensemble members as a function of preprocessing accuracy	123
6.9	Illustration of the general workflow of reconstructing the stochastic response	124
A.1	1D Benchmark model configuration	153
A.2	2D Benchmark model configuration	155

LIST OF TABLES

3.1	Boundary conditions.	42
3.2	Reservoir and simulation parameters.	43
3.3	Numerical performance Whitby simulations	49
3.4	Numerical performance Brejoes simulations	50
5.1	Simple connectivity list example	86
5.2	Cell aggregation	88
5.3	Interfaces l contained in each cell i for level 0. The interfaces are expressed as connection pairs, describing it.	90
5.4	List of faces (corresponding connection pairs) for each coarse cell in the coarse grid.	91
5.5	Computational effort.	108
5.6	Boundary conditions geothermal models (section 5.1, 5.2, and 5.3).	110
5.7	Reservoir and simulation parameters geothermal models (section 5.1, 5.2, and 5.3).	110
5.8	Boundary conditions chemical model (section 5.4).	110
5.8	Boundary conditions chemical model (section 5.4).	111
5.9	Reservoir and simulation parameters chemical model (section 5.4).	111
A.1	Values for all the relevant fluid and rock properties.	152
A.2	Boundary conditions and other simulation parameters.	153
A.3	Kinetic and equilibrium constants.	154
A.4	Boundary conditions and other simulation parameters.	155
A.5	Values for all the relevant fluid and rock properties.	156
A.6	Log_{10} of the equilibrium constants for extended chemical system (A.4).	156
A.7	Initial molar fractions for the extended chemical model	157

1

INTRODUCTION

1.1. SOCIETAL RELEVANCE

The availability of energy is of monumental importance to modern society. It is utilized for industry, agriculture, transportation, households, and often used as an index for a standard of living (Joyeux & Ripple, 2007). Energy consumption has been steadily growing for the past decades, especially in developing countries (Kaygusuz, 2012). A large amount of this consumption still relies on fossil fuels (IEA, 2020). To meet the current climate goals, we need to improve our use of the earth's subsurface for cleaner energy applications and storage solutions.

The current and future (i.e., prognoses) primary energy demand is shown in Figure 1.1. The different scenarios in Figure 1.1 are Stated Policies Scenario (STEPS), Delayed Recovery Scenario (DRS), Sustainable Development Scenario (SDS), and Net Zero Emissions by 2050 (NZE2050). STEPS is under the current policy settings. DRS takes a more prolonged recovery from the COVID pandemic into account (i.e., longer than 2021). SDS requires a structural transformation of the energy section, alongside significant investment in more efficient and cleaner capital stock. A large part of this scenario is tailored to developing countries. The next very ambitious energy sector transformation, NZE2050, will result in a net-zero emission by 2050. This requires a significant further acceleration in the deployment of clean energy technologies alongside wide-ranging behavioral changes (IEA, 2020).

The report by Fleiter et al., 2016 shows that EU-28 countries use 26.5% of their total primary energy for heating and cooling, of which 66% is reliant on fossil fuels. Space heating is the most significant contributor, resulting in around 63.6% of the heating and cooling energy consumption (Eurostat, 2020). A sustainable solution to this problem is expanding the District Heating and Cooling Networks (DHC) (Arnaudo et al., 2021; Arnaudo et al., 2019). A significant reduction in carbon emissions can therefore be achieved by utilizing DHC in the heating sector, especially considering the substantial worldwide geothermal energy potential (Limberger et al., 2018). Therefore, geothermal energy plays a vital role in reaching the NZE2050 scenario.

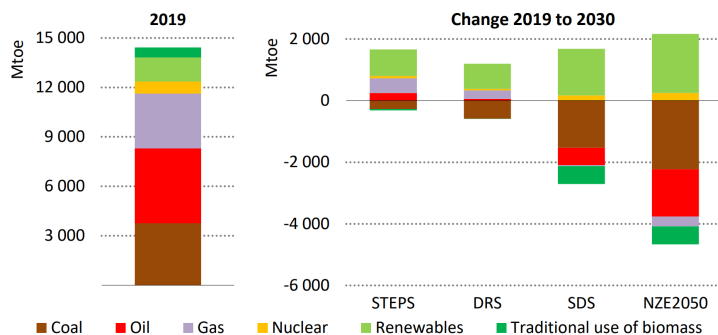


Figure 1.1 Current and future primary energy demand. The different scenarios are: Stated Policies Scenario (STEPS); Delayed Recovery Scenario (DRS); Sustainable Development Scenario (SDS); and Net Zero Emissions by 2050 (NZE2050). Taken from IEA, 2020.

Technical challenges to geothermal energy recovery are often related to hydro-geochemical effects such as precipitation due to temperature reduction by cold-water injection and the inability to properly characterize the reservoir properties (i.e., faults, fractures, permeability, thermal properties). This increases the risks associated with geothermal projects and further limits their widespread use (Compennolle et al., 2019; Witter et al., 2019). Especially challenging reservoirs constitute carbonate reservoirs. They host a large part of the world's hydrocarbon reserves (Akbar et al., 2000) and are currently heavily investigated in the Netherlands for their geothermal energy potential (Reijmer et al., 2017). These reservoirs are often chemically (i.e., karstified) and mechanically (i.e., fractured) altered, resulting in unpredicted hazards. The fluid-flow response and mechanical behavior of these Naturally Fractured Reservoirs (NFR) are highly uncertain due to our limited ability to predict the spatial distribution of fracture networks and karst at the reservoir scale. Performing adequate risk and uncertainty quantification is necessary due to the increasing environmental awareness and regulations. Therefore, we need to understand these fractured and karstified reservoirs better and improve our numerical models.

1.2. NATURAL FRACTURE NETWORKS

Rocks in the subsurface are often naturally fractured as a result of brittle deformation (Bai et al., 2002; Bertotti et al., 2017). Natural fractures typically form in networks and are spatially variable (Laubach et al., 2009). This variability has a significant effect on the relevant flow and mechanical properties of the entire reservoir (rock) (Nelson, 2001; Rijken, 2005). Cemented fractures and sealing faults can act as barriers to flow-fluid (Antonellini & Aydin, 1994; Gale et al., 2007), while open fractures increase the effective permeability of the bulk material (Council et al., 1996; Vidal & Genter, 2018; Wang et al., 2002).

Accurate estimates on the characteristics of the fracture network are required in order to make meaningful predictions on fluid-flow patterns, heat and reactive transport, as well as mechanical stability at the reservoir-scale (Olson et al., 2009; Wang et al.,

2021; Zhao & Paul Young, 2011). Typical sources of information on these characteristics include data from the well, such as borehole images, logs, cores, and transient pressure records. Well-data is severely limited to the near-well region, subject to biased and sparse sampling, and is an indirect measurement that shows the interplay between various sources of heterogeneity (Cinco-Ley, 1996; Wu & Pollard, 2002). Seismic images of the subsurface are not refined enough to reveal the 3D distribution, geometry, and connectivity of the fracture networks and only provide the context of the presence of large-scale faults (Liu & Martinez, 2014). Seismic attributes extracted from a high-resolution seismic survey only provide insights into the intensity of the fracturing (Boersma et al., 2020; Jaglan et al., 2015).

Furthermore, there is outcrop data in the form of drone photogrammetry or scanlines (Bisdorn et al., 2014; Lamarche et al., 2012; Zeeb et al., 2013). These methods provide excellent information on the 2D and potential pseudo-3D characteristics of the fracture network (Bisdorn et al., 2017). However, there is not always a one-to-one correspondence with the state of the fracture network in the subsurface (Li et al., 2018; McGinnis et al., 2015), and the various processes that potentially affect the fracture characteristics during their journey to the surface should be accounted for (Bertotti et al., 2017; Fossen, 2016). A major downside of large-scale outcrop images of fracture networks acquired with drone photogrammetry is that manual interpretation is often required to get a geologically realistic picture of the fracture network. However, this is subject to interpretation bias and can lead to a time-consuming endeavor. Recent advances in automatic fracture detection allow for the use of large-scale outcrop images in fracture network characterization in a timely manner (Prabhakaran et al., 2021). There are also forward models and laboratory experiments that attempt to reveal the effect of layering and local stress perturbations on different fracture network geometries (Boersma et al., 2018; Douma et al., 2019; Rijken, 2005).

The generation of discrete fracture networks (DFN) is often done using statistical tools that require fracture size and spacing, a (random) distribution of fracture orientation, and fracture density as input parameters (Bonneau et al., 2013; Chilès, 2005; Huang et al., 2017a). These methods often poorly consider fracture connectivity and geological realism (Liu et al., 2009). Recent developments related to multiple-point statistics (MPS) show more realistic fracture network configurations (Bruna et al., 2019; Chugunova et al., 2017). Chapter 6 of this thesis highlights a simple alternative fracture network generation approach that attempts to capture accurate fracture intersections and connectivity.

1.3. CONCEPTUAL AND QUANTITATIVE KARST MODELS

1.3.1. EPIGENIC VS. HYPOGENIC KARST

Speleogenesis and karstology have been rapidly evolving regarding empirical data acquisition and the theoretical framework. Karst formation is typically subdivided into an epigenic and hypogenic realm (Palmer, 2011). Epigenic karst is formed in a (hydraulically) open system with direct contact to the surface, typically from enhanced dissolution by carbonic acid in shallow meteoric waters. Epigenic karst generally evolves via lateral flow in the shallow (undersaturated) subsurface, where topographical lows primarily govern the hydrology. Conduit development occurs according to positive-feedback

mechanisms, mainly competing evolution of porosity alterations rather than uniform dissolution resulting in a branching structure (Klimchouk, 2012).

Although the definition of hypogenic karst differs among authors, two significant distinctions can be made. The emphasis of the first definition lies on the source of aggressiveness of the fluid, particularly that the aggressiveness originated at depth and is therefore independent from overlying soil CO₂ and is generally referred to as the “geochemical definition” (Palmer & Palmer, 2000). The second definition of hypogenic karst is guided by hydrogeology. It stresses the importance of ascending fluids recharging the soluble formation from hydro-stratigraphically lower units. In addition, the fluids and aggressiveness are derived from deeper parts of the basin and independent from the surface (Klimchouk, 2015). Since there are morphological and sedimentological features, as well as mineralogical criteria distinct to hypogenic karst, a division between the two realms can be made based on these three norms (Klimchouk, 2009).

A recent compilation of outcrop studies involving hypogenic karst illustrates the academic interest in understanding the formation and spatial distribution of the karst features (Klimchouk et al., 2017). However, quantitative models and datasets used to explain the proposed hypothesis are areas in which progress can be made. Attempts to quantify time scales associated with hypogenic karst have taken place based on simple volume balances (Palmer, 2011), but extensions of this pragmatic approach to realistic configurations are required. A quantitative database and characterization of cave environments and patterns is currently investigated (Collon et al., 2017; Jouvès et al., 2017). It is proposed by Jouvès et al., 2017 to benchmark stochastically generated cave patterns using topology and the underlying cave morphology and establishes their realism. Jouvès et al., 2017 also states that the Angular Maze (AM) cave pattern exhibits the highest topological complexity and assigns it to the type of flow and source of aggressiveness.

1.3.2. CONCEPTUAL HYPOGENIC MODELS

Figure 1.2 depicts a variety of conceptual models used in literature to explain (transverse) hypogenic speleogenesis. Upwards flow of warm CO₂-enriched water along a soluble inclined fractured aquifer can lead to a “staircase” dissolution pattern (which remotely resembles dissolution patterns observed in the Morro Vermelho cave) (Ford & Williams, 1989; Klimchouk, 2007) (Figure 1.2(A)). Recharge from deep sources through more extensive vertical fractures (often denoted as feeders) into a sub-horizontal soluble fractured aquifer capped with an impermeable layer can lead to prevalent horizontal cave formations (Klimchouk et al., 2016) (Figure 1.2(B)). Another model exists to describe cave formation in a multi-story aquifer with abundant connected vertical fractures where free convection plays an essential role in the resulting geometry (Klimchouk, 2007, 2012) (Figure 1.2(C)).

Besides considerable structural aspects, several underlying mechanisms are proposed for calcium carbonate dissolution at depth. An important factor is the presence of dissolved CO₂ creating an acidic environment and vastly increasing the reaction rate and the amount of dissolved CaCO₃. The increase in pressure mainly causes increased solubility of CO₂ with depth, while increasing temperature with depth attempts to counteract this, resulting in a nonlinear behavior as a function of depth (Klimchouk, 2007) (Figure 1.3(A)). Calcite solubility is not much affected by pressure. However, it is sig-

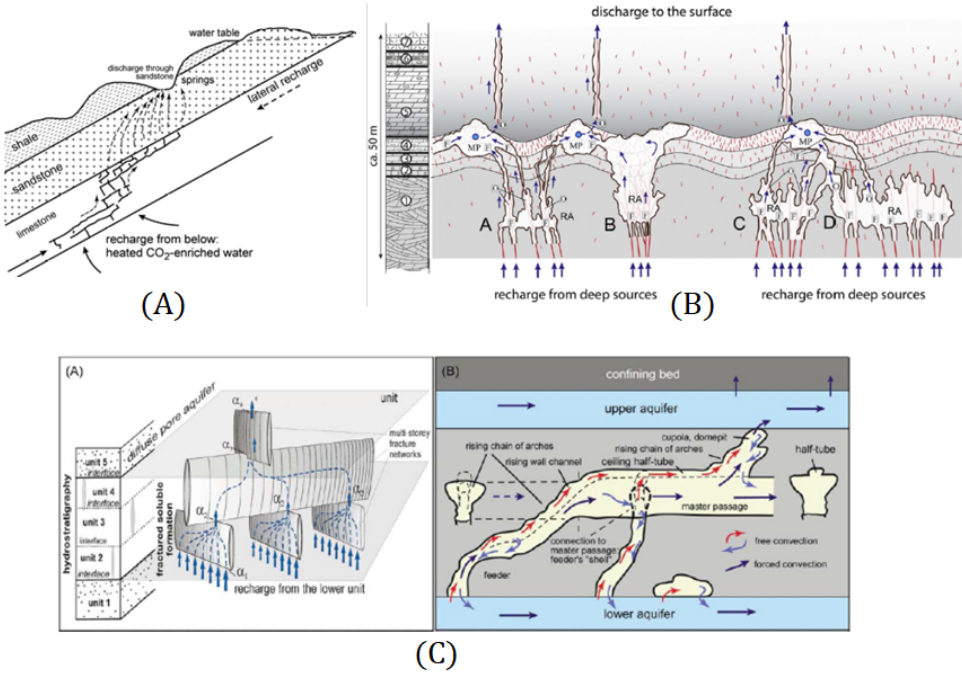


Figure 1.2 Several conceptual models for (transverse) hypogenic speleogenesis. Figure (A) after (Ford & Williams, 1989; Klimchouk, 2007), “staircase” like dissolution patterns resembling observations from the Morro Vermelho cave (chapter 4). Figure (B) after (Klimchouk et al., 2016). Figure (C) after (Klimchouk, 2007, 2012).

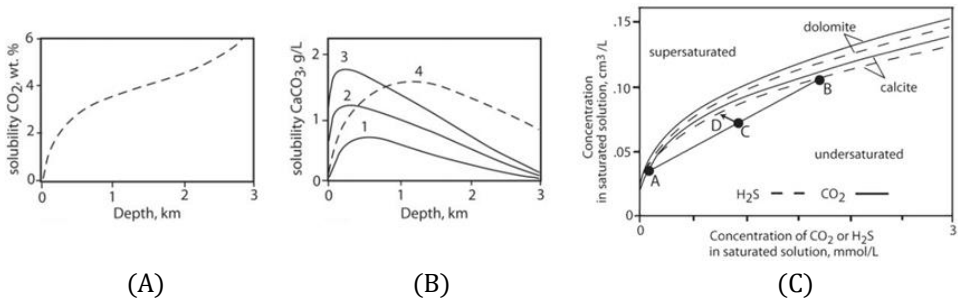


Figure 1.3 Illustration of several dissolution mechanisms. Figure (A) and (B) describe the CO₂ and CaCO₃ solubility with depth (after Dublyansky, 2000; Klimchouk, 2007). Figure (C) shows the typical nonlinear behavior of calcite and dolomite as a function of CO₂ or H₂S (Palmer, 1991).

nificantly reduced by increasing temperature (i.e., CaCO₃ dissolution is an exothermic reaction, which produces heat; therefore, the increasing temperature reduces the calcite solubility). Low temperatures results in substantial solubility in the shallow subsurface (i.e., <500m depth) while solubility significantly decreases with depth (Dublyansky, 2000) (Figure 1.3(B)). Note, however, that if a solution at depth (at equilibrium with surrounding rock) migrates upward, it has a significant potential to dissolve (due to low dissolved CaCO₃ ions and increased solubility with a decrease in temperature). Another mechanism is mixing corrosion caused by mixing two fluids that are at equilibrium composition (i.e., saturated), resulting in a fluid that is undersaturated (Palmer, 1991) (Figure 1.3(C)).

1.3.3. QUANTITATIVE HYPOGENIC MODELS

Early numerical modeling efforts of karst evolution date back to works from Dreybrodt, 1990, Sauter, 1992, Clemens et al., 1997 and Gabrovšek and Dreybrodt, 2001. These works provide elaborate details on the reaction mechanisms occurring in the dissolution process and consist of 1D and 2D modeling domains. Later efforts by Annable, 2003, Kaufmann, 2009, Kaufmann et al., 2010, and Hiller et al., 2011 extended the work to a 3D modeling domain. Typical mathematical formulations in these works consist of the transient pressure equation. A system of pipes generally represents flow in fractures or karst conduits, and the chemical processes are solved using a one-way coupling. In most of the previous works, the flow in the matrix is disregarded, except for the recent paper by Kaufmann, 2016. Generally, the coupling of thermal effects and changes in the stress state due to dissolution are neglected. Also, the main application of the previous works can be considered epigenic karst.

Modeling efforts more applicable to hypogenic karst development, also considering the importance of a vertical flow component, are recognized and can be, roughly, characterized into two sets of works: multi-level aquifer system (Birk et al., 2003; Rehl et al., 2010; Rehl et al., 2008) and hydrothermal (Andre & Rajaram, 2005; Chaudhuri et al., 2013; Rajaram et al., 2009). The results of these modeling efforts seem very promising in predicting potential karst manifestation and evolution in the subsurface. Still, a fully coupled approach honoring all physical processes involved and including accu-

rate representation of the fracture networks and heterogeneities can be improved. For a complete overview of the previous numerical studies regarding conduit development in karst, the reader is referred to the Introduction of Rehr et al., 2008. The main limitations of the previously mentioned work are the negligence of solution enlargement in the continuum model (i.e., matrix and fractures), and the conduit development is initiated at relatively few discontinuities which are predetermined (Rehr et al., 2008).

Typical chemical kinetics employed in numerical models consist of the set of classical papers by Plummer and Wigley, 1976; Plummer et al., 1979; Plummer et al., 1978. Other works Buhmann and Dreybrodt, 1985; Svensson and Dreybrodt, 1992 are also used to describe chemical kinetics, either derived experimentally or analytically. More recent experimental studies include a wider description of the involved fluid chemistry (Morse et al., 2007) and (Saldi et al., 2017), range of pressure and temperature representing actual reservoir conditions (Peng et al., 2015), more realistic rock samples (Kirstein et al., 2016), (Greiserman et al., 2016) and Non-Darcy flow (CHEN, 2011). Experiments on wormhole formation are extensive (Bazin, 2001; Bazin & Abdulhad, 1999; Wang et al., 1993) and various wormhole regimes are identified using both laboratory and numerical experiments (Golfier et al., 2002).

1.4. THESIS OBJECTIVES

Numerical reservoir simulation is vital in developing subsurface resources and making accurate predictions. Furthermore, being efficient and accurate is essential in minimizing the risks associated with such endeavors. Gaining a better understanding of the complex fluid-rock interactions and improving our reservoir models constitute an essential contribution to this thesis. The objectives can be summarized in the following points:

- Utilizing the current capabilities of the Delft Advanced Research Terra Simulator (DARTS) platform and extending it with the implementation of advanced meshing and fracture modeling abilities. This includes the Discrete Fracture Model (DFM) proposed for general-purpose reservoir simulation by Karimi-Fard et al., 2004. This also includes the handling of complex natural fracture networks from outcrop observations or stochastically generated and resolving the well-known meshing problems associated with these networks (Berre et al., 2019; Reichenberger et al., 2006).
- Implementing a reactive transport framework constitutes another objective. This includes chemical and kinetic reactions combined with multi-phase mass and heat transfer capacity. An important step is benchmarking these capabilities with other numerical codes that attempt to solve the same physical problem.
- Combining the numerical domain with real-world observations is another vital objective. Understanding the regimes and conditions which govern certain dissolution patterns is vital in understanding the complex fluid-rock interactions. Acquisition of cave data sets using Light Detection And Ranging (LiDAR) technology and analyzing their geometric patterns. This will comprise a large data set that can be compared to dissolution patterns obtained from numerical simulation results using DARTS.

- Most processes related to reservoir simulation and reactive transport constitute sharp local changes in the solution. This means that a faster simulation can be obtained by applying Adaptive Mesh Refinement (AMR) without severely compromising accuracy. Implementing this constitutes another objective for this project.
- All of these objectives come together in the last objective: fast and robust uncertainty quantification. This will ultimately significantly reduce the risks associated with the aforementioned subsurface activities.

1.5. THESIS OUTLINE

Chapter 2 describes all the relevant mathematical equations and discretization used in DARTS and all the flow simulations in this work.

Chapter 3 shows the advanced DFM capabilities and proposes a preprocessing strategy to handle complex (natural) fracture networks with variable apertures. The algorithm is tested based on several complex geothermal scenarios (i.e., high-enthalpy steam-water system), and static changes (e.g., topology and angle-distribution of the fractures) are considered as well.

Chapter 4 provides some background on the acquired LiDAR data sets and post-processing techniques that extract and analyze the internal geometry of the caves. This chapter also investigates dissolution in a fracture network and varies several parameters to investigate the instigated patterns in different chemical- and flow regimes.

Chapter 5 describes the AMR implementation in DARTS. It is implemented outside of the simulation loop and can be generalized for any other existing reservoir simulation tool. It is tested on several geothermal scenarios and wormholing phenomena occurring in carbonate dissolution.

Chapter 6 describes a fast and robust scheme for uncertainty quantification in fractured reservoirs. This includes utilizing the preprocessing strategy to create a hierarchical ensemble of possible reservoir models and simulating these on a coarser scale to partition the ensemble and perform a reduced uncertainty quantification on a subset of fine-scale models based on partition representatives.

2

METHODOLOGY

2.1. GOVERNING EQUATIONS IN CONTINUOUS FORM

This section briefly covers the governing equations of the multiphase multi-component reactive transport framework used for modelling efforts and expanded upon by this dissertation. The main contributions here comprise chemical (i.e., equilibrium and kinetic) formulation in the Operator-Based Linearization (OBL) approach and an efficient transmissibility update after porosity and permeability changes. All the fluid-flow and heat transfer results throughout this thesis are obtained using the equations outlined below which form the basis of the Delft Advanced Research Terra Simulator (DARTS) developed at the Delft University of Technology (DARTS, 2019).

The basic mass balance equations including the effect of chemical reactions as source/sink term following Kala and Voskov, 2020 are:

$$\frac{\partial n_c}{\partial t} + l_c + q_c = \sum_{k=1}^K v_{ck} r_k^K + \sum_{q=1}^Q v_{cq} r_q^Q, \quad c = 1, \dots, C + M, \quad (2.1)$$

where C is a number of fluid species and M is the number of mineral species, n_c is the overall mass of component, l_c is the total flux associated with that component, q_c is the total well flow rate associated with that component, v_{ck} is the stoichiometric coefficient associated with kinetic reaction k for the component c and v_{cq} is the stoichiometric coefficient associated with equilibrium reaction q for component c , r_k^K is the rate for kinetic reaction and r_q^Q is the equilibrium reaction rate.

The overall mass of components is defined as

$$n_c = \phi^T \sum_{j=1}^P (\rho_j s_j x_{cj}), \quad c = 1, \dots, C. \quad (2.2)$$

Here P stands for the total number of fluid phases, ρ_j is the density and s_j is the saturation of fluid phase j respectively, and x_{cj} is the mole fraction of component c in phase

j . This term indicates total mass of component c in all the fluid phases. For the solid mineral components, we use the following relationship:

$$n_m = \phi^T \rho_m z_m, \quad m = C + 1, \dots, M, \quad (2.3)$$

where ρ_m is the molar density of mineral phase m , \hat{s}_m is the mineral composition, and the total porosity ϕ^T term will be explained later.

The term l_c defines the flux of component c and is given as:

$$l_c = \nabla \cdot \sum_{j=1}^P (\rho_j x_{cj} \mathbf{u}_j - \rho_j \phi s_j d_{cj} \nabla x_{cj}), \quad c = 1, \dots, C, \quad (2.4)$$

where the term d_{cj} corresponds to the dispersion of component c in phase j . The term \mathbf{u}_j is the velocity of the phase j and is defined by Darcy's law:

$$\mathbf{u}_j = -\mathbf{K} \frac{k_{rj}}{\mu_j} (\nabla p - \rho_j g \nabla h) \quad j = 1, \dots, P. \quad (2.5)$$

Equation 2.1 can be written in a vector form:

$$\frac{\partial \mathbf{n}}{\partial t} + \mathbf{l} + \mathbf{q} = \mathbf{V}^Q \mathbf{r}^Q + \mathbf{V}^K \mathbf{r}^K, \quad (2.6)$$

where $\mathbf{n} = (n_1, \dots, n_{C+M})^T$, $\mathbf{l} = (l_1, \dots, l_C)^T$, $\mathbf{q} = (q_1, \dots, q_C)^T$ is the well flow rate, \mathbf{V}^Q and \mathbf{V}^K are the stoichiometric matrix respectively for the equilibrium and kinetic reactions while $\mathbf{r}^Q = (r_1^Q, \dots, r_Q^Q)^T$ and $\mathbf{r}^K = (r_1^K, \dots, r_K^K)^T$ are the equilibrium and kinetic reaction rate vectors.

If chemical equilibrium reactions are included into the calculation, this means that several chemical species can be in local equilibrium at each nonlinear iteration and therefore the dimensionality of the physical system (i.e., the number of global equations that are solved, $C + M$) can be reduced accordingly. This method in reactive transport literature is known as the total concentration method Lichtner, 1996 where the global equations are solved for primary species. In the reservoir simulation literature this is typically referred to as element conservation Fan et al., 2012; Farshidi et al., 2013; Kala and Voskov, 2020; Sriyanong, 2013. In the special case of having only equilibrium reactions, it is possible to find a matrix \mathbf{E} , also called the rate annihilation matrix, that lies in the left nullspace of \mathbf{V} such that $\mathbf{E}\mathbf{V} = \mathbf{0}$. In the general case of having both kinetic and equilibrium reactions, the matrix is defined as

$$\mathbf{E} = \begin{bmatrix} \mathbf{E}^K \\ \mathbf{E}^Q \end{bmatrix}, \quad (2.7)$$

such that

$$\mathbf{E}\mathbf{V}\mathbf{r} = \begin{bmatrix} \mathbf{E}^K \mathbf{V}^K \mathbf{r}^K \\ \mathbf{E}^Q \mathbf{V}^Q \mathbf{r}^Q \end{bmatrix} = \begin{bmatrix} \mathbf{r}^K \\ \mathbf{0} \end{bmatrix}, \quad (2.8)$$

where \mathbf{E}^K is the part related to the kinetic reactions with size $K \times n_c$ and \mathbf{E}^Q is the part related to the equilibrium reactions with size $Q \times n_c$. Therefore, when multiplying equation (2.6) with the \mathbf{E} matrix we obtain

$$\frac{\partial \mathbf{E}\mathbf{n}}{\partial t} + \mathbf{E}\mathbf{l} = \begin{bmatrix} \mathbf{r}^K \\ \mathbf{0} \end{bmatrix}_{(K+n_e) \times 1}, \quad (2.9)$$

where the first K equations are related to the kinetic equations present in the system and the remaining n_e equations are related to the element conservation equations (here element refers to any entity that cannot be broken down into smaller pieces).

The following equation describes the conservation of energy required for the geothermal simulations:

$$\frac{\partial}{\partial t} \left(\phi \sum_{p=1}^P \rho_p s_p U_p + (1 - \phi) U_r \right) + \nabla \cdot \sum_{p=1}^P h_p \rho_p \mathbf{v}_p + \nabla \cdot (\kappa \nabla T) + \sum_{p=1}^P h_p \rho_p q_p = 0, \quad (2.10)$$

where U_p is the internal energy of fluid phase p , U_r is the rock internal energy, h_p is the enthalpy of phase p , κ is the thermal conduction, and T is the temperature. All governing assumptions and properties can be found in (Wang et al., 2021; Wang et al., 2020).

2.2. PHASE BEHAVIOR OF COMPOSITIONAL SYSTEM

The following equations are used for thermodynamic equilibrium of multicomponent system. A component is in thermodynamic equilibrium if the chemical potential of the components in both phases are equal:

$$f_{c1} - f_{cj} = 0, \quad c = 1, \dots, C, \quad j = 2, \dots, P. \quad (2.11)$$

The fugacity of a component in a particular phase is given by

$$f_{cj} = \phi_{cj} x_{cj} p, \quad c = 1, \dots, C, \quad j = 1, \dots, P, \quad (2.12)$$

where ϕ_{cj} is the fugacity coefficient of an ideal mixture. Equation 2.11 can also be written in terms of the partition coefficients $K_{cj} = \phi_{cj} / \phi_{c1}$:

$$K_{cj} x_{c,1} - x_{cj} = 0, \quad c = 1, \dots, C, \quad j = 2, \dots, P. \quad (2.13)$$

The system of equations (2.11) or (2.13) can be directly coupled with conservation equations (2.6) and solved in a fully coupled manner using the global Newton solver. Such formulation is often called global or natural formulation. However, when a new phase appears in the process of simulation, the phase equilibrium should be calculated based on the local approximation of the mass from equation (2.6).

The system of equations can be closed with the following algebraic constraints:

$$\sum_{p=1}^P s_p = 1, \quad (2.14)$$

and

$$\sum_{c=1}^C x_{cj} = 1, \quad j = 1, \dots, P \quad (2.15)$$

In case of equilibrium reactions, we need to add the law of mass action to either global or local systems (depends on the preferred nonlinear formulation) which is given as:

$$Q_q - K_q = \prod_{c=1}^C a_{cw}^{v_{cq}} - K_q = 0, \quad q = 1, \dots, Q. \quad (2.16)$$

Here Q is the number of equilibrium reactions, Q_q is the reaction quotient whereas K_q is the equilibrium reaction quotient or equilibrium solubility limit in case of dissolution/-precipitation of minerals, a_{cw} is the activity of the component c in the aqueous phase, and v_{cq} is the reaction stoichiometric coefficient.

2

2.3. POROSITY TREATMENT

For an accurate treatment of solid phase dissolution and precipitation at the continuous level, the treatment of the rock porosity should be adjusted. Conventionally the control volume (denoted as bulk volume) is subdivided into two regions, void space (occupied by all mobile phases, such as liquid and vapor phase) and solid skeleton (occupied by immobile species, for example, carbonate rock).

In most contributions from the literature, the porosity ϕ depends on the concentrations of the minerals according to the relationship:

$$\phi = 1 - \sum_{m=1}^M \frac{\mathcal{M}_m c_{ms}}{\rho_m}, \quad (2.17)$$

where M is the number of reactive minerals, \mathcal{M}_m is the molar mass of mineral m , ρ_m is the mass density of mineral m and c_{ms} represents and the molar concentration of mineral m .

In equation (2.17), it is not clear which properties are spatially correlated and which are changing in time due to dissolution or precipitation reactions. Following the approach suggested in Farshidi, 2016, we can subdivide the volume of the solid skeleton further into a reactive part which can be modified by chemical reactions and a non-reactive part (which is unaltered by any chemical reaction, and therefore constant throughout the simulation) (Figure 2.1).

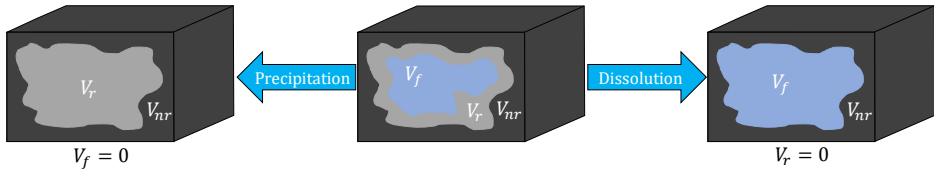


Figure 2.1 Schematic of the different (continuum) volumes in the computational domain. The domain consists of three distinct regions, the fluid volume which is occupies by all the mobile phases (liquid and gaseous in the case of two phase flow), the reactive volume which consist of solid phases that can react or precipitate, and finally the nonreactive volume (the part of the control volume which doesn't participate in any chemical reaction).

Mathematically this is expressed as follows

$$V_b = V_f + V_r + V_{nr}, \quad (2.18)$$

and V_r denotes reactive volume and V_{nr} represents the non-reactive volume (not altered by any chemical reaction). Dividing this by the total (bulk) volume gives

$$1 = \phi + \phi_r + \phi_{nr} = \phi^T + \phi_{nr}, \quad (2.19)$$

where ϕ_r represents the reactive volume fraction, ϕ_{nr} is the non-reactive volume fraction, and ϕ^T is the total porosity defined as the sum of the fluid porosity and reactive volume fraction. Since only the reactive volume and fluid porosity can change due to chemical reactions, it follows directly that the total porosity remains constant throughout simulation (when neglecting compressibility). This and the changes in volume fractions due to precipitation and dissolution is illustrated in Figure 2.1.

Note that the fluid porosity can always be obtained with the following constitutive equation

$$\phi = \phi^T \left(1 - \sum_{m=1}^M \hat{s}_m \right), \quad (2.20)$$

where M is the number of solid phases (occupying the reactive volume fraction) and \hat{s}_m is the saturation of solid phase. Please note that the s_α is the fluid saturation (defined over the pore volume) while \hat{s}_m is the solid saturation of mineral phase m (defined over the pore and reactive rock volume).

Solid saturation in the total porosity formulation can be found with the following equation

$$\hat{s}_m = \frac{V_{r,m}}{V_r + V_f}, \quad (2.21)$$

where $V_{r,m}$ is the volume of mineral phase m defined as

$$V_{r,m} = \frac{\mathcal{M}_m}{\rho_m} n_m^r, \quad (2.22)$$

where n_m^r is the total number of moles of mineral m that can participate in any reaction. This means that in the total porosity formulation, the molar concentration of mineral m is defined as

$$\hat{c}_m = \frac{n_m^r}{V_r + V_f}. \quad (2.23)$$

and since

$$c_{ms} = \frac{n_m^r + n_m^{nr}}{V_b} = \frac{n_m^r}{V_f + V_r} \frac{V_f + V_r}{V_b} + \frac{n_m^{nr}}{V_b} = \hat{c}_m \phi^T + \frac{n_m^{nr}}{V_b}, \quad (2.24)$$

where n_m^{nr} is the total number of moles of mineral m that cannot participate in any reaction. Therefore, using eq. (2.17) and eq. (2.24), we get

$$\begin{aligned} \phi &= 1 - \sum_{m=1}^M \frac{\mathcal{M}_m c_{ms}}{\rho_m} \\ &= 1 - \sum_{m=1}^M \frac{\mathcal{M}_m}{\rho_m} \left(\hat{c}_m \phi^T + \frac{n_m^{nr}}{V_b} \right) \\ &= 1 - \sum_{m=1}^M \hat{s}_m \phi^T - \phi_{nr} \\ &= (\phi^T + \phi_{nr}) - \sum_{m=1}^M \hat{s}_m \phi^T - \phi_{nr} \\ &= \phi^T \left(1 - \sum_{m=1}^M \hat{s}_m \right). \end{aligned} \quad (2.25)$$

2.4. FLUID AND ROCK DESCRIPTION

The relative permeability functions used in throughout this thesis consist of the Brooks-Corey description, more precisely

$$k_{r,\alpha} = k_{r,\alpha}^e \left(\frac{s_\alpha - s_{r,\alpha}}{1 - \sum_{p \in P} s_{r,p}} \right)^{n_\alpha}, \quad (2.26)$$

where $k_{r,\alpha}$ is the relative permeability, $k_{r,\alpha}^e$ is the maximum relative permeability, $s_{r,\alpha}$ is the residual saturation, and n_α is the Corey exponent of phase α respectively. In the absence of any residual saturation and $P = \{w, g\}$ (i.e., liquid (water) and vapor (gas) phase present as fluid phases in the system), this results in

$$k_{rw} = k_{rw}^e (s_w)^{n_w}, \quad (2.27)$$

for the water and

$$k_{rg} = k_{rg}^e (1 - s_w)^{n_g}, \quad (2.28)$$

for the gas relative permeability.

For the phase density, a slightly compressible fluid is assumed, particularly

$$\rho_\alpha = \rho_{\alpha,0} (1 + C_\alpha (p - p_0)). \quad (2.29)$$

Here C_α is compressibility and $\rho_{\alpha,0}$ is density at pressure p_0 . This is assumed to hold for each of the three phases present in the system, water, gas, and solid. Additional physical complexity can be obtained by adopting a fully compressible model for the gas phase.

2.5. DISCRETIZATION

After applying a finite-volume discretization on a general unstructured grid (using a two-point flux approximation for the fluxes across interfaces with upstream weighting) and a backward (implicit) Euler time discretization strategy we obtain the discretized conservation equation (ignoring capillarity and gravity) for fluid species

$$\begin{aligned} \frac{V}{\Delta t} \left[\left(\phi^T \sum_{j=1}^P (\rho_j s_j x_{cj}) \right)^{n+1} - \left(\phi^T \sum_{j=1}^P (\rho_j s_j x_{cj}) \right)^n \right] - \sum_l \left(\sum_{j=1}^P x_{cj}^l \rho_j^l \Gamma_{nr}^l \Gamma^{M,l} \Delta p \right) \\ - \sum_l \left(\sum_{j=1}^P \rho_j \phi s_j d_{cj} \Gamma_d^l \Delta x_{cj} \right) + \sum_{j=1}^P \rho_j x_{cj} q_j = V \sum_k^K v_{ck} r_k^K + V \sum_q^Q v_{cq} r_q^Q, \quad c = 1, \dots, C \end{aligned} \quad (2.30)$$

where Γ_{nr}^l is the static advective transmissibility component, $\Gamma^{M,l}$ is the transmissibility multiplier, and Γ_d^l is the static diffusive transmissibility component for interface l respectively. The discretized conservation equation for the mineral species is given as follows

$$\frac{V}{\Delta t} \left[(\phi^T \rho_m z_m)^{n+1} - (\phi^T \rho_m z_m)^n \right] = V \sum_k^K v_{mk} r_k^K + V \sum_q^Q v_{mq} r_q^Q, \quad m = 1, \dots, M \quad (2.31)$$

and the discretized energy conservation equation

$$\begin{aligned} \frac{V}{\Delta t} \left[\left(\phi \sum_{j=1}^P \rho_j s_j U_j + (1-\phi) U_r \right)^{n+1} - \left(\phi \sum_{j=1}^P \rho_j s_j U_j + (1-\phi) U_r \right)^n \right] \\ - \sum_l \left(\sum_{j=1}^P h_j^l \rho_j^l \Gamma_{nr}^l \Gamma^{M,l} \Delta p + \Gamma_c^l \Delta T^l \right) + \sum_{j=1}^P h_j \rho_j q_j = 0 \end{aligned} \quad (2.32)$$

2.5.1. DISCRETE FRACTURE MODEL (DFM)

The general unstructured discretization follows the Discrete Fracture Model (DFM). The ideas of the modern DFM approach can be found in Gureghian, 1975 where Finite Element Methods (FEM) was applied, and in Helmig et al., 1997 where Finite Volume Method (FVM) was used. In modern reservoir simulation, which includes highly implicit time approximation using finite-volume discretization on unstructured grids, the DFM methodology has been introduced by Karimi-Fard et al., 2004. This approach has been implemented in Delft Advanced Research Terra Simulator (DARTS). In the DMF approach, fractures are represented by a lower dimensional feature in the gridding domain (lines in 2D and planes in 3D). However, in the simulation domain the fractures are assigned a width depending on their aperture (i.e., in a 3D computational domain each fracture control volume is 3D as well) (Figure 2.2).

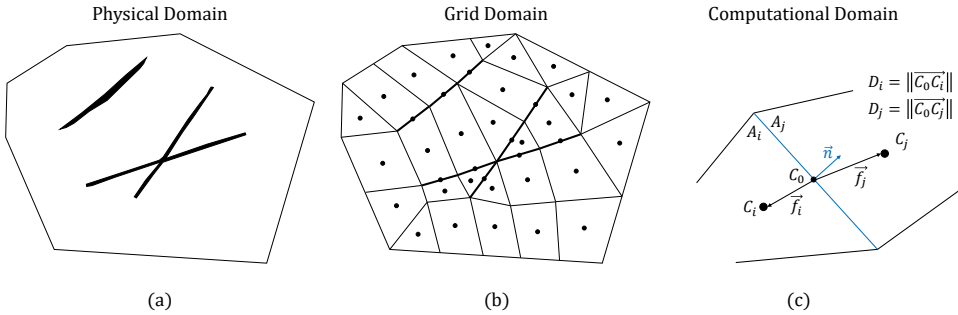


Figure 2.2 Schematic representation of the DFM model (modified from Wang et al., 2021).

The transmissibility between any two control volumes is given by the following equation

$$T_{ij} = \frac{\alpha_i \alpha_j}{\alpha_i + \alpha_j}, \quad (2.33)$$

where α_i is given by

$$\alpha_i = \frac{A_i k_i}{D_i} \mathbf{n}_i \cdot \mathbf{f}_i, \quad (2.34)$$

where A_i is the area of interface i , D_i is the distance from the i -th cell to the i -th interface, \mathbf{n}_i is the unit normal vector acting perpendicularly on the centroid of the i -th interface, and \mathbf{f}_i is the unit vector through the centroid of the i -th interface and the centroid

of the i -th grid block respectively. When more than two fractures intersect, the star-delta transformation is applied. The small control volume of intersecting fractures are omitted using the following two assumptions: $k_0 \approx k_1$ and $D_0 \ll D_1$ therefore $T_{01} = \alpha_1$ and $T_{12} = (\alpha_1 \alpha_2) / (\alpha_1 + \alpha_2)$, where the subscript 0 refers to the smaller intermediate volume of the two intersecting fractures (1, 2).

2.5.2. TRANSMISSIBILITY MULTIPLIER

Permeability is generally a function of porosity, grain-size distribution, tortuosity, and specific surface area (Steeffel et al., 2015). Dissolution and precipitation processes affect rock characteristics and therefore the permeability. Changes in permeability are often modeled as an explicit function of changes in porosity, ignoring other rock characteristics. An example of this is the well-known and commonly used power-law approximation of the Carman-Kozeny relation (Bear, 2013), given as follows

$$k = k_0 \left(\frac{\phi^T}{\phi^0} \right)^A, \quad (2.35)$$

where k is the current permeability, k_0 is the initial permeability, ϕ^0 is the initial fluid porosity, and A is typically determined from experimental data (core experiments).

This simple expression for the porosity–permeability relations may not reflect the complex relationship of porosity and permeability in geologic media that depends on an interplay of many factors, such as pore size distribution, pore shapes, and connectivity (Steeffel et al., 2015; Verma & Pruess, 1988). However, laboratory experiments have shown that modest reductions in porosity from mineral precipitation can cause large reductions in permeability (Vaughan, 1987).

The non-reactive permeability is defined here as the maximum attainable permeability, namely at $\phi_r = 0$ or $\phi = \phi^T$. Which follows directly from plugging into equation 5.18

$$k_{nr} = k_0 \left(\frac{\phi^T}{\phi^0} \right)^A. \quad (2.36)$$

Furthermore, the geometric part of the transmissibility is defined in the following way

$$\Gamma(k_{nr}^a, k_{nr}^b, \phi^{a,b}) = \Gamma_{nr}(k_{nr}^a, k_{nr}^b) \cdot \Gamma^M(\phi^{a,b}), \quad (2.37)$$

where the superscripts indicate grid-block a and b , and the non-reactive part of the transmissibility is defined as

$$\Gamma_{nr}(k_{nr}^a, k_{nr}^b) = \frac{\alpha_{nr}^a \alpha_{nr}^b}{\alpha_{nr}^a + \alpha_{nr}^b}. \quad (2.38)$$

Here α_{nr}^i is the projected non-reactive permeability of the i -th grid-block on the currently investigated interface, defined as

$$\alpha_{nr}^i = \frac{A^i k_{nr}^i}{D^i} \mathbf{n}^i \cdot \mathbf{f}^i, \quad (2.39)$$

where A^i is the area of interface i , D^i is the distance from the i -th cell to the i -th interface, \mathbf{n}^i is the unit normal vector acting perpendicularly on the centroid of the i -th interface, and \mathbf{f}^i is the unit vector through the centroid of the i -th interface and the centroid of the i -th grid block respectively.

In the DARTS framework it is possible to use upstream weighed porosity for the transmissibility multiplier as well as interface weighed porosity for the multiplier. The interface porosity used in the transmissibility multiplier is therefore defined as

$$\phi^{a,b} = \begin{cases} \phi_a, & \text{if } p^a > p^b, \\ \phi_b, & \text{if } p^b > p^a, \end{cases} \quad (2.40)$$

in the case of upstream weighted or as

$$\phi^{a,b} = \frac{\phi^a + \phi^b}{2} \quad (2.41)$$

in the case of interface averaged. The resulting multiplier is defined mathematically as follows

$$\Gamma^M(\phi^{a,b}) = \left(\frac{\phi^{a,b}}{\phi^T} \right)^A = \left(\frac{\phi^T (1 - \sum_{m=1}^M \hat{s}_m)}{\phi^T} \right)^A = \left(1 - \sum_{m=1}^M \hat{s}_m \right)^A. \quad (2.42)$$

It is clear that the Γ^M is solely a function of the state, particularly the fluid porosity or solid saturation in either block a , b , or both. Since in DARTS only a single state is known at the time when operators are computed (precisely the upstream state), and the transmissibility multiplier is included in the flux operator, some adjustments are necessary. An extra operator is generated, namely the porosity operator which is defined as

$$\Phi(\omega) = 1 - \sum_{m=1}^M \hat{s}_m, \quad (2.43)$$

where ω is the state vector (with pressure and compositions).

The multiplier is defined in such a way that it satisfies two conditions, namely

- $\hat{s}_m = 0 \rightarrow \phi = \phi^T \rightarrow \Gamma^M(\phi^T) = 1$, such that $\Gamma(k_{nr}^a, k_{nr}^b, \phi^{a,b}) = \Gamma_{nr}(k_{nr}^a, k_{nr}^b)$,
- $\hat{s}_m = 1 \rightarrow \phi = 0 \rightarrow \Gamma^M(0) = 0$ such that $\Gamma = 0$.

Since $\phi \in [0, \phi^T]$, the multiplier $\Gamma^M(\phi^{a,b})$ becomes a monotonically increasing function on the closed interval $[0, 1]$, and for any solid saturation the transmissibility value can be approximated and capture permeability changes due to dissolution/precipitation. Furthermore, if a more complicated transmissibility multiplier is used, e.g. not the power law approximation but the Carman-Kozeny relation, the transmissibility multiplier becomes a function of both the fluid porosity as well as the total porosity. Since the total porosity is space dependent, it is necessary to separate the multiplier into two parts (space and state dependent).

2.6. OPERATOR-BASED LINEARIZATION (OBL)

Operator-Based Linearization (OBL) is used to linearize the system of nonlinear conservation equations. OBL is a novel way of performing the linearization step. The discrete form of the mathematical equations is grouped into state-dependent operators and space-dependent relations. The parameter space of the problem is discretized, where each axis is split by the uniformly distributed set of supporting points. Any point in the parameter space belongs to a certain hypercube bounded by supporting points. Next, the nonlinear operators are subsequently calculated exactly in a set of supporting points at a preprocessing stage or adaptively. At the simulation stage, the operators' values and their derivatives are evaluated using multi-linear interpolation inside a particular hypercube in the parameter space where the specific simulation state belongs. The multi-linear interpolation of the most nonlinear part of the governing equations provides simple, exact, and above all flexible Jacobian assemble for the nonlinear solution procedure. Following Khait and Voskov, 2018a; Khait and Voskov, 2017; Voskov, 2017, the equations in operator form are written as follows:

$$V\phi^T[\alpha_c(\omega) - \alpha_c(\omega_n)] - \Delta t \sum_{l \in L(i)} \sum_{j=1}^P [\Gamma_{nr}^l \Gamma^{M,l} \beta_{cj}^l(\omega^u) \Delta p^l + \phi^T \Gamma_d^l \gamma_j^l(\omega) \Delta \chi_{cj}] + \Delta t V \delta_c(\omega) = 0. \quad (2.44)$$

where V is the control volume, ω_n is the physical state of block i at the previous timestep, ω is the physical state of block i at the new timestep, ω^u is the physical state of upstream block, and $L(i)$ is a set of interfaces for gridblock i .

With state-dependent operators defined as:

$$\alpha_{cf}(\omega) = \left(1 - \sum_{m=1}^M \hat{s}_m\right) \left(1 + c_r(p - p_{ref})\right) \sum_{j=1}^{n_p} x_{cj} \rho_j s_j, \quad c = 1, \dots, C; \quad (2.45)$$

$$\alpha_{ms}(\omega) = \rho_m z_m, \quad m = 1, \dots, M; \quad (2.46)$$

$$\beta_{cj}(\omega) = x_{cj} \rho_j k_{rj} / \mu_j, \quad c = 1, \dots, C, \quad j = 1, \dots, P; \quad (2.47)$$

$$\gamma_j(\omega) = \left(1 - \sum_{m=1}^M \hat{s}_m\right) \left(1 + c_r(p - p_{ref})\right) s_j, \quad j = 1, \dots, P; \quad (2.48)$$

$$\chi_{cj}(\omega) = D_{cj} \rho_j x_{cj}, \quad c = 1, \dots, C, \quad j = 1, \dots, P; \quad (2.49)$$

$$\delta_c(\omega) = \sum_{j=1}^{n_p} v_{cj} r_j(\omega), \quad c = 1, \dots, C. \quad (2.50)$$

The discretized energy conservation equation in operator form can be written as:

$$\begin{aligned} V\phi_0[\alpha_{ef}(\omega) - \alpha_{ef}(\omega_n)] - \Delta t \sum_{l \in L(i)} \sum_{j=1}^P [\Gamma^l \beta_{ej}^l(\omega^u) \Delta p^l + \Gamma_d^l \gamma_j(\omega) \Delta \chi_{ej}] + \Delta t V \delta_e(\omega) \\ + (1 - \phi_0) V U_r [\alpha_{er}(\omega) - \alpha_{er}(\omega_n)] - \Delta t \sum_{l \in L(i)} (1 - \phi_0) \Gamma_d^l \kappa_r \alpha_{er}(\omega) \Delta \chi_{er} = 0, \end{aligned} \quad (2.51)$$

where:

$$\alpha_{ef}(\omega) = \left(1 - \sum_{m=1}^M \hat{s}_m\right) \left(1 + c_r(p - p_{ref})\right) \sum_{j=1}^P \rho_j s_j U_j; \quad (2.52)$$

$$\beta_{ej}(\omega) = h_j \rho_j k_{rj} / \mu_j, \quad j = 1, \dots, P; \quad (2.53)$$

$$\chi_{ej}(\omega) = \kappa_j T_j, \quad j = 1, \dots, P; \quad (2.54)$$

$$\delta_e(\omega) = \sum_{j=1}^{n_j} v_{ej} r_{ej}(\omega) \quad (2.55)$$

In addition, for accounting the energy of rock, three additional operators should be defined:

$$\alpha_{eri}(\omega) = \frac{U_r}{1 + c_r(p - p_{ref})}, \quad \alpha_{erc}(\omega) = \frac{1}{1 + c_r(p - p_{ref})}, \quad \chi_{er}(\omega) = T_r. \quad (2.56)$$

α_{eri} and α_{erc} represent the rock internal energy and rock conduction, respectively. U_r is a state-dependent parameter, thus these two rock energy terms are treated separately.

3

AN ADVANCED DISCRETE FRACTURE METHODOLOGY FOR FAST, ROBUST, AND ACCURATE SIMULATION OF ENERGY PRODUCTION FROM COMPLEX FRACTURE NETWORKS

Fracture networks are abundant in subsurface applications (e.g., geothermal energy production). Fractured reservoirs often have a very complex structure, making modeling flow and transport in such networks slow and unstable. Consequently, this limits our ability to perform uncertainty quantification and increases development costs and environmental risks. This study provides an advanced methodology for simulation based on Discrete Fracture Model (DFM) approach. The preprocessing framework results in a fully conformal, uniformly distributed grid for realistic 2D fracture networks at a required level of precision. The simplified geometry and topology of the resulting network are compared with input (i.e., unchanged) data to evaluate the preprocessing influence. The resulting mesh-related parameters, such as volume distributions and orthogonality of control volume connections, are analyzed. Furthermore, changes in fluid-flow response related to preprocessing are evaluated using a high-enthalpy two-phase flow geothermal simulator. The simplified topology directly improves meshing results and, consequently, the accuracy and efficiency of numerical simulation. The main novelty of this work is the introduction of an automatic preprocessing framework allowing us to simplify the fracture network

Parts of this chapter have been published in Water Resources Research **58**, e2021WR030743 (2022) de Hoop et al., [2021b](#).

down to required level of complexity and addition of a fracture aperture correction capable of handling heterogeneous aperture distributions, low connectivity fracture networks, and sealing fractures. The graph-based framework is fully open-source and explicitly resolves small-angle intersections within the fracture network. A rigorous analysis of changes in the static and dynamic impact of the preprocessing algorithm demonstrates that explicit fracture representation can be computationally efficient, enabling their use in large-scale uncertainty quantification studies.

3

3.1. INTRODUCTION

Many subsurface energy applications (e.g., geothermal energy production) rely on accurate numerical simulations of fluid flow and mass or heat transport in fractured porous media. A large class of methods is available for numerical modeling of fracture networks. It may consist of various approaches to the homogenization of fractures network, including Dual Porosity (Barenblatt, 1960; Warren & Root, 1963) and various MINC models (Karimi-Fard et al., 2006; Pruess & Narasimhan, 1982), or different versions of Embedded Discrete Fracture Models (EDFM) starting from already classic approaches (Hajibeygi et al., 2011; Li & Lee, 2008) to projection-based technique (HosseiniMehri et al., 2020; Ҙene et al., 2017). Some hybrid versions combining EDFM with homogenized fractured networks at two different scales also exist (Li & Voskov, 2021).

Another class of model is Discrete Fracture Model (DFM), where fracture segments are described as a lower-dimensional object on the mesh. The ideas of the modern DFM approach can be found in Gureghian, 1975 where Finite Element Methods (FEM) was applied, and in Helmig et al., 1997 where Finite Volume Method (FVM) was used. In modern reservoir simulation, which includes highly implicit time approximation using finite-volume discretization on unstructured grids, the DFM methodology has been introduced by Karimi-Fard et al., 2004. The DFM approach is often preferred in detailed geological studies due to its accuracy (Berre et al., 2019; Flemisch et al., 2018; Moinfar et al., 2011; Wong et al., 2020). DFM models typically require a high meshing accuracy to resolve the fracture networks' complex geometry, thereby drastically increasing the computational complexity and rendering them unusable for uncertainty quantification purposes (Jung et al., 2013; Nejadi et al., 2017; Spooner et al., 2021). More recently, the DFM approach in reservoir simulation has been enhanced for practical applications by fully coupling geomechanics (Garipov et al., 2016) and fracture propagation (Gallyamov et al., 2018). These complex physical processes typically require a fine modeling resolution to capture all the effects, further exposing the limitations of incorporating uncertainty quantification.

These limitations severely constrain the necessary low-risk, sustainable, and energy-efficient subsurface activities that are desired. One of the main factors of the considerable computational complexity of DFM models is the meshing artifacts (i.e., skinny triangles, small control volume sizes, and a large number of degrees of freedom) that result from using conformal meshes and related convergence issues (Geiger & Matthäi, 2014; Koohbor et al., 2020; Li & Li, 2019). Fracture network input data is typically acquired from outcrop analysis or statistical models. In outcrop analysis, raw output, either by manual or automatic interpretation, results in difficulties for the meshing software. These meshing artifacts are highlighted in Figure 3.1 and are well known in the existing litera-

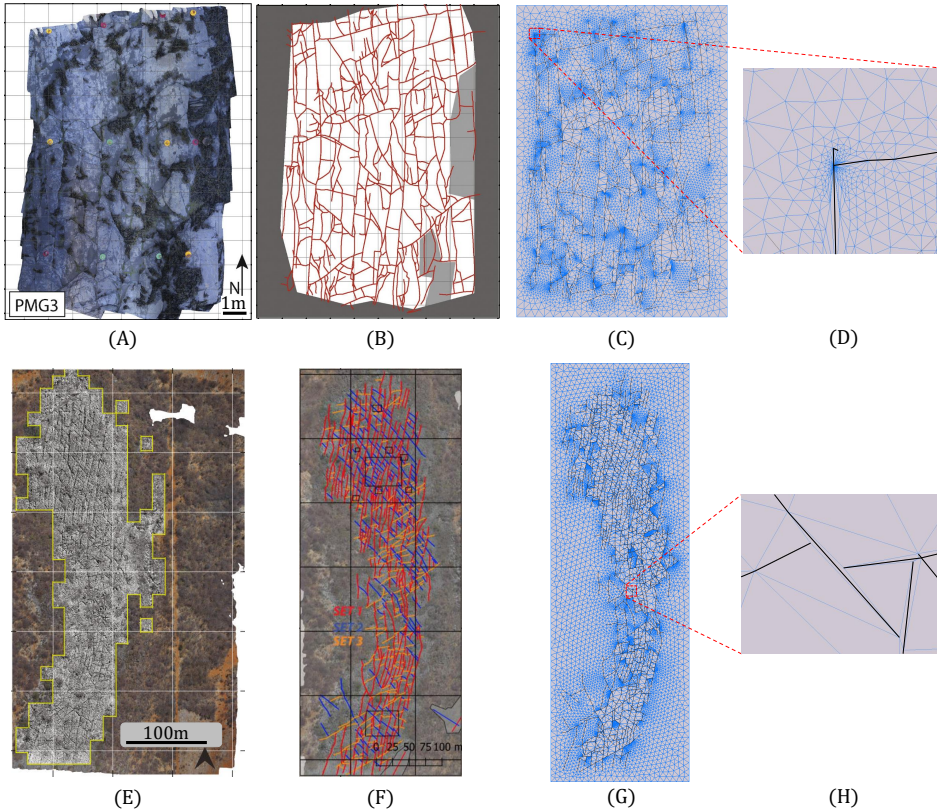


Figure 3.1 Fracture data acquisition, interpretation, and modeling steps. (A) and (E) Outcrop images obtained from the Whitby and Brejeões fieldwork area. (B) and (F) Manual interpretation of the fracture networks. (C) and (G) Conformal meshing results based on the raw interpretation. (D) and (H) is a zoom of the meshing artifacts due to complex fracture interaction. (A) and (B) Taken from Houben et al., 2017. (E) and (F) Taken from Boersma et al., 2019.

ture (Berre et al., 2019; Karimi-Fard & Durlofsky, 2016; Mallison et al., 2010; Mustapha & Mustapha, 2007; Reichenberger et al., 2006).

Several preprocessing strategies have been proposed in the literature to address the challenges of constructing a conformal mesh for complex natural fracture networks. However, the investigation of a numerically convergent solution after applying the preprocessing procedure, a thorough examination of the topology changes as a function of discretization accuracy, and the application to uncertainty quantification have not been adequately studied. Furthermore, in most existing methods, the meshing challenges related to fracture segments intersecting at a small angle are only implicitly resolved. For example, in most studies, an algebraic constraint is used for merging nodes, but the angle at which fractures intersect is not explicitly checked. This means that some meshing issues are not resolved. Finally, in the existing fracture preprocessing methods, variability of the fracture aperture is not taken into account.

Therefore, we have developed an open-source preprocessing framework that borrows concepts from early work in this area (Koudina et al., 1998; Maryška et al., 2005) and more recent approaches (Karimi-Fard & Durlofsky, 2016; Mallison et al., 2010; Mustapha & Mustapha, 2007). It differs from other graph simplification works, such as Wellman et al., 2009, where small (low permeable) fractures are iteratively removed. According to prescribed algebraic constraints, our preprocessing procedure merges nodes and resolves fractures that intersect at a significantly small angle that would otherwise introduce additional meshing challenges. To capture variable aperture distribution and low connectivity networks, in addition to previous methodologies, an aperture correction is added to the method presented here. Most of the operations are formulated using graph theory, which results in simple bookkeeping of the incidence matrix operations (West et al., 2001). Using the developed framework, we can create a fully conformal uniformly distributed grid based on any realistic fracture network at the required level of accuracy.

Most data obtained from outcrop studies is in planar 2D view (Bisdorn et al., 2017). The available 3D data on fractures in the subsurface often consists of very coarse seismic cubes or borehole imaging logs. The attributes of the seismic cube are often too coarse to extract the exact fracture pattern, and the imaging logs only provide limited information at the well location (Boersma et al., 2020). Therefore, this paper focuses on 2D fracture characterization and the preprocessing technique, which improves the meshing and subsequent fluid-flow modeling. We analyze the static and dynamic performance of the preprocessing on changes in geometry and topology of the fracture network and resulting mesh and changes in flow response. Ultimately, this leads to a robust way of constructing a hierarchy of DFMs for uncertainty quantification of natural fracture networks (de Hoop & Voskov, 2021).

Notice that the main ingredients of the developed framework and flow modeling are not limited to 2D and can be effectively applied for fully 3D fracture networks (as shown by Karimi-Fard and Durlofsky, 2016 from which we borrow several concepts). In 3D, all the fractures are represented by planes and discretized into segments (i.e., sub-planes) using an unstructured mesh. The vertices and edges of the meshed fractures will constitute the graph of the 3D fracture network, and the same preprocessing algorithm we propose in this paper (i.e., merging nodes) can be applied. Fracture apertures can be assigned to each edge of the discretized fracture, implying that the fracture aperture correction could also be used. However, some difficulties (e.g., projection of fracture aperture from the sub-plane to the edge and back) may introduce specific difficulties. A more straightforward approach could be making several slices through the 3D volume, projecting the fractures onto each slice and performing the same preprocessing on each slice (Sanderson et al., 2019).

The paper is organized as follows. We start with the description of the input data used in this study followed by the theory for preprocessing, topology analysis, and fluid flow and energy transport modeling. Next, we describe all essential ingredients of the proposed framework, including intersection, node merging, straightening, and removing acute angles. The results section contains the analysis of the static and dynamic performance of the preprocessing framework. We finish the paper with a detailed discussion and conclusion.

3.2. MATERIALS AND METHODS

The accurate numerical representation of fracture networks in the subsurface is not the end goal of the modeling effort. The modeling objective is often to make better predictions on subsurface activities and their associated risks. Therefore, it is essential to test our preprocessing framework accordingly. This is done by investigating the changes introduced by the algorithm on the dynamic behavior of the subsurface (i.e., fluid flow response). Mainly, geothermal energy production is chosen (i.e., injection of cold water and production of hot water via a well doublet) to examine this. The methodology is presented here. First, a brief description of the fracture networks used in this work is given; second is a brief introduction to graph theory; third, a brief theoretical background on the topology of fracture networks is presented; fourth, the preprocessing method is presented; fifth, the relevant equations to model the physical processes are given; and, finally, the numerical approximation of governing equations is introduced.

3.2.1. FRACTURE NETWORK INPUT DATA

The performance of the preprocessing algorithm is examined for two realistic fracture networks, a synthetic test case, and a variable aperture distribution applied to one of the realistic fracture networks. The first is found in the Whitby Mudstone outcrop along the cliff coast North of Whitby (UK) (Houben et al., 2017). The second example is the fracture network observed in the carbonate outcrop in Brejões, Brazil (Boersma et al., 2019). Both networks are interpreted by hand; however, the developed method would also be very suitable for automatic fracture detection algorithms as presented in (Prabhakaran et al., 2019). The synthetic test case consists of a high permeable matrix and low permeable fractures with a narrow opening in the middle of the domain. The variable aperture model is applied to the Whitby fracture network (Figure 3.2).

The outcrop images and the manual interpretation of the fracture networks are displayed in Figure 3.1. Both networks show good connectivity at first glance. The main difference between the two networks is the angle at which the fractures intersect. In the Brejoes network, this angle is around 60, while the angle is closer to 90 degrees for the Whitby network. The proposed fracture networks significantly differ in scale (Brejoes 100-1000 m vs. Whitby 1-10 m scale). Both networks are scaled up to characteristic reservoir size in a geothermal doublet system (Willems & Nick, 2019) by a scalar multiplication to preserve relative lengths and angles, which simplifies the static and dynamic analysis. The scalar is chosen for each network such that the resulting length in the y-direction is roughly 1000 [m] for both cases which is a typical distance between wells in a geothermal doublet system. This scaling with a scalar multiplier can be safely done because of the fractal nature of fracture networks (i.e., the same pattern exists at several length scales) as discussed in Acuna and Yortsos, 1995.

For the dynamic analysis, it is assumed that the two realistic fracture network models have very low permeability (i.e., convective flow is mainly limited by the fracture network) to ensure that the effect of changes to the fracture network on the flow response can be observed. An important note is that not all manual interpretations record the intersection between all fracture segments (i.e., only the end nodes of the fractures are registered). This becomes important in the following section, where the graph is constructed based on the fracture network data. The two data arrays describing the frac-

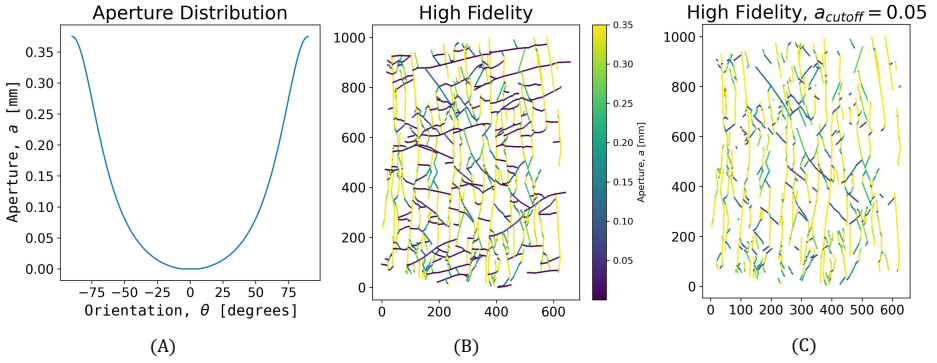


Figure 3.2 (A) and (B) Aperture distribution as a function of angle with the x -axis (i.e., E-W direction is zero degree angle) (similar to Boersma et al., 2021). (C) Shows only the high-permeable fractures and illustrates that variable aperture models can lead to low connectivity fracture networks.

ture networks used in this study can be found by the following link: <https://github.com/MakeLikePaperrr/Fracture-Preprocessing-Code>.

To incorporate geological realism, a variable aperture distribution is applied to the Whitby fracture network, similar to the aperture model in Boersma et al., 2021. The distribution and resulting apertures are visualized in Figure 3.2. Fractures oriented N-S are highly permeable, while fractures oriented E-W are low permeable. Figure 3.2 also depicts how a variable aperture leads to a much lower connectivity fracture network. Choosing a cutoff around 13% of the maximum conductivity leads to a large number of isolated fractures, hence, low connectivity.

3.2.2. GRAPH THEORY

As defined in Bollobás, 2013, a graph G is an ordered pair of disjoint sets (V, E) . The set of all vertices of graph G is denoted as $V = V(G)$, while the set of all edges of the graph G is denoted as $E = E(G)$. Edges of a graph join two vertices i and j such that $(i, j) \in E(G)$ and $i, j \in V(G)$. If $(i, j) \in E(G)$, it implies that i and j are *adjacent* vertices of G , and i and j are *incident* with the edge (i, j) .

Important matrix representations of the graph G are the following four matrices:

1. Incidence matrix: $B(G)$, which is a $n \times m$ matrix, where n is the number of vertices and m the number of edges of the graph. As previously indicated, whenever a vertex i is on an edge (i, \cdot) , the vertex i is incident with edge (i, \cdot) . Hence $B_{ij} = 1$ if vertex i is on the j -th edge otherwise $B_{ij} = 0$;
2. Degree matrix: $D(G)$, which is a $n \times n$ matrix describing the number of edges attached to each vertex. The degree matrix can be obtained using the follow equation $D = \text{diag}(B\mathbf{1})$, where $\text{diag}(\mathbf{v})$ is a function that constructs a square matrix with vector \mathbf{v} on its diagonal, and $\mathbf{1}$ is a vector of ones with size $m \times 1$. The degree matrix denotes the number of edges leaving a specific vertex.
3. Adjacency matrix: $A(G)$, which is a square $n \times n$ matrix, where n is the number of

vertices of the graph G . As previously mentioned, if the pair of vertices $(i, j) \in E(G)$, they are said to be adjacent. Hence $A_{ij} = 1$ if vertices i and j are on the edge (i, j) . Furthermore, for our purposes, it is assumed that the main diagonal is zero (i.e., $A_{ii} = 0$), which implies that no nodes are connected to itself. Note that A , B , and D are related through the following equation $A = BB^T - D$.

4. Discrete Laplacian matrix: $L(G)$ which can be found via the following equation $L = D - A = 2D - BB^T$. This matrix will be used for an alternative connectivity measure in the static analysis. The Discrete Laplacian is a matrix representation of the relationships defined in a graph.

A typical input data array \mathcal{F} that describes the fracture network contains the pairwise x- and y-coordinates of each fracture segment in the network. The first step is to convert this array into two different forms: an array that contains all the unique vertices in the graph (i.e., V) and the incidence matrix (B). This is done by using Algorithm 1 which is found in the Appendix. An important assumption of this construction of V and B is that no subsegments can intersect in other places than the vertices of the particular subsegments. As mentioned before, this is often not the case in the manual interpretation of fracture networks; hence we need to calculate all possible intersections before applying Algorithm 1 shown in the Appendix. A simple intersection calculation algorithm is provided in Section 3.2.4.

3.2.3. THE TOPOLOGY AND GEOMETRY OF FRACTURE NETWORKS

In this section, the required mathematical relations for performing the static analysis on the effect of the preprocessing method on fracture networks are explained. Topology is used to understand how the connectivity and abutment-intersection relations of the fracture network are changing due to the preprocessing. Furthermore, it is also essential to look at how several geometrical properties of the fracture network are changing (e.g., angles and lengths) through preprocessing.

Several authors have thoroughly investigated the application of topology to fracture networks (Manzocchi, 2002; Sanderson & Nixon, 2015). Isolated nodes are typically denoted with an I, abutments are characterized by a Y-node, and X-nodes are used to indicate intersecting fracture segments. This is illustrated in Figure 3.3. Translating the type of nodes to the graph notation, node I is of degree one, node Y is of degree three, and node X is degree four. In general, it is unusual that more than two lines intersect at exactly one point. However, our preprocessing method merges nodes and causes several nodes to have a degree > 4 . This causes us to consider all intersections of node degrees larger than four to be X type of nodes. This is used to plot the results in a ternary diagram (as shown in Figure 3.3). Classifying the fracture networks topology in this way allows us to use a proxy for the connectivity. Connectivity is often defined in this context as the average number of intersections per line. This changes slightly when allowing for nodes with a degree higher than four. Instead of the definition used in Balberg and Binenbaum, 1983

$$C_L = 4 \frac{N_Y + N_X}{N_I + N_Y}, \quad (3.1)$$

where N_I is the total number of I nodes, N_Y is the total number of Y nodes, and N_X is

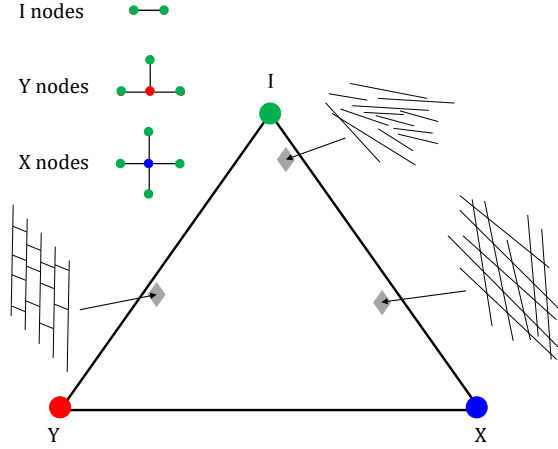


Figure 3.3 Illustration of topology in fracture networks. After Sanderson and Nixon, 2015.

the total number of X nodes, we use

$$C_L = 2 \frac{\sum_i^d w_i N_i}{N_I + N_Y}, \quad (3.2)$$

where w_i are the weights, N_i the total number of i node types in the network, and $i = \{Y, X, X+, X++ \dots\}$. $X+$ represents a vertex which is one degree higher than an X (i.e., degree five instead of four), $X++$ two degrees higher, etc. The weights are determined by the number of lines (but not edges) involved in the vertex type (e.g., N_Y involves two lines therefore $w_Y = 2$ while N_{X++} involves six edges and hence three lines therefore $w_{X++} = 3$). Please also note that all vertices of degree two are not used nor important in this analysis (i.e., a curved or a straight line are topologically the same).

An alternative connectivity measure is obtained by using the Discrete Laplacian of the graph. This matrix can be used for finding spanning trees of a given graph (i.e., connected fracture sets in the fracture network). Notably, each element of the Laplacian's null-space rational basis describes a connected component of the graph (Spielman, 2010). With this basis, we can find the number of connected fracture sets in our network and also each fracture that belongs to these components (i.e., sub-graphs). The connectivity measure is then calculated as the ratio between the cumulative length of the fractures in the largest spanning cluster and the cumulative length of all the fractures in the full network.

Geometrical properties such as angles and lengths of the fractures are obtained using simple trigonometry rules. An easy and fast way to calculate the angles of a fracture relative to the x-axis is to decompose the fracture into two components (i.e., $\Delta x = x_2 - x_1$ and $\Delta y = y_2 - y_1$). Then, the angle can be obtained using the following equation

$$\theta = \arctan\left(\frac{\Delta y}{\Delta x + \epsilon}\right), \quad (3.3)$$

where ϵ is a small perturbation to prevent the case of $\Delta x = 0$.

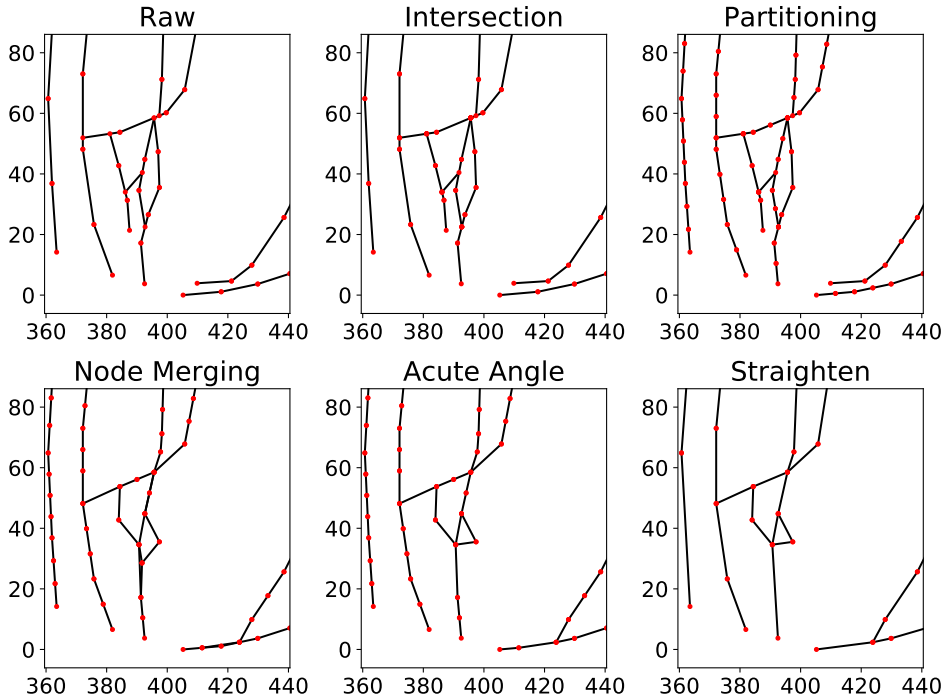


Figure 3.4 Illustration of the steps in the preprocessing workflow, from the raw data to a fully processed fracture network. The partitioning and node merging steps are a function of l_f while the acute angle and straighten steps are a function of $\theta_{a,min}$ and $\theta_{s,min}$ respectively. The smaller the l_f , the more precise the preprocessed network represents the raw data. However, small l_f means that the subsequent steps in the algorithm take substantially more time.

3.2.4. PREPROCESSING ALGORITHM

For an accurate and efficient graph-based approach, a correct graph representation of the fracture network is necessary. Since not all intersections are always given via the fracture network's geological (or automatic) interpretation, we need to calculate all the intersections to construct the correct graph for a fracture network. After finding all the intersections, the large fractures are partitioned into smaller fracture segments with length l_f . Then, any two nodes that are too close in proximity are merged. Subsequently, segments that intersect at an angle below a certain threshold denoted as $\theta_{a,min}$ are merged as well. Furthermore, an optional straightening of the fractures can be applied to simplify the meshing procedure further if fractures intersect within $[180 - \theta_{s,min}, 180 + \theta_{s,min}]$. These steps are illustrated in Figure 3.4 and thoroughly explained in the following sections. Lastly, an aperture correction procedure is proposed, which deals with variable apertures and connecting previously disconnected fractures.

INTERSECTIONS

Here the intersection detection method is described. The intersections are found by checking all combinations of any two edges. The combinations can be found via the binomial formula. All edges are parameterized, and a 2×2 linear system is solved for each pair of edges. Any intersection that occurs splits the two edges into four, and a vertex is added.

Let $\mathcal{X} = V \in \mathbb{R}^{n \times d}$ be the set of coordinates in the physical space of all unique vertices in the graph, where n is the number of vertices and d is the dimension of the physical space associated with the graph (i.e., fracture network). Then, let $\mathcal{P} = E \in \mathbb{R}^{m \times 2}$ be the set of all edges in the graph, where m is the number of edges and 2 represents the number of vertices associated with each edge. In other words, the j -th element of \mathcal{P} , $p_j \in \mathbb{N}^{2 \times 1}$, represents the set of two natural numbers associated with the two vertices of edge j . This means that $\mathcal{X}(p_j^1) = V(p_j^1, \cdot) = \mathbf{x}_j^1$ and $\mathcal{X}(p_j^2) = V(p_j^2, \cdot) = \mathbf{x}_j^2$, where $\mathbf{x}_j^1, \mathbf{x}_j^2 \in \mathbb{R}^d$ are the two vertices associated with edge j .

Finding all the intersections between any two edges, without any assumption on the location or orientation of the edge, can be done as follows. First parameterize all segments, using the following equation:

$$\mathbf{r}_j(t) = \mathbf{x}_j^1 + t(\mathbf{x}_j^2 - \mathbf{x}_j^1), \quad j = 1, \dots, m, \quad (3.4)$$

where $\mathbf{r}_j(t)$ represents a point on the fracture segments and t varies from 0 to 1 (from both end-points of the fracture segment). Find the pairs/combinations of edges, (i, j) , that can possibly intersect,

$$\binom{m}{2} = \frac{(m)^2}{2}, \quad (3.5)$$

and solve the following equation for each such combination

$$\mathbf{r}_j(t) = \mathbf{r}_i(s). \quad (3.6)$$

The two edges intersect directly whenever $0 < t, s < 1$ is true (note: $<$ instead of \leq indicates that the intersections at the end-points of segments are excluded). This simplifies to solving a $2 \times d$ system of equations for each intersection, such as

$$A\mathbf{x} = \mathbf{b}, \quad (3.7)$$

where $A = [\mathbf{x}_i^2 - \mathbf{x}_i^1, -(\mathbf{x}_j^2 - \mathbf{x}_j^1)]$, $\mathbf{x} = [t, s]^T$, and $\mathbf{b} = [\mathbf{x}_i^1 - \mathbf{x}_j^1]$.

The actual point of intersection is calculated by plugging the t that is obtained from Equation 3.7 into Equation 3.4. Every intersection involves exactly two segments, and the intersection id for those segments and x- and y-coordinate are stored in an array. After all the segments have been checked, a loop over this array allows us to manipulate intersections accordingly. For \mathcal{X} , this amounts to n_{int} new points, where n_{int} refers to the total number of intersection points. And for \mathcal{P} , each $p_j \in \mathcal{P}$ that contains at least one intersection gets replaced by $n_{int}^j + 1$ new segments, where n_{int}^j refers to the number of intersections on the j -th segment.

This naive way of finding the intersection has the downside of having a large computational complexity (as indicated above). To circumvent this, we applied a method

that takes advantage of the fact that most time is spent solving the linear 2×2 system in Equation 3.7. A simple check is applied for each pair of fracture segments to indicate if there can exist an intersection or not. Assuming the vertices of each edge (i.e., fracture) are ordered from smallest x-coordinate to largest, two edges can only have a possible intersection if the smallest x-coordinate of one of the two edges is smaller than the largest x-coordinate of the other edge (and vice versa for the y-coordinate). This significantly reduces the overall computational time of the algorithm as shown in the results section. Further reduction in computational time is achieved by parallelizing the algorithm, which is our ongoing development.

NODE MERGING

The node merging algorithm, in essence, is sequential. Each vertex (i.e., node) is added to the domain if it doesn't violate the algebraic constraint. This means that the distance between the newly added node and any other node already in the domain must be larger than $l_f \cdot h$, the node is merged into the closest node already in the domain. Parameter l_f refers to the accuracy at which the original fracture network will be processed and subsequently influences the optimal grid resolution, while h is a scaling parameter on the closed interval $[0.5, 0.86]$. The larger h is, the more simplified the resulting network becomes. Here, 0.5 is chosen as a lower bound such that any point on a fracture segment will get merged into one of the endpoints, while 0.86 is chosen as an upper bound such that any vertex perpendicular to the fracture segment with a distance equal to the height of an equilateral triangle with length l_f at the midpoint will get merged. The sequential nature of the algorithm implies that the order in which we add nodes to the domain affects the final result. Nodes that are added first are most likely placed in their exact location. Another essential consideration is the fracture aperture, since the conductive fractures often have a large impact on the fluid flow. Therefore, the fracture segments are ordered based on their aperture. If a single aperture model is applied, then segments are sorted based on the length of the fractures to minimize changes to the global structure of the network.

The length of each fracture segment, $L \in \mathbb{R}^m$, can be calculated in the following way:

$$L = \begin{pmatrix} \|\mathbf{x}_1^1 - \mathbf{x}_1^2\| \\ \vdots \\ \|\mathbf{x}_m^1 - \mathbf{x}_m^2\| \end{pmatrix}. \quad (3.8)$$

Then we define the order of adding segments, O_{segm} , from largest to smallest:

$$O_{\text{segm}} = \begin{cases} \{i \in \mathbb{N} \mid \forall l_i \in L, l_i \geq l_{i+1}\}, & \text{if } a_i = a \\ \{i \in \mathbb{N} \mid \forall a_i \in A, a_i \geq a_{i+1}\}, & \text{otherwise} \end{cases} \quad (3.9)$$

where a_i is the aperture of fracture segment i , and A is the list of all fracture apertures.

From now on, for simplicity, it is assumed that $h = 1/2$. This means that $\frac{l_f}{2}$ is the minimum distance between each vertex in the simplified graph. To achieve this, a partitioning algorithm that divides each fracture segment in $m_i = \max(1, \text{round}(l_i/l_f))$ sub-segments is executed. See Algorithm 2 for the detailed description.

Now we can construct the graph representation of the ordered and partitioned fracture network, using Algorithm 1 and substituting \mathcal{F} with \mathcal{F}_{new} and m with m_{new} . Furthermore, the problem is that vertices are added to the domain and not necessarily edges. Therefore, we need to determine the order in which vertices should be added to the domain. The order of the vertices, O_{vertices} , can be found with Algorithm 3.

After the order is determined and B and \mathcal{X} are sorted, the primary node merging algorithm can be applied. It simply consists of sequentially checking, from highest to lowest priority vertices, if a newly added node violates the algebraic constraint (i.e., is within $\frac{l_f}{2}$ from any nodes already in the domain). This is thoroughly described in Algorithm 4.

The main parameter in the partitioning and subsequent node merging algorithm is the preprocessing accuracy l_f . This parameter determines the minimum distance between any vertex in the simplified graph. The computational time of the algorithm scales proportionally to the l_f and the number of fractures.

STRAIGHTENING AND REMOVING ACUTE ANGLES

Another (optional) modification to the fracture network is the straightening of fracture segments. This amounts to checking each vertex with order two and calculating the angle between the two edges leaving this vertex. If this angle is within some threshold, particularly within $[180 - \theta_{s,\min}, 180 + \theta_{s,\min}]$, the node can be removed since the fracture is considered straight. The angle $\theta_{s,\min}$ is typically chosen on the interval $[0, 7.5]$, depending on how severely the user wants to straighten the fractures. The straightening of fractures can be beneficial when considering meshing tools such as GMSH (Geuzaine & Remacle, 2009). The reason for this is that conformal meshing techniques require the fracture to be embedded into the domain. Less embedded fractures mean faster and easier meshing.

Simply merging the conflicting nodes doesn't resolve all the artifacts associated with meshing DFMs. This is mainly caused by the fact that the algebraic constraint, $\frac{l_f}{2}$, is constant. Whenever nodes are merged, the corresponding edge (i.e., fracture segment) might be stretched and have a length greater than l_f . This might result in vertices being placed near existing edges and not flagged as problematic nodes by the node merging algorithm. Therefore, an additional correction to the network is required to obtain the optimal representation for meshing purposes.

The algorithm for removing the acute angles is very similar to Algorithm 5; however, now the loop is over all nodes with a degree bigger than one. Instead of calculating one angle, $\binom{d_i}{2}$ angles are computed between all edges leaving the vertex i , where d_i is the degree of vertex i . The two edges corresponding to the smallest angle below a certain threshold will be merged. The smaller segment will be merged in the larger segment, and the non-coinciding vertex will be merged in the closest vertex of the larger segment. This ensures minimal changes to the fracture network due to other possible edges leaving the merged vertex. The tolerance for the minimal angle $\theta_{a,\min}$ is typically chosen on the interval $[0, 18]$ degrees. Larger $\theta_{a,\min}$ means a more simplified fracture network since potentially more fracture intersections are flagged as problematic.

APERTURE CORRECTION

In order to incorporate low connectivity and fracture networks with variable apertures, a fracture aperture correction is applied during the cleaning procedure. Connected fractures are treated analogous to resistors in an electric circuit. Resistance is equal to the inverse of the hydraulic conductivity, which in turn is a function of the square of the fracture aperture. Figure 3.5 displays the two different corrections (Type 1 vs. Type 2). Type 1 corrections result in the overlap of two segments after merging of vertices. Type 2 is subdivided further into 2a, which results in an edge collapse, and 2b, which connects two previously disconnected edges. The following equation gives the correction for Type 1

$$\hat{R} = \left(\sum_{i=1}^{n=2} \frac{1}{R_i} \right)^{-1}, \quad (3.10)$$

where R_i is the resistance of edge i defined as

$$R_i = \frac{L_i}{a_i^2}, \quad (3.11)$$

where L_i is the length and a_i is the aperture of the i -th edge respectively, such that the effective aperture of the corrected edge is given by

$$\hat{a} = \sqrt{\hat{L} \sum_{i=1}^{n=2} \frac{a_i^2}{L_i}}, \quad (3.12)$$

where \hat{L} is the length of the new edge.

The Type 2a correction is given by

$$\hat{R} = \sum_{i=1}^{n=2} R_i, \quad (3.13)$$

resulting in

$$\hat{a} = \sqrt{\frac{\hat{L}}{\sum_{i=1}^{n=2} \frac{L_i}{a_i^2}}}. \quad (3.14)$$

In the case of Type 2b, an effective matrix aperture is obtained by inverting the permeability of parallel plate flow such that

$$a_{mat} = \sqrt{12k_{mat}}, \quad (3.15)$$

where k_{mat} is the matrix permeability at the location of the particular edge. A further addition to the Type 2b correction is added to preserve the characteristics of impermeable fractures/faults and high permeable matrix, given by

$$\hat{a} = \begin{cases} \frac{1}{\hat{L}} (a_{mat} L_{mat} + a_i L_i), & \text{if } a_{mat} > a_i \\ \frac{1}{\frac{1 - (L_i / (L_i + L_{mat}))^n}{a_i} + \frac{(L_{mat} / (L_i + L_{mat}))^n}{a_{mat}}}, & \text{if } a_{mat} \leq a_i, \end{cases} \quad (3.16)$$

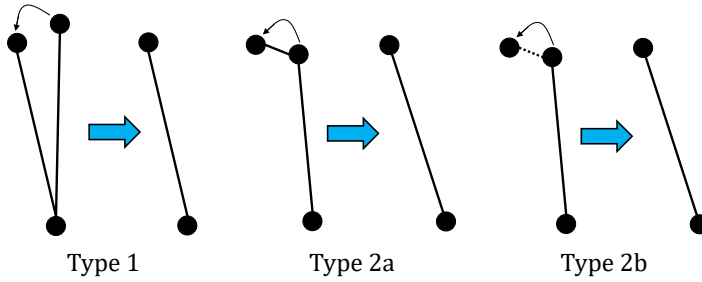


Figure 3.5 Illustration of the types of aperture corrections. Merging the non-shared vertex results in a Type 1 correction (parallel resistor), while merging the shared vertex results in a Type 2 correction (sequential resistor). An effective matrix aperture is used if the two edges are disconnected (Type 2b).

where L_{mat} is the gap between the vertices and n is determined by fitting a least-squares solution to tracer simulation on two disconnected fractures with different gaps and characteristic cleaning lengths, given by

$$n = 9.56 \frac{L_{mat}}{L_i + L_{mat}} + 1.18. \quad (3.17)$$

If $n \approx 1$ we have the normal harmonic mean, while $n \rightarrow \infty$ is the same as not applying any aperture correction. The parameter n effectively limits the aperture penalty when connecting disconnected fractures, as it was observed from simple numerical experiments that the aperture correction, in some cases, over-penalizes the effective aperture. Also, note that n is bounded since L_{mat} can never exceed l_{fh} , since otherwise, these vertices would not apply for merging.

To deal with vertices that are connected through a path in the neighborhood of the vertices, a sub-graph is extracted around the vertex that is merged. The shortest path is computed using Dijkstra's algorithm implementation described in Csardi, Nepusz, et al., 2006. Whenever there is no shortest path (i.e., even in the neighborhood the two vertices remain disconnected), the effective matrix aperture is used for the resistance instead. This is represented in Figure 3.6

Figure 3.6 illustrates an essential feature of the aperture correction. Merging vertex 12 into vertex 11 results in a reduction of the aperture of the edges connecting vertex 10 and 12 as well as 12 and 13. This is undesirable because we want to preserve this connectivity. Since the vertex merging happens sequentially, it has become evident at this point that sorting based on aperture (highest to lowest) is more effective for an accurate representation of fluid flow in the fracture network than simply sorting based on length.

All the code related to the algorithms described above is implemented in Python and can be found at <https://github.com/MakeLikePaperrr/Fracture-Preprocessing-Code>. We have made use of the following packages: NumPy (Harris et al., 2020), SciPy (Virtanen et al., 2020), and igraph (Csardi, Nepusz, et al., 2006).

3.2.5. GOVERNING EQUATIONS

In order to evaluate the dynamic performance of the preprocessing algorithm, several flow scenarios are considered, for which the governing equations are specified in Chap-

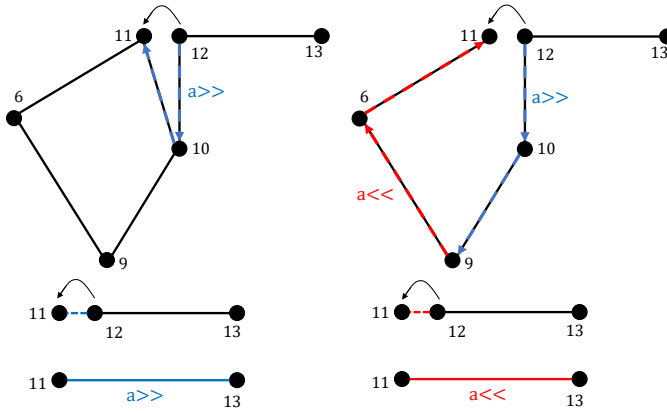


Figure 3.6 Vertices that don't share an edge might be connected through a path in the neighborhood of the vertices. A sub-graph is extracted and using Dijkstra's shortest path; the effective resistance is computed. If no shortest path exists (i.e., even in the neighborhood the two vertices remain disconnected), the effective matrix aperture is used instead.

ter 2.

3.2.6. NUMERICAL SOLUTION

Finite-volume discretization is applied to a general unstructured grid (using a Two-Point Flux Approximation (TPFA) for the fluxes across interfaces with upstream weighting) and a backward (implicit) Euler time discretization strategy to both the conservation equations (assuming no gravity and capillarity), see Chapter 2 for more details. Operator-Based Linearization (OBL) is used to linearize the system of nonlinear equations, which is also described in detail in Chapter 2.

The proposed fracture network processing framework has been fully integrated with the open-source Delft Advanced Research Terra Simulator (DARTS). DARTS is a scalable parallel simulation framework, which has been successfully applied for modeling of energy transition applications, including hydrocarbon (Khait & Voskov, 2018b; Lyu et al., 2021a), geothermal (Khait & Voskov, 2018c; Wang et al., 2020) and CO₂ sequestration (Kala & Voskov, 2020; Lyu et al., 2021b) cases. The ongoing effort to include fully coupled geomechanical modeling into DARTS allowed us to directly address induced seismicity problems (Novikov et al., 2021) which is another challenge in energy transition usually directly relevant to fracture networks.

3.3. RESULTS

This section presents the investigation of the performance of the preprocessing method described in the previous section. The performance is assessed in terms of static and dynamic qualities and is therefore subdivided accordingly. It is important to stress the difference between the preprocessing accuracy l_f and the meshing accuracy l_m . The parameter l_f refers to the minimum distance between any two vertices in the preprocessed fracture network. In contrast, l_m refers to the characteristic length of the control volumes

after applying a particular meshing strategy (i.e., Frontal-Delaunay as a 2D meshing algorithm in this work, see Geuzaine and Remacle, 2009 for details).

Following the definition of those two parameters, there is a significant distinction between the two preprocessing strategies described below. The first approach is defined as the “clean” strategy. In this approach, the preprocessing algorithm is executed once with a $l_f = 1$, $\theta_{a,min} = 18^\circ$, and $\theta_{s,min} = 2.5^\circ$. The l_f remains unchanged in the clean strategy for subsequent coarser meshing results. The second strategy is denoted as the “optimal” strategy. In this strategy, for each subsequent coarser model, the preprocessing algorithm is executed with $l_f = l_m$. This means that the fracture network in the “clean” strategy remains unchanged when coarsening the mesh. In the “optimal” strategy, the fracture network changes when constructing the coarser models.

3.3.1. STATIC PERFORMANCE OF THE PREPROCESSING FRAMEWORK CHANGES IN CONFIGURATION

Figure 3.7 illustrates several changes to the raw fracture network after applying successive coarsening. An apparent reduction in the number of nodes (red dots) can be seen with increasing l_f , which significantly reduces the number of fracture segments. Fewer fracture segments typically indicate a lower network complexity (simply by having fewer degrees of freedom). Multilinear segments become linear (i.e., straight) because of the reduction in fracture segments, further reducing network complexity. Ultimately, small and complex features of the fracture network start to disappear while the main pattern (backbone) remains visible. The average spacing of the North-South fractures (40-50 meters) remains unchanged up to $l_f = 32$. Around $l_f = 64$, which exceeds this average spacing, the fracture configuration changes substantially, as shown in Figure 3.8.

ANGLE DISTRIBUTION

A critical characteristic in fracture networks is the angle distribution, particularly weighted by the length of the fractures, especially when considering variable apertures (Baghbanan & Jing, 2008; Bisdorn et al., 2016a). This usually gives an insight into the potential flow response of the network while also providing possible information on the paleostress that caused the network formation. Since multiple nodes are merged in the preprocessing approach, it is expected that these angles can change substantially when using a large l_f , where large is relative to the scale at which the raw data is collected. This can be clearly seen when looking at Figure 3.8. For small l_f , the deviation in angles is almost unnoticeable, while around $l_f = 32$, a small deviation of roughly 10% in the orientation is observed in the Whitby network. Around $l_f = 64$, the deviation becomes significant (> 20%), but the dominant orientation (N-S) is still similar to that of the raw results. Finally, at $l_f = 128$, the angle distribution is very different from the raw data (> 30%), even the dominant orientation, and doesn't resemble the original network.

Similar behavior but at earlier resolution is observed for the Brejoes network. At $l_m = 16$ the deviation is roughly 20%. The dominant NNW-SSE orientation disappears already at $l_f = 64$. The average spacing of the NNW-SSE fractures in the Brejoes network is roughly 12 meters. This shorter spacing correlates with the earlier deviation in the angle distribution in the Brejoes network when compared to Whitby.

TOPOLOGY

Besides the angle distribution, it is also important to look at connectivity and in particular, the topology changes to the fracture network. Figure 3.9 shows the topology of the raw and preprocessed fracture networks in the ternary topology diagram (as explained in Figure 3.3). A large deviation between the raw and preprocessed data is observed, even with the small $l_f = 1$ [m]. The raw network contains roughly 55% I-nodes, 20% Y-nodes, and 25% X-nodes. The finest preprocessed network (i.e., $l_f = 1$ [m]) contains approximately 20% I-nodes, 75% Y-nodes, and 5% X-nodes. Furthermore, with increasing l_f , the preprocessed networks increasingly deviates towards a large X-node percentage (from 5% at $l_f = 1$ to almost 70% at $l_f = 128$ for Whitby and from 10% at $l_f = 2$ to 70% at $l_f = 64$ for Brejoes).

To illuminate the differences in topology between the fine $l_f = 1$ and the raw data, the degree of the raw and cleaned network nodes is shown in Figure 3.10. Even after

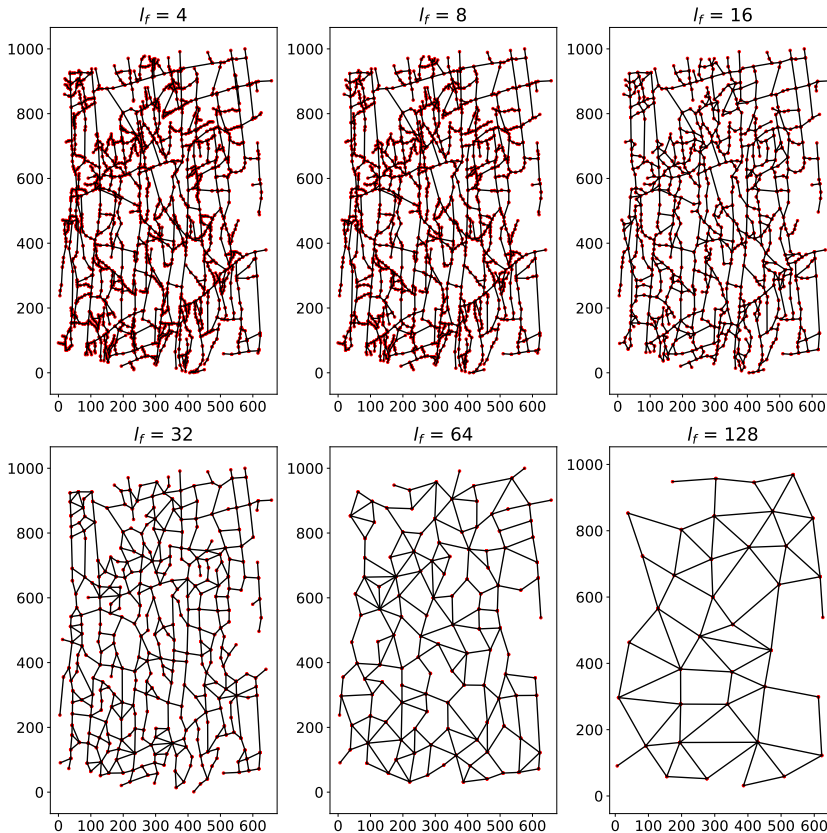


Figure 3.7 Changes to fracture network as a function of preprocessing accuracy l_f . The network's complexity is greatly reduced by the decrease in fracture segments with increasing l_f . The angles of the N-S fractures remain unchanged up to $l_f = 64$ [m].

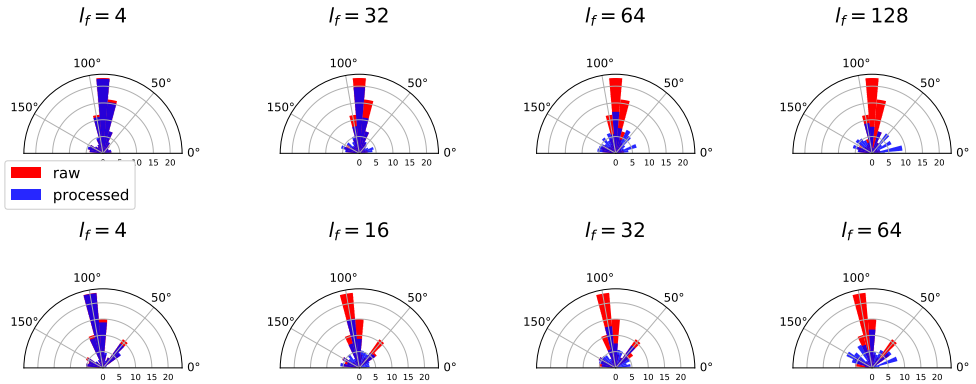


Figure 3.8 Angle distribution as a function of fracture cleaning accuracy. The top row corresponds to the Whitby network, while the bottom row corresponds to the Brejeos network. The cleaning shows no significant change between $l_f = 4$ and $l_f = 16$ for the Whitby network; that's why these steps are omitted in the figure. However, the Brejeos network does show significant deviation at $l_f = 16$. The preprocessed Whitby network is no longer representative of the raw network at $l_f = 128$, while this already happens at $l_f = 64$ for the Brejeos case.

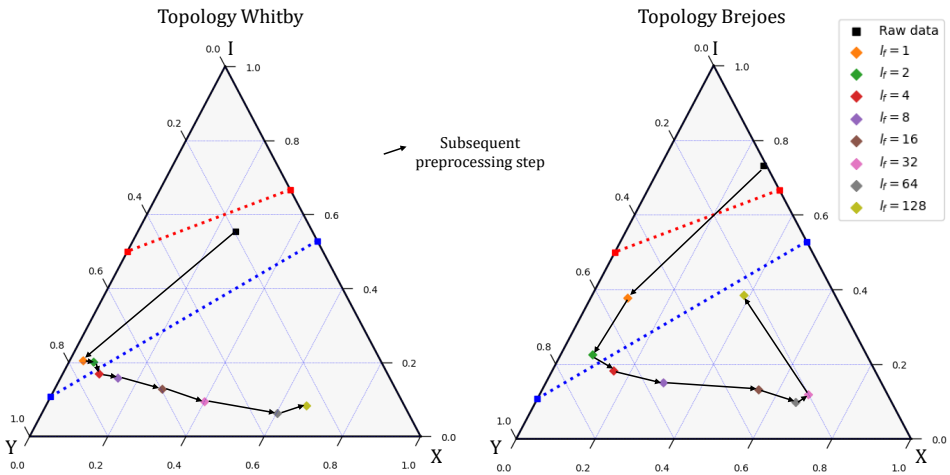


Figure 3.9 A large deviation between the raw data and the processed network's topology in both fracture networks is observed. The reason for this is explained in Figure 3.10. The Brejeos network converges to the raw data for low $l_f < 1$. The jump in the large $l_f = 128$ for the Brejeos case is expected due to the fracture network becoming extremely coarse. Only a few fractures actually remain, meaning the relative proportion of end-nodes greatly increases.

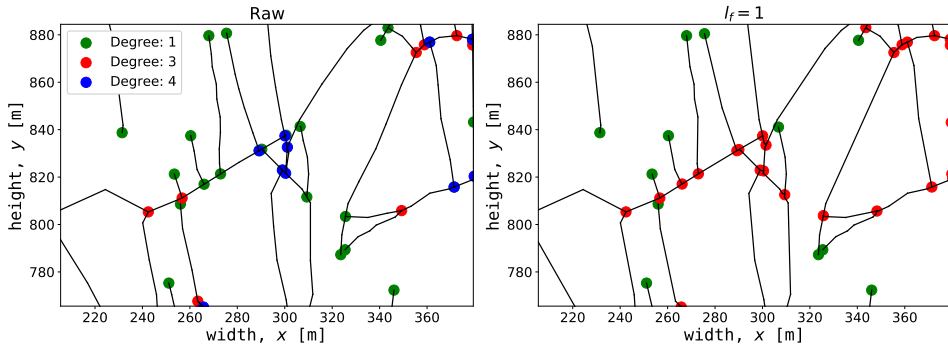


Figure 3.10 Detailed view of the fracture network topology of the Whitby network. The left image displays the raw input topology, while the right image shows the topology after applying the preprocessing algorithm with $l_f = 1$. Due to the manual interpretation, it can be seen that a lot of nodes are characterized as I-nodes (degree 1) or X-nodes (degree ≥ 4) in the left plot, while most seem to be Y-nodes (degree 3) (when considering usual abutment relationships in fracture mechanics and the resolution of the outcrop image).

zooming in at the nodes of the raw network, a significant amount remains misclassified as I-nodes while they would be more suitably classified as Y-nodes or X-nodes (at this scale of observation). This is the result of two fracture segments essentially intersecting, but not exactly due to inaccuracy in image interpretation. The same behavior arises for the X-nodes that are misclassified as Y-nodes. This happens when two fracture segments only intersect with a minimal extension of one of the segments across the point of intersection.

IMPACT OF CHANGES ON MESHING

Because the complexity of the fracture network decreases, the conformal meshing procedure becomes substantially easier. This is shown in Figure 3.11. A significant reduction in the number of control volumes and a more homogeneous distribution is observed for the preprocessed meshing results compared to the raw network. The dark blue areas in the raw meshing results indicate a concentration of small control volumes. Furthermore, very flat triangular elements are observed at some locations in the raw meshing results. Therefore, it seems that the volume distribution and quality of the mesh elements are improved in the preprocessed results. This is quantified in Figure 3.12 and Figure 3.13 respectively. Please note that the fluid flow simulations are carried out in the 3D domain and therefore the model is assigned a thickness ($2.5D$).

Mesh quality here refers to a similar definition as used in Mustapha and Dimitrakopoulos, 2011, particularly using the following equation

$$q = 4\sqrt{3} \frac{A}{a+b+c}, \quad (3.18)$$

where A is the area of the triangle and $a/b/c$ are the lengths of the three sides of the triangle, respectively. This means that when $q = 1$ we have a high mesh quality since the triangle is equilateral (i.e., the optimal shape for TPFA fluid-flow simulation), while a low-quality mesh element (i.e., $q \ll 1$) refers to a large deviation from an equilateral

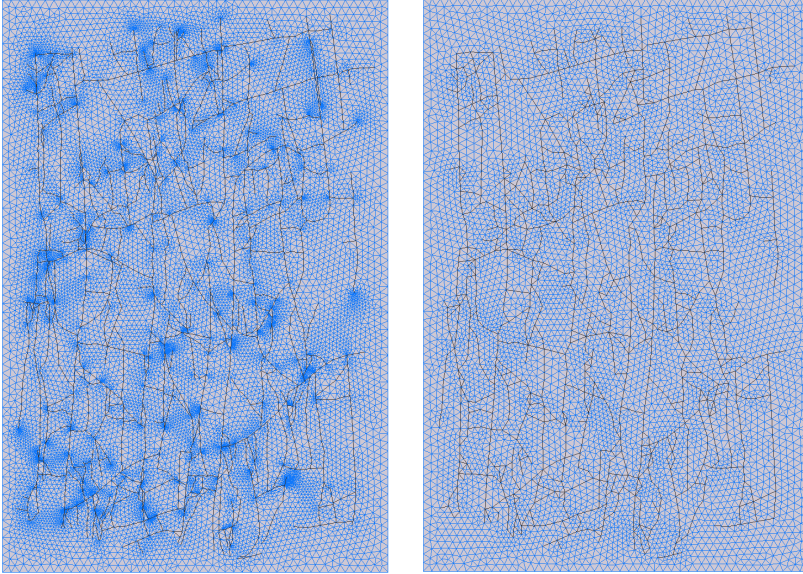


Figure 3.11 Visual comparison between the meshing result of the raw (left) versus the cleaned (right). Meshing and preprocessing accuracy are both 32 [m] (i.e., $l_m = l_f = 32$). The darker blue spots in the image on the left represent clusters of small control volumes. These appear at locations of complex fracture interactions on a scale way below the meshing resolution l_m .

triangle. The mesh elements in the 2.5D model are triangular prisms which means that this mesh element quality indicator also works for this type of geometry. The reason for this is that the centroid of the triangular prism lies in the same xy-plane as the centroid of the triangle and is therefore not changing the orthogonality relationship between neighboring control volumes.

Ultimately, the purpose of using and generating fracture networks is to utilize them in specific industrial applications. In this work, the chosen application is geothermal energy production from the subsurface. This application usually requires multiple numerical simulations to address general uncertainty in subsurface parameters. The accuracy and speed of convergence of these simulations are highly dependent on the mesh quality and, specifically for fracture networks, the orthogonality of the control volume intersections and the volume distribution. Therefore, we quantify the effect of the preprocessing method on these two properties, where mesh quality is a proxy for the orthogonality of the control volume intersections. Figure 3.12 shows the volume distribution as a function of l_f and l_m , while Figure 3.13 shows the distribution of mesh element quality.

The volume distribution obtained after meshing the raw fracture network input is not normally distributed. It has a peak around zero, which indicates a large number of small control volumes. This effect becomes more substantial with increasing l_m . At $l_m = 32$ the volume distribution of the raw network input is entirely concentrated around zero. The volume distribution obtained after meshing the optimal preprocessed fracture network input does show a normal distribution. The distribution becomes wider and more

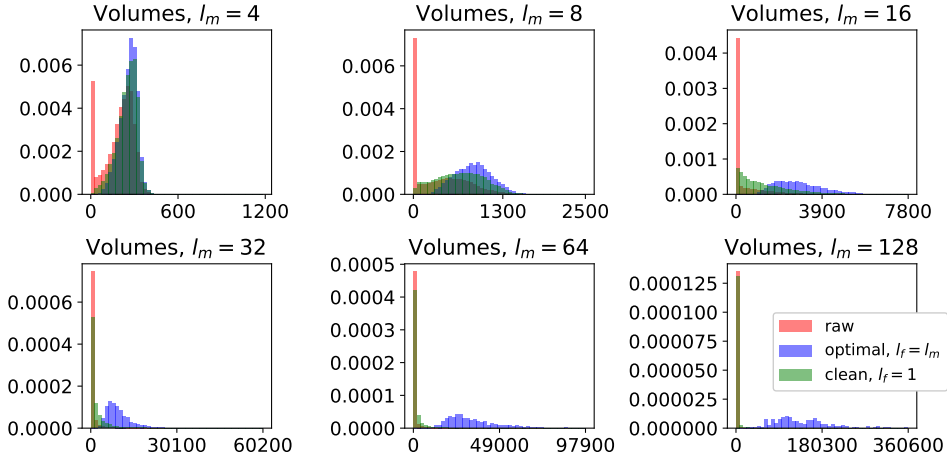


Figure 3.12 Control volume size distribution as a function of preprocessing accuracy for the Whitby network. *Optimal* refers to the preprocessing strategy where the fracture network is cleaned at the same accuracy as the mesh is generated. *Clean* refers to preprocessing the fracture network once at a small l_f and then simply decreasing the meshing resolution l_m while keeping the fracture network unchanged.

skewed with increasing the l_m . No small control volumes are observed for the optimal preprocessed results, even in $l_m = 128$ [m]. The clean preprocessing strategy shows similar behavior to the optimal strategy for small l_m , while converging to the behavior of the raw input network for $l_m \geq 32$.

The mesh element quality obtained after meshing with a small l_m behaves similarly for the raw and preprocessed input fracture data, except for a relatively small amount of flat triangles (i.e., $q \approx 0$). An increase in the number of flat triangles (i.e., $q \leq 0.01$) from 0.32% to 1.29% and a reduction of the overall quality is observed for the raw input data with increasing l_m . However, the mesh quality for the preprocessed results remains above $q = 0.40$ even for $l_m = 128$ [m]. Low mesh quality (i.e., $q \leq 0.01$) can be seen as an indicator for poor simulation convergence since a few of these elements can ruin the nonlinear convergence behavior of the numerical simulation (more than the mean mesh element quality or the whole distribution).

3.3.2. DYNAMIC PERFORMANCE OF PREPROCESSING FRAMEWORK

HIGH ENTHALPY SINGLE APERTURE

The dynamic performance is analyzed by applying geothermal simulation (i.e., solving mass and heat conservation equations) to the different DFM models obtained after meshing (i.e., clean and optimal for different l_m). Geothermal simulation typically consists of a doublet system: at one point, cold water is injected, and at another point, hot water or steam is produced. Mathematically speaking, this amounts to solving Equation 2.6 and 2.10 presented in Section 3.2.5. The injection point is in the bottom left of the domain, while the production point is at the top right of the domain (Figure 3.14). Both wells are perforating a fracture segment. First, the temperature fields of both net-

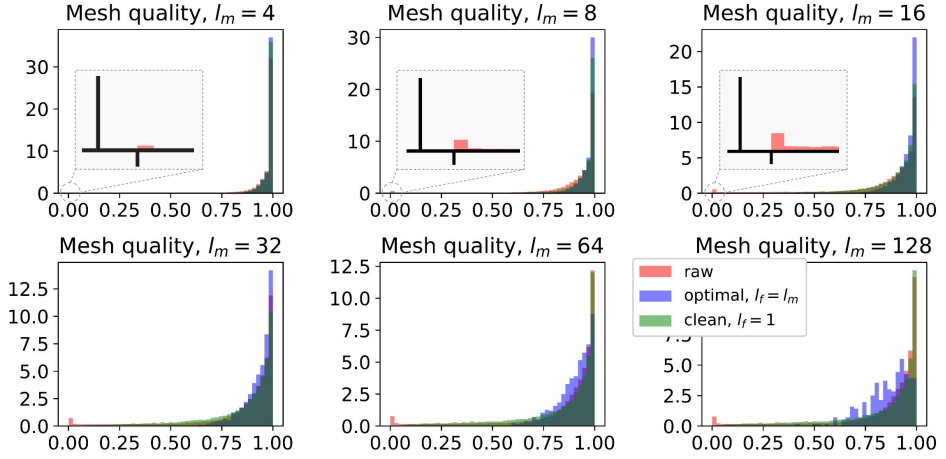


Figure 3.13 Mesh element quality distribution as a function of preprocessing accuracy for the Whitby network.

works are shown (Figure 3.14 and 3.15). The water saturation field is shown for the Brejoes network (Figure 3.16), and finally, the temperature at the production well over time (Figure 3.17).

The boundary conditions and modeling parameters can be found in Table 5.6 and 5.7. The simulation parameters model a situation that is investigated throughout the world for its geothermal energy potential (Moeck, 2014). Particularly, we study geothermal energy production from a tight fractured reservoir with advective flow happening predominantly through the fracture network. It is important to observe how changes to the fracture network affect the simulation results in such a setup. If the fracture permeability is much larger than the matrix permeability, the fractures will evidently play a dominant role in the fluid flow patterns. There are a particular set of parameters for each network. The first set of parameters simulates initially high-enthalpy single-phase super-critical water according to IAPWS 97 equation of state (Wagner & Kretzschmar, 2008) used in DARTS. This set of parameters is applied to the Whitby case. The second set simulates high-enthalpy steam flow conditions and is applied to the Brejoes case.

Table 3.1 Boundary conditions.

Parameter	Whitby	Brejoes
Rock heat conduction, κ_r [kJ/m/day/K]	165	150
Rock heat capacity, C_r [kJ/m ³ /K]	2500	2200
Initial pressure, p_0 [bar]	500	100
Initial temperature, T_0 [K]	423.15	583.15
Injection rate, Q_{inj} [m ³ /day]	1000	300
Injection temperature, T_{inj} [K]	303.15	308.15
Production bottom hole pressure, p_{prod} [bar]	475	100

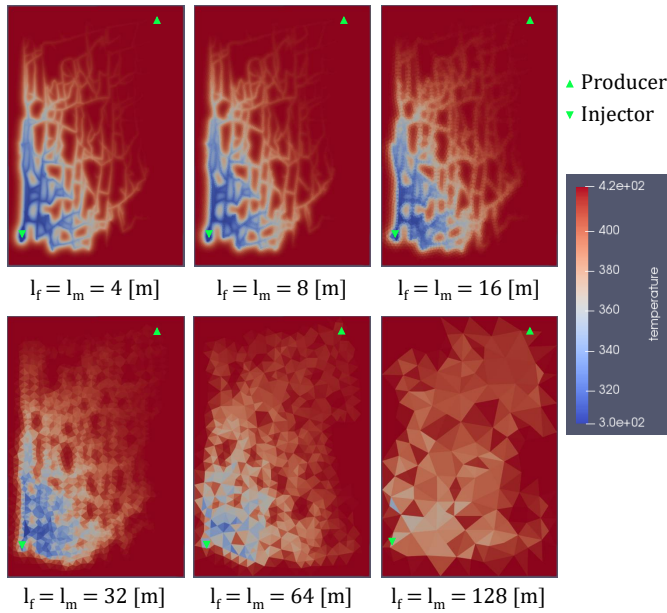


Figure 3.14 Temperature distribution as a function of preprocessing and meshing accuracy for the optimal strategy after 3150 [days] (Whitby network).

Table 3.2 Reservoir and simulation parameters.

Parameter	Whitby	Brejoes
Matrix permeability, k_{mat} [mD]	1e-3	1e-2
Matrix porosity, ϕ_{mat} [-]	0.3	0.04
Fracture permeability, k_{frac} [mD]	8.3e7	7.5e6
Fracture porosity, ϕ_{frac} [-]	1	1
Length domain, L_x [m]	1050	700
Width domain, L_y [m]	1050	350
Simulation time, t [days]	10950	10950

The temperature field after 3150 [days] of simulation for the Whitby network is presented in Figure 3.14. The temperature is reduced near the injection point from the initial 423.15 [K] to the injection temperature of 303.15 [K]. Fluid flow primarily happens through the fractures, hence the largest temperature variations occur closer to the fractures. This is more apparent in the finer models (i.e., smaller l_m). Larger diffusion of the temperature profile is observed for increasing l_m . The main fracture pattern becomes invisible at $l_m = 64$ [m]. The temperature distribution for the Brejoes network is shown in Figure 3.15. In terms of temperature distribution, a comparable trend was observed regarding the Whitby network. The water saturation field is shown in Figure 3.16 after 150 days of simulation. Accurate representation of the water saturation is more sensitive to the resolution than temperature.

The energy rate and temperature profile at the production well showed similar be-

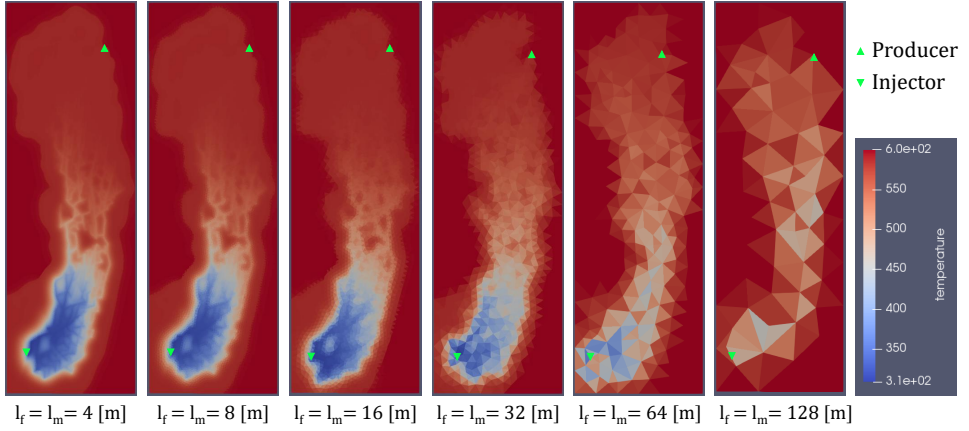


Figure 3.15 Temperature distribution as a function of preprocessing and meshing accuracy for the optimal strategy after 3150 [days] (Brejoes network).

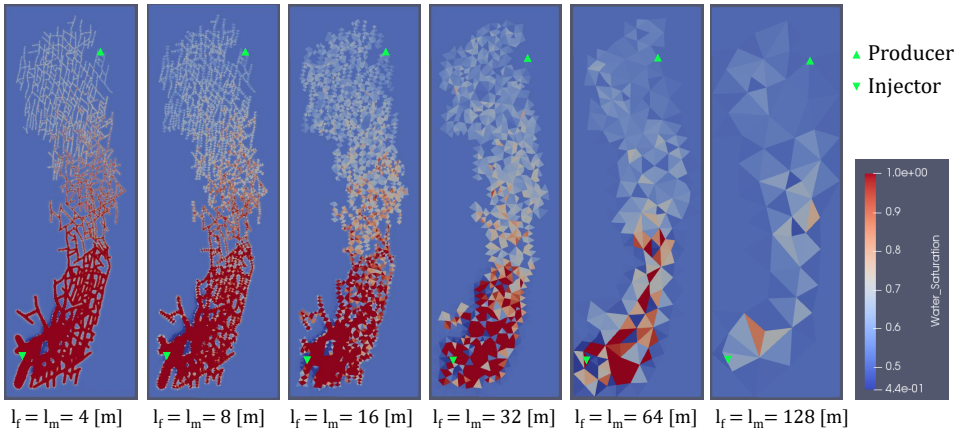


Figure 3.16 Water saturation distribution as a function of preprocessing and meshing accuracy for the optimal strategy after 150 [days] (Brejoes network).

havior; therefore, only the temperature profiles are shown in Figure 3.17. A commonly used metric to analyze the flow behavior of geothermal systems is the doublet lifetime. The lifetime is typically reached when the water temperature at the production well has decreased with 10-20% of the difference between initial and injection temperature. The optimal strategy (i.e., $l_f = l_m$) in the Whitby network starts deviating from the finer scales at $l_f = 32$ [m], particularly the lifetime is reduced by 670 [days]. From $l_f = 64$ [m] the deviation becomes more significant, notably a 2700 [days] difference in lifetime due to early breakthrough of the cold water. At $l_f = 128$ [m], the response does not resemble the finer scales specifically the lifetime is reduced to 500 [days] due to almost instant cold water breakthrough.

The clean strategy (i.e., $l_f = 1$ and $l_m = l_m$) shows an analogous result to the optimal strategy for the small l_m . For larger l_m the result of the clean strategy is significantly closer to the finer scales; particularly, there is no deviation in breakthrough times between the scales. This is expected since the fracture network is not changing (i.e., $l_f = 1$ for all simulations) with increasing l_m . Therefore, no changes in connectivity or the path from injector to producer occur, which is important in this tight fractured reservoir setting. Meshing artifacts in the clean strategy increase the number of control volumes for larger l_m , contributing to small changes across the scales (see Table 3.3). The difference between the clean and optimal strategy (i.e., $l_f = l_m$) for small l_m (≤ 32) in terms of flow-response is negligible; however, the performance of the optimal strategy is significantly better.

A more significant deviation in Brejoes temperature profile for the optimal case is observed. This is in line with the other observations. This pattern is observed in the angle distribution in the previous section (Figure 3.8). Furthermore, Brejoes fracture density is larger (i.e., spacing between fractures is shorter), which leads to a more diffused and less complex temperature distribution. The large connectivity also means a shorter and highly conductive path from injector to producer, resulting in an early cold-water breakthrough.

HIGH PERMEABLE MATRIX (LOW PERMEABLE FRACTURE)

Fractures are often seen as high-permeable conduits, but there are cases where fractures or other discontinuities end up blocking fluid-flow (Gale et al., 2004). The test case presented here consists of a single phase-steady state simulation in a reservoir with a high permeable matrix and low permeable fractures. A small gap between the fractures exists in the middle of the domain $(x, y) = (500, 500)$. Since the gap exists below the meshing resolution accuracy, the preprocessing algorithm connects the fractures. In the case of no aperture correction, the flow can only go around the fractures. With aperture correction, the preprocessed model correctly represents a similar flow pattern as in the high fidelity model with streamlines passing through the middle of the domain (Figure 3.18).

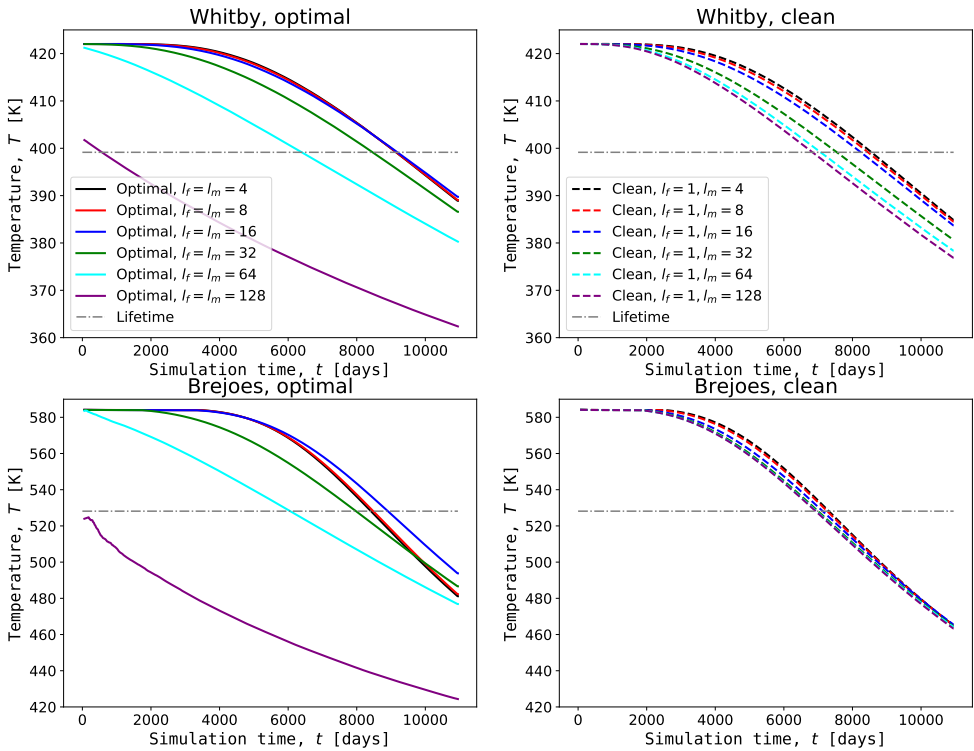


Figure 3.17 The temperature at the production well over time for optimal (left column) and clean (right column) preprocessing strategies for both the Whitby (top row) and Brejoes (bottom row) networks. Substantial deviation for large $l_f = l_m$ in the optimal strategy was observed. This does not happen in the clean strategy. This is because the fracture network is unchanged while the mesh is coarsened. This also causes the number of control volumes to remain considerable even for large l_m thereby reducing the numerical diffusion (see Table 3.3 and Table 3.4).

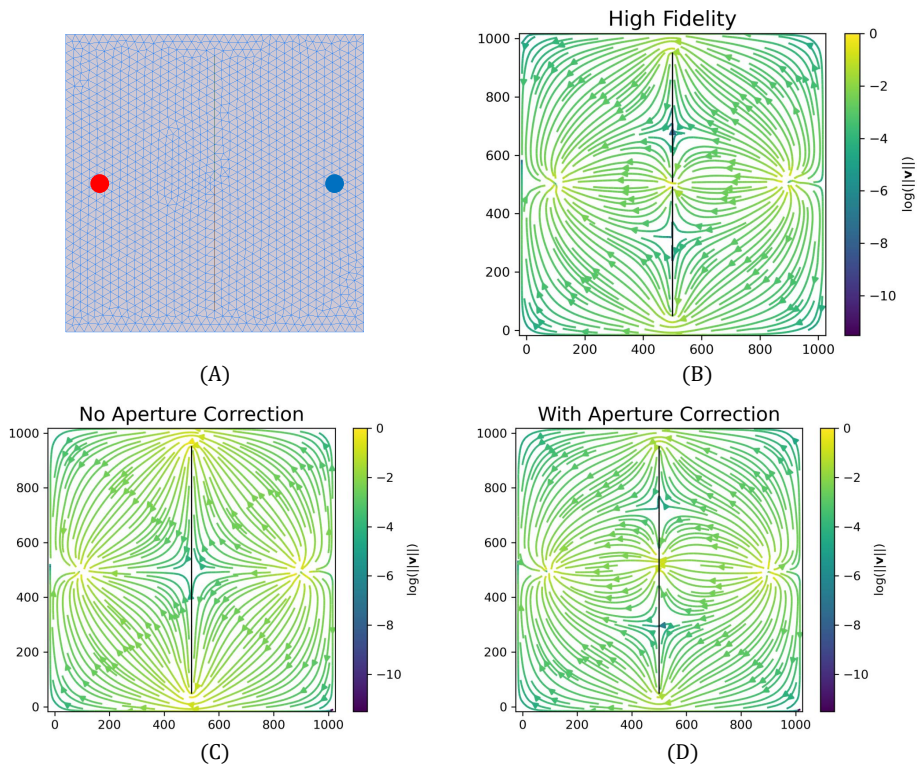


Figure 3.18 Single phase steady-state simulation of a high-permeable matrix and low permeable fractures. There is a small gap between the fractures in the high fidelity model allowing for fluid to pass. Not applying any fracture correction blocks the flow, while the aperture correction accurately depicts the high fidelity behavior.

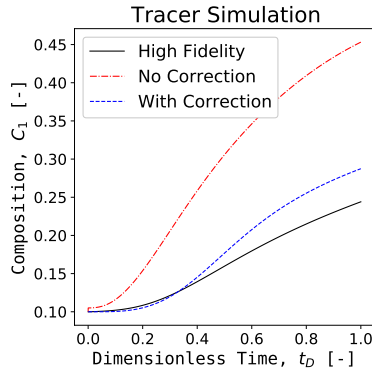


Figure 3.19 Single phase tracer simulation on the Whitby network with the variable aperture model depicted in Figure 3.2. A better match in breakthrough times is obtained after using the aperture correction.

LOW CONNECTIVITY (VARIABLE APERTURE)

The final test case consists of the variable aperture model applied to the Whitby fracture network (Figure 3.2). Since most of the high permeable fractures (N-S oriented) are connected through low permeable fracture (E-W oriented), this variable aperture model results in a low connectivity fracture model. A single-phase tracer simulation shows that the aperture correction is able to preserve the low connectivity of the network up to the numerical accuracy corresponding to the higher numerical dispersion in the coarser model. The early breakthrough of the tracer without aperture correction is obvious (Figure 3.19).

3.3.3. NUMERICAL PERFORMANCE HIGH ENTHALPY

The numerical performance of the two strategies can be found in Table 3.3 and Table 3.4 for Whitby and Brejoes, respectively. No timestep cuts are observed in both strategies for the Whitby simulations. However, several timestep cuts were observed in both strategies for the Brejoes simulations. This is reflected in the larger amount of nonlinear and linear iterations. The convergence issues can be explained by the combination of complex two-phase physics (steam condensation) and DFM in the case of high-enthalpy two-phase flow. A more sophisticated nonlinear strategy can be utilized to limit the timestep cuts (Wang & Voskov, 2019), but the main goal of this study is to have a fair comparison between the two preprocessing strategies for the conventional nonlinear solver.

It is observed that the optimal strategy shows a better convergence in both networks. A reduction in nonlinear iterations of roughly 20% for the coarse models in the Whitby simulations is observed. In the Brejoes simulations, this reduction is almost 45%. The total CPU time for the optimal strategy in the Brejoes network increases slightly at the coarsest level due to a higher number of control volumes when the coarsest strategy is applied since the scale of the cleaning mainly constrains the meshing. For the optimal strategy at the coarsest scale, the simulation time is primarily dominated by the linearization step (i.e., construction of the operators for the OBL method) and therefore doesn't reduce below 32 seconds.

Table 3.3 Numerical performance Whitby simulations. N_{blocks} corresponds to the total number of control volumes, N_{fracs} to the number of fracture control volumes, N_{newt} to the number of Newton-iterations, N_{lin} to the number of linear-iterations, and T_{CPU} to the total simulation time. l_f refers to the preprocessing accuracy, and l_m refers to the meshing accuracy.

	N_{blocks}	N_{fracs}	N_{newt}	N_{lin}	T_{CPU} [s]
Clean ($l_f = 1, l_m = 4$)	91,780	6,800	3,543	53,210	4,159
Clean ($l_f = 1, l_m = 8$)	41,119	4,311	3,277	46,830	1,290
Clean ($l_f = 1, l_m = 16$)	24,044	3,152	3,199	40,566	538
Clean ($l_f = 1, l_m = 32$)	22,879	2,841	3,112	39,667	364
Clean ($l_f = 1, l_m = 64$)	20,142	2,824	3,087	39,340	400
Clean ($l_f = 1, l_m = 128$)	20,222	2,824	3,085	38,903	422
Optimal ($l_f = l_m = 4$)	80,672	6,362	3,436	50,573	4,079
Optimal ($l_f = l_m = 8$)	26,553	3,363	2,890	37,988	813
Optimal ($l_f = l_m = 16$)	8,718	1,594	2,680	32,600	196
Optimal ($l_f = l_m = 32$)	2,417	563	2,533	27,434	53
Optimal ($l_f = l_m = 64$)	605	147	2,395	23,119	18
Optimal ($l_f = l_m = 128$)	166	32	2,403	17,147	6

The number of control volumes N_{blocks} in the clean strategy does not drop below 48-50 thousand for Whitby and 22-26 thousand for Brejoes. This is because the fracture network, at the preprocessing accuracy of $l_f = 1$, is too complex for the meshing software at large l_m . The result is a substantial amount of elements with low mesh quality (see Figure 3.13) and no further reduction in N_{blocks} with increasing l_m . This significantly increases the computational time for the clean strategy when compared with the optimal strategy. For example, at $l_f = l_m = 32$ the optimal strategy only takes 14.6% of the clean strategy simulation time. However, this comes at the cost of a less accurate simulation response (see Figure 3.17).

3.4. DISCUSSION

The existing preprocessing strategies described in the literature only implicitly resolve the fracture segments that intersect at a small angle via node merging. We augment this with an extra step where all the low-angle intersections are explicitly resolved and improve the volume distribution, mesh quality, and the convergence of subsequent numerical simulation. Furthermore, we presented an aperture correction technique that allows handling of realistic aperture distributions and low connected fracture networks. We also contribute a comprehensive investigation of the geometry and topology changes as a function of discretization accuracy and its effect on the dynamic reservoir behavior.

3.4.1. TOPOLOGY

The inherent bias of artificial connectivity in the coarser models is evident in the static analysis. Especially the topology is sensitive to subtle changes in the fracture network. The preprocessing method does seem to converge given that the distance in the ternary topology diagram appears to decrease with decreasing l_f (except for two jumps in the Brejoes topology data for $l_f = 1$ and $l_f = 128$ [m]).

Table 3.4 Numerical performance Brejoes simulations. N_{blocks} corresponds to the total number of control volumes, N_{fracs} to the number of fracture control volumes, N_{newt} to the number of Newton-iterations, N_{lin} to the number of linear-iterations, and T_{CPU} to the total simulation time. l_f refers to the preprocessing accuracy, and l_m refers to the meshing accuracy.

	N_{blocks}	N_{fracs}	N_{newton}	N_{linear}	T_{CPU} [s]
Clean ($l_f = 1, l_m = 4$)	157,105	8,079	6,970	163,388	6,803
Clean ($l_f = 1, l_m = 8$)	58,912	4,682	4,947	87,940	1,607
Clean ($l_f = 1, l_m = 16$)	30,739	3,035	5,129	80,568	856
Clean ($l_f = 1, l_m = 32$)	22,918	2,402	4,784	77,690	766
Clean ($l_f = 1, l_m = 64$)	24,955	2,233	5,038	78,795	618
Clean ($l_f = 1, l_m = 128$)	26,127	2,211	4,851	75,687	551
Optimal ($l_f = l_m = 4$)	150,566	7,852	4,354	108,073	3,909
Optimal ($l_f = l_m = 8$)	46,811	4,115	3,308	52,374	564
Optimal ($l_f = l_m = 16$)	15,139	2,093	2,979	38,458	167
Optimal ($l_f = l_m = 32$)	4,899	967	2,747	27,698	50
Optimal ($l_f = l_m = 64$)	1,471	371	2,632	20,254	32
Optimal ($l_f = l_m = 128$)	400	122	2,562	14,203	34

The large deviation from the raw topology can be explained through several points. Manual interpretation is usually made in some software (e.g., QGIS) or on the image directly. Every fracture is interpreted as a line, and two points are connected, particularly the beginning- and end-point of the fracture. Even if the interpreter meant for the two fractures to abut against each other, beginning- or end-points are rarely placed exactly on top of the existing line. The computer processing interprets the point as I- or X-node, while the interpreter meant the node to be a Y-node. This can be omitted if some snipping tool during the interpretation is used or a semi-automated (Vasuki et al., 2014) or fully automated (Prabhakaran et al., 2019) interpretation method. However, this is not always the case as shown for two networks chosen in this study.

The other problem is the scale of the image. The Brejoes data set has a huge resolution (20 mm/pixel) (Prabhakaran et al., 2019). It can be argued that you would roughly need 15-25 pixels to be sure about the interaction of two or more fractures due to shading, contrast, and other optical effects in the image. Considering this, it would mean that intersection and abutment relationships cannot be interpreted at a scale smaller than 300-500 [mm] (for this particular image).

Furthermore, the image shows a 2D representation of the fracture network. In 3D, fractures are represented by planes. Any deviation from perfectly vertical planes would increase the chance of nodes classified as I-nodes turning into Y-nodes. All of this leads to the argument that the raw network data should not be used in the topological assessment of fracture networks. However, a small cleaning should be applied for the analysis to provide meaningful results.

3.4.2. FLUID FLOW

As shown in Figure 3.14 and 3.15, the predictions on flow response do not seem to be affected by small details in the fracture network. However, they are substantially dif-

ferent after successive coarsening (i.e., increasing l_c). The main reason for the earlier water breakthrough observed in Figure 3.17 can be attributed to an increase in connectivity of the fracture network (see also Figure 3.9). Furthermore, the shortest flow path through the fracture network from the injector to the producer is significantly reduced in the coarser models; hence the cold water arrives earlier. Finally, since the volume of the fractures is unchanged, even if two fracture segments are merged, the fluid velocity through a merged fracture is higher for the same injection rate. All of these things affect the time the water has to heat up (i.e., recharge) and reduce the breakthrough time of the cold water in the coarser models.

Even without using flow-based upscaling when coarsening the mesh (i.e., increasing l_m), the flow-response for the coarser models remains accurate (up to $l_m = 32$ for the Whitby simulation and up to $l_m = 16$ for Brejoes). This implies that for a fraction of the computational time of the high-fidelity model (i.e., 1.3% for Whitby and 4.3% for Brejoes), we are still able to obtain a representative flow and heat transfer for this complex physical process. This opens up avenues for replacing effective media models in common optimization and uncertainty quantification practices, such as Arnold et al., 2016 and Spooner et al., 2019, with more accurate DFM models (de Hoop & Voskov, 2021).

The main idea is that adding a fracture to an already connected network is not necessarily a problem. Connecting whole clusters that were not previously connected can pose a significant issue and significantly affects the flow and heat transfer in the reservoir. To remedy this, we added a novel aperture correction that penalizes connecting fracture segments that do not already share a connection. The tracer simulation applied to the Whitby fracture network with variable aperture distribution significantly improves the match between the coarser representation and the high-fidelity model in terms of breakthrough time (see Figure 3.19). Furthermore, the aperture correction allows us to deal with coarsening of sealing fractures that potentially block fluid-flow, as observed in the synthetic test case in Figure 3.18.

3.4.3. APPLICATION AND RECOMMENDATIONS

It seems from the study presented in this paper that the flow-response is less sensitive to changes in the fracture network than initially thought. The orientation of the fractures (i.e., angle distribution) is also less sensitive than the topology. This could serve as a recommendation to geologists and modelers that the scale and complexity at which the data is collected and the models are constructed is unnecessarily refined. It would save time and improve the ambiguity of our models to set a certain interpretation scale at which you can be certain of the intersection and abutment relationships before making the interpretation.

The preprocessing method effectively extracts the backbone of a complex fracture network. Therefore, it can be used to extract the main pattern of the network and might be useful when generating training images for algorithms such as Bruna et al., 2019.

3.5. CONCLUSION

This study demonstrates a strategy to simplify complex fracture networks in terms of flow response based on a robust preprocessing approach using graph theory. We show

that using raw fracture data for topological analysis and dynamic modeling is unwise and that some preprocessing should be applied to investigate the patterns that exist in the studied network. Our method simplifies the topology of the fracture network by merging fracture nodes (i.e., vertices) within a certain radius. Consequently, this amounts to taking the union of the incidence matrix's rows of each vertex, thereby preserving all the connectivity within the fracture network. Furthermore, it explicitly removes problematic fracture intersections that occur at an angle below a certain threshold. Finally, our framework extends the current preprocessing methods, such as Mustapha and Mustapha, 2007 and Karimi-Fard and Durlofsky, 2016, by taking into consideration an aperture correction when vertices are merged to better preserve the original connectivity and handle heterogeneous aperture distributions.

Our preprocessing framework can create a fully conformal uniformly distributed grid for a given realistic fracture network with variable aperture at the required level of accuracy. The changes introduced by the method are analyzed in terms of geometry (i.e., angle distribution of the fracture network), meshing results (i.e., volume and quality of the elements), and dynamic response of the reservoir when subjected to geothermal high-enthalpy production conditions. Results are analysed for two realistic fracture networks based on outcrop studies, a synthetic case with sealing fractures, and a variable aperture model. Topology is more affected by the preprocessing than the geometry and flow response in studied networks.

Uncertainty quantification relies on a large number of numerical simulations. The presented method decreases the computational complexity of DFM models. Therefore, our approach opens up avenues for using efficient DFM models with similar computational complexity as embedded-DFM (EDFM) and even Dual-Porosity models while accurately capturing the discrete nature of fracture networks for uncertainty quantification and history matching purposes. This is especially true for the optimal preprocessing strategy where cleaning and optimizing the fracture network, including treatment of intersections, node merging, and straightening, are combined.

The open-source computational framework performing all the preprocessing stages can be found at <https://github.com/MakeLikePaperrr/Fracture-Preprocessing-Code>.

3.6. ACKNOWLEDGEMENTS

The project was performed with a subsidy (reference TKI2017-07-UG) from the Ministry of Economic Affairs, National schemes EZ subsidies, Top sector Energy, carried out by the Netherlands Enterprise Agency. We also want to thank Mohammed Karimi-Fard for his insightful comments and suggestions regarding the preprocessing strategy. Finally, we want to thank Alexandros Daniilidis for his valuable discussion regarding the aperture correction procedure. The data and source code is available at <https://github.com/MakeLikePaperrr/Fracture-Preprocessing-Code>.

3.7. APPENDIX: VARIOUS ALGORITHMS FOR DFN PREPROCESSING

Algorithm 1 Construct graph

```

1:  $V = \{\}$ 
2:  $n = 0$ 
3: for  $(x_i, y_i, x_j, y_j) \in \mathcal{F}$  do
4:   if  $(x_i, y_i) \notin V$  then
5:      $V = V \cup (x_i, y_i)$ 
6:      $n += 1$ 
7:
8:   if  $(x_j, y_j) \notin V$  then
9:      $V = V \cup (x_j, y_j)$ 
10:     $n += 1$ 
11:
12:  $B = \text{zeros}(n, m)$ 
13: for  $(x_i, y_i) \in V$  do
14:    $\text{ids} = \text{find}(\forall(x_i, y_i) \in \mathcal{F}(\cdot, [1, 2]) \wedge \forall(x_i, y_i) \in \mathcal{F}(\cdot, [3, 4]))$ 
15:    $B(i, \text{ids}) = 1$ 
16:
17:  $D = \text{diag}(B\mathbf{1}_{m \times 1})$ 
18:  $A = BB^T - D$ 
19:  $L = D - A$ 

```

Algorithm 2 Partition segments

```

1:  $m_{\text{new}} = \sum_i^m \max(1, \text{round}(l_i/l_f))$ 
2:  $\mathcal{F}_{\text{new}} = \text{zeros}(m_{\text{new}}, 4)$ 
3:  $\text{count} = 1$ 
4: for  $k \in O_{\text{segm}}$  do
5:    $m_k = \max(1, \text{round}(l_k/l_f))$ 
6:    $\text{ids} = [1, \dots, m_k]$ 
7:    $\mathcal{F}_{\text{new}}(\text{count} : (\text{count} + m_k), 1) = \mathcal{F}(k, 1) + (\text{ids} - 1) / m_k (\mathcal{F}(k, 3) - \mathcal{F}(k, 1))$ 
8:    $\mathcal{F}_{\text{new}}(\text{count} : (\text{count} + m_k), 2) = \mathcal{F}(k, 2) + (\text{ids} - 1) / m_k (\mathcal{F}(k, 4) - \mathcal{F}(k, 2))$ 
9:    $\mathcal{F}_{\text{new}}(\text{count} : (\text{count} + m_k), 3) = \mathcal{F}(k, 1) + \text{ids} / m_k (\mathcal{F}(k, 3) - \mathcal{F}(k, 1))$ 
10:   $\mathcal{F}_{\text{new}}(\text{count} : (\text{count} + m_k), 4) = \mathcal{F}(k, 2) + \text{ids} / m_k (\mathcal{F}(k, 4) - \mathcal{F}(k, 2))$ 
11:   $\text{count} += m_k$ 
12:
13:  $O_{\text{segm}, \text{new}} = [1, \dots, m_{\text{new}}]$  //since  $\mathcal{F}_{\text{new}}$  is already ordered now!

```

Algorithm 3 Determine order vertices

```

1:  $B = B(\cdot, O_{\text{segm}})$  //order the columns of  $B$ 
2:  $O_{\text{vertices}} = \text{zeros}(n, 1)$ 
3:  $\text{count} = 0$ 
4: for  $k = 1$  to  $m$  do
5:    $(i, j) = \text{find}(B(\cdot, k) == 1)$ 
6:   if  $i \notin O_{\text{vertices}}$  then
7:      $\text{count} += 1$ 
8:      $O_{\text{vertices}}(\text{count}) = i$ 
9:
10:  if  $j \notin O_{\text{vertices}}$  then
11:     $\text{count} += 1$ 
12:     $O_{\text{vertices}}(\text{count}) = j$ 
13:
14:  $\mathcal{X} = \mathcal{X}(O_{\text{vertices}}, \cdot)$  //sort vertices
15:  $B = B(O_{\text{vertices}}, \cdot)$  //sort rows of incidence matrix accordingly

```

Algorithm 4 Node merging

```

1:  $D_X = \text{pdist}(\mathcal{X})$  //pairwise symmetric  $n \times n$  distance matrix for each vertex in  $\mathcal{X}$ 
2:  $\text{mergelist} = \text{zeros}(n, 1)$ 
3: for  $k = 2$  to  $n$  do
4:    $\text{id}_{\min} = \min(\{d_{k,i} \in D_X \mid \forall i \in \mathbb{N}, i < k\})$  //closest vertex already in domain
5:   if  $D_X(k, \text{id}_{\min}) < l_f/2$  then
6:      $\text{mergelist}(k) = \text{id}_{\min}$ 
7:      $B(\text{id}_{\min}, \cdot) = B(\text{id}_{\min}, \cdot) \cup B(k, \cdot)$  //record new connections from node merging
8:      $B(k, \cdot) = 0$  //remove merged node from graph
9:      $D_X(k, \cdot) = \infty$  //reset distance from removed node
10:     $D_X(\cdot, k) = \infty$  //reset distance from removed node
11:
12:  $\text{mask} = \{i \in \mathbb{N} \mid \forall i \notin \text{mergelist}, i \leq n\}$ 
13:  $\mathcal{X} = \mathcal{X}(\text{mask})$ 
14:  $n = \text{card}(\mathcal{X})$ 
15:  $B = B(\text{mask}, \cdot)$ 
16:  $B = B(\cdot, \mathbf{1}_{1 \times n} B > 1)$  //remove ‘‘collapsed’’ edges
17:  $B = \text{unique}(B, \text{'cols'})$  //remove overlapping edges

```

Algorithm 5 Straighten fractures

```

1:  $\text{nodelist} = \{d_i \in D(G) \mid d_i == 2\}$ 
2:  $\text{mergelistnodes} = \text{zeros}(n, 1)$ 
3:  $\text{mergelistsegms} = \text{zeros}(m, 1)$ 
4: for  $k \in \text{nodelist}$  do
5:    $\text{idsegms} = \text{nonzero}(B(k, \cdot))$ 
6:    $\mathbf{v}_1 = \mathcal{F}(\text{idsegms}(1), [1, 2]) - \mathcal{F}(\text{idsegms}(1), [3, 4])$ 
7:    $\mathbf{v}_2 = \mathcal{F}(\text{idsegms}(2), [1, 2]) - \mathcal{F}(\text{idsegms}(2), [3, 4])$ 
8:    $\text{dotproduct} = \min(1, \max(-1, \frac{\mathbf{v}_1^T \mathbf{v}_2}{\|\mathbf{v}_1\| \|\mathbf{v}_2\|}))$ 
9:    $\theta = \arccos(\text{dotproduct})180/\pi$ 
10:  if  $\theta < \theta_{\text{tol}}$  then
11:     $\text{mergelistnodes} = k$ 
12:     $B(k, \cdot) = 0$ 
13:     $\text{mergelistsegms} = \text{idsegms}(2)$ 
14:     $\text{idnodes} = \text{nonzero}(B(\cdot, \text{idsegms}(1))) \cup \text{nonzero}(B(\cdot, \text{idsegms}(2)))$ 
15:     $B(\cdot, \text{idsegms}(2)) = 0$ 
16:     $B(\text{idnodes} \neq k, \text{idsegms}(1)) = 1$ 
17:
18: //B and  $\mathcal{X}$  are updated similarly to Algorithm 4 using ‘‘mergelistnodes’’ and
    ‘‘mergelistsegms’’ for the removed vertices and edges respectively

```

4

COMPREHENSIVE INVESTIGATION OF KARSTIFICATION: LiDAR DATA AND REACTIVE TRANSPORT SIMULATIONS

Growing demand for cleaner energy sources has led to the comprehensive investigation of high-enthalpy carbonate reservoirs. These reservoirs are often chemically and mechanically altered and hence contain a significant uncertainty in the spatial distribution of the reservoir parameters. The resulting discontinuity features commonly include complex fracture networks, large inter-connected cave systems, and other flow barriers/conduits. Several conceptual models exist for simulation of such systems; however, the main driving forces behind the resulting geometry are not fully understood, complicating quantitative predictions. To improve the reservoir characterization of these complex reservoirs, high-resolution LiDAR datasets from several outcrops were acquired. Statistical analysis is performed on the geometry of the resulting cave networks. Several geometrical parameters are deduced from the LiDAR surveys, which correlate with the possible physical processes involved. The effect of the heterogeneity of the porous media and fracture network is studied extensively using the newly developed reactive transport module in the Delft Advanced Research Terra Simulator (DARTS) framework. DARTS uses the Operator Based Linearization approach, which transfers the governing nonlinear Partial Differential Equations into a linearized operator-form where the Jacobian is constructed as a product of a matrix of derivatives with respect to state variables and discretization operators. The state-dependent operators are only evaluated adaptively at vertices of the mesh introduced in the parameter space. The continuous representation of state-dependent operators and their derivatives is achieved by using a multi-linear interpolation in parameter

Parts of this chapter have been published in ECMOR XVII Conference Proceedings, European Association of Geoscientists & Engineers (2020) de Hoop et al., [2020](#).

space, significantly improving simulation performance. We extend the reactive transport module for both kinetic and equilibrium reactions, allowing for more complex chemical interactions in the simulation framework. Linking the processes of wormholes creation with the aid of numerical simulations and the measured manifestation of the discontinuity networks will substantially improve the reservoir modeling process and subsequent uncertainty quantification.

4.1. INTRODUCTION

A large part of the world's hydrocarbon reserves, approximately 60% of the oil and 40% of the gas reserves, are hosted in carbonate rocks (Akbar et al., 2000). An increase in this percentage is expected due to several significant discoveries made in the past decade, such as pre-salt carbonates in off-shore Brazil (Boyd et al., 2015; Mello et al., 2011) and the Tarim basin in China (Huang et al., 2017b). Besides hydrocarbon accumulations, the ongoing energy transition has resulted in an increase in geothermal discoveries as well, for example, the geothermal potential in Dutch onshore Carboniferous carbonates (Reijmer et al., 2017).

Heavily fractured and karstified reservoirs have been encountered during the drilling process, resulting in unpredicted hazards. The fluid-flow response and mechanical behavior of Naturally Fractured Reservoirs (NFR) are highly uncertain due to our limited ability to predict the spatial distribution of fracture networks and karst at the reservoir scale. Performing adequate risk and uncertainty quantification is necessary due to the increasing environmental awareness and regulations. Therefore, improving the accuracy and efficiency of the modeling of subsurface-related activities is essential. Constructing geologically realistic a priori models of fractured karst systems, extracted from the LiDAR surveys, is key to a successful history matching approach (Arnold et al., 2019).

Several recent papers have investigated karstified reservoirs (see also Chapter 1). Methods to detect karstification in the subsurface exists (Chen et al., 2005; Esrafil-Dizaji & Rahimpour-Bonab, 2019; Reijmer et al., 2017; Zhang et al., 2020; Zhiwen et al., 2020), as well as numerical simulation efforts for fluid flow in karstified reservoirs (Correia et al., 2019; Murad et al., 2020; Popov et al., 2007). However, the input parameters for such modeling efforts are still unclear. A few studies have investigated the geometric patterns existing in cave systems (Collon et al., 2017; Jouvès et al., 2017). Nonetheless, the interaction of cave systems and fracture networks at the reservoir scale is still not fully understood. Realistic reservoir modeling parameters and a rigorous uncertainty quantification workflow are also missing (Mohammed et al., 2021).

The influence of fractures on cave development is highlighted by several authors (Balsamo et al., 2020; Boersma et al., 2019; Kassa et al., 2012). Therefore, when studying cave development through numerical simulations, it is essential to capture the discrete nature of the fractures accurately. The use of a Discrete Fracture Matrix (DFM) model, which explicitly represents the fracture geometry, is therefore preferred (Moinfar et al., 2011). Arising complications and solutions of conformal meshing due to DFM approach are addressed in Chapter 3.

Fractures in the subsurface are usually inferred from several different data sources (e.g., seismic imaging, wire-line logs, borehole images, and well-test data). This causes the spatial distribution and aperture of the fractures to have a non-unique solution.

Given a set of observations, the challenge is determining which fracture networks are more likely to occur in the subsurface. Furthermore, different fracture networks may result in different dissolution patterns. Assuming the dissolution patterns are potentially related to fractures that can be observed in the different data sources (i.e., fractures were present before large-scale dissolution occurred), it is possible to construct a set of possible dissolution patterns if the aperture and other fracture network characteristics can be inferred. These patterns can then be history matched to other available data to improve our knowledge of the dissolution patterns found in the subsurface and improve predictions on geothermal or hydrocarbon energy recovery in such karstified reservoirs. The possibility of using numerical simulation results for training images as input to Multiple Point Geostatistics (MPS) algorithms is briefly discussed.

4.2. LiDAR DATA ACQUISITION

4

4.2.1. BRIEF BACKGROUND ON AREA OF TWO EXPEDITIONS

In the years 2018 and 2019, several data sets were collected during fieldwork expeditions to hypogenic and epigenic caves in the State of Bahia, Brazil. The data consists of dense point clouds (resolution of around 3-10 cm), and the size of the caves ranges from 10s to 100s of meters. The data is collected with the mobile Light Detection And Ranging (LiDAR) device (GeoSLAM ZEB Revo). This device relies on Simultaneous Localization and Mapping (SLAM) technology. SLAM LiDAR is a suitable alternative to georeferenced photogrammetry in subterranean caves due to poor illumination and the non-availability of GPS signals. Mobile LiDAR is also preferred over stationary LiDAR due to the narrow passages in the caves (e.g., setup time, bulky equipment). Furthermore, the resulting point cloud gives an exact representation of the inner cave surfaces providing a distinct advantage to manual cave maps, as well as allowing more sophisticated 3D analysis of the cave and speleogenetic features (Bosse et al., 2012; Zlot & Bosse, 2014a, 2014b).

The study area is located in the central part of Bahia State, Brazil, particularly the Irecê Basin (Figure 4.1). It is located in the northern part of the São Francisco Craton, on which, during the Late Proterozoic, an extensive carbonate platform had formed. In terms of stratigraphy, the carbonates of the Una and Bambuí Groups overly Paleoproterozoic sedimentary and Archean metamorphic units (Misi et al., 2011). Two formations make up the Una Group, particularly the Bebedouro and Salitre Formations. At approximately 1 Ga, a major glacial event led to the deposition of glaciomarine sediments, which comprise the Bebedouro Formation. Between 750 and 650 Ma, the Salitre Formation accumulated a thickness of several hundreds of meters. Many cave systems in Brazil, including several of the caves examined in these two fieldwork expeditions, are located in the Salitre Formation; therefore, it is of primary importance to this study.

Several fold belts border the São Francisco Craton, particularly Brasília, Rio Preto, Riacho do Pontal, Sergipano, and the Aracuai fold belts. During the fragmentation of Rodinia, extensional events lead to the tectonic evolution of the Neoproterozoic sedimentary basin. The São Francisco basin, which lies west to the Irecê basin, developed during later tectonic inversion and compressional movement. The same tectonic events that formed the São Francisco basin has likely caused the development of the Irecê basin

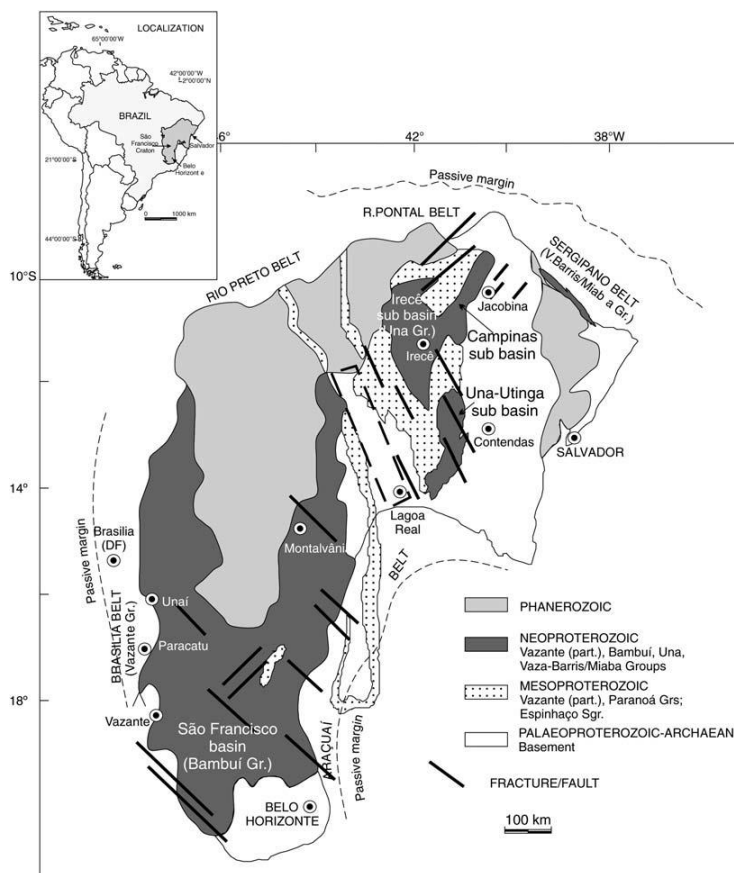


Figure 4.1 Neoproterozoic cover (São Francisco Supergroup) of the São Francisco Craton and the folded belts surrounding the cratonic area in NE Brazil. From Misi et al., 2011.

(Misi & Kyle, 1994). The collisions between the São Francisco Craton and the bordering fold belts (i.e., formed during Brasiliano orogeny) caused deformation in the Neoproterozoic units of these basins (Ennes-Silva et al., 2016). According to structural analysis by the same authors, there is evidence of superposed folding on the Neoproterozoic sedimentary units. Two phases of deformation are highlighted in these units. Folds and thrusts striking NNE-SSW comprise the first phase, while folds and thrusts striking E-W the second, both correspond to collisional events that occurred on the margin of the craton (Ennes-Silva et al., 2016).

Having highlighted the geological history of the study area, an overview of all the caves is given in Figure 4.2.

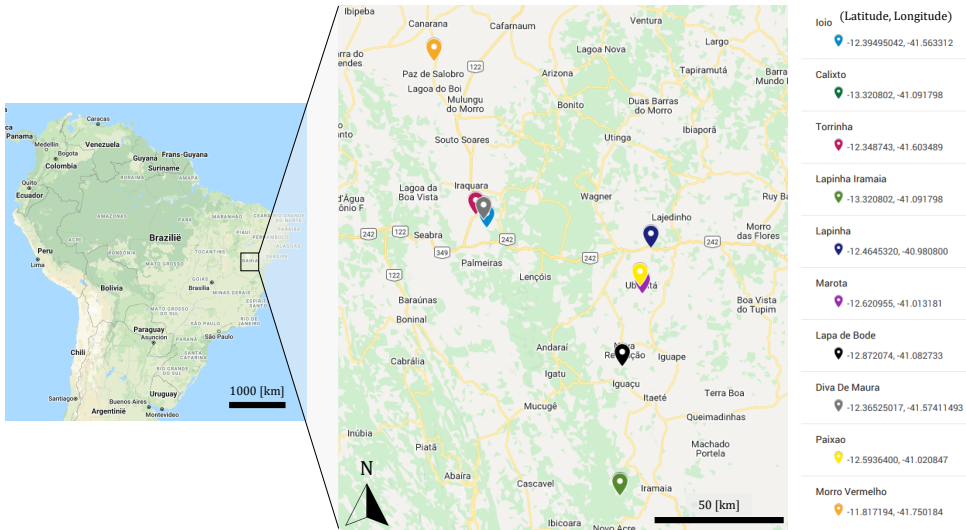


Figure 4.2 Overview of the location of the studied caves.

4.2.2. ZEB REVO (RT) AND SLAM

The first expedition (2018) was carried out using the ZEB Revo, while the second (2019) was carried out using the ZEB Revo RT. The main difference is the real-time point generation of the RT. This is very useful, especially in cave environments, since you can immediately check the quality of the survey using either your phone or a tablet and estimate if you have to redo the survey. Both scanners have similar specifications, particularly: weight scanner 1kg, weight data logger 1.4kg, range 15-30m, resolution 3-30cm, field of view of $360^{\circ} \times 270^{\circ}$, and 43000 points/sec. The SLAM algorithm, utilized by both versions, allows mobile data collection, especially useful in tortuous cave environments.

Some preparation is required for efficient and successful scanning practices. Besides the apparent reading of the manual and ensuring all batteries are charged and enough storage is available on the device, it is essential to plan your survey before starting. This is done for two reasons: 1) making sure the survey length does not exceed 25min; 2) making sure the route has enough features (rocks, boulders, anything other than a straight, smooth wall). The second point is crucial for the SLAM algorithm and error distribution; a simple straight tunnel with no features present might run into issues because of this particular reason. Finally, if you want to save processing time, make sure no one moves through your survey while recording.

Acquiring the survey is done systematically. Always start and end at the exact(!) location. Always include several loops throughout the survey, and make sure you go slowly through narrow passages. Keeping an eye out for the quality indication that the RT provides is critical in reducing post-processing issues later on. Anything within 10cm of the scanner is not scanned, as a result of this limiting scanning yourself while surveying (i.e., noise). Combined with the scanning resolution ratio of 1:10, the accuracy is roughly 3cm. An example of the LiDAR use is shown in Figure 4.3 (as well as a comparison of part

of a LiDAR survey with an actual photo). Always make sure to include sufficient overlap between the survey and recognizable objects.

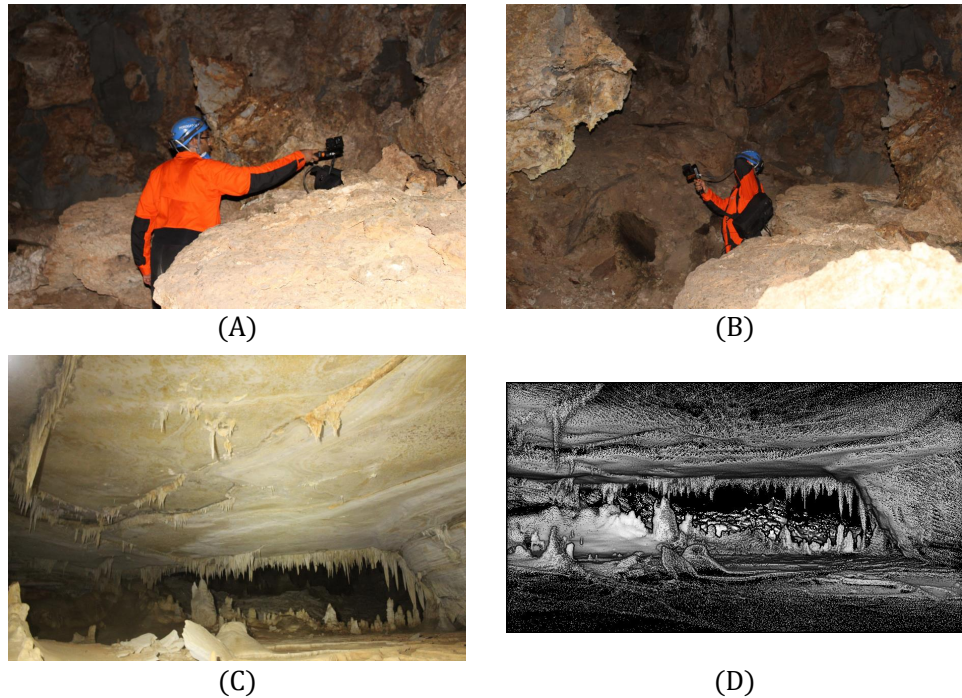


Figure 4.3 LiDAR usage and comparison. (A) Starting LiDAR survey from fixed position (for initialization). (B) Capturing the reflection of the inner cave surface while moving through the cave. (C) and (D) Comparison between photo and LiDAR survey, roughly acquired at the same location.

4.2.3. DATA POST-PROCESSING

The first step when processing the data is done using the GeoSLAM Hub software. The data storage unit is connected to a laptop via cable or using the WiFi of the datalogger. The Hub software converts the raw scan data to usual point cloud formats (e.g., las or laz format). Processing time is proportional to the scanning time of the particular survey. After obtaining the las files and trajectory of the surveys, it is time to import them into the software of your choice.

CloudCompare is a typical point cloud editing and processing software, excellent for any post-processing tasks (Girardeau-Montaut, 2016). Due to the 25min survey limitation and the necessity of creating several loops, one needs several surveys to map an entire cave system. This means, in order to obtain a single point cloud of the full cave, the individual surveys need to be registered (i.e., stitched together). This is why it is vital to include overlap and plenty of recognizable objects between two adjacent surveys. The easiest way to register any two surveys is using these steps (following the manual from CloudCompare): (1) use manual translations and rotations to approximately align

each survey to the reference survey, (2) extract a small subset of each survey which has overlapping points, (3) apply iterative closest point (ICP) (Besl & McKay, 1992) to finely register these subsets to the reference cloud, (4) apply the obtained transformation matrix from the ICP to the entire point clouds to obtain the fully aligned surveys, and (5) merge the aligned individual surveys and obtain one complete continuous survey of the cave.

4.3. LiDAR SHAPE ANALYSIS

4.3.1. EXAMPLE OF VISIBLE SPELEOGENETIC FEATURES IN LiDAR DATA

The investigated caves show very different patterns, possibly related to different structural (e.g., presence of fractures, bedding orientation) and hydrogeological (e.g., flow barriers, origin, and chemistry of invading fluid) controls. One cave, in particular, Morro Vermelho Cave (MVC), has been thoroughly investigated by Bertotti et al., 2020b. The cave experienced little interaction with meteoric processes and served as an excellent example of a hypogenic cave formed in a strike-slip tectonic regime. During an initial stage, bedding parallel flow led to extensive dolomitization of a 102m thick body of rock experiencing distributed deformation above a deep-seated strike-slip fault. With progressive displacement, the fault grew upward, connecting the two aquifers of the sedimentary succession (quartzarenite and overlying carbonates), allowing for the invasion of SiO₂ rich fluids in the carbonates and creating caves with a variety of exotic minerals (e.g., barite). Similar minerals are recognized in the Dinantian rocks in Belgium and surrounding areas.

This research indicates that the presence of strike-slip faults in the vicinity of deep-seated carbonate aquifers can lead to extensive mineralization and large-scale dissolution along fractures, severely altering the reservoir properties (e.g., porosity and permeability). The high-resolution LiDAR dataset also allowed for easy detection of small-scale speleogenetic features indicating pathways for rising fluids and other diagnostic features such as “cupolas”, as shown in Figure 4.4.

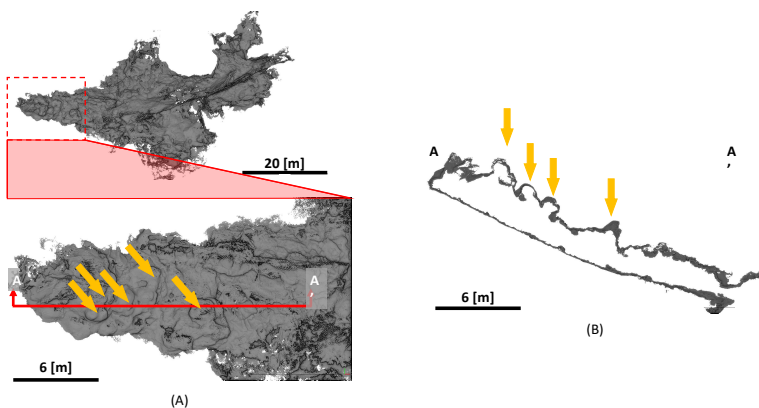


Figure 4.4 (A) High-resolution LiDAR data from the Morro Vermelho cave in Bahia, Brazil. (B) Visible speleogenetic features (i.e., “cupolas”). Modified from Bertotti et al., 2020b.

4.3.2. EXTRACT SKELETON

The fickle nature of the MVC does not lend itself to comprehensive shape analysis using the skeletonization approach. Several caves that were encountered fit this approach, one in particular is presented (i.e., Lapa de Bode). This cave shows the typical maze-cave pattern and is an excellent test case for the proposed methodology.

A topological skeleton is a thinner version of the original object that is equidistant to each boundary (Yang et al., 2019). There are several skeletonization algorithms for obtaining the skeleton of a 3D point cloud: L1-medial (Huang et al., 2013), curve skeleton (Tagliasacchi et al., 2009), voxelizing point cloud (Ramamurthy et al., 2015), or based on binary images (projected 2D or full 3D) (Lee et al., 1994). In this chapter, due to the 2.5D nature of the cave (i.e., cave passages manifest mostly in a single plane), it was decided to project the point cloud onto a 2D plane. This plane can be rotated such that it aligns with the bedding in which the cave originates. A 2D skeletonization algorithm, similar to Lee et al., 1994 implemented in MATLAB, is then used on the image to obtain a skeleton. Then, we apply the fracture preprocessing method to trim some skeleton edges and straighten them to a certain degree.

4.3.3. EXTRACT SUB-CLOUD, PROJECTION AND CURVE FITTING

Once the skeleton is obtained, the next step is extracting the sub-cloud around a particular limb (i.e., edge) of the skeleton. Calculate the normal vector to the particular limb, go a certain w along the normal vector in both directions, go a certain t perpendicular to the normal vector, and finally extract all the points within this regular hexahedron (Figure 4.5(A)).

After the sub-point cloud is extracted, a further subset has to be selected. In order to make an accurate curve fit through the actual cross-section of the cave passage, it is necessary only to extract these points. Since not all cave passages have the same width, w must be chosen large enough to capture the largest width. If several cave passages are parallel, this point-density cut-off criteria is excellent at identifying the extent of the actual cave passage (Figure 4.5(B)).

After the final subset is obtained, a simple projection onto the plane perpendicular to the skeleton limb is made. Finally, a 2D curve fitting through the projected points results in a parametrized geometry of the cave passage at the particular limb. Many choices can be made regarding what type of curve fitting is employed; in this case, a simple polynomial fit is applied (i.e., allowing ellipses) (Figure 4.5(C) and (D)).

4.3.4. RESULTS

The Lapa de Bode cave is an excellent example of a maze cave and is well-suited for the algorithm proposed in the previous section. Figure 4.6 displays the different shapes of the cave along each passage. Quite regular shapes and spacing are observed for the cave passages. Noticeably, the smaller cave passages in the SW-NE direction in the middle of the domain are considerably narrower, this is also true for some of the end-points of the branches in the south-side of the cave section (Figure 4.7). Enlargement of intersecting cave passages can also be observed, all of which points to converging and preferential flow-paths (enlarging some passages more than others). On average, the cave displays highly regular width and heights throughout the domain. These results suc-

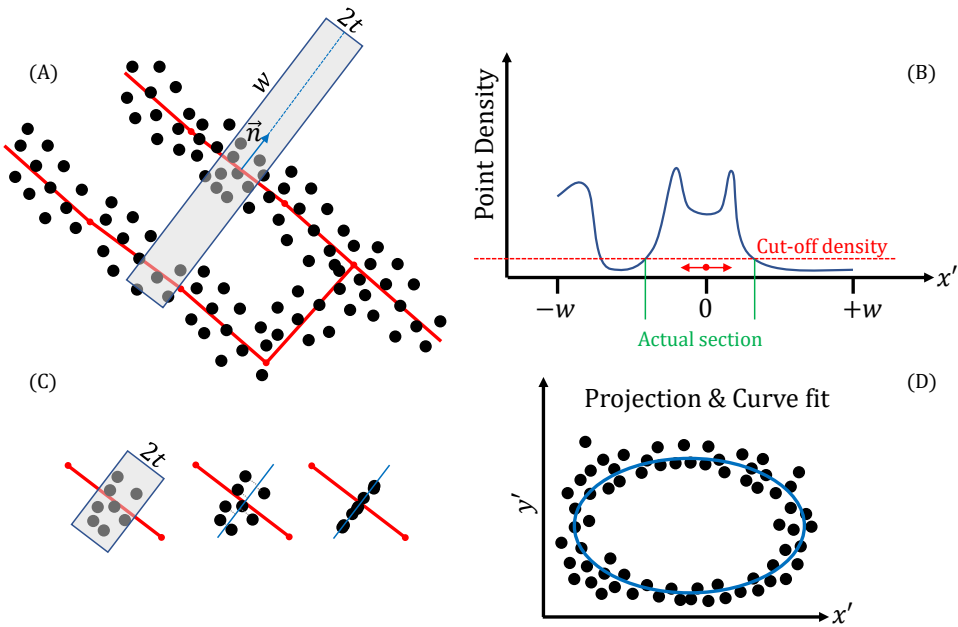


Figure 4.5 (A) Schematic 2D topview of point cloud with bounding box of points comprising the sub-point cloud. (B) Extraction method for identifying the actual cave passage. (C) Final subset extraction and projection onto the plane perpendicular to the skeleton limb. (D) Schematic of a curve fitting through the project subset of points.

cessfully demonstrate the application of an automatic extraction of 3D parameters of complex cave geometry.

Ultimately, many different cave patterns were encountered during the two fieldwork expeditions. Figure 4.8 attempts to visualize these differences both in shapes, the number of cave passages, and scale. In order to successfully use these observations for aiding in the geological modeling workflow of karstified reservoirs, the difference in patterns between those caves has to be explained by differences in formational processes. This is attempted in the remaining chapter, where different wormhole numbers, length, and presence of fractures on resulting dissolution patterns are examined. However, even after a link might be established, inferring these parameters and conditions from observations in the subsurface (i.e., well and seismic data) is a difficult task. History matching based on some set of realistic prior karst models/configurations (i.e., similar to the configurations in Figure 4.8) might be an option.

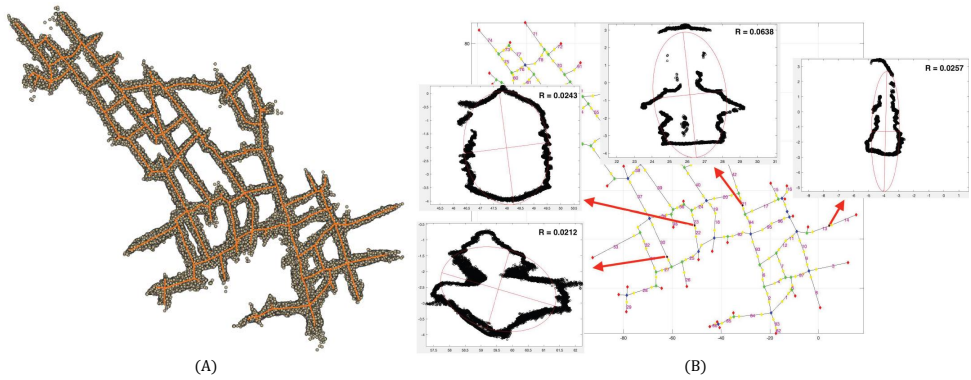


Figure 4.6 (A) Point cloud and skeleton of Lapa de Bode. (B) Examples of some projected sections along limbs of the skeleton. Modified from Rossetto, 2020.

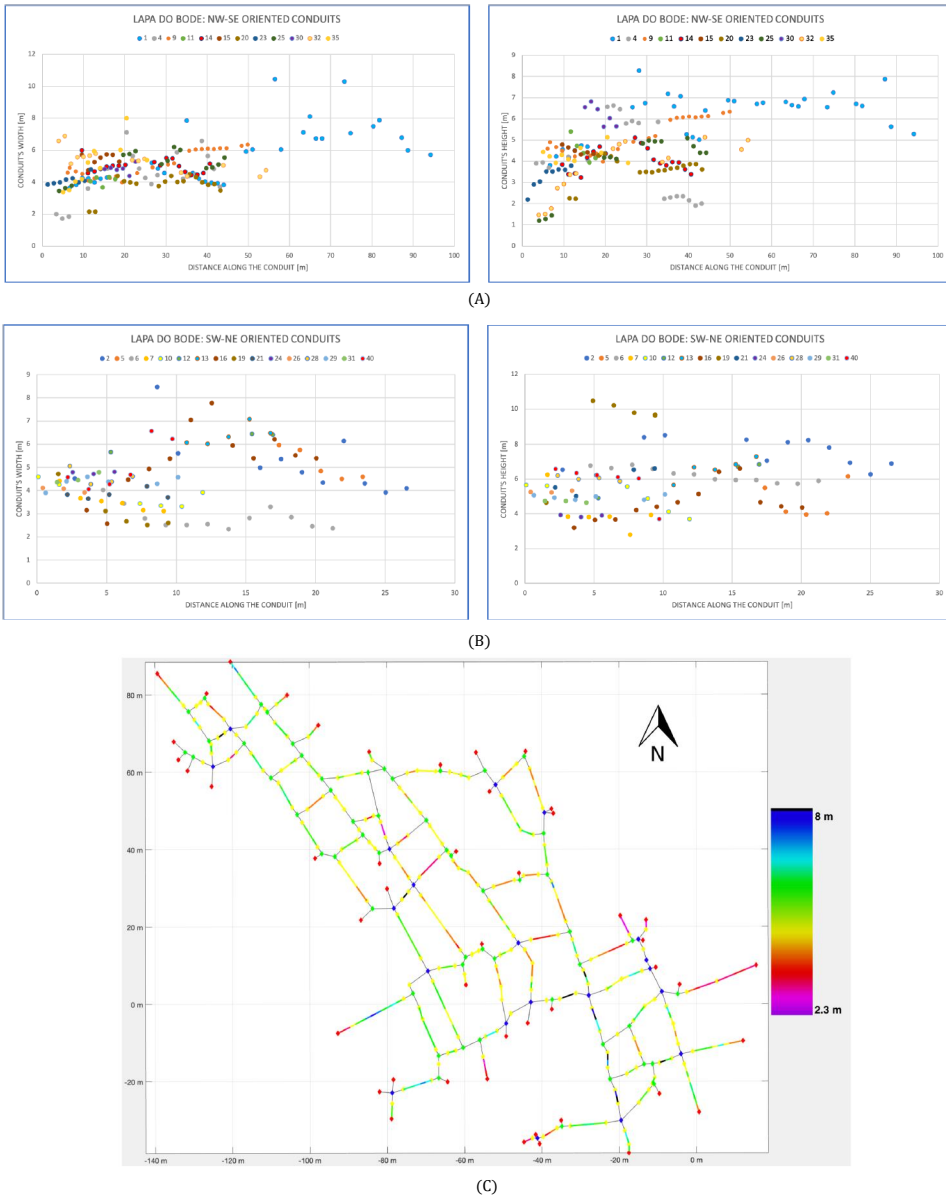


Figure 4.7 (A) Width and height of the NW-SE cave segments. (B) Width and height of the SW-NE cave segments. (C) Width of each cave segments. Modified from Rossetto, 2020.

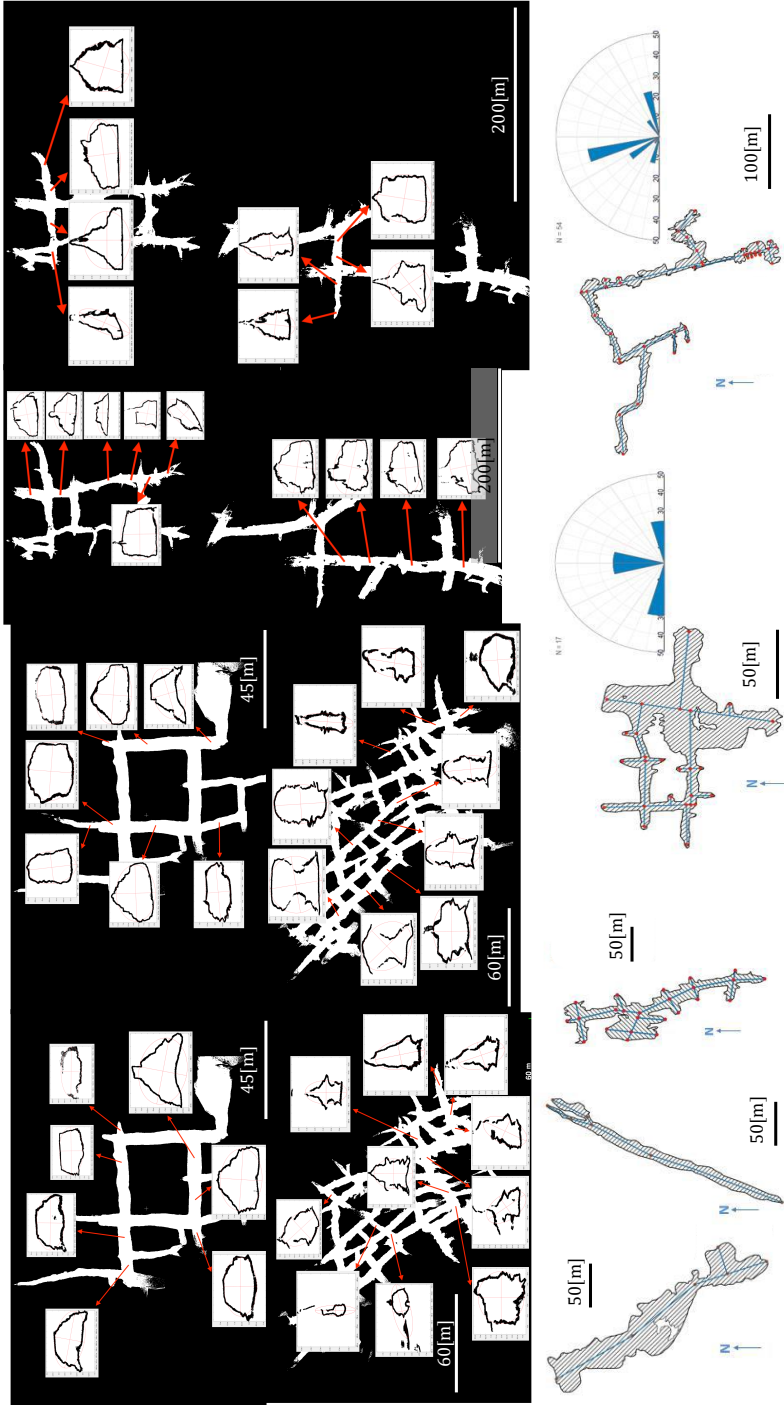


Figure 4.8 Impression of all the different geometries, scales, and number of cave passages that were observed during the fieldwork expeditions. Modified from El Ahmar, 2019; Rossetto, 2020.

Parametrizing caves does provide a direct use in fluid-flow simulation. Figure 4.9 shows an example of fluid-flow simulation in a discrete cave model, where cells in the cave domain have been assigned a large porosity and permeability. Simplified cave representations open up avenues for object-based modeling or even training images (TI) for Multiple-Point Statistics (MPS). Accurate physical simulation in these complex triple media (matrix-fracture-cave) geometries is of vital importance (Ali et al., 2020; Wu et al., 2011).

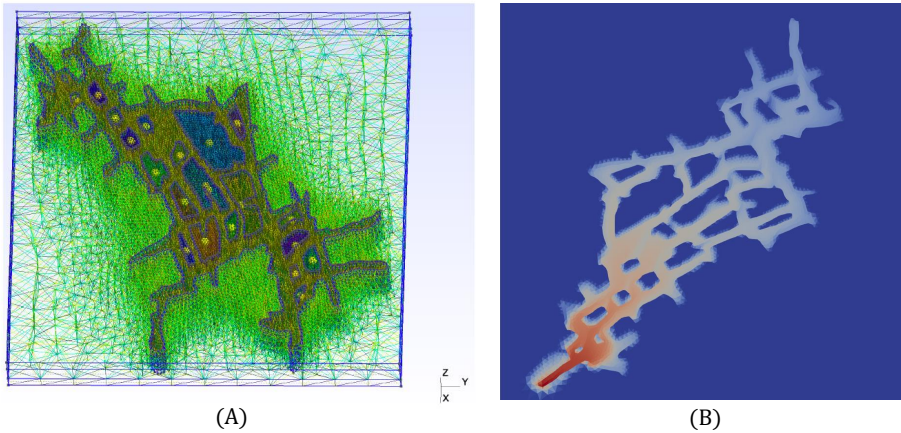


Figure 4.9 (A) 3D Cave model in GMSH after parametrizing the cave region and successive inner matrix regions. (B) Two-phase fluid-flow simulation in 3D cave model. Large velocity in cave region results in almost instant water breakthrough and small diffusion into the matrix (very similar to the fluid-flow patterns in conductive fracture networks). From Rossetto, 2020.

4.4. CHEMICAL MODELING

4.4.1. CHEMICAL REACTIONS

Fundamentally, any chemical reaction can be broken down into a sequence of one or more elementary reactions. Elementary reactions can be classified into three categories: 1) unimolecular; 2) bimolecular; 3) termolecular (Stumm & Morgan, 2012). A unimolecular reaction describes the process of dissociation of a single reactant molecule. A simple example is the dissociation of H_2O into H^+ and OH^- ($\text{H}_2\text{O} = \text{H}^+ + \text{OH}^-$), or the dissociation of Oxygen at high pressures ($\text{O}_2^{4-} = \text{O}^{2-} + \text{O}^{2-}$). Another example of a unimolecular reaction is radioactive decay. Bimolecular reactions involve the collision between two reactive molecules ($\text{A} + \text{B} = \text{AB}$). An example of a bimolecular reaction is $\text{CO}_{(\text{g})} + \text{NO}_{3(\text{g})} \rightarrow \text{NO}_{2(\text{g})} + \text{CO}_{2(\text{g})}$. Finally, in sporadic cases of extremely high-pressure conditions, a collision between three reactant molecules can occur, which is denoted as termolecular (Vallance, 2017).

In the first example, the proton (H^+) is almost instantaneously hydrated to form hydronium (H_3O^+) or sometimes referred to as a protonated water cluster. The overall reaction is therefore often written as $2 \text{H}_2\text{O} = \text{H}_3\text{O}^+ + \text{OH}^-$. At first sight this might seem like a bimolecular reaction, nonetheless, it is actually a sequence of two steps: a unimolecular

reaction $\text{H}_2\text{O}=\text{H}^+ + \text{OH}^-$ and a bimolecular reaction $\text{H}_2\text{O} + \text{H}^+ \rightarrow \text{H}_3\text{O}^+$. Following the reaction steps we arrive at the ‘complex’ reaction $2 \text{H}_2\text{O}=\text{H}_3\text{O}^+ + \text{OH}^-$.

Elementary reactions generally contain a transition between two states, separated by a potential or energy barrier which is often denoted as the activation energy of the reaction. The rate at which the reaction occurs is partially determined by the magnitude of the activation energy (size of the potential barrier). High activation energy means that for the reaction to occur, a large amount of (kinetic) energy is required during the collision to overcome the energy barrier (Laidler, 1987; Lasaga, 1981, 1984), subsequently reach the excited state and eventually form the product of the reaction. Since the temperature of a system is a measure of the average kinetic energy of the molecules in the system (Lasaga, 1981), an increase in temperature generally increases the reaction rate. Change in the equilibrium constant of a reaction with respect to temperature was first formalized by Van’t Hoff, 1884, when assuming standard conditions is expressed as:

$$\frac{d}{dT} \ln K_{eq} = \frac{\Delta H^\ominus}{RT^2}, \quad (4.1)$$

where T is the temperature in Kelvin, K_{eq} is the equilibrium constant, ΔH^\ominus is the standard enthalpy of reaction, and R is the universal gas constant. The standard enthalpy of reaction is positive for an endothermic reaction and negative for an exothermic reaction. Integrating equation (4.1) from T_2 to T_1 results in

$$\ln\left(\frac{K_2}{K_1}\right) = -\frac{\Delta H^\ominus}{R} \left(\frac{1}{T_2} - \frac{1}{T_1}\right), \quad (4.2)$$

from which it is clear that if $T_2 > T_1$ and $\Delta H^\ominus > 0$, endothermic, the equilibrium constant is increasing (forward reaction is favorable) while if $\Delta H^\ominus < 0$, exothermic, the backward reaction is favored. This is also typically explained using Le Chatelier’s Principle (Le Chatelier, 1884), which states that when changes are applied to a system that is at equilibrium, the system reacts to counteract these changes. Consider the following exothermic reaction: $\text{C}=\text{A} + \text{B} + \text{Heat}$, note that heat is a product; when temperature increases the heat content of the system increases, and the equilibrium is shifted towards the left by favoring the backward reaction. A real world example of such an exothermic reaction is calcite dissolution (He & Morse, 1993; Singurindy & Berkowitz, 2003): $\text{CaCO}_3=\text{Ca}^{2+} + \text{CO}_3^{2-} + \text{Heat}$. Dissolution potential related to hydrothermal karstification is often formed due to cooling of ascending thermal fluids in combination with the mixing of two fluids with different chemistry resulting in mixing corrosion (Dublyansky, 2000; Klimchouk, 2012; Palmer, 1991).

Based on the work of van Van ’t Hoff, Arrhenius, 1889 proposed his equation to describe the dependence of the kinetic rate constant on temperature:

$$k = A \exp\left\{\left(\frac{-E_a}{RT}\right)\right\}, \quad (4.3)$$

where k is the rate constant, A is the pre-exponential factor, and E_a is the activation energy (or potential barrier). The pre-exponential factor A , according to collision theory, is related to the frequency of collisions in which the colliding molecules attain the correct

orientation for the reaction to take place (Menzinger & Wolfgang, 1969). Present-day, this equation is still regarded as an excellent empirical equation describing the temperature dependence of the kinetic reaction rate constant (House, 2007; Wright, 2005).

Besides the dependence of the reaction rate on the system's temperature, the law of mass action, first described by Waage and Gulberg, 1986, proposes additional dependence. It states that the reaction rate is proportional to the product of the activities of the reactants. Note that this is typically only true for elementary (one-step) reactions. The reaction mechanism is usually determined experimentally in a complex kinetic reaction, accompanied by the rate-limiting step description. When the steps of complex reaction happen sequentially, for example, $A + B \rightarrow C$ followed by $C + D \rightarrow E$, the rate limiting step is the slowest reaction. When the steps of the complex reaction happen in parallel, for example, $A + B \rightarrow C$ and $D + E \rightarrow C$, the rate limiting step is the fastest reaction (Stumm, Morgan, et al., 1970).

4.4.2. EXAMPLES

Consider the following two kinetic reactions:

1. $A \rightarrow C$ (unimolecular elementary reaction)
2. $A + B \rightarrow C$ (bimolecular elementary reaction)

The reaction rate of the first reaction is given by $v_1 = k[A]$, whereas the reaction rate of the second reaction is given by $v_2 = k[A][B]$. In order to obtain an explicit function for the concentration of the reactant(s), the rate is expressed in differential form:

$$\frac{d[A]}{dt} = -v_1 = -k[A], \quad (4.4)$$

for the first reaction and:

$$\frac{d[A]}{dt} = -v_2 = -k[A][B], \quad (4.5)$$

One way to obtain an expression for the concentration of reactant A is by integration. For the first equation, this results in:

$$[A] = [A]_0 - kt, \quad (4.6)$$

while for the second equation, this results in:

$$kt = \frac{1}{[B]_0 - [A]_0} \ln\left(\frac{[B]_0[A]}{[A]_0[B]}\right). \quad (4.7)$$

Consider now if the bimolecular elementary reaction is actually an equilibrium reaction given by: $A + B \rightleftharpoons AB$. The differential form is now expressed as:

$$\frac{d[A]}{dt} = k_-[AB] - k_+[A][B], \quad (4.8)$$

where k_- is the backward and k_+ is the forward reaction rate constant respectively. At equilibrium, this equation equals zero. Setting $\frac{d[A]}{dt} = 0$ in equation (4.8) gives

$$k_-[AB] - k_+[A][B] = 0$$

$$\frac{[AB]}{[A][B]} = \frac{k_+}{k_-} = K_{eq}. \quad (4.9)$$

Note: this doesn't mean that no reaction occurs at all. Chemical equilibrium is usually interpreted as a dynamic equilibrium where the forward reaction (creation of molecule AB) occurs at the same rate as the backward reaction (product of molecule A and B), rather than no reaction occurring at all (Wright, 2005). In this context, kinetic reactions are interpreted as having a dominant direction in which the reaction occurs (e.g., $k_- \gg k_+$ or vice versa).

Please note the fundamental difference between equation (4.2) and (4.3): the equilibrium concentration (e.g., the solubility of a mineral) can both increase or decrease with increasing temperature due to the reaction being either endo- or exothermic; however, the kinetic rate constant for Arrhenius type of reactions solely increases with increasing temperature (excluding non-Arrhenius and anti-Arrhenius reactions). This is also used in chemical engineering (e.g., ammonia production). Since this is an exothermic process, increasing the temperature reduces the produced ammonia; however, at lower temperatures, the ammonia is produced at an unfavorable rate, and a compromise is made between equilibrium concentration and rate of production (Modak, 2002).

4

4.4.3. TREATMENT OF REACTIONS IN REACTIVE TRANSPORT SIMULATIONS

The type of chemical reaction used in the mathematical formulation of a conservation law is typically related to the reaction rate relative to the rate of other reactions in the system and the flow velocity. A reaction with a fast reaction rate (e.g., homogeneous or inter-aqueous reactions) in a system with relatively low flow velocity is best approximated with an equilibrium reaction (Stumm, Morgan, et al., 1970; Stumm & Morgan, 2012). A reaction with a prolonged reaction rate (e.g., heterogeneous reactions) in a system with fast flow velocity is best approximated using a kinetic reaction (Morel et al., 1993).

Equilibrium reactions, as shown above, are expressed using the law of mass action. Calcite dissolution/precipitation expressed as an equilibrium reaction results in $\text{CaCO}_3 = \text{Ca}^{2+} + \text{CO}_3^{2-}$, which at equilibrium must equal to:

$$\begin{aligned} \frac{\{Ca_{(aq)}\}\{CO_{3(aq)}\}}{\{CaCO_{3(s)}\}} &= K \\ \{Ca_{(aq)}\}\{CO_{3(aq)}\} &= K \\ Q &= K \end{aligned} \tag{4.10}$$

where Q represents the Ion Activity Product (IAP) and the activity of the solid species ($CaCO_{3(s)}$ is taken as unity. Note: For completeness, the square brackets that denote the molar concentration of species i are substituted by curly brackets that denote species activity i . This is following general hydro-chemistry literature. In the reservoir simulation literature, the molar concentration of species i is usually denoted as m_i and activity as a_i , respectively. The general reservoir simulation notation is followed in the remainder of this document.

Kinetic reactions in reactive transport code describing mineral dissolution/precipitation are typically expressed through the use of Transition State Theory (TST) rate laws (Steeffel et al., 2015). General form of such a (reversible) TST is given by (Aagaard & Helge-

son, 1982; Lasaga, 1984):

$$\begin{aligned} R_m &= \text{sgn}(\Omega) A_m k_m \left(\prod a^n \right) \left| \exp \left\{ \left(\frac{\eta \Delta G}{RT} \right) \right\} - 1 \right|^m \\ R_m &= \text{sgn}(\Omega) A_m k_m \left(\prod a^n \right) \left| \left(\frac{Q_m}{K_{eq}} \right)^\eta - 1 \right|^m, \end{aligned} \quad (4.11)$$

where Ω is the saturation index defined as $\Omega = \log \left(\frac{Q_m}{K_{eq}} \right)$, A_m is the reactive surface area, k_m is the kinetic rate constant, ΔG is the Gibbs free energy, the exponents η and m are experimentally derived constant, and the exponent n is the stoichiometric coefficient. Sometimes also given in the simplified version

$$R_m = A_m k_m \left(\prod a^n \right) \left(\left(\frac{Q_m}{K_{eq}} \right)^\eta - 1 \right). \quad (4.12)$$

For the use of a fully irreversible dissolution or precipitation reaction, the following reaction is typically used (Steefel et al., 2015):

$$R_m = A_m k_m \left(\prod a^n \right). \quad (4.13)$$

To avoid additional numerical convergence problems, the rate law should be a continuously differentiable function (Lichtner, 1996; Steefel et al., 2015). Both of the above rate laws satisfy these conditions and are suitable for modeling dissolution and precipitation reactions.

One of the other fundamental aspects of mineral dissolution and precipitation processes is accurately capturing porosity changes, especially its effect on the permeability and therefore pressure (Lichtner, 1996). Fracture permeability is usually updated according to a power-law function:

$$k_{n+1} = k_n \left(\frac{\phi_{n+1}}{\phi_n} \right)^A, \quad (4.14)$$

where k_{n+1} is the new fracture permeability and k_n the old respectively, while ϕ_{n+1} is the new fracture porosity or relative aperture and ϕ_n is the old respectively, and finally A is the power-law exponent usually taken as 3.

Matrix permeability is usually updated using the Carman-Kozeny relationship:

$$k_{n+1} = k_n \left(\frac{\phi_{n+1}}{\phi_n} \right)^3 \left(\frac{1 - \phi_n}{1 - \phi_{n+1}} \right)^2 \quad (4.15)$$

In practice, a transmissibility multiplier is used to avoid recalculation of the transmissibility list at every Newton iteration (for unstructured grids, this can be pretty time-consuming).

4.4.4. FRACTURE NETWORK PREPROCESSING

The fluid flow evaluations are performed using the Delft Advanced Research Terra Simulator (DARTS), recently developed at the Delft University of Technology (Khait & Voskov, 2018a, 2018d; Khait & Voskov, 2017). DARTS is capable of solving thermal flow and transport problems in complex and realistic fractured reservoirs by using the DFM model

adapted from (Karimi-Fard et al., 2004). For a detailed mathematical description of the relevant flow equations, discretization, and modeling of permeability changes, see Chapter 2. The current DFM implementation in DARTS relies on a Two-Point Flux Approximation (TPFA) scheme where fractures are represented explicitly in the numerical model. However, explicit representations of the fractures, especially in fracture networks generated from outcrops, often contain complex fracture intersections that might pose meshing difficulties. Therefore, the resulting mesh can contain abundant artifacts that negatively impact the performance of the reservoir simulator. See Chapter 3 for a detailed analysis of the advanced DFM preprocessing method.

4.5. RESULTS REACTIVE TRANSPORT MODELING

4.5.1. INFLUENCE DAMKÖHLER AND PÉCLET

We conducted a large amount of portable LiDAR surveys to scan the interior of several caves in the East of Brazil. The goal was to better understand the spatial distribution of the cave networks and possibly explain the link between resulting cave geometry and several features such as sedimentology, structural control, and boundary conditions. Different cave geometries were observed, see for example (Bertotti et al., 2020a; Pontes et al., 2020), in comparison to the results presented in Figure 4.10. In this figure, very regular spacing of the cave tunnels can be observed (i.e., average of 6.5[m] between each tunnel). However, fracture measurements inside the caves displayed a shorter spacing between fractures than the cave tunnels display. This ties together with how much the fractures are involved in the resulting cave geometry: do they fully constrain the development of the dissolution features or only represent a small perturbation for the physical instability to develop?

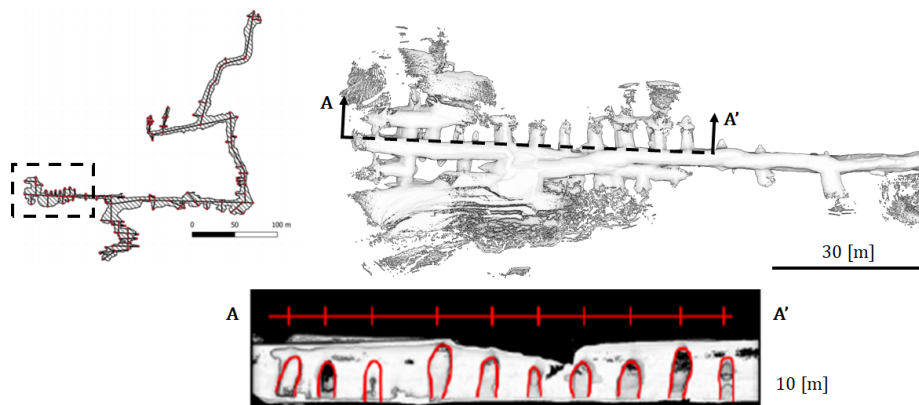


Figure 4.10 Left: Map view of the Torrinha cave in Brazil. Right: Detailed top- and cross-sectional view of the obtained LiDAR dataset displaying several, regularly spaced (i.e., 6.5[m]), cave tunnels.

The numerical code, based on the equations discussed in Chapter 2, has the capability of including chemical equilibrium as well as kinetic reactions. Equilibrium reactions are compared to its direct kinetic counterpart (equilibrium reactions interpreted as ki-

netic reactions)(Figure 4.11). Small differences between sub-branches of the wormhole and wormhole thickness are observed due to the highly nonlinear and unstable nature of the dissolution process where flow is tightly coupled with changes in permeability (similar to the nonlinear behaviour of viscous instabilities). The nonlinear solver for the kinetic reactions with very high kinetic rates struggles to converge without a good chopping strategy to guide Newton (i.e., iterative method for solving nonlinear equations) to the correct solution without oscillations.

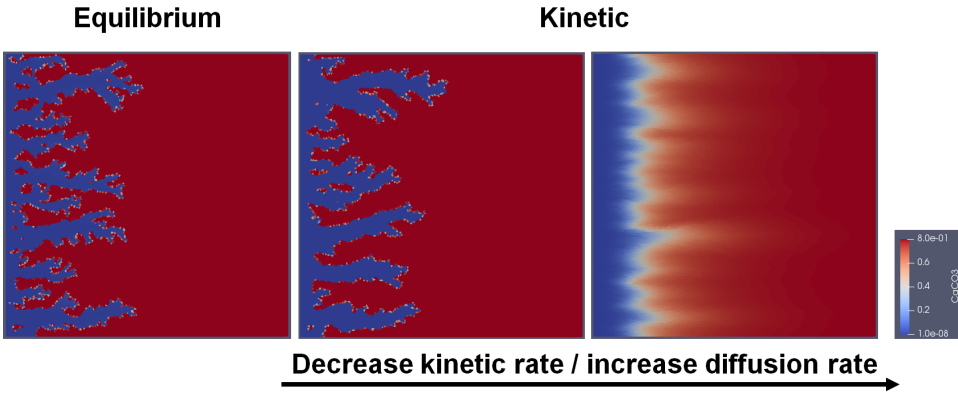


Figure 4.11 Comparison between chemical equilibrium and kinetic reactions (of varying kinetic rates). The results are obtained with the numerical simulation framework (DARTS) described in the previous section.

The Damköhler (Da) number is defined as the ratio between the reaction rate and advective mass transport rate. In contrast, the Péclet (Pe) number is the ratio between the advective mass transport rate and the diffusive transport rate. Low Da can be interpreted as either low reaction rate or fast advective mass transfer, while high Da implies the inverse. Low Pe can be interpreted as either slow advective mass transfer or fast diffusive mass transfer, while high Pe implies the inverse. Many authors have identified the influence of these dimensionless numbers on the resulting dissolution regimes (Cohen et al., 2008; Golfier et al., 2002; Kang et al., 2003; Koehn et al., 2021; Wang et al., 1993). Golfier et al., 2002 illustrated these regimes with experimental and numerical data and further labeled the wormhole types (previously mainly limited to compact, ramified, and uniform)(Figure 4.12). A very small reaction rate relative to the diffusive and advective transport results in uniform dissolution. Very fast reaction rate relative to diffusive and advective transport in compact dissolution. Ramified wormholes occur when diffusion is significantly larger than the reaction rate. Conical wormholes occur when the reaction rate influence is significantly larger than the diffusive transport. The dominant wormhole regime occurs after reaching a certain threshold (Da and $Pe = 1e-2$), and increasing the Da or Pe remains in the dominant wormhole regime. Numerical results by Cohen et al., 2008 show similar wormhole regimes (Figure 4.12).

Linking cave development to these wormhole types is a difficult task since, as shown later in this chapter, similar patterns can occur when fractures are involved. However, one can still observe the similarities between the observations from the field (Figure 4.8) and the different wormhole types (Figure 4.12). For example, the occurrence of a sin-

gle (large) cave passage can be linked to either the conical wormhole dissolution regime or potentially to a completely dissolved fracture corridor (requires a large diffusive influence relative to advective and reactive transfer). A maze cave pattern is likely somewhere between the dominant and ramified wormhole regime or could be formed in an orthogonal fracture network with intermediate influence of diffusive transport relative to advective and kinetic transfer rate (Figure 4.18).

Please note, Palmer, 1991 states: “the nature of the ground-water recharge is the most important factor in determining whether a cave will be a branchwork or a maze”. All these experiments are done with constant flow boundary conditions, which according to Palmer, 1991 is more likely to result in maze patterns. In order to fully predict cave patterns using numerical reactive transport models, more realistic boundary conditions based on regional hydrology should be considered.

4

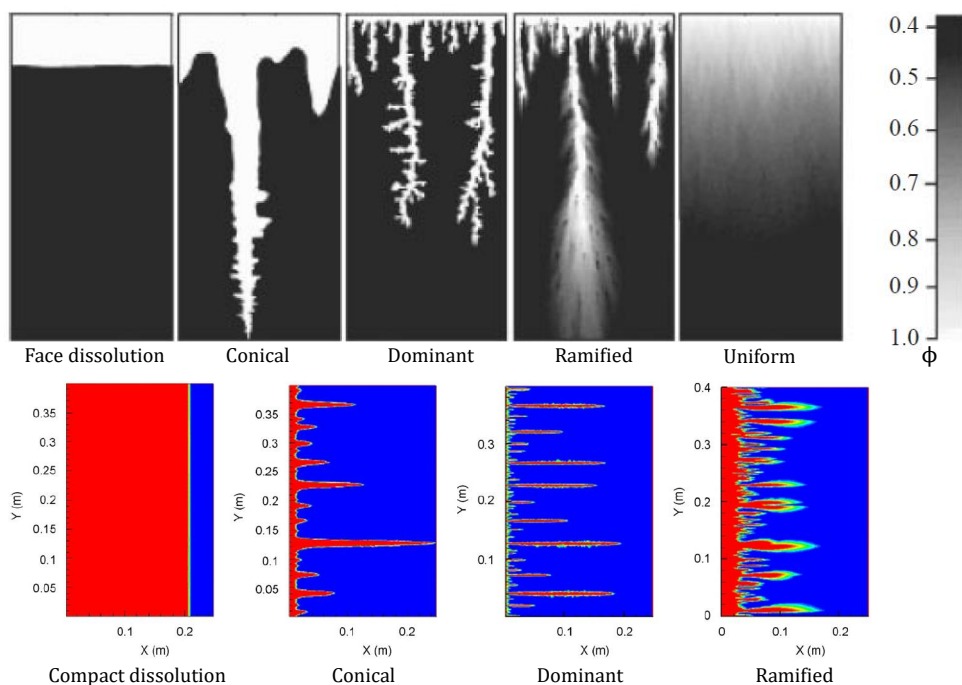


Figure 4.12 Different types of wormholes depending on the Da and Pe numbers. The top row are numerical results from Golfier et al., 2002 and the bottom row corresponds to numerical results from Cohen et al., 2008.

4.5.2. INFLUENCE BOUNDARY CONDITIONS AND RESOLUTION

The influence of boundary conditions on the resulting dissolution patterns from the numerical simulation cannot be underestimated. Suppose one wants to predict potential shapes and distributions of the subsurface karst network. In that case, careful consideration has to be made based on the resolution of the model, the presence of fractures, and the type of boundary condition. Besides the chemical composition and temperature

of the fluids involved, even something as simple as constant flow boundary conditions (i.e., Neumann) might be non-trivial. In reservoir simulation, we typically prescribe the boundary conditions via wells. Two choices can be made to mimic a constant flow injection along a specific boundary: a single well that perforates all boundary cells or a separate well for each cell along the boundary.

Two basic numerical experiments were done to investigate the difference between a single well versus multiple wells. The first experiment compares breakthrough times between the different setups, while the second shows breakthrough time. The random permeability is generated on the coarsest mesh (i.e., 50×100 for the first experiment and 12×20 for the second), and is downscaled to each finer scale by simply subdividing the coarse cell into 2×2 , 3×3 , etc. fine cells (Figure 4.13(A) and (B)). The permeability field of the first experiment is generated following a Gaussian (correlated) random field with correlation length > 0 , while the second one is generated using random noise of around 5% around the mean permeability. The size of the domain in both cases is 50×100 [m] in the x- and y-direction. Note, the $\Delta x = \Delta y$ and $\Delta x < \Delta y$ in the two respective setups. The fluid and rock parameters are described in the Appendix A. Pure water is injected at a constant rate of 200 [m³/day] on the left, and on the right, constant pressure of 95 [bar] is maintained (for both experiments).

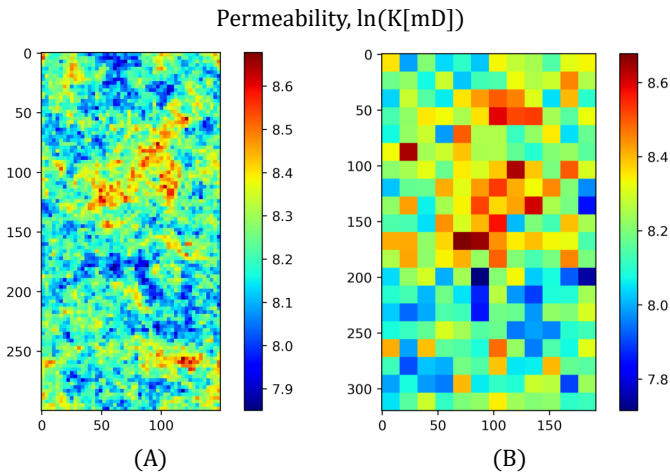


Figure 4.13 Maps of initial permeability of two experimental setups. The random permeability is generated on the coarsest mesh (i.e., 50×100 for the first experiment and 12×20 for the second), and is downscaled to each finer scale by simply subdividing the coarse cell into 2×2 , 3×3 , etc. fine cells. The actual size of both domains is 50×100 [m] in the x- and y-direction (meaning, $\Delta x = \Delta y$ and $\Delta x < \Delta y$ in the two respective setups).

A sensitivity study on the numerical convergence (i.e., changes in solution when refining the mesh) shows that a single well with multiple perforations, as often used in reservoir simulation, significantly increases dominant wormhole formation and reduces breakthrough times with mesh refinement (Figure 4.14). This is most likely caused due to two things. Refining the mesh speeds up the development of the unstable dissolution front. This, in turn, increases the convergence of fluids towards higher permeabil-

ity zones (i.e., where the material is dissolved already). A single well with multiple perforations is already prone to distributing the fluid unevenly. The cumulative effect is faster wormhole propagation. It can be argued which boundary condition implementation is more “realistic”. A fixed pressure (i.e., Dirichlet) or Robin (i.e., a combination between Dirichlet and Neumann) might be more realistic but means one cannot control the dimensionless numbers such as Da and Pe because constant pressure in combination with increasing effective permeability due to dissolution results in an increasing flowrate. Note that implementing a separate well for each cell on the boundary causes linear convergence issues, and a direct solver was applied instead of the standard iterative solver. This is why 150×300 is the finest resolution tested in the sensitivity study.

4

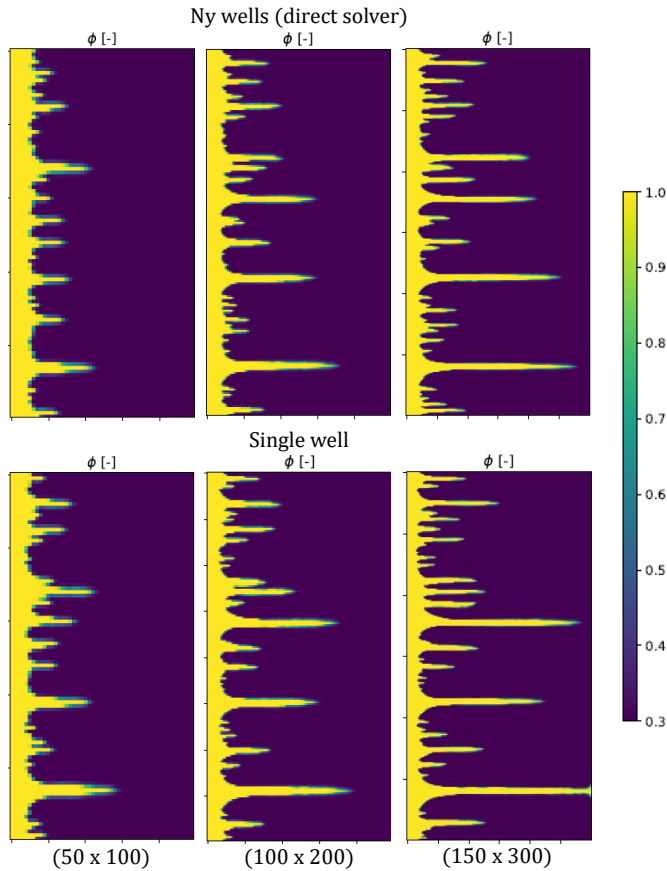


Figure 4.14 Effect of boundary conditions on porosity map after dissolution (using permeability field in (Figure 4.13(A))). The plot shows two rows (i.e., multiple wells vs. single well) and three rows (i.e., coarsest to finest scale). Early breakthrough of the leading wormhole is observed as well as an increase in the number of smaller wormholes when refining the mesh.

A further quantitative analysis, similar to the Pore Volume Breakthrough Time (PVBT)

of the leading wormhole in Cohen et al., 2008; Maheshwari et al., 2013; Shaik et al., 2017, is presented. The number of fully developed wormholes is stabilizing as well at the finest resolution (no difference when coarsening one level) (Figure 4.15). Following the observations of Shaik et al., 2017, the PVBT is decreasing with mesh refinement, and the curve is approaching zero change with resolution at the finest resolution (Figure 4.16).

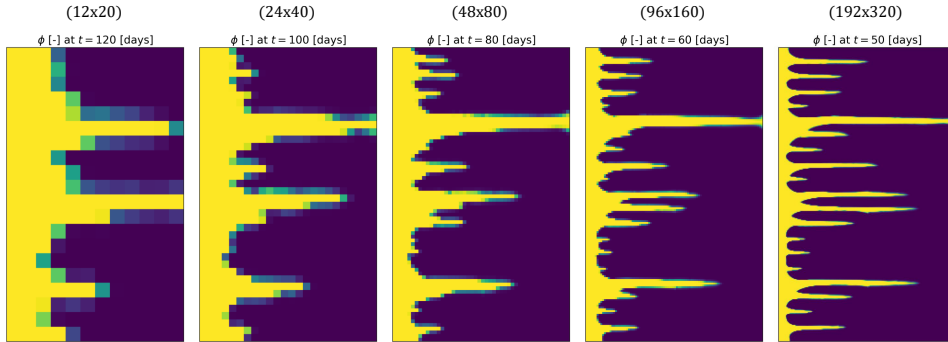


Figure 4.15 Porosity map as a function of resolution for constant flowrate with a single well/multiple perforations (using permeability field in (Figure 4.13(B)). Note, the time at which the snapshot is visualized differs amongst realizations and is taken at the time of breakthrough. The number of wormholes is stabilizing when refining the mesh as while the PVBT is increasing when refining the mesh (similar to the observations in Shaik et al., 2017).

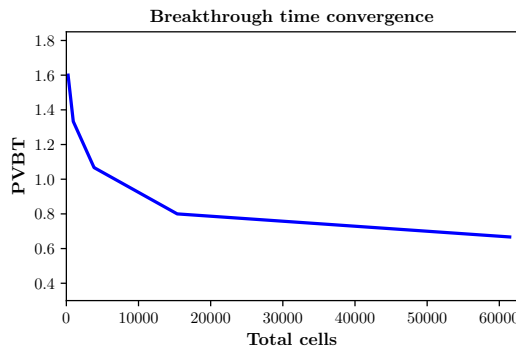


Figure 4.16 PVBT curves for constant flowrate with a single well/multiple perforations when refining the mesh (using permeability field in (Figure 4.13(B)). In accordance with the observations of Shaik et al., 2017, the PVBT is decreasing with mesh refinement and the curve is approaching zero change with resolution at the finest resolution.

4.5.3. PRESENCE OF FRACTURES

We furthermore use the numerical simulation framework to examine qualitatively how significant the impact of fractures is on the dissolution patterns. This is done by varying the fractures' aperture (i.e., conductivity). It can be observed that with a large fracture aperture, the resulting dissolution pattern is completely governed by the fracture distri-

bution, while when decreasing the fracture aperture, similar patterns as shown in Figure 4.10 can be observed. Therefore, it is important to understand the initial and boundary conditions of the geological system, especially in terms of fracture distribution and characteristics, if we want to predict the dissolution patterns in the subsurface successfully. These predictions, however, can be improved/constrained by the use of history matching/Bayesian inference of several parameters using present-day observations.

Fracture aperture has a large impact on the resulting dissolution pattern (Figure 4.17). Increasing the fracture aperture results in a more localized dissolution from within the fracture network (i.e., maze pattern as observed in Lapa de Bode). Reducing the fracture aperture seems to generate a similar pattern as observed in Torrinha (Figure 4.10).

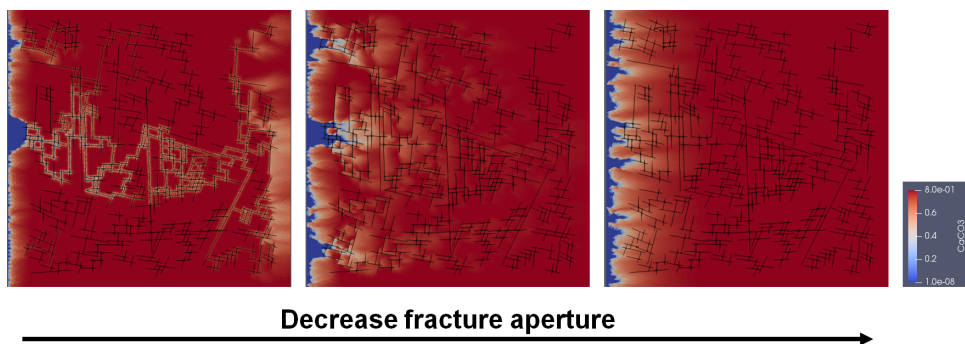


Figure 4.17 Illustration of the effect of fracture aperture on the resulting dissolution patterns. Smaller fracture aperture seem to generate a similar pattern as observed in the LiDAR data. The results are obtained with the numerical simulation framework (DARTS) described in the previous section.

Results obtained by varying dispersive influences (i.e., keeping constant injection and kinetic reaction constants but increasing the effective dispersivity) are displayed in Figure 4.18. It can be clearly seen that substantial effective dispersion almost negates the influence of the fractures. At the same time, too small effective dispersion results in a complete bypass of the dissolution in the fracture network (i.e., no fluid penetrates the matrix surrounding the fracture walls, and nothing is dissolved). In between are two regions: highly dispersed giant tunnel and wide-spread dissolution closer to the source (i.e., location with higher dissolution potential); very regular dissolution patterns around the fracture walls similar to patterns observed in Lapa de Bode.

Figure 4.19 shows the different dissolution patterns when varying the mesh resolution (for the same simulation parameters as the third regime in Figure 4.18. Sufficient resolution is required when considering the highly localized dissolution around the fracture walls. Qualitatively, the coarsest scale does not capture the same behaviour as the other two finer scales.

4.6. CONCLUSIONS

Reservoir modeling of karstified and fractured reservoirs becomes a focus of modern research due to the importance of such systems in various subsurface applications (e.g., geothermal energy or hydrocarbon production). There are techniques available to de-

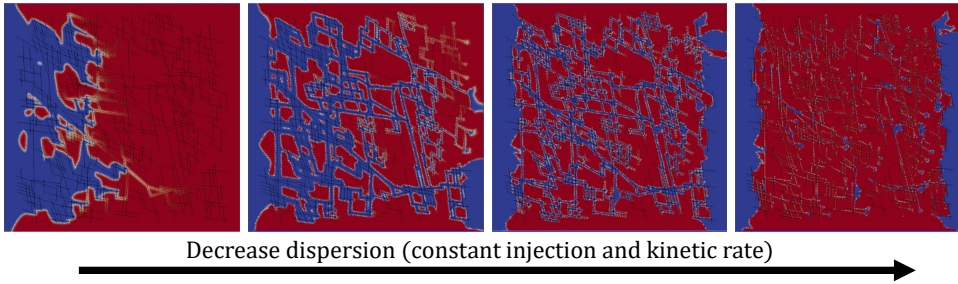


Figure 4.18 Different dissolution patterns when varying the effective dispersion. No maze caves are formed in either end-point regimes (too strong/weak effective dispersion). Large variety in cave passage width is obtained with high dispersive forces, while very regular width of cave passages is obtained in the intermediate effective dispersion regime.

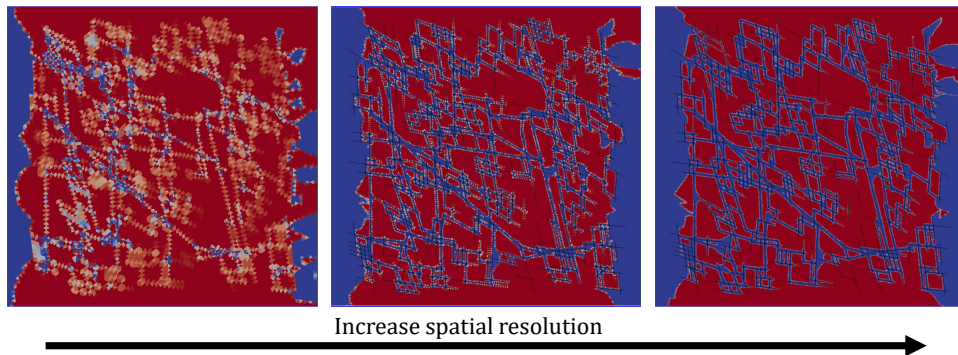


Figure 4.19 Effect of grid resolution on dissolution patterns. As is the case without fractures, dissolution requires a large spatial accuracy to reflect the complex physical fluid-rock interaction. Local refinement might be a solution.

tect, at some scale, if karstification or other chemical and mechanical alterations exists. However, it remains unclear how to model them on a reservoir scale and produce a realistic representation of the subsurface. This chapter attempts to explore the relationship between heterogeneity (i.e., permeability and presence of fractures), different interplay of reactive, advective, and diffusive transport rates, and the resulting dissolution patterns using LiDAR observations from real caves and numerical reactive transport results.

In order to analyze the shape of the caves, the point cloud data is converted into an image from which the skeleton is extracted. A slice is made through the point cloud along each skeleton limb, and the points are projected on the plane perpendicular to the skeleton limb. A curve is fitted through the project points resulting in an approximation of the shape of the cave at the particular limb of the skeleton. The shape is analyzed for a specific cave (i.e., Lapa de Bode). Very regular spacing between the cave passages is observed, and regular width and heights of the cave passages. Except at some end-points or connecting fractures in a NE-SW direction, possibly indicating converging flow and preferential dissolution.

Next, we combine our fracture modeling technique with the reactive flow and transport framework utilized Operator-Based Linearization approach. The preprocessing algorithm in Chapter 3.2.4 is used for handling the fracture networks. We introduce a robust treatment of matrix dissolution based on a combination of kinetic and equilibrium chemistry with changes in porosity and permeability. The developed framework allowed us to simulate various geogenesis scenarios where different system parameters such as chemical treatment, fracture aperture, and spatial distribution are stochastically populated. Qualitative simulation results are presented further to explore interactions between flow in fractured media and dissolution.

Furthermore, the influence of effective dispersion on dissolution patterns in fracture networks is analyzed. Intermediate ranges result in the localized regular dissolution distribution (at fracture walls) similar to some caves. While end points of effective dispersion (too small/large) reduces the influence of the fracture network on the dissolution patterns. It is also shown that numerical simulation results require sufficient resolution to capture maze cave patterns. In order to predict all cave patterns mentioned in Palmer, 1991, more realistic boundary conditions which represent the regional hydrology should be considered. Convergence behavior of DARTS based on PVBT and number of wormholes is in accordance with results from AD-GPRS (Shaik et al., 2017). The significant difference between a single well but multiple perforations and multiple wells is highlighted, further stressing that actual wormhole configuration is complicated to predict.

A future goal of our research is to define a straightforward approach on how to model these different permeability and porosity distributions based on a set of observations. Due to the lack of direct measurements and sparsity of these observations, uncertainty on the state of the subsurface plays an important role. Uncertainty can be accounted for through the use of statistical approaches (e.g., MPS), where the different dissolution patterns can serve as training images. Subsequently, additional observations can be used to obtain a posterior distribution of the reservoir parameters. However, defining and understanding what these reservoir parameters should embody within karstified reservoirs remains a big challenge.

4.7. ACKNOWLEDGEMENTS

Hereby we would like to acknowledge the funding from the TKI-geoenergy CarbFrac project and Shell Brazil. We also want to thank Mohammed Karimi-Fard for his insightful comments and suggestions regarding the preprocessing strategy. Furthermore, we would like to express our sincere gratitude to the collaborative fieldwork with the Federal University of Rio Grande do Norte, particularly Hilario Bezzera, Cayo Pontes, and Rebeca Seabra.

5

ACCURATE GEOTHERMAL AND CHEMICAL DISSOLUTION SIMULATION USING ADAPTIVE MESH REFINEMENT ON GENERIC UNSTRUCTURED GRIDS

A coupled description of flow and thermal-reactive transport is spanning a wide range of scales in space and time, which often introduces a significant complexity for the modelling of such processes. Subsurface reservoir heterogeneity with complex multi-scale features increases the modelling complexity even further. Traditional multiscale techniques are usually focused on the accuracy of the pressure solution and often ignore the transport. Improving the transport solution can however be quite significant for the performance of the simulation, especially in complex applications related to thermal-compositional flow. The use of an Adaptive Mesh Refinement enables the grid to adapt dynamically during the simulation, which facilitates the efficient use of computational resources. This is especially important in applications with thermal flow and transport where the region requires high-resolution calculations as often localized in space. In this work, the aim is to develop an Adaptive Mesh Refinement framework for geothermal reservoir simulation. The approach uses a multi-level connection list and can be applied to fully unstructured grids. The adaptivity of the grid in the developed framework is based on a hierarchical connectivity list. First, the fine-scale model is constructed, which accurately approximates all reservoir heterogeneity. Next, a global flow-based upscaling is applied, where an unstructured partitioning of the original grid is created. Once the full hierarchy of levels is

Parts of this chapter have been published in *Advances in Water Resources* **154**, 103977 (2021) de Hoop et al., 2021a.

constructed, the simulation is started at the coarsest grid. Grid space refinement criteria is based on the local changes and can be adjusted for specific models and governing physics. The multi-level connectivity lists are redefined at each timestep and used as an input for the next. The developed Adaptive Mesh Refinement framework was implemented in Delft Advanced Research Terra Simulator which uses the Operator-Based Linearization technique. The performance of the proposed approach is illustrated for several challenging geothermal applications of practical interest.

5.1. INTRODUCTION

Production development of prospective reservoirs includes the use of various technologies that provide information at many different scales. These scales range from core plugs being a few centimeters in size to well logs detecting properties a few meters around the well, and to seismic imaging covering a significant volume with limited resolution (few meters vertically and 10's of meters horizontally). However, time and capital limitations result in sparse direct sampling of reservoir rock and fluid properties. This is why the construction of reservoir models, through integration of these data using geostatistical reservoir description algorithms, has become a crucial step in resource development (Branets et al., 2009). These algorithms conventionally result in fine-scale descriptions of reservoir properties (porosity, permeability) on grids of tens of millions of cells (Christie, 1996).

An issue of considerable importance is the risk and uncertainty assessment of reservoir performance. The uncertainty can be gauged by simulating an ensemble of different geological realizations (Chen et al., 2015). This may require to run thousands of simulations to cover a wide range of parameter variation. It is however not computationally feasible or desirable to perform these simulations on the high-fidelity (fine-grid) model. Significantly upscaled models (i.e., the mapping of rock and fluid properties to a coarser resolution) are therefore required, where these models should ideally be even coarser than typical reservoir simulators, which can handle on the order of $10^5 - 10^6$ simulation cells (Durlofsky, 2005). In the presence of more complex physics, excessive upscaling may, however, result in non-satisfactory results, which necessitate the use of advanced algorithms and solvers to allow for higher resolution grids to be employed (Cusini et al., 2016).

Traditional Multiscale techniques (Jenny et al., 2003; Wang et al., 2014), developed to solve the elliptic (or parabolic) pressure equation in sequentially coupled simulations, mainly focus on the pressure solution and often ignore the transport. However, in complex applications related to chemical and compositional EOR (Enhanced Oil Recovery), reservoir storage and geothermal industry, the number of conserved chemical species can be large which makes any improvement in transport solution quite significant for the performance and robustness of the simulation. A technique called *Adaptive Mesh Refinement* (AMR) provides an effective means for adapting the resolution of a model to solution requirements. This method is well developed in many areas of computational physics (e.g. fluid dynamics and solid mechanics) but is however not widely used for practical reservoir simulation (Karimi-Fard & Durlofsky, 2014).

In today's literature, several researchers have developed and proposed AMR procedures to capture the local nature of transport processes. Bahrainian and Dezfuli, 2014

have developed a novel unstructured grid generation algorithm which considers the effect of geological features and well locations in the grid resolution. This strategy involves the definition and construction of the initial grid based on the geological model, geometry adaptation of geological features and grid resolution control. Trangenstein, 2002 used the combination of high-resolution discretization methods with dynamically adaptive mesh refinement for a two-component single-phase model for miscible flooding. Pau et al., 2012 proposed an AMR algorithm for compressible two-phase flow in porous media. The method is implemented within a block structured adaptive mesh refinement framework which allows the grids to dynamically adapt to flow features and enables efficient parallelization of the algorithm. The coarse-scale permeability was obtained by averaging the fine-scale permeability. Similar techniques have been developed for compositional simulation (Sammon et al., 2003), thermal problems (Christensen et al., 2004), improved/enhanced oil recovery processes (Van Batenburg et al., 2011), Discrete Fracture Networks (Berrone et al., 2019), and many more applications.

In this work, the aim was to develop a dynamic AMR scheme using an unstructured multi-level gridding framework, for geothermal simulation in complex reservoirs. The focus lied particularly on thermal-reactive flow and transport formulation which are required for a wide range of subsurface applications relevant to the energy transition including geothermal. Notice that heterogeneity plays a very important role in geothermal applications (Babaei & Nick, 2019; Shetty et al., 2018). The geothermal doublet lifetime and heat recovery rate usually vary a lot with both reservoir parameters and operational management where uncertainties due to heterogeneity are dominating (Willems & Nick, 2019). Besides, heterogeneity in flow path and shale facies play an important role in water heat recharge which directly affects doublet performance at low net-to-gross ratio (Crooijmans et al., 2016). Besides, complex heat extraction process and corresponding chemical interactions can also amplify the effect of heterogeneity (Cui et al., 2016; Kala & Voskov, 2020).

As a starting point of our framework, a fine-scale geological model has to be constructed accurately approximating all reservoir heterogeneity. In reservoir simulation, this model is often represented by a list of volumes, depths and a connectivity list (Lim et al., 1995) describing each control volume. Next, a global flow-based upscaling was applied and an unstructured partitioning of the original grid was constructed as suggested in (Karimi-Fard & Durlafsky, 2014). This partitioning provides coarser levels of the original model which is also described by a list of volumes, depths and a connectivity list. A coarser connectivity list includes connections between control volumes at the given level as well as interconnections between the levels. Once the full hierarchy of levels is constructed, the simulation is started at the coarsest grid. Grid space refinement criterion is developed for particular applications. The multi-level connection list is reconstructed at each time step and used for the simulation. The proposed approach was implemented in *Delft Advanced Research Terra Simulator* (DARTS) (Kala & Voskov, 2020; Wang et al., 2020).

5.2. METHODOLOGY

For the governing equations used for the flow simulations in this chapter, the reader is referred to Chapter 2. For the discretization approach and linearization using OBL, the

reader is referred to Chapter 2.

5.2.1. CONNECTIVITY LIST

The proposed AMR technique uses the Finite Volume Method (FVM) for discretization. The implementation of the finite volume discretization method to the mass conservation equation requires the evaluation of the flow between two adjacent control volumes in terms of the cell pressures. Using a Two-Point Flux Approximation (TPFA), the flow rate is defined as:

$$Q_{ij} = \Gamma_p^{ij} (P_i - P_j), \quad (5.1)$$

where:

- Q_{ij} : flow rate at interface of cells i and j ,
- Γ_p^{ij} : phase transmissibility at interface of cells i and j ,
- P_i : pressure of cell i ,
- P_j : pressure of cell j .

Similarly, the heat flux between two adjacent control volumes is expressed in terms of thermal transmissibility Γ_c and is, also using a TPFA, defined as:

$$Q_{ij}^h = \Gamma_c^{ij} (T_i - T_j), \quad (5.2)$$

where Γ_c^{ij} is the thermal transmissibility at interface ij , T_i and T_j are the temperatures of cell i and j respectively, and Q_{ij}^h is the heat flux at interface ij .

To evaluate the flux between two adjacent control volumes, a so-called *connectivity list* is constructed, i.e. for each interface between two neighbouring control volumes, the indices of these cells are listed together with the transmissibility (Lim et al., 1995). The result is a list with all connection pairs present in the grid. A few important points to be noted are:

- Each connection consists of only two elements,
- The connection pairs are not repetitive,
- No-flow boundaries imply the absence of connections and are hence not listed in the connectivity list.

The figure below shows a simple example of a 2D Cartesian structured grid, with corresponding cell indexing. Table 5.1 shows its connectivity list. The list is expressed as two arrays, cell i and cell j , where each column represent a connection pair. Each pair has an associated interface transmissibility stored in the connectivity list.

Table 5.1 Connectivity list of the example grid from figure 5.1.

		Dual connections																						
Cell i	0	0	1	1	2	2	3	4	4	5	5	6	6	7	8	8	9	9	10	10	11	12	13	14
Cell j	1	4	2	5	3	6	7	5	8	6	9	7	10	11	9	12	10	13	11	14	15	13	14	15

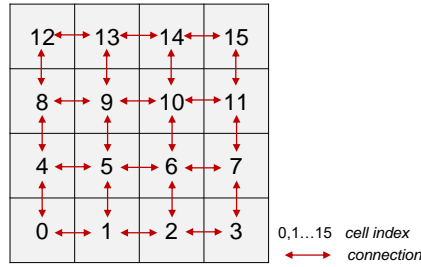


Figure 5.1 4x4 Cartesian grid denoting cell indexing and showing neighbouring connections. Indexing is based on a Cartesian structured mesh for simplicity.

5.3. MULTI-LEVEL GRID GENERATION

The adaptivity of the grid in the developed AMR scheme is based on a hierarchical representation of connectivity list. The simulation grid is composed of several predefined *levels* representing the same geological properties at different resolutions. We start with a fine-scale model (*static geological model*) which accurately represents all reservoir heterogeneity. This grid is defined as *level 0* and represents our finest level. The modeling grid is defined by a list of control volumes, depths, reservoir properties (all spatially distributed properties required to solve the discretized relations 2.31 and 2.32) for each mesh element, and a list of connectivity with corresponding transmissibility between neighbouring cells.

Next, *level 1* is defined, where control volumes are constructed by aggregating fine grid cells. Upscaling is applied to redefine volume, depth and reservoir properties at a coarser level. A connectivity list, with corresponding transmissibility, is constructed for this level and inter-level connections are defined in addition. Similarly, more levels of coarsening can be constructed. A control volume in grid-level n always consists of cells from grid-level $(n - 1)$, resulting in a hierarchical relationship (Karimi-Fard & Durlofsky, 2014). The simulation grid is then obtained by combining control volumes from grids of different levels. A schematic representation of this procedure is illustrated in figure 5.2 below.

5.3.1. CELL AGGREGATION

A mesh consists of a set of finite elements, each having vertices with allocated coordinates. To conduct cell aggregation, the centroid is first computed for each mesh element within the grid. Figure 5.3 shows an example 2D unstructured grid to illustrate how cell aggregation is conducted. As can be seen, in this particular example, each cell has 3 vertices, and a centroid (represented in red) with coordinates x_c and y_c defined as $(\frac{x_1+x_2+x_3}{3}, \frac{y_1+y_2+y_3}{3})$, where x_i and y_i are the coordinates of the vertices. Each mesh element has an assigned index number.

Cell aggregation is then carried out by dividing the grid in the x - and y -direction (and in the z -direction for 3D models) into equidistant intervals Δx and Δy using a predefined scaling factor. Each interval has coordinates $[i, i + \Delta x]$ in the x -direction and $[j, j + \Delta y]$ in the y -direction. Centroids of cells whose coordinates are within a given xy -area are

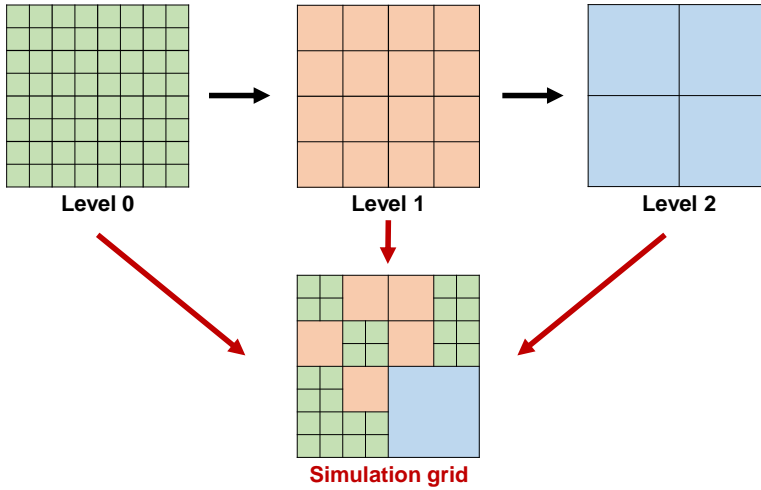


Figure 5.2 2D Multi-level grid with three pre-constructed grids (levels) with an example simulation grid which is constructed by aggregating control volumes from different levels.

5

aggregated to form one coarse cell. To check whether a fine cell f is within a given plane which will form coarse cell F , the following algorithm is implemented for the coordinates x_{c_f} and y_{c_f} of the centroid of fine cell f :

$$\text{if } i \leq x_{c_f} < i + \Delta x \text{ and } j \leq y_{c_f} < j + \Delta y, \text{ cell } f \in \text{cell } F. \quad (5.3)$$

Figure 5.3 shows the range partitioning (illustrated by the white lines) for a 2D unstructured grid. The x - and y -range were divided in 5 and 3 equidistant intervals respectively. The yellow-highlighted 2D plane has range $[i, i + \Delta x]$ in the x -direction and $[j, j + \Delta y]$ in the y -direction. For this given example, all cell centroids whose coordinates fall within this plane, are aggregated to form one coarse cell. For example, cells 41, 46, 68, 77, 84, 92, 106, 111 and 118 form coarse cell 0.

For the given 2D unstructured grid example in figure 5.3, the so-called *level 1* - i.e. the next level of coarsening - is shown in figure 5.4. The numbers represent the assigned indices of the newly constructed coarse cells. If one wants to construct an additional level, the same procedure can be followed with a larger x - and y -range partitioning, where grid cells of level 1 are aggregated to form level 2.

For further steps into the generation of the levels, a list - "*finer in coarse*" - is constructed where the corresponding indices of the aggregated fine cells are listed for each coarse cell. Table 5.2 below tabulates this list for the example above (figures 5.3 to 5.4). This type of list is generated for each coarse level (level > 0) in the hierarchical grid. These lists are stored for the construction of the cell properties (e.g. volume, porosity) of the coarse levels, where the cell data from the fine level is needed during upscaling.

Table 5.2 "*finer_in_coarse*" list of the example 2D unstructured grid of figures 5.3 - 5.4. This list describes for each coarse cell, the aggregated fine cells of level $n - 1$ to form the coarse cell of level n .

Coarse cell	Fine cells
0	41, 46, 68, 77, 84, 92, 106, 111, 118
1	2, 4, 12, 51, 55, 65, 78, 122
2	8, 25, 26, 27, 28, 29, 30
3	3, 5, 13, 44, 52, 79
4	16, 42, 45, 49, 74, 87, 90, 104, 114, 117
5	21, 34, 37, 61, 63, 71, 73, 82
6	15, 18, 56, 88, 96, 100, 102, 109, 110, 123
7	23, 35, 57, 94, 97, 98, 99, 101, 107, 108
8	14, 24, 64, 67, 89, 95, 115, 121
9	20, 33, 38, 60, 62, 70, 72, 83
10	17, 40, 47, 50, 75, 86, 91, 105, 113, 116
11	1, 7, 11, 53, 58, 81
12	9, 19, 22, 31, 32, 36, 39
13	0, 6, 10, 54, 59, 69, 80, 120
14	43, 48, 66, 76, 85, 93, 103, 112, 119

Note that cell aggregation can also be conducted while taking care of highlighting geological features (e.g. fractures) and different facies in the model. For example, cell aggregation can be conducted by grouping domains with the same facies together into one coarse cell, or, in fractured reservoirs, by aggregating cells by isobar contours similar to (Karimi-Fard & Durlofsky, 2014).

After cell aggregation is conducted, the connectivity list is then constructed describing all connections within each level and the inter-level connections. To illustrate the methodology, we use the simple structured grid from figure 5.1, where cell aggregation was performed to form one coarse level.

In the proposed AMR scheme, the connectivity list of each level is determined systematically. Each mesh element consists of a set of vertices \mathbf{x} . E.g. a triangular mesh element comprises 3 vertices, and a Cartesian grid comprises 4 vertices. These vertices are numbered uniquely. The vertices \mathbf{x} comprised in a cell i are stored in a list; this is done for each mesh element in level 0. To determine whether two control volumes i and j are adjacent, we take the intersection of both sets of vertices. That is:

$$\{\mathbf{x}|\mathbf{x} \in i\} \cap \{\mathbf{x}|\mathbf{x} \in j\}. \quad (5.4)$$

Each geometry has a different criterion. For 2D shaped mesh elements, the interface is a line; for 3D shaped cells, the interface is a plane. Hence the criterion is that the intersection length should equal 2 for 2D shapes and 3 or more for 3D shapes. This methodology is applied to the finest level of refinement - level 0. The result is a connectivity list representing all the unique connection pairs within level 0. The interface area is subsequently computed (and stored for transmissibility computation in further steps) for each connection.

For the construction of the coarse level connectivity list, we first store for each cell i , connection pairs (interfaces) which consist of cell i , describing its faces. Table 5.3 below illustrates this methodology for the fine grid of the example above (see figure 5.5).

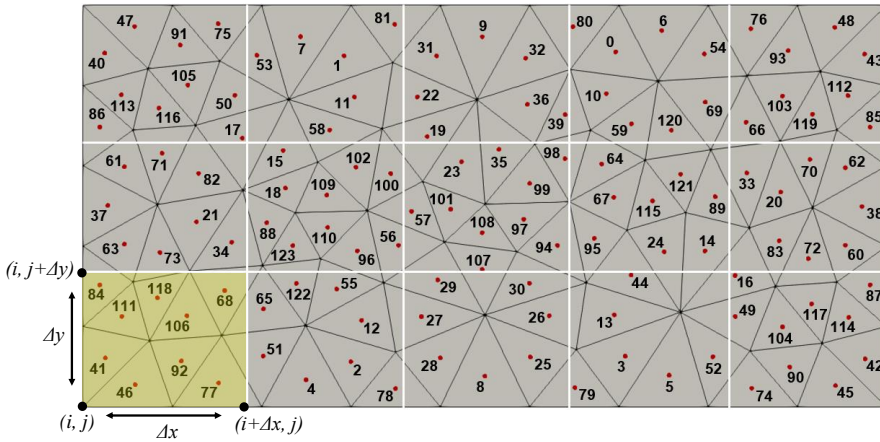


Figure 5.3 2D unstructured grid with centroids and with range partitioning (represented by the white lines) in the x - and y -direction with Δx and Δy spacing respectively. Aggregation is carried out for cells whose centroid fall within a given x - ($i : i + \Delta x$) and y -range ($j : j + \Delta y$). E.g., all cells whose centroids are found within the yellow-highlighted 2D range are aggregated to form one coarse cell.

5

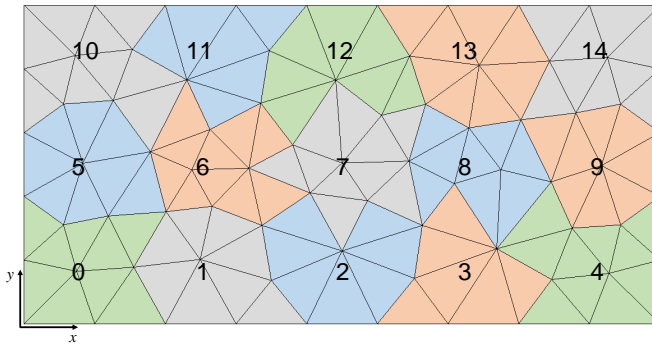


Figure 5.4 2D unstructured grid of figure 5.3 after cell aggregation. This grid represents the next level of coarsening of the finest grid: level 1.

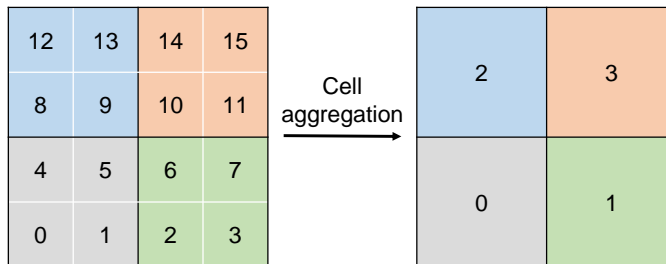


Figure 5.5 4×4 Cartesian grid showing cell aggregation, resulting in four coarse grid cells.

Table 5.3 Interfaces l contained in each cell i for level 0. The interfaces are expressed as connection pairs, describing it.

Cell i	Faces
0	(0, 1), (0, 4)

Coarse cell I	Faces
1	(0, 1), (1, 2), (1, 5)
2	(1, 2), (2, 3), (2, 6)
3	(2, 3), (3, 7)
4	(0, 4), (4, 5), (4, 8)
5	(1, 5), (4, 5), (5, 6), (5, 9)
6	(2, 6), (5, 6), (6, 7), (6, 10)
7	(4, 7), (6, 7), (7, 8)
8	(4, 8), (8, 9), (8, 12)
9	(5, 9), (8, 9), (9, 10), (9, 13)
10	(6, 10), (9, 10), (10, 11), (10, 14)
11	(7, 11), (10, 11), (11, 15)
12	(8, 12), (12, 13)
13	(9, 13), (13, 14)
14	(10, 14), (13, 14), (14, 15)
15	(11, 15), (14, 15)

A similar list is constructed for coarser levels (level > 0), which is constructed by aggregating the faces of the fine grid cells i (table 5.3 in this example) contained in each coarse cell I . Inner fine interfaces are unaccounted for, as they are not contained in the coarse interface. For the example above, this results in the following list:

Table 5.4 List of faces (corresponding connection pairs) for each coarse cell in the coarse grid.

Coarse cell I	Faces
0	(1, 2), (4, 8), (5, 6), (5, 9)
1	(1, 2), (5, 6), (6, 10), (7, 11)
2	(4, 8), (5, 9), (9, 10), (13, 14)
3	(6, 10), (7, 11), (9, 10), (13, 14)

Next, the common faces between each coarse cell are determined. This is implemented by evaluating the intersection between the set of faces \mathbf{f} belonging to coarse cell I and the set of faces \mathbf{f} forming coarse cell J . This is expressed as:

$$\{\mathbf{f} | \mathbf{f} \in I\} \cap \{\mathbf{f} | \mathbf{f} \in J\}. \quad (5.5)$$

If a given coarse cell I has one or multiple common faces f with another coarse cell J , these two cells form neighbouring blocks. For transmissibility computation in further steps, the area of the connecting interface is stored, which is here expressed as the sum of the intersecting fine grid faces.

For inter-level connections, a similar method is implemented. For each coarse cell I in level n , the intersection of its set of faces \mathbf{f} with the set of faces \mathbf{f} of a given fine cell i is determined. This operation is conducted for every fine cell i in level $(n - 1)$, except for the fine cells comprised in the evaluated coarse cell I ($i \in I$). This is expressed mathematically as follows:

$$\{\mathbf{f} | \mathbf{f} \in I\} \cap \{\mathbf{f} | \mathbf{f} \in i\}, \quad \text{where } \{i | i \notin I\} \quad (5.6)$$

Similarly, if a given coarse cell I has a common face with a fine cell i , the two cells are connected. This procedure is applied between all levels n and $(n - 1)$. The result is a list of connections within level 0, a list of connections for each level n , and an inter-level connectivity list, which describe the full hierarchical grid.

5.3.2. TRANSMISSIBILITY AND UPSCALING

In this work, the AMR method is implemented for unstructured grids of any geometry. The definition of the transmissibility for unstructured grids is expressed as:

$$\Gamma_p^{12} = \Gamma^{12} \lambda \quad \text{with} \quad \Gamma^{12} = \left(\frac{\alpha_1 \alpha_2}{\alpha_1 + \alpha_2} \right) \quad \text{and} \quad \alpha_i = A \frac{k_i}{D_i} n \cdot d_i, \quad (5.7)$$

where:

Γ_p^{12} : transmissibility between cells 1 and 2,

Γ^{12} : constant geometrical part of the transmissibility,

λ : mobility of a given phase p ,

A : interface area,

k_i : permeability of cell i ,

D_i : distance between centroid of cell i to interface area A ,

n : unit vector normal to the interface,

d_i : unit vector along the line joining centroid of cell i to the center of interface A .

Here, the directional permeability of each cell is expressed as the magnitude of the cell's $[k_x, k_y, k_z]$ coordinates multiplied by the unit vector d_i .

To solve the mass conservation equation, the flow rate must be computed for the interface of every neighbouring cells. It is therefore necessary to compute the transmissibility for each dual connection listed in the connectivity list. The result is a list consisting of all connections, with their corresponding transmissibility. This methodology is applied at the finest level of refinement, level 0.

For thermal problems, another type of transmissibility Γ_c^l must be computed to approximate thermal conductive flux in the energy equation. Since thermal rock conduction is not as heterogeneous as permeability, the thermal transmissibility is defined as the geometric coefficient, that is, the area of the interface l divided by the sum of the distances D_1 and D_2 from centroids to interface l , multiplied by the average conduction κ_{12} :

$$\Gamma_c^{12} = \kappa_{12} \frac{A}{D_1 + D_2}. \quad (5.8)$$

As mentioned earlier, level 0 is represented by a list of volumes, depths and reservoir properties which are derived from the static geological model. Once the hierarchical grid is constructed, all cell properties must be redefined for the coarser levels (level > 0). This is done by upscaling the properties of the corresponding fine grid cells. The volume is upscaled by simply summing the volumes of the aggregated fine grid cells v_i ;

$$V_I = \sum_{i \in I} v_i. \quad (5.9)$$

Depth upscaling is done by taking the average of the fine scale depths. The porosity, thermal conductivity, and rock heat capacity are upscaled using a volumetric averaging.

For example, the sum of the porosity ϕ_i multiplied by the corresponding cell volume v_i of each fine cell i is taken over the total volume of the coarse cell V_I ;

$$\bar{\phi}_I = \frac{1}{V_I} \sum_{i \in I} v_i \phi_i. \quad (5.10)$$

In this study, for the upscaling of permeability, we use the flow-based upscaling technique developed by (Gong et al., 2008; Karimi-Fard & Durlofsky, 2012; Karimi-Fard et al., 2006). This technique uses the pressure solution when the system has reached steady-state to compute the flow across each interface. The transmissibility can then be derived by rearranging the flow equation 5.1. These approaches can be applied to unstructured coarse grids with generally-shaped control volumes (Karimi-Fard & Durlofsky, 2014). The coarsening technique defines the coarse transmissibility Γ_p^{IJ} between two adjacent control volumes I and J . This is expressed as:

$$\Gamma_p^{IJ} = \left| \frac{Q_{IJ}}{P_I - P_J} \right|. \quad (5.11)$$

The coarse-grid average pressures P_I and P_J , and the coarse-grid flow rate Q_{IJ} , are computed using a fine-grid pressure solution. These quantities are given by:

$$P_I = \frac{1}{V_I} \sum_{i \in I} v_i p_i, \quad P_J = \frac{1}{V_J} \sum_{j \in J} v_j p_j, \quad Q_{IJ} = \sum_{(i \in I, j \in J)} Q_{ij} = \sum_{(i \in I, j \in J)} \Gamma_p^{ij} (p_i - p_j), \quad (5.12)$$

where p_i and p_j define the fine-scale pressures in the corresponding coarse blocks. In the flow rate expression Q_{ij} , ij indicates the interface between fine cells i and j and Γ_p^{ij} denotes the transmissibility for this interface. This ij interface comprises a portion of the interface between coarse blocks I and J . For inter-level connections, a similar approach is used. For a given fine cell i and coarse cell J with interface ij , equation 5.12 is used with $P_I = p_i$, the pressure of fine cell i , and P_J the pressure of coarse cell J . This procedure is conducted for each inter-level connection found within the hierarchical grid.

For thermal problems, a similar method can be implemented, but is however not computationally efficient as temperature takes significantly longer to reach a steady state. We therefore use equation 5.8 to compute the upscaled thermal transmissibility, where the area is expressed as the sum of the fine-scale faces which compose interface IJ , and the distances D_I and D_J represent the distances between the cell centroid and the centroid of the coarse interface.

GLOBAL INDEXING

Once all needed parameters at every hierarchical level are evaluated, which include cell properties, a connectivity list with associated transmissibility for each level and between levels, it is necessary to combine the levels in order to form a global hierarchical set of grids. To combine the levels, it is however necessary to assign a unique indexing to each and every mesh element contained in the multi-level grid. This is where global indexing plays a role. For convenience, indexing is ordered starting from the coarsest level. An example of global indexing is shown in the figure below.

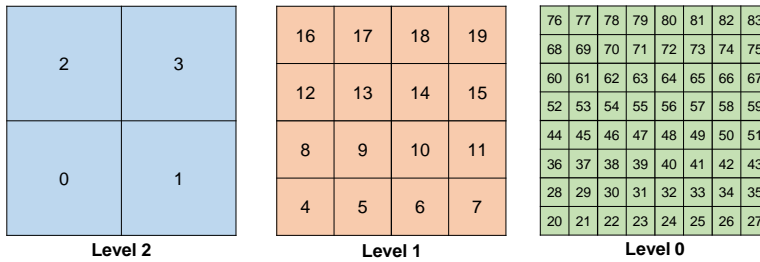


Figure 5.6 Example of a Cartesian structured 3-level hierarchical grid with global indexing. Numbering starts at the coarsest level and finishes at the finest level of refinement.

The procedure used to assign global indexing is to simply add the number of cells of the previous level(s) to the current level. E.g., for level 1 from the figure above, numbering starts at the total number of cells of level 2 n_2 ; for level 0, numbering starts at $n_2 + n_1$. This procedure is applied to the bookkeeping lists such as "fines in coarse" and to the connectivity list of the corresponding levels. After the global indexing is applied to the connectivity lists, the connectivity list at each level and the inter-level connection lists are combined into one list. This is conducted by concatenating these lists to form one list describing all existing connections within the hierarchical grid. Regarding the list of cell properties, global indexing is applied by simply concatenating the lists together in the right order, i.e. from the coarsest level to the finest level. This way, indexing is done in the same order as the global indexing. The result is a global list of volumes, depths and relevant reservoir properties describing each mesh element within the hierarchical grid. Having constructed the hierarchical grid and assigned it global indexing, the pre-processing stage is complete and the simulation with dynamic adaptivity can be performed.

5.4. DYNAMIC ADAPTIVITY FRAMEWORK

To determine whether grid adaptivity is necessary, we define refinement and coarsening criteria, which are dependent on the application used. In this study, we adopted an approach where the difference in solution variable is analysed between neighbouring blocks. Therefore, the difference in the solution variable of interest X is computed between each pair of cells active in the simulation grid. If this difference is higher than a given threshold, both neighbouring blocks are refined. For the coarsening of a set of fine cells, belonging to a given coarse cell, the difference between all the corresponding fine cells and their neighbouring cells is computed; if each and every one of these connections have a difference in solution variable below a given threshold, the fine cells are coarsened to the next consecutive level.

For cells marked for refinement, the corresponding fine cells from the level below are added to the list of active blocks, which is used for implementation of the next time step, while the indices of the coarse cells in question are suppressed. Similarly, the cells marked for coarsening are suppressed from the active cells, and the corresponding coarse blocks are added. Figure 5.7 below shows an example of a two-level hierarchical

grid. The current time step simulation grid is represented on the bottom left. After a check for adaptivity was conducted, cells 1 and 2 were marked for refinement. Hence as explained above, the cell indices 1 and 2 are suppressed from the list of active blocks, and their corresponding fine cell indices are added (6, 7, 10 and 11 for coarse cell 1, and 12, 13, 16 and 17 for coarse cell 2). The scheme at the bottom right of the figure shows the simulation grid which will be used for the next time step. Cell adaptivity results in an unstructured indexing as shown in the figure below.

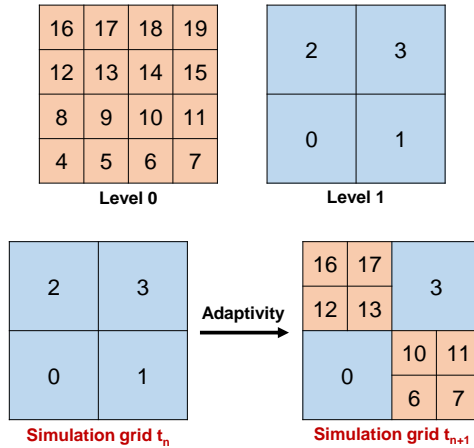


Figure 5.7 Schematic representation of a 2-level hierarchical grid, with illustrated the adaptivity procedure and the redefinition of the active blocks for the simulation grid of the next time step t_{n+1} .

Once the simulation grid is redefined and the list of active cells is updated, the connectivity list and corresponding transmissibility must be redefined. This is done by copying the list of connections for the whole hierarchical grid, where only the connections and corresponding transmissibility involving the active cells are kept, while connections involving non-active cells and their corresponding transmissibility are suppressed. Similarly, the same holds for the list of volume, depth and relevant properties. Only the cell properties of the active blocks are stored.

For computation of the next time step solution X_{n+1} , the solution of the previous time step X_n is required (see equations 2.31 and 2.32). However, X_n doesn't have the same grid configuration as the next time step t_{n+1} . It is therefore necessary to convert the grid of solution X_n to the same configuration as the simulation grid at t_{n+1} . To do so, we use simple mapping techniques. A prolongation operator is firstly used to redefine the solution variable X at each cell of the finest level of refinement (level 0). A so-called *constant prolongation* is implemented; i.e., all sub-domain values X_i are set to the coarse value solution variable X_I :

$$X_i = X_I, \quad \forall i \in I. \tag{5.13}$$

Subsequently, restriction to the new simulation grid is conducted on the prolonged solution; i.e., for cells already at the finest level, the solution stays the same; when several control volumes are grouped into a single coarser control volume, the coarse value

X_I is set to the volume-weighted average of all sub-domain values X_i (Karimi-Fard & Durlofsky, 2014):

$$X_I = \frac{1}{V_I} \sum_{i \in I} v_i X_i. \quad (5.14)$$

A schematic representation of this procedure for the 2-level hierarchical grid and for the new simulation grid of figure 5.7 (t_{n+1}) is shown in figure 5.8 below.

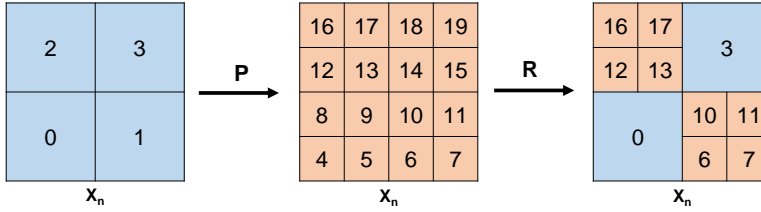


Figure 5.8 Schematic representation of the prolongation and restriction for the example in figure 5.7.

5

The model, however, necessitates sequential numbering for mesh generation. It can be seen in figure 5.7 that indexing is non-consecutive when grid adaptivity is applied. This is where local indexing comes in play. That is, the active blocks indices are re-numbered in a sequential order to prevent undefined indices in the mesh. The global indexing is stored in a so-called *Global to Local* array for conversion back to the global indices for adaptivity check in the next time step. The described procedure, which redefines the grid configuration for the next simulation, is repeated at each time t . It is also important to note that all previously computed operators in the OBL method are re-used after each successive timestep. This is possible since the parameter space for each state dependent operator in the OBL method is decoupled from any spatial property or discretization. This provides a significant speeds-up of the computation especially when simulation property is expensive to evaluate.

In the synthetic examples used to illustrate the performance of the AMR framework, the first time step simulation is started at the coarsest level. For improved accuracy, the cells containing the wells are kept at the finest level of refinement, level 0.

5.5. APPLICATIONS FOR GEOTHERMAL RESERVOIRS

Geothermal technology has recently received substantial attention as an alternative source of energy. However, geothermal production systems have a relatively low return on investment, where uncertainties related to lack of detailed information about subsurface formations can significantly affect the quantification of the economic planning and feasibility of geothermal projects (Willems, 2017). It is therefore important to reduce the uncertainty and produce a high accuracy solution while keeping the computational costs low. Geothermal systems therefore represent a good candidate for implementation of our AMR framework since it keeps the accuracy of simulation process close to the fine-scale while the performance is close to coarse-scale models.

Simulation of geothermal reservoirs implicates the solution of both mass and energy conservation equations where pressure and enthalpy are the solution variables. We are

mostly interested in the accurate prediction of the temperature displacement front and resulting thermal breakthrough time. Dynamic adaptivity will be illustrated for 2 synthetic geothermal examples:

- A homogeneous reservoir with unstructured meshing,
- A heterogeneous fluvial system from (Shetty et al., 2018) with low net-to-gross ratio.

In *DARTS*, the enthalpy is used as nonlinear unknown instead of the temperature. The adaptivity criteria are therefore applied to the enthalpy solution where the difference in enthalpy between two adjacent control volumes is analysed. This is done for each pair of connection within the simulation grid. Here, we applied the following adaptivity criteria:

$$\begin{cases} \text{if } \Delta h_{ij} > 70 \text{ kJ,} & \text{mark cells } i \text{ and } j \text{ for refinement,} \\ \text{if } \Delta h_l < 40 \text{ kJ, } \forall l \in I, & \text{mark cells } \{\forall i \in I\} \text{ for coarsening.} \end{cases} \quad (5.15)$$

This adaptivity criteria is a simple heuristic and serves a practical purpose in this work. The proposed AMR method would greatly benefit from a more sophisticated criteria, for example, a criteria based on a posteriori error estimates similar to (Vohralik & Wheeler, 2013; Vohralik & Yousef, 2018).

The geothermal examples are illustrated by showing the fine-scale solution at different time steps versus the AMR solution and the coarse-scale solution. Each synthetic example was analyzed quantitatively by conducting an error analysis where the error of both AMR and coarse solution are computed relative to the fine-scale solution. Both the L2 norm and L-infinity norm were calculated for each time step throughout the simulation. Moreover, to define the performance of the AMR method in terms of computational resources, the percentage of grid cells utilized in the simulation using the AMR grid, relative to the total number of cells in the fine-scale model was plotted for each example.

5.5.1. CASE 1: HOMOGENEOUS MODEL

The first model is a simple 2D homogeneous reservoir (constant permeability) with unstructured triangular mesh. We consider a single injector (I) and a single producer (P) configuration. A two-level hierarchical grid is used, with 1420 cells in level 0 and 75 cells in level 1. Figure 5.9 below illustrates both levels, along with the permeability field (constant permeability of 2000 mD), and the well locations. The simulation parameters for this model are specified in Table 5.6 and 5.7 in the Appendix. The level 1 is illustrated above where each color represents a coarse cell. As can be seen, cell aggregation was conducted by dividing the x- and y- axes into 5 and 15 equidistant intervals. The cells at the well locations are kept fine at all times. The simulation was conducted for a period of 5500 days. The temperature solution at three different times is shown in figure 5.10. Figure (a) represents the temperature solution at fine scale, figure (b) the solution on the AMR grid, figure (c) shows the coarse-scale solution, and figure (d) shows the node distribution for the AMR simulation run.

The solution on the AMR grid demonstrates a particularly good match with the fine-scale solution. The node distribution shows high concentration along the front and at

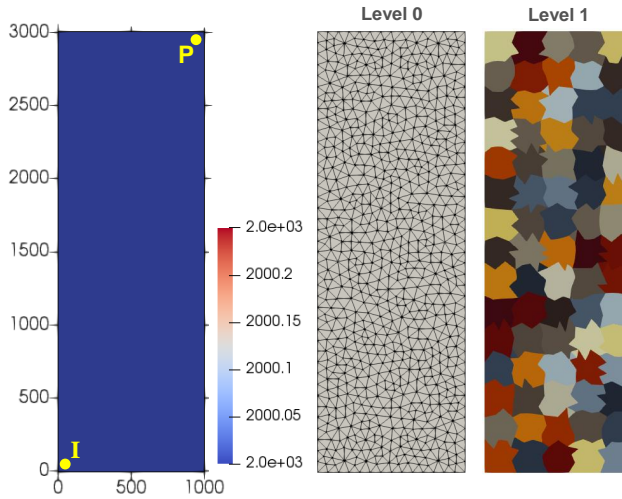


Figure 5.9 Hierarchical grid of the unstructured homogeneous model. Left figure: permeability field with reservoir dimensions and well locations; middle figure: level 0, the finest level of refinement, with unstructured gridding; right figure: coarser level, level 1 where each color represents a coarse cell.

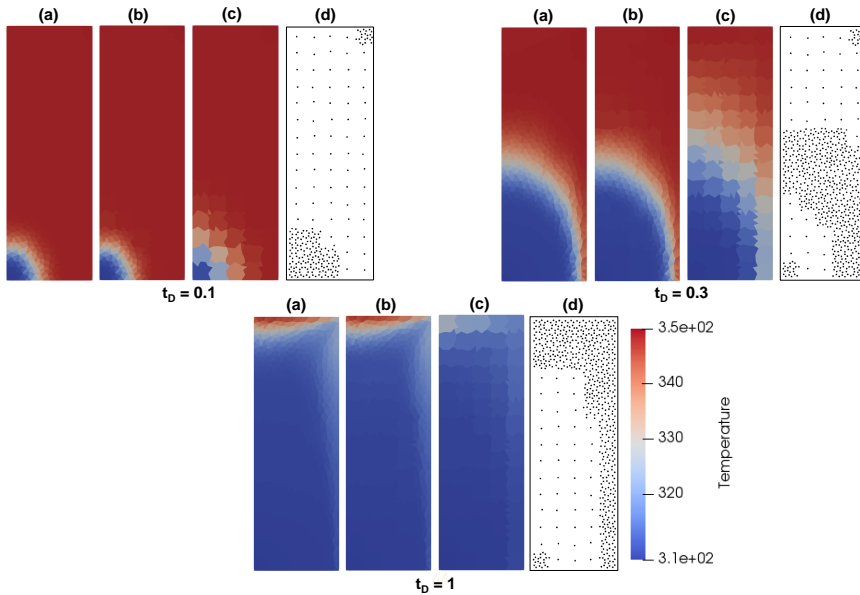


Figure 5.10 Temperature solution of the homogeneous reservoir with unstructured gridding at $t_D = 0.01, 0.3$ and 1 . (a) represents the fine-scale solution; (b) represents the AMR solution; (c) is the coarse-scale solution; (d) is the node distribution of the AMR grid.

the well locations, and low concentration behind and ahead of the front, where no significant changes are observed. This considerably lowers the computational time as com-

pared to running the fine-scale model. The coarse-scale solution differs notably from the AMR and fine-scale solution, with a faster cold front propagation at the coarse grid which is more pronounced in comparison at late times $t_D = 0.3$ and 1.

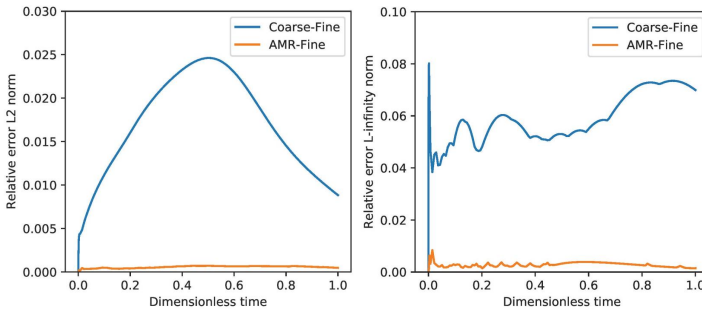


Figure 5.11 L2 norm (left) and L-infinity norm (right) of the difference between the coarse model and the fine model, and between the AMR model and the fine model, both relative to the fine-scale solution, for the homogeneous model with unstructured gridding from figures 5.9 to 5.10.

The relative error of the AMR solution is significantly lower than the coarse solution in both the L2 and L-infinity norm (figure 5.11). Moreover, the number of cells is considerably reduced (see figure 5.12), ranging from 8 to 60%. The trend shows an overall increase as the front propagates, and a decrease when the cold front has reached the producing well, which results in coarsening at locations where no more thermal variations are detected. This considerably improves the performance of simulation since the AMR approach is much more favourable in terms of efficient use of computational resources (see Table 5.5).

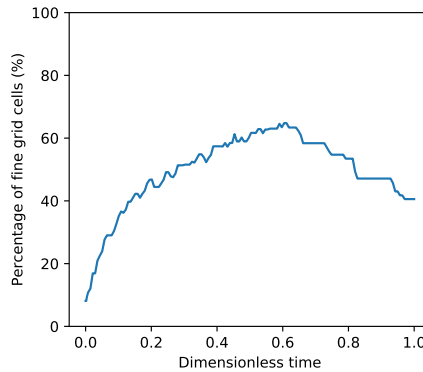


Figure 5.12 Percentage of mesh elements used during the simulation of the AMR model, relative to the total number of cells in the fine-scale model in time for the homogeneous model from figures 5.9 to 5.10.

5.5.2. CASE 2: SUGAR-CUBE SHALE MODEL

Shales are often neglected in conventional reservoir simulation as the convective flow is never acquired in shales due to low permeability. For geothermal applications, they

represent an important source of heat for thermal recharge of the cold water front. Modelling of the shales however significantly increases computational time since shales often occupy a significant amount of computational grid. Here, we test an application of our AMR approach to a sugar-cube model where cubes represents shale bodies and space between them fluvial channels. We use a simple 2D setup, with in total, a 5 by 6 shale block configuration. Shale blocks have a permeability of 10^{-2} mD while the sand bodies have a permeability of 10^3 mD. The injector and producer are placed at opposite corners of the reservoir as shown in the figure 5.13. Level 0 consists of 4588 fine cells. Level 1 is constructed differently from the conventional AMR approach with the sand channels kept at fine level, and only the shale blocks are coarsened by a ratio of 100 (10×10). The coarse grid, level 1, contains 1618 cells. The simulation parameters for this model are specified in Table 5.6 and 5.7 in the Appendix.

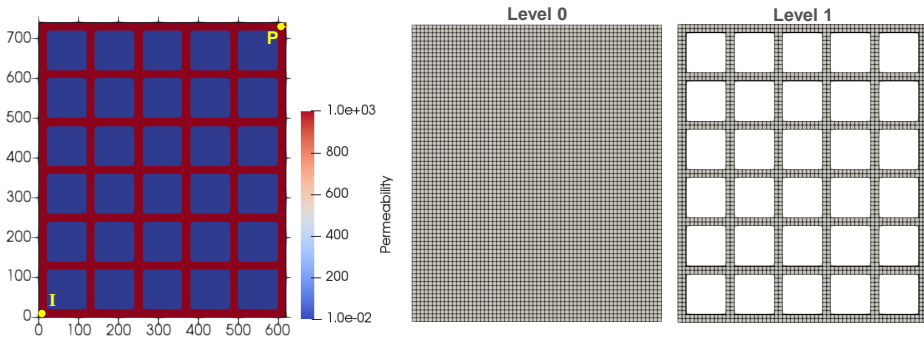


Figure 5.13 Hierarchical grid of the model with shale blocks. Left figure: permeability field with reservoir dimensions and well locations; middle figure: level 0; right figure: coarser level, level 1.

Figure 5.14 below depicts the temperature solution at three different times throughout the simulation: $t_D = 0.1, 0.3$ and 0.7 . Similarly to the previous example, the solution is shown for (a) the fine grid, (b) the AMR grid and (c) the coarse grid. As can be seen on the AMR figure (b), the grid refines as soon as the cold front arrives at proximity to a shale body. The cold front is accurately represented on the AMR grid and there are no differences compared to the fine grid. On the coarse grid however, the cold front propagates further than for the fine and AMR model, which is clearly visible at the late time recording $t_D = 0.7$ in the figure above. When the cold front passes part of the shales blocks and these have cooled down, coarsening occurs as observed at $t_D = 0.7$.

Figure 5.15 below depicts the error distribution through time of both the AMR and coarse model relative to the fine model. As can be seen in figure 5.15, the error of the coarse model is significantly larger than for the AMR model, where the error is close to zero. The high frequency changes in the error, especially observed in the L_∞ norm, seem to correlate with refinement and coarsening of the mesh in between timesteps, similar to what was observed in Berrone, 2010. The percentage of cells used in the AMR grid relative to the number of cells used in the fine grid is shown in figure 5.16 below. As can be seen, the percentage of cells ranges from roughly 35% to around 90% halfway through the simulation, when the cold front reaches the producing well, and then lowers to 65%

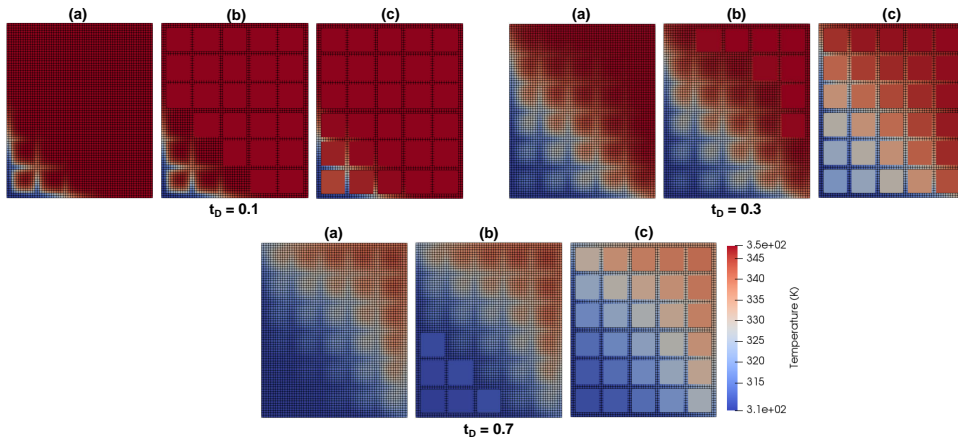


Figure 5.14 Temperature solution of the shale blocks model at three different times: $t_D = 0.1, 0.3$ and 0.7 . (a) is the fine-scale solution (level 0); (b) is the AMR solution; (c) is the coarse-scale solution (level 1).

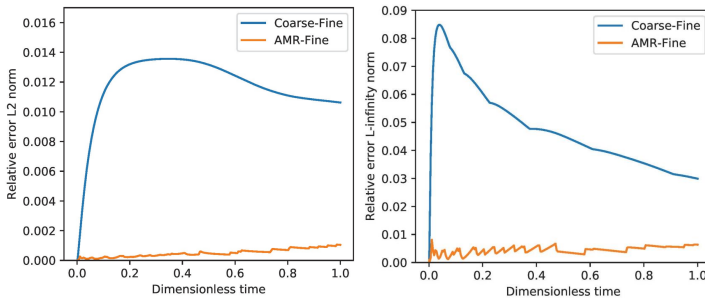


Figure 5.15 L2 norm (left) and L-infinity norm (right) of the difference between the coarse model and the fine model, and between the AMR model and the fine model, both relative to the fine-scale solution, for the shale blocks model from figures 5.13 to 5.14.

when shale blocks proximal to the injector wells have cooled down to injection temperature, and hence coarsening occurs. As observed, the computational time and effort was considerably reduced throughout the simulation, and the AMR solution outcome shows a very accurate representation of the fine-scale model (see Table 5.5).

5.5.3. CASE 3: FLUVIAL HETEROGENEOUS MODEL

Our AMR framework was tested for a heterogeneous reservoir with a low net-to-gross ratio ($N/G = 35\%$). The permeability field ranges from 5 to 3400 mD with a significant amount of shale regions present. The hierarchical grid for this example is a structured grid and it comprises two levels. The finest grid, level 0, consists of 2400 grid cells with 40 cells in the x-direction and 60 cells in the y-direction. Level 1 was reduced to 150 mesh elements, where aggregation was done using 4×4 fine mesh elements, resulting in 10 grid cells in the x-direction and 15 grid cells in the y-direction. The permeability field along with the hierarchical grid for this example is shown in figure 5.17 below. The location of

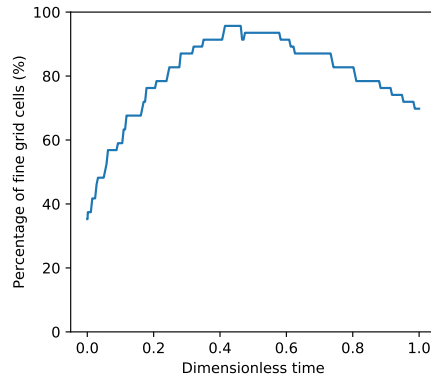


Figure 5.16 Percentage of mesh elements used during the simulation of the AMR model, relative to the total number of cells in the fine-scale model in time for the shale blocks model from figures 5.13 to 5.14.

5

the injector (I) and producer (P) are depicted in yellow on the permeability distribution figure below. The simulation parameters for this model are specified in Table 5.6 and 5.7 in the Appendix.

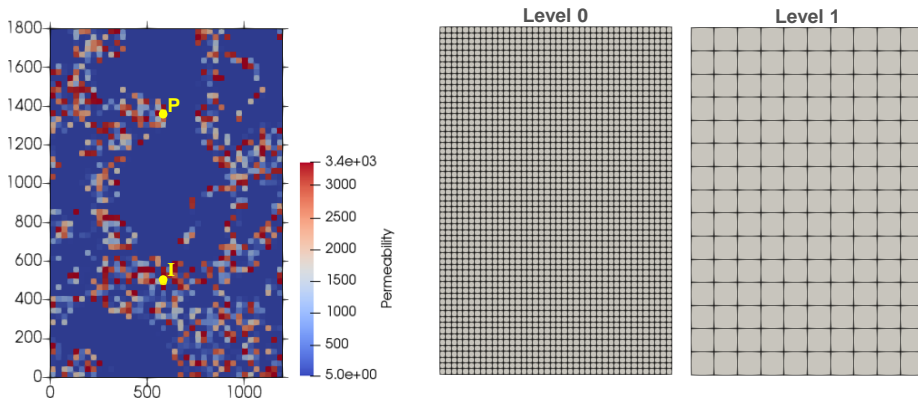


Figure 5.17 Hierarchical grid of the heterogeneous model with low net-to-gross ratio. Left figure: permeability field with reservoir dimensions and well locations; middle figure: level 0, the finest level of refinement; right figure: coarser level, level 1.

The simulation was conducted until cold water breakthrough reached the producing well. Figure 5.18 below illustrates the temperature solution at different times throughout the simulation. For each time shown, figure (a) represents the fine-scale solution, figure (b) is the AMR solution, and figure (c) is the coarse-scale solution. The grid is kept at its finest level at well locations.

The AMR mesh exhibits a significant improvement in temperature solution compared to the solution on the coarse grid. Refinement is mainly focused at the front and slightly beyond the front, while areas where insignificant changes occur remain coarse. Important details, such as fingering effects at the cold water front, which are neglected

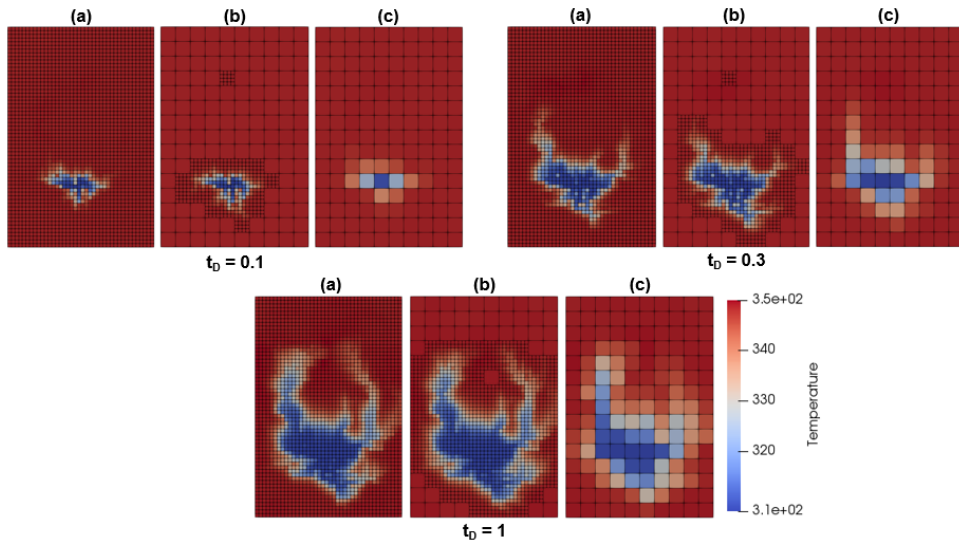


Figure 5.18 Temperature solution of the heterogeneous model with low net-to-gross ratio at three different times: at $t_D = 0.1, 0.3$ and 1 . (a) is the fine-scale solution (level 0); (b) is the AMR solution; (c) is the coarse-scale solution (level 1).

on the coarse grid, are clearly visible in both fine and AMR solutions, which results in a more accurate representation of this physical phenomenon.

The relative error throughout the simulation run was recorded, where the fine model is taken as reference solution, for comparison between the coarse and AMR model. Figure 5.19 below shows the L2 norm and the L-infinity norm error in time.

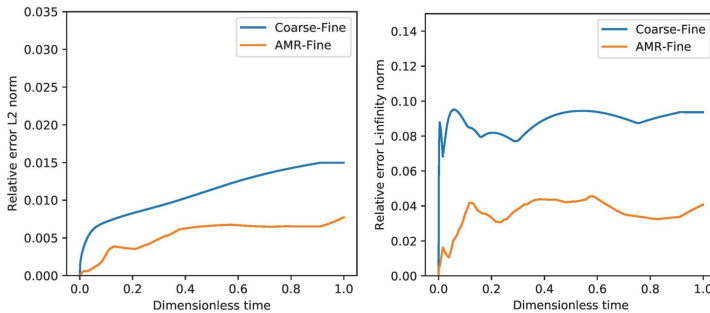


Figure 5.19 L2 norm (left) and L-infinity norm (right) of the difference between the coarse model and the fine model, and between the AMR model and the fine model, both relative to the fine-scale solution, for the heterogeneous model with low net-to-gross ratio from figures 5.17 to 5.18.

As can be seen, the marked improvement is also recorded in the error analysis, where the error between the coarse and fine model is notably larger than the error between the AMR and fine model. The L2 norm remains relatively constant for the AMR solution whereas it increases slightly in time for the coarse solution.

The number of grid-cells used in the simulation ranges from 8 to 70% throughout the simulation (see figure 5.20). This represents a significant improvement in computational effort and time, while still capturing important features (see Table 5.5).

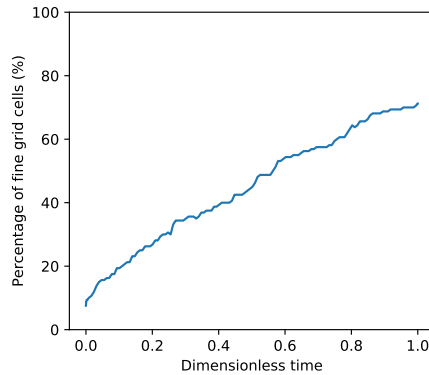


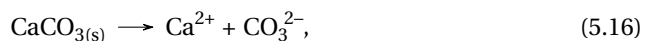
Figure 5.20 Percentage of mesh elements used during the simulation of the AMR model, relative to the total number of cells in the fine-scale model in time for the heterogeneous model with low net-to-gross ratio from figures 5.17 to 5.18.

5.5.4. CASE 4: REACTIVE TRANSPORT

Carbonate reservoirs host a major part of the world's hydrocarbon reserves. But besides hydrocarbon reserves, the ongoing energy transition has resulted in an increase interest in geothermal systems where many are hosted by carbonate rocks. These reservoirs can have heavily fractured and karstified intervals, resulting in unforeseen hazards during drilling. Furthermore, naturally fractured carbonate reservoirs contain a large uncertainty in flow response due to the poor ability to predict the spatial distribution of discontinuity networks at reservoir-scale. Another important process related to dissolution is well acidization used to increase the production. This process involves the dissolution of reservoir rock to stimulate flow towards the wells. These chemical reactions are localized and form important features for accurate representation of the flow response. Furthermore, reaction rates which occur during dissolution are high, resulting in a sharp front in the flow response.

Moreover, during dissolution, formation and development of an unstable dissolution front with multiple wormholes can occur and its modeling is quite sensitive to the resolution (Shaik et al., 2018). In near-well acidization processes, the regime which forms a single dominating wormhole is the most preferable. It is therefore important to accurately predict this unstable dissolution while keeping the computational time reasonable. AMR is therefore a good solution to model these reservoirs and chemical processes to solution requirements.

In the flow example analyzed in this study, dissolution involves the following simple reaction where carbonate is dissolved:



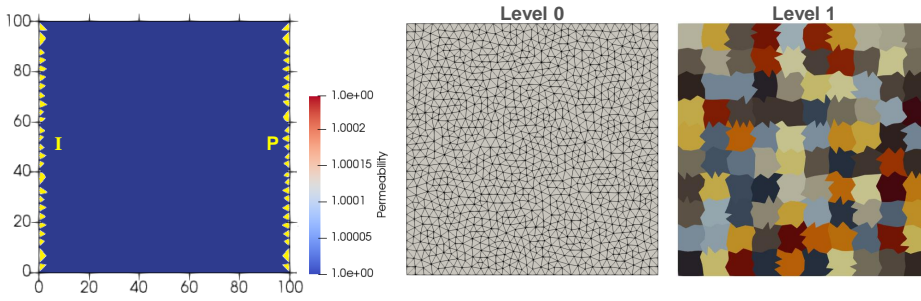


Figure 5.21 Hierarchical grid of the wormhole model. Left figure: permeability field with reservoir dimensions and well locations; middle figure: level 0, the finest level of refinement; right figure: coarser level, level 1.

The kinetic reaction rate for this simple reaction is

$$r_k = AK_k \left(1 - \frac{Q}{K_{sp}}\right) s_s, \quad (5.17)$$

where A is the mineral surface area, K_k is the kinetic reaction constant, Q is the ion activity product, K_{sp} is the equilibrium product, and s_s is the solid saturation. Permeability is updated using a power-law relationship defined as follows

$$k = k_0 \left(\frac{\phi}{\phi_0}\right)^n, \quad (5.18)$$

where k_0 and ϕ_0 are the initial permeability and porosity, and n is the power-law exponent.

The model we use simulates the phenomenon of unstable wormhole formation triggered by small perturbations in permeability. On one side of the reservoir, an injector well is placed which is perforated throughout the whole thickness. On the other side, the producer well is placed, also spanning the entire thickness of the reservoir. The model described in this example has dimensions of 100 by 100 meters. A constant permeability of 1 mD is used with 5% of random noise. The left illustration in figure 5.21 shows the well locations, along with the permeability of the reservoir. The hierarchical grid consists of two levels, where level 0 is an unstructured grid containing 2194 triangular cells. Cell aggregation was conducted to construct level 1, where the x- and y- axes were divided in 10 equidistant intervals, resulting in a grid with only 100 cells. Level 0 and 1 are shown in figure 5.21. The simulation parameters for this model are specified in Table 5.8 and 5.9 in the Appendix.

The AMR simulation was started at the coarse level, while keeping the well cells at the finest level throughout the entire simulation run. For this application, the adaptivity criterion is based on the solid composition, $x[CaCO_3]$. The adaptivity criteria used in this example are defined as follows:

$$\begin{cases} \text{if } \Delta x[CaCO_3]_{ij} > 0.02, & \text{mark cells } i \text{ and } j \text{ for refinement,} \\ \text{if } \Delta x[CaCO_3]_l < 0.01, \quad \forall l \in I, & \text{mark cells } \{\forall i \in I\} \text{ for coarsening,} \end{cases} \quad (5.19)$$

where $\Delta x[CaCO_3]$ is the difference in composition of the calcium carbonate $CaCO_3$ component.

The simulation was recorded at three different times: 0.13, 0.25 and at the final time (expressed in dimensionless time). Figure 5.22 depicts the solid composition - the composition of $CaCO_3$ - in time, where figure (a) is the fine-scale solution, figure (b) is the AMR solution, figure (c) is the coarse-scale solution, and figure (d) represents the node distribution of the AMR grid.

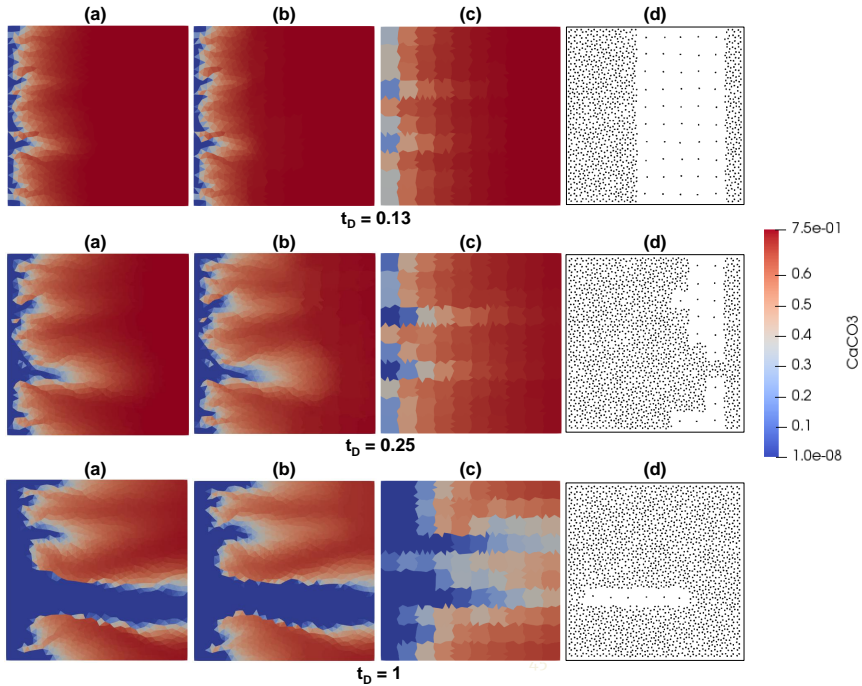


Figure 5.22 Solid composition solution of the wormhole model at three different times. (a) is the fine-scale solution (level 0); (b) is the AMR solution; (c) is the coarse-scale solution (level 1).

As can be seen, the AMR solution is considerably more accurate than the coarse-scale solution. The far-propagating wormhole (at $t_D = 1$), which is present in both the fine-scale solution and the AMR solution, is not well represented on the coarse-scale solution, where two extensive wormholes are present. The AMR solution however shows a very good representation of the fine-scale solution throughout time. The most extensive wormhole exhibits slight differences in thickness and some minor variations are observed at the other smaller wormholes. The node distribution follows the front, which is in this example quite dispersed, resulting in refinement spanning a wide area, especially at the last time step. However, considerable computational resources are saved at the early stage of the simulation.

To quantify the differences between fine-scale solution, AMR solution and coarse-scale solution, an error analysis was conducted. Here again, both the L2 norm and the L-infinity norm were computed for the AMR and coarse model, relative to the fine-scale

solution. The graphs in figure 5.23 below depict the outcome. As can be seen, the AMR error is once more significantly less than the coarse model, for both norms. For the L2 norm, the coarse-fine relative error is three times greater than the AMR-fine error at the final time step. The L-infinity norm of the coarse-fine error starts low at the first time step, where no extensive propagation is observed and where the model is close to the initial conditions, but then rapidly increases to 0.8 and remains more or less constant throughout. The L-infinity norm of the AMR-fine error seems to increase in time. This is due to the propagation of initially small errors in the solution. Note however that the relatively big error for both the AMR and coarse-scale model are not representative for this example and are related to another type of instability in the solution.

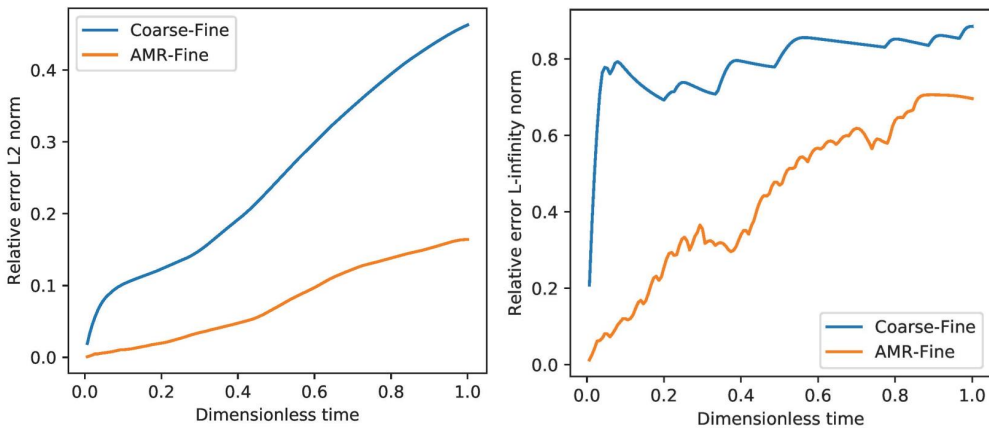


Figure 5.23 L2 norm and L-infinity norm of the difference between the coarse model and the fine model, and between the AMR model and the fine model, both relative to the fine-scale solution, for the wormhole model from figures 5.21 to 5.22.

Similarly to the previous example, we have analyzed the total number of cells used in the AMR model, relative to the total number of cells contained in the fine-scale grid. The graph in figure 5.24 below shows this quantity expressed in percentage.

As can be seen, the number of cells used during the AMR simulation is overall less than the number of cells present in the fine-scale model. Initially, the number of cells starts at 20%, which represents the use of the coarsest level, with both left and right boundaries kept at the finest level. It then increases, fairly steeply, to around 95% due to the high injection velocity which corresponds to the dominating wormhole regime. Around the end of the simulation, the number of cells starts to decrease, which indicates coarsening at some locations. See Table 5.5 for the actual computational time. Although almost 100% of the cells is used at two thirds of the simulation, which is computationally expensive, considerable resources are saved in the beginning. Moreover, this problem is sensitive to the resolution which requires refinement at many locations in order to accurately capture the wormhole propagation.

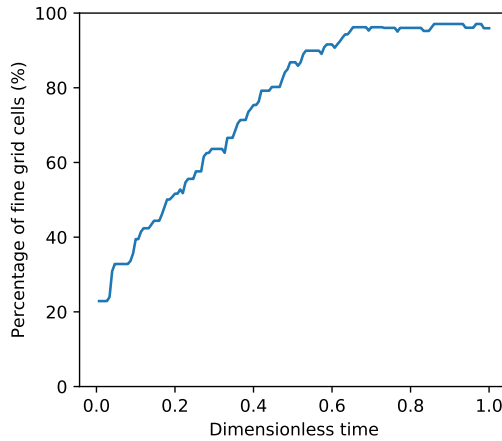


Figure 5.24 Percentage of mesh elements used during the simulation of the AMR model, relative to the total number of cells in the fine-scale model in time for the wormhole model from figures 5.21 to 5.22.

5.6. DISCUSSION

In the results section, all computational speed-up was indicated in terms of % of active cells w.r.t. fine-scale. In this section, the actual CPU times are highlighted for all cases. In order to have a fair comparison, the same nonlinear solver (Newton's based update with a fixed number of iterations), linear solver (direct one) and time-stepping strategy is used for the fine, coarse, and AMR runs. All these results shown in Table 5.5.

Even though the overhead of the AMR method is substantial, this can easily be explained by the non-vectorized Python implementation of the AMR procedure vs highly optimized Python and C++ implementation of the conventional simulation used in the coarse and fine simulation. Since the scope of this work is a proof of concept of the proposed AMR procedure prototyped outside of the simulation loop, our AMR code has not been optimized yet. This can be solved by either an application of Numba (just-in-time compiler for Python) or rewriting the procedure in C++. An expected speed-up, in our experience, is around two orders of magnitude when compared to the original Python implementation, thereby reducing the overhead to around 1.5% of the runtime of the AMR method and making it a viable strategy for geoscience applications.

Table 5.5 Computational effort.

CPU Time	Case 1 [s]	Case 2 [s]	Case 3 [s]	Case 4 [s]
Runtime Coarse	1.28	1.70	1.60	13.61
Runtime Fine	12.33	4.35	21.73	167.33
Runtime AMR	5.94	3.06	8.87	91.85
Overhead AMR	9.03	36.33	15.54	321.86

The framework presented in this paper is developed in the DARTS platform which can be used for a more general set of applications related to the energy transition. However, it is important to note the major differences in various energy applications. For

example, in two types of applications shown in this study (geothermal and chemical dissolution cases), the coarser representation still capable to accurately capture important features of the geothermal dynamic behaviour. The coarse-scale simulation in chemical dissolution, however, completely fails to represent the same dynamic behaviour (dissolution pattern) and effective characterization of the process (e.g. effective rock dissolution). It is therefore evident, as is also pointed out in the literature, that problems contained localized sharp gradients can greatly benefit from the AMR technique.

5.7. CONCLUSIONS

This study aimed at developing an Adaptive Mesh Refinement (AMR) technique in *Delft Advanced Research Terra Simulator* (DARTS) for general-purpose reservoir simulation. The developed AMR framework consists of a multi-level hierarchical grid, where levels are constructed through a mesh partitioning of the fine-scale model - the static geological model - which is represented by a list of properties (e.g. volume and porosity). The framework consists of the construction of the coarse levels through cell aggregation of the next consecutive fine level at the pre-processing stage. The method used to aggregate fine cells includes the grouping of subdomains whose centroids are found within a predefined 3D domain. In this study, domains are grouped by the partitioning of the x-, y- and z- axes into equidistant intervals. However, this strategy can be easily changed and improved.

The aggregation of the subdomains to form a coarser level is stored as a list of indices for the next stages, which consists of the indices of the fine cells comprised in its coarse control volume for each coarse cell. Next, in order to solve the relevant governing equations, the flow must be computed at each interface present in the mesh. We, therefore, generate a list - called a connectivity list - describing all neighbouring cells within each level and between levels. The fine-scale transmissibility is then computed using the permeability field. Hereafter, a flow-based upscaling is applied in order to acquire the transmissibility of coarser levels and the inter-level transmissibility. Each control volume has defined parameters that are relevant for solving the system (volume, porosity, depth etc).

Once the hierarchy of levels is complete, the simulation can be started. Adaptivity check is performed at every time step, using criteria specific to the application. Once the regions for coarsening and refinement are defined, the solution is prolonged to the finest meshing level, and subsequently restricted from fine to the adaptive simulation grid. A new connection list and grid properties are constructed for the new coarsened schema. Once it is completed, the simulation runs for the next time step using the constructed simulation model.

The accuracy of the method was demonstrated for geothermal applications. Two models were tested, including a homogeneous model with unstructured gridding, a synthetic sugar-cube-like model with high permeability channels surrounded by shale blocks and a heterogeneous fluvial system model with a low net-to-gross ratio. High levels of solution accuracy relative to the reference fine-scale results are observed for both cases. An error analysis was conducted to record the differences between the AMR and the coarse solution relative to the reference fine-scale solution. The error resulting from the AMR model is significantly lower than for the coarse model, for all tested problems. The overall percentage of grid cells used in the AMR model relative to the fine-scale model is

considerably decreased for most problems.

To conclude, the developed AMR method shows high levels of accuracy for both homogeneous and heterogeneous models and can be used for geothermal applications as well as for other applications implemented in DARTS. The number of cells in the AMR simulation, relative to the total number of cells of the finest level, is considerably reduced, which is very favourable in terms of efficient use of computational resources. The framework is applicable to two- and three-dimensional models and for unstructured as well as structured meshes. The applicability of the method to unstructured grids provides an effective means for solving complex geological systems.

5.8. ACKNOWLEDGEMENTS

We would like to thank the entire DARTS group for their assistance and help. We would also like to acknowledge financial support from the SFB1313 research group at University of Stuttgart and particularly like to thank Beatrix Becker and Prof. Rainer Helmig for their valuable time and help.

5.9. APPENDIX

Table 5.6 Boundary conditions geothermal models (section 5.1, 5.2, and 5.3).

Parameter	Value
Rock heat conduction, κ_r [kJ/m/day/K]	200
Rock heat capacity, C_r [kJ/m ³ /K]	2500
Initial pressure, p_0 [bar]	100
Initial temperature, T_0 [K]	348.15
Injection pressure, p_{inj} [bar]	150
Injection temperature, T_{inj} [K]	308.15
Production pressure, p_{prod} [bar]	60

Table 5.7 Reservoir and simulation parameters geothermal models (section 5.1, 5.2, and 5.3).

Parameter	Value (section 5.1)	Value (section 5.2)	Value (section 5.3)
Sand permeability, k_{sa} [mD]	2000	1000	3000 ± 12.5%
Sand porosity, ϕ_{sa} [-]	0.25	0.25	0.3 ± 12.5%
Shale permeability, k_{sh} [mD]	N/A	1e-2	5
Shale porosity, ϕ_{sh} [-]	N/A	0.001	0.1
Length domain, L_x [m]	1000	600	1200
Width domain, L_y [m]	3000	700	1800
Simulation time, t [days]	5500	1200	7600
Control volumes level 0 [-]	1420	4588	2400
Control volumes level 1 [-]	75	1618	150

Table 5.8 Boundary conditions chemical model (section 5.4).

Parameter	Value
Mineral surface area, A [m ²]	1
Kinetic reaction constant, K_k [kmole/day]	1e-3

Table 5.8 Boundary conditions chemical model (section 5.4).

Parameter	Value
Equilibrium product, K_{sp} [-]	0.24
Power-law exponent, n [-]	3
Initial pressure, p_0 [bar]	95
Initial composition, $z_{c,0}$ [$\text{Ca}^{2+} + \text{CO}_3^{2-}$, CaCO_3 , H_2O]	[0.24, 0.75, 0.01]
Injection rate, q_{inj} [m^3/day]	0.05
Injection composition, $z_{c,inj}$ [$\text{Ca}^{2+} + \text{CO}_3^{2-}$, CaCO_3 , H_2O]	[0.01, 0.0, 0.99]
Production pressure, p_{prod} [bar]	65

Table 5.9 Reservoir and simulation parameters chemical model (section 5.4).

Parameter	Value
Initial permeability, k_0 [mD]	$1 \pm 5\%$
Initial porosity, ϕ_0 [-]	0.26
Length domain, L_x [m]	100
Width domain, L_y [m]	100
Simulation time, t [days]	2e6
Control volumes level 0 [-]	2194
Control volumes level 1 [-]	100

6

FAST AND ROBUST SCHEME FOR UNCERTAINTY QUANTIFICATION IN NATURALLY FRACTURED RESERVOIRS

The main objective of this study is to perform Uncertainty Quantification (UQ) using a detailed representation of fractured reservoirs. This is achieved by creating a simplified representation of the fracture network while preserving the main characteristics of the high-fidelity model. We include information at different scales in the UQ workflow which allows for a large reduction in the computational time while converging to the high-fidelity full ensemble statistics. Ultimately, it allows us to make accurate predictions on geothermal energy production in highly heterogeneous fractured porous media. The numerical reservoir simulation tool we use in this work is the Delft Advanced Research Terra Simulator (DARTS). It is based on Finite Volume approximation in space, fully coupled explicit approximation in time, and uses the novel linearization technique called Operator-Based Linearization (OBL) for the system of discretized nonlinear governing equations. We use a fracture network generation algorithm that uses distributions for length, angles, size of fracture sets, and connectivity as its main input. This allows us to generate a large number of complex fracture networks at the reservoir scale. We developed a pre-processing algorithm to simplify the fracture network and use graph theory to analyze the connectivity before and after pre-processing. Furthermore, we use metric space modeling methods for statistical analysis. A robust coarsening method for the Discrete Fracture Matrix model (DFM) is developed which allows for great control over the degree of simplification of the network's topology and connectivity. We apply the framework to modeling of geothermal energy extraction. The pre-processing algorithm allows for a hierarchical representation

Parts of this chapter have been published in SPE Reservoir Simulation Conference Proceedings, OnePetro (2021) de Hoop and Voskov, 2021.

of the fracture network, which in turn is utilized in the reduced UQ methodology. The reduced UQ workflow uses the coarser representation of the fracture networks to partition/rank the high-fidelity parameter space. Then a small subset of high-fidelity models is chosen to represent the full ensemble statistics. Hereby, the computational time of the UQ is reduced by two/three orders of magnitude, while converging to similar statistics as the high-fidelity full ensemble statistics. The methods developed in this study are part of a larger project on a prediction of energy production from carboniferous carbonates. The final goal is to perform UQ in pre-salt reservoirs which are characterized by complex reservoir architecture (i.e., large karstification and fracture networks). The UQ of fractured reservoirs is typically done in the petroleum industry using effective media models. We present a methodology that can efficiently handle a large ensemble of DFM models, which represent complex fracture networks and allow for making decisions under uncertainty using more detailed high-resolution numerical models.

6.1. INTRODUCTION

Society heavily depends on the availability of energy (e.g., industry and agriculture, logistics, and households) and raw materials (e.g., plastic, medicine, tires, and solvents). Carbonate reservoirs host a major part of the world's hydrocarbon reserves, approximately 60% of the oil and 40% of the gas reserves (Akbar et al., 2000). This percentage is likely to increase due to several large discoveries made in the past decade, such as pre-salt carbonates in off-shore Brazil (Boyd et al., 2015; Mello et al., 2011) and the Tarim basin in China (Huang et al., 2017b). The ongoing energy transition has also resulted in an increase in geothermal discoveries, for example, the geothermal potential in Dutch onshore Carboniferous carbonates (Reijmer et al., 2017).

Developments of any project related to the subsurface are often associated with large uncertainty and risks (Caers, 2011). The main reason for this is the lack of information on some of the modeling parameters, such as, in the case of natural fracture networks, the spatial distribution of matrix permeability and fracture aperture. These parameters largely control the resulting fluid-flow and geomechanical behavior of the porous media, hence greatly impact any decision making related to these subsurface activities.

A popular remedy for the lack of information is to assume, based on the available data, some (prior) distribution of the modeling parameters and generate a large set of models. This set of models, generally denoted as an ensemble, is subjected to the modeling effort and subsequently attempts to explain the uncertainty in the flow- or geomechanical response. This class of uncertainty quantification (UQ) methods belongs to the Monte Carlo (MC) methods (Hammersley, 2013). MC methods often need a large amount of random samples to converge and, in the case of large fractured reservoirs, this can lead to an insurmountable computational effort.

In response, the ensemble of fractured reservoir models is regularly upscaled to effective media models (e.g., dual-porosity or Embedded Discrete Fracture Models) to reduce the computational time and still attempt to make meaningful predictions. However, in the case of realistically complicated fracture orientation and connectivity, these models might not actually reflect reality. Therefore, the use of a Discrete Fracture Matrix (DFM) model, which explicitly represents the fracture geometry, is preferred (Moinfar et al., 2011).

Since the mesh is conformal to the fractures in DFM models, the main problem, especially in the case of complex realistic fracture networks, is the gridding step. This is particularly problematic whenever complex fracture intersections are present. The resulting mesh will often contain several artifacts: non-orthogonal control volume connections, control volumes with a large aspect ratio (i.e., flat triangles), and a massive difference in the size of the control volumes. This will eventually diminish the quality of the resulting numerical solution and also lead to poor nonlinear convergence of the simulation process. Therefore, we have developed a pre-processing algorithm, which borrows concepts from early work done in this area (Koudina et al., 1998; Maryška et al., 2005) as well as more recent approaches (Karimi-Fard & Durlofsky, 2016; Mallison et al., 2010; Mustapha & Mustapha, 2007). The main idea is to simplify the fracture network such that the meshing artifacts are reduced while keeping the main characteristics of the fracture network intact. This allows for a reliable and fast way of constructing DFM models on any desired scale.

Finally, we present a methodology that can efficiently handle a large ensemble of DFM models, which represent complex fracture networks and allow for making decisions under uncertainty using more detailed high-resolution numerical models. This approach is similar to those in de Hoop et al., 2018; Scheidt and Caers, 2009; Scheidt et al., 2011, however, here we utilize information of coarse-scale models, obtained via our efficient and robust pre-processing procedure, to rank and partition the high-fidelity parameter space. Subsequently, a small subset of high-fidelity models is chosen to represent the full ensemble statistics. Hereby, the computational time of the UQ is reduced by several orders of magnitude, while the reduced approach is converging to similar statistics as the full high-fidelity ensemble of models.

6.2. METHOD AND THEORY

For the advanced DFM preprocessing algorithm, the reader is referred to Chapter 3. The governing equations of the physical system that were used in the uncertainty quantification workflow, particularly the equations describing geothermal energy production, as well as their discretization and linearization using OBL are described in detail in Chapter 2.

6.2.1. GENERATION FRACTURE NETWORKS

In this section, we present a generic framework which allows us to generate various types of fracture networks with different properties (e.g., connectivity, orientation, length, etc.). Fractures, as observed in outcrops, typically occur in sets with characteristic angles of intersection, connectivity, and spacing (Bakay et al., 2016; Bour & Davy, 1997; Manzocchi, 2002). Therefore, we propose to generate the fractures as sets which are parameterized by the number of fractures in the set, lengths, and the angles at which they intersect. Connectivity of the final network, expressed as the total length of the largest connected sub-network divided by the total length of all the fractures in the domain, is calculated and adjusted (i.e., fracture sets are connected or disconnected) based on the target connectivity.

Fracture networks themselves are only a means in any modeling workflow and (al-

most) never constitute the final objective. Usually the objective is to make predictions on a subsurface system, which in turn can contain a fracture network. Our proposed algorithm considers the discretization accuracy, denoted as l_c , at which the final high-fidelity subsurface model will be constructed from the start of the generation. Fractures that belong to the same fracture set will not intersect at a scale or have a spacing that is smaller than l_c . This results in a uniform discretization of each fracture set and minimizes the numerical artifacts which are often observed in Discrete Fracture Network (DFM) models (Berre et al., 2019). Interaction of different fracture sets can still result in a complex fracture network where intersections occur below the discretization accuracy, hence the need for a robust pre-processing method as explained below in section ??.

The algorithm sequentially populates the domain with fractures sets, where the characteristics of the fracture sets are sampled from a specified distribution. For example, the length of the fractures is repeatedly described by a power-law distribution, but you could use any distribution that models your input data (outcrop analogue, seismic, or borehole data). The length of each fracture in the domain is some (random) multiple of the discretization accuracy l_c . Before adding a fracture to the domain, it is split into n_i^s segments of length l_c , where n_i^s is the number of smaller fracture segments of fracture i . Additional fractures of the same set as fracture i always intersect at the nodes of the smaller segments, hence a uniform distribution of control volumes is expected after meshing the fracture network.

The following parameters are input to the generation framework:

- Connectivity, C ;
- Number of fractures pairs, N_f ;
- Maximum number of fracture pairs per set, $N_{f,s}$;
- Set of length distributions, L_f ;
- Set of angle distributions, Θ_f .

Since the number of fractures and maximum number of fractures per set are highly correlated with the total connectivity of the network, you can choose to express those parameters as a function of connectivity. For example, $N_f = N_f^0 \sqrt{C}$, where N_f^0 is the some base number of fractures (e.g., at maximum connectivity). Also, as could be inferred from the parameters above, the fractures are always added in pairs within each fracture set. This means that there are two length and angle distributions per fracture set. We designed a detailed algorithm for sequential generation of fracture network following the approach suggested in (Sartori Suarez, 2018).

After the algorithm has finished and N_f fracture pairs are added to the domain, the connectivity is calculated using graph theory. First construct the unweighted undirected graph $G = (E, V)$, where V is the set of vertices of the graph and E is the set of paired vertices called edges. Based on these two sets we can construct the following matrices:

- Incidence matrix: $B(G)$, which is a $n \times m$ matrix, where n is the number of vertices and m the number of edges in the graph. $B_{ij} = 1$ if vertex i is on edge j otherwise $B_{ij} = 0$;

- Degree matrix: $D(G)$, which is a $n \times n$ matrix describing the number edges attached to each vertex. The degree matrix can be obtained using the follow equation $D = \text{diag}(B\mathbf{1})$, where $\text{diag}(\mathbf{v})$ is a function that constructs a square matrix with vector \mathbf{v} on its diagonal and $\mathbf{1}$ is a vector of ones with size $m \times 1$;
- Discrete Laplacian matrix: $L(G)$ which can be found via the following equation $L = D - BB^T$.

The Laplacian of the graph can be used for finding spanning trees of a given graph (i.e., connected fracture sets in the fracture network). Particularly, each element of the rational basis of the null-space of the Laplacian describes a connected component of the graph (Spielman, 2010). With this basis we can find the number of connected fracture sets in our network but also the connectivity of the network (as defined above). If this connectivity is larger than the specified connectivity, fracture sets are disconnected until the actual connectivity reaches the desired connectivity (within some threshold). The reverse (i.e., connecting fracture sets) is done when the specified connectivity is lower than the desired connectivity. Components of the graph are sequentially merged or disconnected based on this smallest distance between each vertex in the component of the graph and each vertex in the fracture sets.

6.2.2. UNCERTAINTY QUANTIFICATION FRAMEWORK

The uncertainty quantification workflow utilizes a distance-based method and ranking procedure similar to those proposed in de Hoop et al., 2018; Scheidt and Caers, 2009; Scheidt et al., 2011. Distance-based methods attempt to reduce the dimensionality and complexity of the modeling task. They can be extremely effective for visualizing the variability of an ensemble of models, which is often high dimensional. This dimensionality reduction is achieved by projecting onto a (much) lower-dimensional space. This is especially efficient when a distance, or dissimilarity measure, is used that has a high correlation with the modeling objective (e.g., predicting the distribution of total energy produced of the ensemble) (Caers, 2011). Subsequently, the global and local structure of the response uncertainty can be visually and quantitatively analyzed in this reduced space.

A commonly used approach for dimensionality reduction is the Multidimensional Scaling (MDS) algorithm (Borg & Groenen, 2005). In MDS, the square symmetric distance matrix \mathbf{D} , obtained by taking the distances of a particular property between each ensemble member, is projected onto a Cartesian hyperplane (after double centering it around a origin) of dimension $N_{\text{reduced}} = N_m \ll N_M$, where N_M is the size of the ensemble \mathbf{M} . For the details of the MDS algorithm we refer the reader to Borg and Groenen, 2005 chapter 12 and Caers, 2011.

The dimension N_m of the hyperplane required to accurately replicate the original \mathbf{D} , depends on the magnitude of the eigenvalues of the decomposition of the distance matrix. Typically N_m attains one or two when production data from wells are used in the computation of \mathbf{D} . Generally in geoscience problems N_m can range from one until six dimension(s) (Caers, 2011). The following simple example shows both the effectiveness of reducing the size as well as detecting possible redundancy in the output space.

Fluid-flow simulations generally have high dimensional input data in the form of

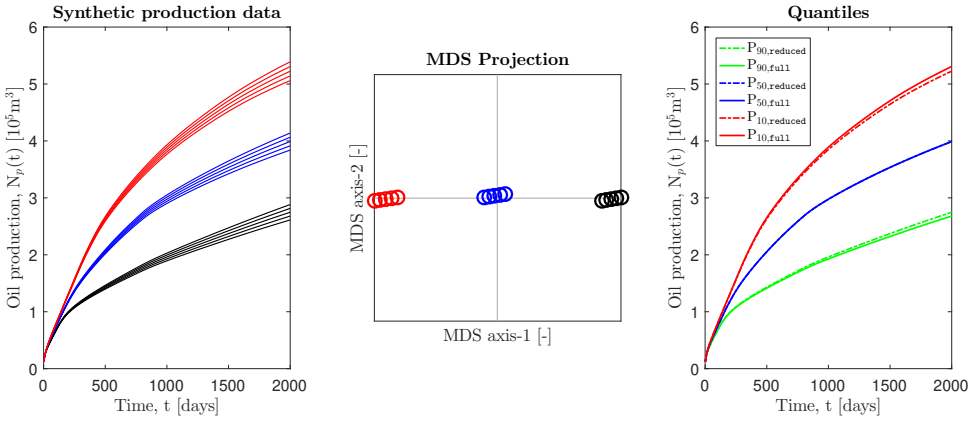


Figure 6.1 Distances and similarities in the high-dimensional flow-response output space are preserved in the reduced dimensional space (left and middle graph). Clustering will identify similar responses and this subset of models converges to the full ensemble uncertainty characteristics (right graph). Taken from de Hoop et al., 2018.

complex high-fidelity models. However, decision are usually made on simple statistics, such as the amount of energy produced from a (relatively) small set of wells. This often leads to redundancies in the output space of the simulations. Sadly, due to the non-linearity of the simulations, it is not necessarily easy to (a priori) predict which models behave similarly. Therefore, using a fast way of detecting these possible redundancies in the output space is the basis of the reduced UQ methodology. If we can predict which subset of models explains the same variability of the full ensemble (i.e., first two stochastic moments), we can greatly reduce the computational time of the UQ process.

In this work we utilize the coarse information, obtained from our pre-processing algorithm, to construct the squared dissimilarity matrix, $\mathbf{D}^{(2)}$, of the full ensemble. Subsequently, we apply the MDS procedure to this matrix and perform clustering based on the projected variability of the coarse representation of the full ensemble. The medoids of the clusters are the representative subset of models which are simulated on the high-fidelity scale. Finally, three quantiles, particularly the P10, P50, and P90, are used to quantify the mismatch between the full ensemble statistics and the approximate statistics from the subset of models. Precisely, we calculate the mismatch with the following equation (Scheidt, Caers, et al., 2009)

$$\epsilon_{N_K} = \frac{1}{3N_t} \sum_t^{N_t} \left(|P_{10}^{\text{full}}(t_i) - P_{10}^{\text{sub}}(t_i)| + |P_{50}^{\text{full}}(t_i) - P_{50}^{\text{sub}}(t_i)| + |P_{90}^{\text{full}}(t_i) - P_{90}^{\text{sub}}(t_i)| \right), \quad (6.1)$$

where N_K represents the number of clusters (i.e., size of the subset of HF models), N_t is the number of time-steps, and t_i represents the i -th time step.

6.3. RESULTS

In this section the results of the fracture generation and cleaning are presented followed by the results of the reduced uncertainty quantification workflow.

6.3.1. FRACTURE GENERATION RESULTS

Figure 6.2 shows three examples of fracture networks generated with the above described algorithm. In these examples the number of fractures and size of the fracture sets is a function of connectivity. The angles for each fracture set are sampled from a random distribution. Characteristic length l_c is chosen substantially small in order to achieve a complex fracture network.

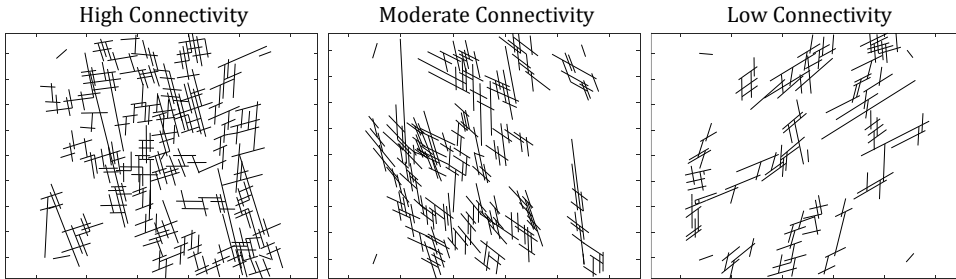


Figure 6.2 Three examples of the fracture networks with different connectivity, generated using the algorithm in section [Generation fracture networks](#).

An ensemble of fracture networks was generated for the analysis of the pre-processing strategy and subsequent uncertainty quantification. A total number of 600 fracture networks were generated with a varying degree of connectivity (200 low, 200 moderate, and 200 high connectivity fracture networks respectively), number of fractures, and orientation of the fracture sets. The fluid-flow results presented in the next section were performed on the 184 models with the largest connectivity. Moderate to low connectivity results will be included in the future work.

6.3.2. FRACTURE PRE-PROCESSING RESULTS

The pre-processing algorithm and its performance is first illustrated using a realistic fracture network, generated from outcrop data (Bisdom et al., 2016b). The meshes in Figure 6.3 are obtained using the free software Gmsh (Geuzaine & Remacle, 2009). The figure attempts to illustrate the comparison between the meshing results obtained from the unprocessed fracture input versus the pre-processed fracture network. A large reduction in the degrees of freedom is observed in part (A) while a more uniform volume distribution is observed in part (B).

Figure 6.4 illustrates the differences between each level of coarsening for a geothermal simulation. The numbers below the temperature fields correspond to the degrees of freedom in fracture and matrix cells respectively. Even though large variations can be observed in the temperature fields, due to the large reduction in spatial resolution, a similar response in terms of temperature at the production well can be observed.

Besides studying the effect of the pre-processing on a single realizations, it is important to see the effect on stochastic properties. Usually, decisions are made based on an ensemble of models, for example, the ensemble of models generated in section [Fracture generation results](#). It is important to see how the quantiles are changing for each level of

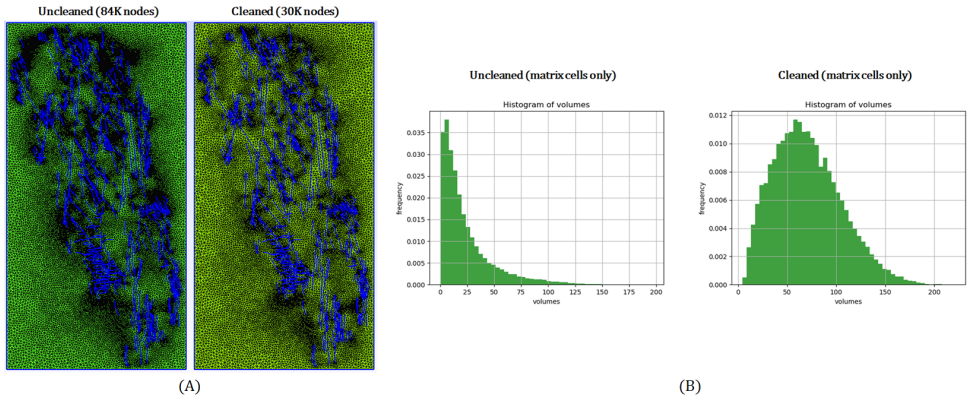


Figure 6.3 (A) Comparison between meshing results of the uncleaned and cleaned network. (B) Comparison of the control volume size distribution of the uncleaned and cleaned fracture network. Modified from (de Hoop et al., 2020)

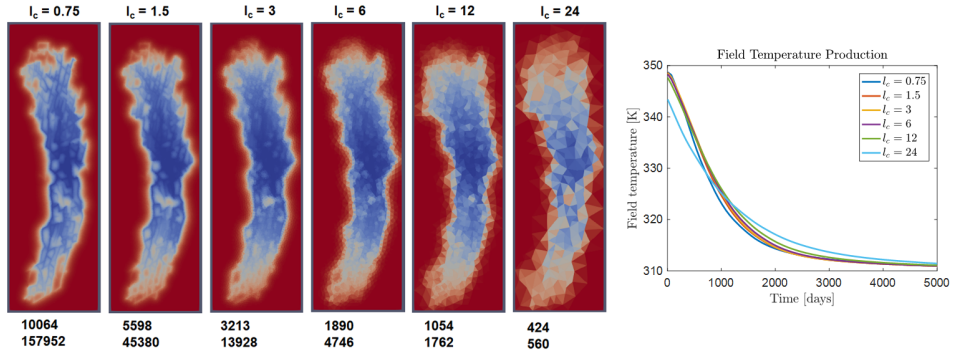


Figure 6.4 Temperature response of the fracture network at different scales (field on the left and rates on the right). The two numbers below the temperature fields at different scales indicate the number of fracture and matrix cells respectively. Modified from (de Hoop et al., 2020)

coarsening. In order to investigate this, numerical simulations were performed.

For the geothermal simulations, cold water is injected in the bottom left of the domain and water is produced from the top right of the domain. Each well (i.e., doublet system) penetrates a fractures and the distance between each well is roughly 800 meters. The simulation models have no flow boundary conditions on each side of the domain. The injection well is controlled by rate ($500 \text{ m}^3/\text{day}$) and an injection temperature of 30 degrees Celsius, while the production well is set to bhp control (450 bar). The initial reservoir temperature is 150 degrees Celsius and the initial pressure is 400 bar (i.e., high-enthalpy geothermal system). The matrix permeability is set to 1 mD and the fracture aperture is 1 mm , resulting in a contrast in permeability of roughly 10^8 (K_{frac}/K_{matrix}), resembling an average naturally fractured carbonate system. Figure 6.5 shows the energy production rate for the 184 high connectivity models. Figure 6.6 shows how the

quantiles are changing for each of the coarsening level.

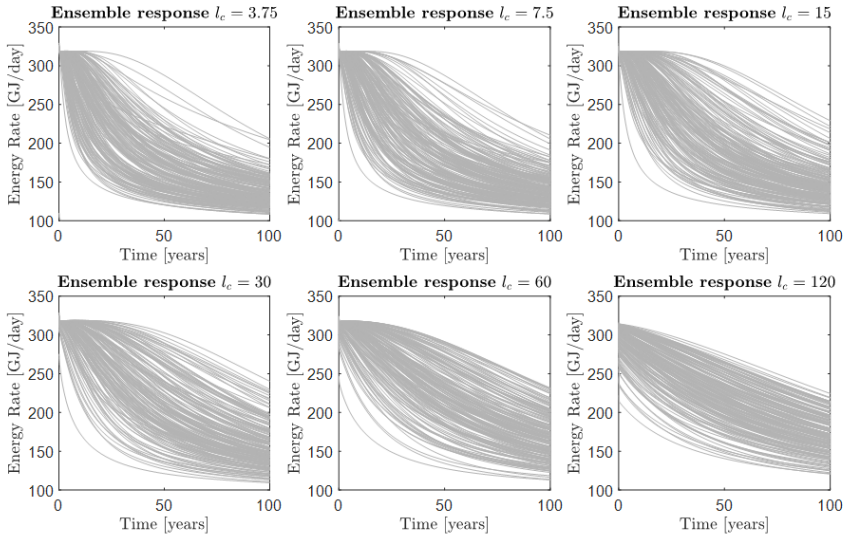


Figure 6.5 Flow response of the ensemble of fracture networks for each coarsening level.

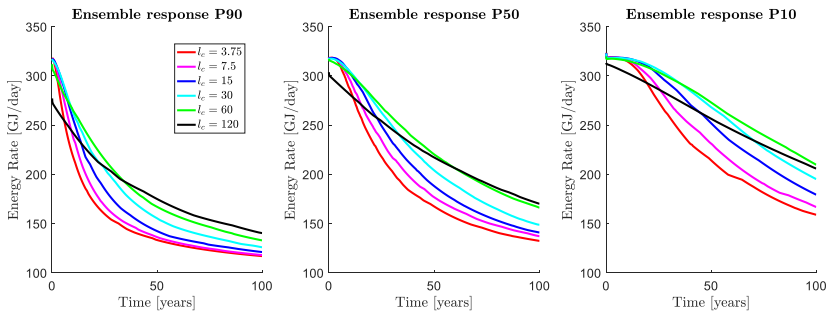


Figure 6.6 Quantiles of energy production for each ensemble scale. Monotonous deviation of each coarse-scale ensemble from the fine-scale can be observed, as well as an increase in the energy production for each quantile. This is most likely caused by the increase in connectivity when coarsened is increased.

One artifact of the pre-processing algorithm is that disconnected networks become connected when increasing the characteristic length scale l_c (i.e., discretization accuracy). See Figure 6.7 as an example. This is also observed in the flow-response as an increase in energy production due to a larger area of the reservoir being depleted. Please note that matrix permeability and conductivity are not upscaled in these coarse-scale realizations which also contributes to deviation from fine-scale response. This seems to imply that the low to moderate connectivity models will deviate more from the fine-scale

than the higher connectivity models. For the UQ workflow, this would mean that the distance used for the MDS procedure would be less representative of the distance between fine-scale ensemble members. To remedy this, we could keep track to which fracture set each individual fracture belongs in the pre-processing algorithm and ultimately disconnect fractures that were not connected in the unprocessed input data.

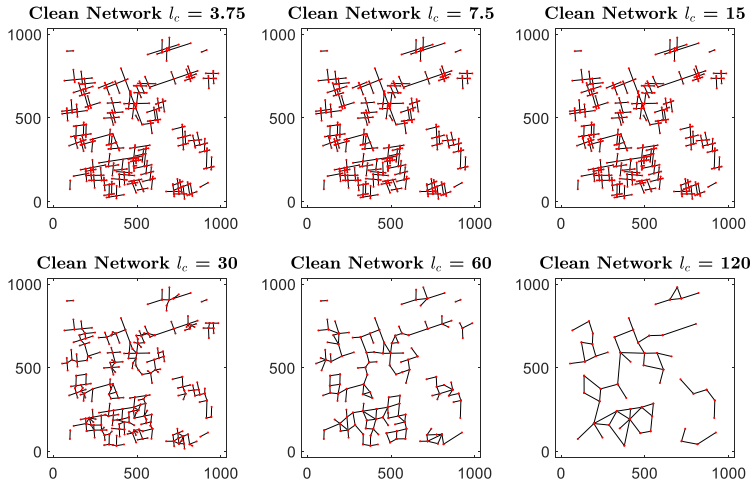


Figure 6.7 Example of alterations to the fracture network based on desired discretization accuracy l_c . The proposed remedy for ensuring similar flow-behavior in the coarse scale models is to disconnect fractures that have become connected due to coarsening.

In Figure 6.7, the $l_c = 60$ (i.e., $16 \times l_c^{\text{finest}}$) can be seen as a scale at which the coarsening fails to accurately represent the fine-scale fracture network (in terms of topology, orientation of fractures, and connectivity). The question remains if this scale can still be used for ranking and selecting representative models for the reduced UQ workflow, which will be answered for highly connected networks in the following section. Finally, to further illustrate the performance of the cleaning, Figure 6.8 shows the connectivity of the pre-processed versus connectivity of the input data for each level of coarsening.

6.3.3. UNCERTAINTY QUANTIFICATION RESULTS

As mentioned in [Uncertainty quantification framework](#), performing high-fidelity DFM simulations on a large ensemble is often unfeasible and impractical. Instead of using dual-porosity models to speed up the computation, we propose to utilize the more realistic DFM models at a coarser scale to identify representative models. Ultimately, simulating this subset of high-fidelity models should convergence to the same statistics as the full ensemble.

For the reduced UQ workflow in this section, we present the analysis on the 184 highest connectivity models, as mentioned in the previous section. The coarse scale response that we utilize in the example is based on the $l_c = 60$ model scale. The reason for this is

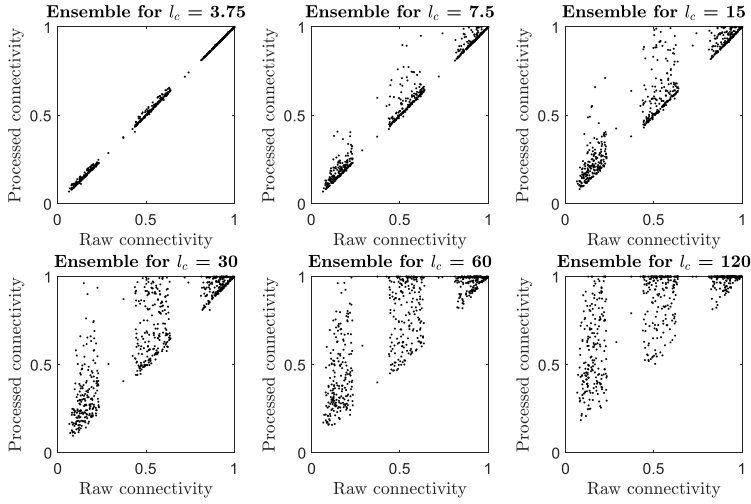


Figure 6.8 Displaying the behavior of the connectivity of the processed vs. raw input data as a function of coarsening levels.

a trade-off between the quality of the distance (higher for lower l_c) and the computational gain of using a larger l_c . Using a lower quality distance for the MDS procedure will likely increase the number of representatives you need to select, since the correlation between the coarse-scale and the fine-scale response is lower for larger l_c . This will increase the overall computational time since more representative models are required (which are simulated on the finest scale). The total simulation time of the reduced UQ, as a function of l_c , is given by

$$t_{\text{red.UQ}}(l_c) = N_M \times t_{\text{processing}}(l_c) + N_M \times t_{\text{sim.coarse}}(l_c) + N_K(l_c) \times t_{\text{sim.fine}}. \quad (6.2)$$

The $t_{\text{red.UQ}}$ is expect to be much smaller than $t_{\text{fullUQ}} = N_M \times t_{\text{sim.fine}}$, since $t_{\text{sim.fine}} \gg t_{\text{sim.coarse}}$ and $N_M \gg N_K$. Computational time for the MDS and clustering procedure is negligible compared to the total time. Processing time is dependent on the l_c as well, but much smaller than $t_{\text{sim.fine}}$. Therefore, the objective is to minimize $t_{\text{red.UQ}}$ while also minimizing ϵ_{N_K} .

The results of the reduced UQ workflow are depicted in Figure 6.9. The coarse-scale response is translated to z-scores (subtract mean and normalize by the standard deviation of the energy rate at each time-step). Then the distances are projected into lower dimensional space using MDS and clustering is performed using k-medoids algorithm. The centroids of each cluster is chosen as a representative and comprises the subset of models. These models are then simulated on the fine-scale and for the computation of the cumulative distribution function (CDF) the responses are weighted by the size of the cluster which they present (similar to (Scheidt, Caers, et al., 2009)).

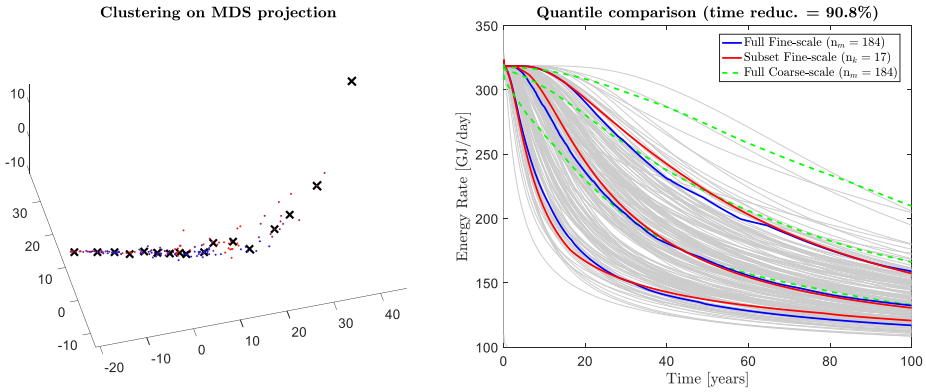


Figure 6.9 The general workflow of reconstructing the stochastic response. First, use coarse scale information to construct distances between ensemble members. Project into lower dimensional space using MDS and perform clustering. Reconstruct the quantiles based on subset and compare with full ensemble statistics.

6

6.4. CONCLUSIONS

In this work we have presented three main aspects which contribute to a robust and UQ quantification workflow for naturally fractured reservoirs. Instead of the using a simplified effective media models (i.e., dual-porosity), we show that it's possible to use high-fidelity DFM models to accurately represent the complex geometry of the fracture networks. We achieve this by utilizing coarse-scale information and selecting a subset of high-fidelity models which describe the same statistics as the full-ensemble of models.

The fracture network generation algorithm allows us to quickly generate a large ensemble of models, depending on some input parameters (e.g., connectivity, number of fractures, orientation, etc.). Connectivity of the final model is ensured by disconnected or connected realizations until target connectivity is achieved. Creating a graph and computing its Laplacian allows for an easy computation of connected fracture sets and therefore speed up this process.

The developed pre-processing method is essential in the reduced UQ workflow. Particularly, it allows us to generate a uniformly meshed DFM model of complex fracture networks for a desired scale l_c , which has a large mesh quality and therefore smooth numerical convergence. This allows for a quick way and reliable way of ranking and partitioning the ensemble space in order to identify representative ensemble members. The pre-processing method seems to be working bests for highly connected networks. Moderate to low connectivity fracture networks seem to be more affected by the pre-processing strategy. Hence it is expected that the coarser realizations result in a lower quality distance for the uncertainty quantification procedure. A remedy for this will be included in future work and consists of a connectivity modification, where necessary, to preserve the main flow characteristics.

6.5. ACKNOWLEDGEMENTS

The project was carried out with a subsidy (reference TKI2017-07-UG) from the Ministry of Economic Affairs, National schemes EZ subsidies, Top sector Energy, carried out by the Netherlands Enterprise Agency. We also want to thank Mohammed Karimi-Fard for his insightful comments and suggestions regarding the pre-processing strategy. Finally we would like to thank Andrea Sartori for the initial development of the fracture generation algorithm.

7

CONCLUSION

The main contribution of this thesis is a collection of methods that aid in uncertainty quantification workflows for fractured and karstified reservoirs. They can all be used in a unified framework, or each component can be used independently. By applying meaningful simplifications to the raw input data or high-fidelity model, an alternative (i.e., coarser) representation is obtained which allows for large-scale uncertainty quantification practices. Presented cave parametrization methods allow the extraction of a large amount of statistics from LiDAR surveys and provide insights for modelling of karstified carbonate reservoirs.

7.1. ADVANCED MESHING CAPABILITIES

Chapter 3 contains a fracture preprocessing strategy, which can create a fully conformal, uniformly distributed grid for a given realistic fracture network with a variable aperture at the required level of accuracy. Besides the application towards large-scale UQ, this framework has other benefits, such as cleaning and preparing the raw fracture input data for topological and graph-based analysis of the inherent structure and characteristics of the fracture network. The framework extends contemporary methods by allowing for a variable aperture distribution of the fracture network and accommodating for this during the merging of fracture segments. The changes introduced by the method are analyzed in terms of geometry (i.e., angle distribution of the fracture network), meshing results (i.e., volume and quality of the elements), and dynamic response of the reservoir when subjected to geothermal high-enthalpy production conditions. Results are analysed for two realistic fracture networks based on outcrop studies, a synthetic case with sealing fractures, and a variable aperture model. Topology is more affected by the preprocessing than the geometry and flow response in studied networks. The open-source graph-based computational framework performing all the preprocessing stages can be found at <https://github.com/MakeLikePaperrr/Fracture-Preprocessing-Code>.

7.2. REACTIVE TRANSPORT FRAMEWORK AND LINK WITH OUT-CROP OBSERVATIONS

In chapter 4, a workflow is presented to analyze LiDAR cave data which extracts an approximation of the complex 3D shape of the cave's interior and provides estimates on variability in lengths and widths along cave passages. This information can be helpful when constructing 3D reservoir models of karstified reservoirs. Numerical simulation results show that cave patterns can be primarily linked to pre-existing fracture networks (via perturbation in the pressure field creating a preferential flow path or fully constrained by the fracture network, depending on the magnitude of the aperture) or to different interplay of Da and Pe numbers. Predicting the actual in-situ geometry of the cave passages (and fracture networks) is unachievable. However, a similar UQ procedure can be applied to karstified reservoirs, as presented in chapter 6, where a range of possible karst configurations is generated and then grouped based on similar flow responses.

7.3. ADAPTIVE MESH REFINEMENT

Also shown in chapter 4 is the required resolution to certain model phenomena such as wormholing and geothermal energy production. The physical phenomena require small grid resolution due to numerical diffusion and transient effects in both cases. Especially the wormhole is not accurately represented using coarse meshes. Therefore, in chapter 5, an adaptive mesh-refinement strategy was implemented to model these sharp and localized features. The multi-level hierarchical grid is constructed using mesh-partitioning of the fine-scale (geological) model. A multi-level connection list is created before simulation, and before every time step, an adaptivity check is done to see where refinement is necessary. Large speed-ups (>30%) are obtained using the AMR strategy.

7.4. UNCERTAINTY QUANTIFICATION

Finally, after all the ingredients are in place, the final addition to the traditional UQ workflow is presented in chapter 6. The main idea is that decisions on the coarsest scale include all sorts of biases due to upscaling and numerical diffusion. Therefore, it seems that the best idea is to make decisions based on finer scales. However, coarse information can be effectively used to partition and group all the possible realizations (i.e., the configuration of properties that potentially represent the subsurface's continuum scale). A representative model is selected and modeled on the fine-scale for each group of similar models. A significant speed-up (>80%) is obtained, meaning more models can be run, meaning lower risk subsurface activities.

ACKNOWLEDGEMENTS

I don't know where to begin writing this because I never thought I would eventually reach this point. To anyone mentioned here, this is as much your achievement as it is mine. Denis, we have known each other for over seven years now. From the start of my Master of Science, you have managed to feed my curiosity about fluid flow in porous media and all the complexities associated with it happening at various scales. Throughout this period, you have been an excellent supervisor. No matter the challenge, you always made me feel like I could do it; you never gave up on me. But besides being a great supervisor, you were like a father sometimes, supporting me through some mentally challenging periods. I want to thank you for all that you have done for me over the past seven years, and I want to say that I loved working together and hope dearly that someday we might work together again. We expected, in the beginning, to tackle more complex problems and go more in-depth in certain areas, but then life happened, and we didn't reach all of our goals. I still hope you can look back at this period and feel like we have accomplished something together; I indeed think that way. I am proud to have worked under your supervision and in your research team; it has taught me many professional and personal lessons.

Then, I want to thank Giovanni and Auke. We might not have met as much as we would have liked during this journey, but thanks to you, every meeting was beneficial and to the point. You have supported me through some challenging parts of my life, and I am forever thankful for your advice and trust. I couldn't work for some time, and you never complained or pushed my recovery; most importantly, you always trusted me during this period which is one of the big reasons why I am here today. Auke, your guidance during the writing of my second paper was essential for my writing development and for better formulating my thoughts into words. Giovanni, I will never forget that moment when I was in isolation due to a severe case of COVID, and you brought a lasagna to my home; I will forever cherish this moment.

I want to thank Mark for his insurmountable help throughout the first two years of my Ph.D. You always made time to help with understanding the newly developed Operator-Based Linearization. Without your time, effort, patience, enthusiasm, and laying the foundation of the Delft Advanced Research Terra Simulator framework, this thesis would not be the same.

I also want to kindly thank my independent doctoral examination committee members Prof.dr.ir. David Smeulders, Prof.dr. Daniel Tartakovsky, Prof.dr. Daniel Kohn, Prof.dr. Sebastian Geiger, and Prof.dr.ir. Pacelli Zitha for agreeing to review my work and be part of my committee.

Thank you to the fantastic support staff at the department of Geoscience and Engineering: Marlijn, Lydia, Anke, Ralf, Lydia, Margot, Marijke, and Marja. Thanks to you, I never had to worry about anything; it made my life 100× easier; thanks!

I want to thank the Molengraaff fund for providing funds to perform the fieldwork expedition in Brazil. This fieldwork would not have been a success if it wasn't for Hilario; thank you so much for your generous hospitality and impeccable planning during this trip. I also want to thank Augusto and Phillippe for their valuable expertise during this time. And, of course, Cayo and Rebecca for showing us around Natal and being great company during the fieldwork. Also, this whole Ph.D. project was performed with a subsidy (reference TKI2017-07-UG) from the Ministry of Economic Affairs, National schemes EZ subsidies, Top sector Energy, carried out by the Netherlands Enterprise Agency. Special thanks Elisa Bergkamp, my colleague at TU Eindhoven, for working on the CarbFrac project together. I'm also particularly grateful to Sorin Pop for inviting me to Hasselt University and showing me the importance of a deeper understanding of the mathematics of what we try to model. Also, thanks to Fred Vermolen for having such patience on the highway near Utrecht, haha.

Thanks, Xiaocong and Yang, for your endless enthusiasm and discussions regarding geothermal energy and CO₂ sequestration. Thank you, Xiaoming, for our exciting discussions regarding dimensionality reduction techniques and history matching. Thank you, Kiarash, for the stimulating conversations on coupled momentum, mass balance, and well-models. Thank you, Aleks, for always being inspiring with the vast mathematical and physical knowledge you possess. You never fail to amaze me with your expertise in many research areas. Thank you, Ilshat, for insightful programming tips and even offering to help with my moving, haha! Thank you, Michiel, for your many discussions regarding fluid-flower, gmsH, and chemical models. Thank you, Gabriel, for the exciting work we are doing together now and for sharing my newfound love for triathlon. Also, thank you, Anne, for the mental support throughout the pandemic. And thank you, Willemijn, for organizing the DARSim meetings; they were always interesting.

Thank you to all my friends and colleagues from Applied Geology: Akeel, Andrea, Aulia, Emilio, Guillaume, Martha, Parvin, Pierre, Quinten, Rahul, Remi, Santosh, and Youwei. I will always cherish the lunches together and the Think & Drink. Rahul, the fieldwork wouldn't have been such a great success without you.

Thank you, Hadi; even though I feel sometimes we perhaps not always gotten along perfectly, you have taught me a great deal. You inspired me to be a better teacher and genuinely understand the fundamentals of what we are studying.

Thanks to Joep Storms for encouraging me to follow a more geological-oriented master's program during my pre-master. Thanks to Prof. Bill Rossen for inspiring me in the beautiful world of physical transport phenomena during my pre-master; I think here is when my scientific journey already started! Also, thank you, Femke Vossepoel, for always making time for me during my Master's and teaching me about exciting things in statistics. Thank you, Andre Jung, for making me curious about geostatistics and allowing me some time in BakerHughes during my Master's to see the application side of everything.

I also want to thank the Master's students I either supervised or worked with during my Ph.D.: Keshav, Elodie, Andrei, Camillo, Lynn, Hanif, Joey, Chenyang, Niek, Arturs, Duncan, Marvin, Andrea, and Martin. I probably learned more from you than you did from me, and it inspired me to become a better supervisor; thanks.

Thank you, Etienne, Michel, and Brahim, for collaborating on the multiphase reactive transport benchmark; I have learned so much from you!

Thanks to Stephen West and Irvin Yalom for strengthening my mind and piquing my interest in philosophy. You have kickstarted my journey into this whole another universe of thinking. You have provided me with weapons against the creatures emerging from the void often created by overthinking even the most straightforward questions in life.

Thank you, Barry, for teaching me the phrase: if it works, it ain't stupid.

Quick shoutout to Jannick, Martijn, and Jordi for making my time living in Delft from 2014 till 2017 fun and not only about studying. Jarno, thank you for the many evenings studying Machine Learning together and the occasional beer afterward.

Thank you, Robert and Ronald, for the fun evenings with lots of beer and drinking games. These were the much-needed cooling-downs after being in my head for too long.

To my chess buddies, Douwe, Han, Arend, and Mathijs. Thanks for listening to my ramblings about academia and my Ph.D. Also, thanks for educating me on the beautiful game of chess and keeping me motivated to play and enjoy the game. Also, thank you, Douwe, for inspiring me to get back into sports, especially to try a triathlon.

Kristian, I was delighted you had chosen to work at the Albert Heijn for some time, else it would have been unlikely that I would earn such a great friend. I wasn't always the person I am today, and I am happy that you forgave me for my mindless teenage self. I greatly value your intelligence, literature insights, and music appreciation. You were the person to get me into more complex board games, which changed my life in a good way.

I will never forget our journey in Finland, Jasper. And then our expedition in Delft, where we very often discussed the misery and advantages of studying all day, haha. You are a great friend; I always appreciate your relativism and outlook on life.

My board game and concert buddies from Utrecht, Paul and Vic. Thanks for the fun evenings playing board games at the Amsterdamsestraatweg. I love both of your musical journeys, and I hope more is to come in the future. The mental support was greatly appreciated during these years in Utrecht, and you made me feel at home in Utrecht.

My former running buddy, Shirah, thanks for getting me back into sports after being (almost) defeated physically by COVID for half a year. I could barely walk the stairs without being out of breath, but with you, we started the great habit of going running, sometimes even twice a week! During these runs, I also greatly appreciate our talks about spirituality, psychology, and life. You have taught me to be more open-minded. I am also very proud of you and the steps you have made in the last few years; never give up!

My new running buddy, Fanny, haha. No, but for real, you have greatly inspired me sometimes to slow down my life, appreciate the small things, and pay more attention to a healthy (mental and physical) lifestyle. I love discussing things with you, no matter the topic, even though it can get heated sometimes. I loved having you in Utrecht, and I am very happy for you and Richard in Sweden.

The messiah of music, Bart, thanks for educating my music palette all these years. Now you finally started making your music, and I couldn't be more proud of you! Through this, you inspire me to pursue things I genuinely want in my life; thanks for that! I also appreciate that you never sugarcoat things and say what is truly on your mind; this has helped me on several occasions, and it most often makes the advice worthwhile.

It feels like yesterday that we were trying to manage these Saturday mornings together at the Albert Heijn, Robin. Thank you very being a terrific friend all these years; no matter what happens, I always feel I can count on you. Significantly, the "just one

more" game of League of Legends and Company of Heroes 2 helped me through this period of my life. Also, your endless patience when discovering new board games was a blessing. I don't know if anyone else would sit with me for a full day and night(!) to learn the rules of a new crazy, complicated board game that I bought.

Timofey Baranov, thanks for being a fantastic colleague and friend. From the very beginning, we hit it off with similar tastes in music and board games. Your musical recommendations and our ranting sessions on what was currently not going well in our Ph.D. journey were always welcome. Always fun to discuss math and programming during some of our digital-working-together sessions. Thanks again for inspiring me to ride my bike more. I enjoyed playing board games with you and Nienke; hope to do it again.

Alexandros and Insa, thank you for opening your home for food and good vibes when I was in Delft many times. They were the boost I needed when I again doubted if I could make it these last months. I wish you the best with your new adventures, and I can't wait for the housewarming in your new place. Alex, thanks for the many words of encouragement and philosophical discussions during these years; I greatly appreciate them.

Even though times are constantly changing and our lives are much different now, I would have never been able to complete this journey if it weren't for you, Natalia. Thank you for all the fantastic things you have taught me throughout these years. You never stopped to inspire me with your unique and kind personality and by never giving up no matter how tough life is. I am very proud of you and wish you all the best in life!

Thanks to Jeannette and Deniz for the always fantastic Christmas day and sometimes Easter. Lovely food, great jokes, and a decent amount of beer and wine always end in a wonderful night. And Deniz, I always love discussing things about science and getting a small history lesson from you, haha.

Thank you, Foppe (my parent's dog), for all the fluffy hugs and mental support.

Then I want to thank my parents, Arie and Truus. You always supported me throughout my life, no matter what I wanted to do. We all show our love in different ways, with food, gifts, or just spending time together. For example, Arie picked us up in the middle of the night when we were stranded after a concert. Truus made a food package for me whenever I came to Apeldoorn for the weekend and back to Delft on Sunday. Thank you for all those moments, and hopefully, many more.

Now, I don't think anyone could wish for a better brother than you, Richard. We have been best friends for a long time, excluding our silly fights as kids, haha. You have taught me many things in life which I will always take with me. I will forever cherish our time living together in Utrecht, both coming back from some hardship in our lives. I am very happy for you and hope you are delighted in the Swedish Apeldoorn. You always inspired me to never give up through all the adversity you faced and overcame.

Lastly, I want to thank myself for never giving in to my inner voice telling me I couldn't do this. Everyone always thinks a Ph.D. is challenging because of math, statistics, science, and solving complicated problems, but the mental aspects are incredibly underrated. So many Ph.Ds (and other academics) suffer from some form of mental distress. Please know you are not alone, even if no one dares to speak up. Please do yourself a favor and take your mental health seriously.

Much love to all,
Stephan

BIBLIOGRAPHY

- Aagaard, P., & Helgeson, H. C. (1982). Thermodynamic and kinetic constraints on reaction rates among minerals and aqueous solutions; i, theoretical considerations. *American journal of Science*, 282(3), 237–285.
- Acuna, J. A., & Yortsos, Y. C. (1995). Application of fractal geometry to the study of networks of fractures and their pressure transient. *Water Resources Research*, 31(3), 527–540.
- Akbar, M., Vissapragada, B., Alghamdi, A. H., Allen, D., Herron, M., Carnegie, A., Dutta, D., Olesen, J.-R., Chourasiya, R., Logan, D., et al. (2000). A snapshot of carbonate reservoir evaluation. *Oilfield Review*, 12(4), 20–21.
- Ali, M. T., Ezzat, A. A., & Nasr-El-Din, H. A. (2020). A model to simulate matrix-acid stimulation for wells in dolomite reservoirs with vugs and natural fractures. *SPE Journal*, 25(02), 609–631.
- Andre, B. J., & Rajaram, H. (2005). Dissolution of limestone fractures by cooling waters: Early development of hypogene karst systems. *Water Resources Research*, 41(1).
- Annable, W. K. (2003). *Numerical analysis of conduit evolution in karstic aquifers*. University of Waterloo [Department of Earth Sciences].
- Antonellini, M., & Aydin, A. (1994). Effect of faulting on fluid flow in porous sandstones: Petrophysical properties. *AAPG bulletin*, 78(3), 355–377.
- Arnaudo, M., Dalgren, J., Topel, M., & Laumert, B. (2021). Waste heat recovery in low temperature networks versus domestic heat pumps—a techno-economic and environmental analysis. *Energy*, 219, 119675.
- Arnaudo, M., Topel, M., Puerto, P., Widl, E., & Laumert, B. (2019). Heat demand peak shaving in urban integrated energy systems by demand side management—a techno-economic and environmental approach. *Energy*, 186, 115887.
- Arnold, D., Demyanov, V., Christie, M., Bakay, A., & Gopa, K. (2016). Optimisation of decision making under uncertainty throughout field lifetime: A fractured reservoir example. *Computers & Geosciences*, 95, 123–139.
- Arnold, D., Demyanov, V., Rojas, T., & Christie, M. (2019). Uncertainty quantification in reservoir prediction: Part 1—model realism in history matching using geological prior definitions. *Mathematical Geosciences*, 51(2), 209–240.
- Arrhenius, S. (1889). Über die dissociationswärme und den einfluss der temperatur auf den dissociationsgrad der elektrolyte. *Zeitschrift für physikalische Chemie*, 4(1), 96–116.
- Babaei, M., & Nick, H. (2019). Performance of low-enthalpy geothermal systems: Interplay of spatially correlated heterogeneity and well-doublet spacings. *Applied Energy*, 253. <https://doi.org/10.1016/j.apenergy.2019.113569>
- Baghbanan, A., & Jing, L. (2008). Stress effects on permeability in a fractured rock mass with correlated fracture length and aperture. *International journal of rock mechanics and mining sciences*, 45(8), 1320–1334.

- Bahrainian, S. S., & Dezfuli, A. D. (2014). A geometry-based adaptive unstructured grid generation algorithm for complex geological media. *Computers & geosciences*, 68, 31–37.
- Bai, T., Maerten, L., Gross, M. R., & Aydin, A. (2002). Orthogonal cross joints: Do they imply a regional stress rotation? *Journal of Structural Geology*, 24(1), 77–88.
- Bakay, A., Demyanov, V., & Arnold, D. (2016). Uncertainty quantification in fractured reservoirs based on outcrop modelling from northeast brazil. *7th EAGE Saint Petersburg International Conference and Exhibition*, cp–480.
- Balberg, I., & Binenbaum, N. (1983). Computer study of the percolation threshold in a two-dimensional anisotropic system of conducting sticks. *Physical Review B*, 28(7), 3799.
- Balsamo, F., Bezerra, F., Klimchouk, A., Cazarin, C., Auler, A., Nogueira, F., & Pontes, C. (2020). Influence of fracture stratigraphy on hypogene cave development and fluid flow anisotropy in layered carbonates, ne brazil. *Marine and Petroleum Geology*, 114, 104207.
- Barenblatt, G. (1960). Basic concepts in the theory of seepage of homogeneous liquids in fissured rocks. *Prikl. Mat. Mekh.*, 24(5), 852–864.
- Bazin, B. (2001). From matrix acidizing to acid fracturing: A laboratory evaluation of acid/rock interactions. *SPE Production & Facilities*, 16(01), 22–29.
- Bazin, B., & Abdulahad, G. (1999). Experimental investigation of some properties of emulsified acid systems for stimulation of carbonate formations. *Middle East Oil Show and Conference*.
- Bear, J. (2013). *Dynamics of fluids in porous media*. Courier Corporation.
- Berre, I., Doster, F., & Keilegavlen, E. (2019). Flow in fractured porous media: A review of conceptual models and discretization approaches. *Transport in Porous Media*, 130(1), 215–236.
- Berrone, S., Borio, A., & Vicini, F. (2019). Reliable a posteriori mesh adaptivity in discrete fracture network flow simulations. *Computer Methods in Applied Mechanics and Engineering*, 354, 904–931.
- Berrone, S. (2010). Skipping transition conditions in a posteriori error estimates for finite element discretizations of parabolic equations. *ESAIM: Mathematical Modelling and Numerical Analysis-Modélisation Mathématique et Analyse Numérique*, 44(3), 455–484.
- Bertotti, G., Audra, P., Auler, A., Bezerra, F., de Hoop, S., Prabhakaran, R., Pontes, C., & Lima, R. (2020a). Characteristics and genesis of hypogenic karsts in carbonate successions: Inferences for hydrocarbon and geothermal systems. *Fourth Naturally Fractured Reservoir Workshop*, 2020(1), 1–5.
- Bertotti, G., Audra, P., Auler, A., Bezerra, F. H., de Hoop, S., Pontes, C., Prabhakaran, R., & Lima, R. (2020b). The morro vermelho hypogenic karst system (brazil): Stratigraphy, fractures, and flow in a carbonate strike-slip fault zone with implications for carbonate reservoirs. *AAPG Bulletin*, 104(10), 2029–2050.
- Bertotti, G., de Graaf, S., Bisdorn, K., Oskam, B., Vonhof, H. B., Bezerra, F. H., Reijmer, J. J., & Cazarin, C. L. (2017). Fracturing and fluid-flow during post-rift subsidence in carbonates of the jandaira formation, potiguar basin, ne brazil. *Basin Research*, 29(6), 836–853.

- Besl, P. J., & McKay, N. D. (1992). Method for registration of 3-d shapes. *Sensor fusion IV: control paradigms and data structures*, 1611, 586–606.
- Birk, S., Liedl, R., Sauter, M., & Teutsch, G. (2003). Hydraulic boundary conditions as a controlling factor in karst genesis: A numerical modeling study on artesian conduit development in gypsum. *Water Resources Research*, 39(1).
- Bisdorn, K., Gauthier, B., Bertotti, G., & Hardebol, N. (2014). Calibrating discrete fracture-network models with a carbonate three-dimensional outcrop fracture network: Implications for naturally fractured reservoir modeling. *AAPG bulletin*, 98(7), 1351–1376.
- Bisdorn, K., Bertotti, G., & Nick, H. M. (2016a). A geometrically based method for predicting stress-induced fracture aperture and flow in discrete fracture networks. *AAPG Bulletin*, 100(7), 1075–1097.
- Bisdorn, K., Bertotti, G., & Nick, H. M. (2016b). The impact of different aperture distribution models and critical stress criteria on equivalent permeability in fractured rocks. *Journal of Geophysical Research: Solid Earth*, 121(5), 4045–4063.
- Bisdorn, K., Nick, H. M., & Bertotti, G. (2017). An integrated workflow for stress and flow modelling using outcrop-derived discrete fracture networks. *Computers & Geosciences*, 103, 21–35.
- Boersma, Q., Athmer, W., Haege, M., Etchebes, M., Haukås, J., & Bertotti, G. (2020). Natural fault and fracture network characterization for the southern ekofisk field: A case study integrating seismic attribute analysis with image log interpretation. *Journal of Structural Geology*, 141, 104197.
- Boersma, Q., Hardebol, N., Barnhoorn, A., & Bertotti, G. (2018). Mechanical factors controlling the development of orthogonal and nested fracture network geometries. *Rock Mechanics and Rock Engineering*, 51(11), 3455–3469.
- Boersma, Q., Prabhakaran, R., Bezerra, F. H., & Bertotti, G. (2019). Linking natural fractures to karst cave development: A case study combining drone imagery, a natural cave network and numerical modelling. *Petroleum Geoscience*, 25(4), 454–469.
- Boersma, Q. D., Bruna, P. O., de Hoop, S., Vinci, E., Tehrani, A. M., & Bertotti, G. (2021). The impact of natural fractures on heat extraction from tight triassic sandstones in the west netherlands basin: A case study combining well, seismic and numerical data. *Netherlands Journal of Geosciences*, 100.
- Bollobás, B. (2013). *Modern graph theory* (Vol. 184). Springer Science & Business Media.
- Bonneau, F., Henrion, V., Caumon, G., Renard, P., & Sausse, J. (2013). A methodology for pseudo-genetic stochastic modeling of discrete fracture networks. *Computers & Geosciences*, 56, 12–22.
- Borg, I., & Groenen, P. J. (2005). *Modern multidimensional scaling: Theory and applications*. Springer Science & Business Media.
- Bosse, M., Zlot, R., & Flick, P. (2012). Zebedee: Design of a spring-mounted 3-d range sensor with application to mobile mapping. *IEEE Transactions on Robotics*, 28(5), 1104–1119.
- Bour, O., & Davy, P. (1997). Connectivity of random fault networks following a power law fault length distribution. *Water Resources Research*, 33(7), 1567–1583.

- Boyd, A., Souza, A., Carneiro, G., Machado, V., Trevizan, W., Santos, B., Netto, P., Bagueira, R., Polinski, R., Bertolini, A., et al. (2015). Presalt carbonate evaluation for Santos basin, offshore Brazil. *Petrophysics*, 56(06), 577–591.
- Branets, L. V., Ghai, S. S., Lyons, S. L., & Wu, X.-H. (2009). Challenges and technologies in reservoir modeling. *Communications in Computational Physics*, 6(1), 1.
- Bruna, P.-O., Straubhaar, J., Prabhakaran, R., Bertotti, G., Bisdom, K., Mariethoz, G., & Meda, M. (2019). A new methodology to train fracture network simulation using multiple-point statistics. *Solid Earth*, 10(2), 537–559.
- Buhmann, D., & Dreybrodt, W. (1985). The kinetics of calcite dissolution and precipitation in geologically relevant situations of karst areas: 1. open system. *Chemical geology*, 48(1-4), 189–211.
- Caers, J. (2011). *Modeling uncertainty in the earth sciences*. John Wiley & Sons.
- Chaudhuri, A., Rajaram, H., & Viswanathan, H. (2013). Early-stage hypogene karstification in a mountain hydrologic system: A coupled thermohydrochemical model incorporating buoyant convection. *Water Resources Research*, 49(9), 5880–5899.
- Chen, G., Pan, W., Sa, L., Han, J., & Guan, W. (2005). Application of prediction techniques in carbonate karst reservoir in Tarim basin. *Applied Geophysics*, 2(2), 111–118.
- Chen, M., Tompson, A., Mellors, R., & Abdalla, O. (2015). An efficient optimization of well placement and control for a geothermal prospect under geological uncertainty. *Applied Energy*, 137, 352–363. <https://doi.org/10.1016/j.apenergy.2014.10.036>
- CHEN, Z. (2011). Experimental study of the non-Darcy flow and solute transport in a channeled single fracture. *Journal of Hydrodynamics*, 23(6), 745–751.
- Chilès, J.-P. (2005). Stochastic modeling of natural fractured media: A review. *Geostatistics Banff 2004*, 285–294.
- Christensen, J., Darche, G., Dechelette, B., Ma, H., Sammon, P., et al. (2004). Applications of dynamic gridding to thermal simulations. *SPE international thermal operations and heavy oil symposium and western regional meeting*.
- Christie, M. A. (1996). Upscaling for reservoir simulation. *Journal of petroleum technology*, 48(11), 1–004.
- Chugunova, T., CorpeL, V., & Gomez, J.-P. (2017). Explicit fracture network modelling: From multiple point statistics to dynamic simulation. *Mathematical Geosciences*, 49(4), 541–553.
- Cinco-Ley, H. (1996). Well-test analysis for naturally fractured reservoirs. *Journal of Petroleum Technology*, 48(01), 51–54.
- Clemens, T., Hueckinghaus, D., Sauter, M., Liedl, R., & Teutsch, G. (1997). Modelling the genesis of karst aquifer systems using a coupled reactive network model. *IAHS PUBLICATION*, 241, 3–10.
- Cohen, C. E., Ding, D., Quintard, M., & Bazin, B. (2008). From pore scale to wellbore scale: Impact of geometry on wormhole growth in carbonate acidization. *Chemical Engineering Science*, 63(12), 3088–3099.
- Collon, P., Bernasconi, D., Vuilleumier, C., & Renard, P. (2017). Statistical metrics for the characterization of karst network geometry and topology. *Geomorphology*, 283, 122–142.

- Compennolle, T., Welkenhuysen, K., Petitclerc, E., Maes, D., & Piessens, K. (2019). The impact of policy measures on profitability and risk in geothermal energy investments. *Energy Economics*, *84*, 104524.
- Correia, M. G., von Hohendorff Filho, J. C., Schiozer, D. J., et al. (2019). Multiscale integration for karst-reservoir flow-simulation models. *SPE Reservoir Evaluation & Engineering*.
- Council, N. R. et al. (1996). *Rock fractures and fluid flow: Contemporary understanding and applications*. National Academies Press.
- Crooijmans, R., Willems, C., Nick, H., & Bruhn, D. (2016). The influence of facies heterogeneity on the doublet performance in low-enthalpy geothermal sedimentary reservoirs. *Geothermics*, *64*, 209–219. <https://doi.org/10.1016/j.geothermics.2016.06.004>
- Csardi, G., Nepusz, T. et al. (2006). The igraph software package for complex network research. *InterJournal, complex systems*, *1695*(5), 1–9.
- Cui, G., Zhang, L., Ren, B., Enechukwu, C., Liu, Y., & Ren, S. (2016). Geothermal exploitation from depleted high temperature gas reservoirs via recycling supercritical CO₂: Heat mining rate and salt precipitation effects. *Applied Energy*, *183*, 837–852. <https://doi.org/10.1016/j.apenergy.2016.09.029>
- Cusini, M., van Kruijsdijk, C., & Hajibeygi, H. (2016). Algebraic dynamic multilevel (ADM) method for fully implicit simulations of multiphase flow in porous media. *Journal of Computational Physics*, *314*, 60–79.
- DARTS. (2019). Delft Advanced Research Terra Simulator [[Online; accessed 29-May-2020]].
- de Hoop, S., Voskov, D., & Bertotti, G. (2020). Studying the effects of heterogeneity on dissolution processes using operator based linearization and high-resolution lidar data. *ECMOR XVII, 2020*(1), 1–13.
- de Hoop, S., Voskov, D., Vossepoel, F., & Jung, A. (2018). Quantification of coarsening effect on response uncertainty in reservoir simulation. *ECMOR XVI-16th European Conference on the Mathematics of Oil Recovery, 2018*(1), 1–16.
- de Hoop, S., Jones, E., & Voskov, D. (2021a). Accurate geothermal and chemical dissolution simulation using adaptive mesh refinement on generic unstructured grids. *Advances in Water Resources*, 103977.
- de Hoop, S., & Voskov, D. (2021). Fast and robust scheme for uncertainty quantification in naturally fractured reservoirs. *SPE Reservoir Simulation Conference*.
- de Hoop, S., Voskov, D., Ahusborde, E., Amaziane, B., & Kern, M. (2022). Reactive multiphase flow in porous media at the darcy scale: A benchmark proposal.
- de Hoop, S., Voskov, D., Bertotti, G., & Barnhoorn, A. (2021b). An advanced discrete fracture methodology for fast, robust, and accurate simulation of energy production from complex fracture networks. *Water Resources Research*, e2021WR030743.
- Douma, L. A., Regelink, J. A., Bertotti, G., Boersma, Q. D., & Barnhoorn, A. (2019). The mechanical contrast between layers controls fracture containment in layered rocks. *Journal of Structural Geology*, *127*, 103856.
- Dreybrodt, W. (1990). The role of dissolution kinetics in the development of karst aquifers in limestone: A model simulation of karst evolution. *The Journal of Geology*, *98*(5), 639–655.

- Dublyansky, Y. (2000). Hydrothermal speleogenesis: Its settings and peculiar features. *Speleogenesis. Evolution of karst aquifers. National Speleological Society*, 292–297.
- Durlofsky, L. J. (2005). Upscaling and gridding of fine scale geological models for flow simulation. *8th International Forum on Reservoir Simulation Iles Borromees, Stresa, Italy, 2004*, 1–59.
- El Ahmar, L. (2019). Characterization of karst geometry and stability analysis of cave tunnels in bahia, brazil.
- Ennes-Silva, R. A., Bezerra, F. H., Nogueira, F. C., Balsamo, E., Klimchouk, A., Cazarin, C. L., & Auler, A. S. (2016). Superposed folding and associated fracturing influence hypogene karst development in neoproterozoic carbonates, são francisco craton, brazil. *Tectonophysics*, 666, 244–259.
- Esrafil-Dizaji, B., & Rahimpour-Bonab, H. (2019). Carbonate reservoir rocks at giant oil and gas fields in sw iran and the adjacent offshore: A review of stratigraphic occurrence and poro-perm characteristics. *Journal of Petroleum Geology*, 42(4), 343–370.
- Eurostat. (2020). *Energy consumption in households 2020*. Retrieved March 4, 2022, from https://ec.europa.eu/eurostat/statistics-explained/index.php?title=Energy_consumption_in_households
- Fan, Y., Durlofsky, L. J., & Tchelepi, H. A. (2012). A fully-coupled flow-reactive-transport formulation based on element conservation, with application to co2 storage simulations. *Advances in Water Resources*, 42, 47–61.
- Farshidi, S. F., Fan, Y., Durlofsky, L. J., Tchelepi, H. A., et al. (2013). Chemical reaction modeling in a compositional reservoir-simulation framework. *SPE Reservoir Simulation Symposium*.
- Farshidi, S. F. (2016). *Compositional reservoir simulation-based reactive-transport formulations, with application to co2 storage in sandstone and ultramafic formations* (Doctoral dissertation). Stanford University.
- Fleiter, T., Steinbach, J., Ragwitz, M., Dengler, J., Köhler, B., Reitze, F., Tuille, F., Hartner, M., Kranzl, L., Forthuber, S., et al. (2016). Mapping and analyses of the current and future (2020-2030) heating/cooling fuel deployment (fossil/renewables). *European Commission, Directorate-General for Energy*.
- Flemisch, B., Berre, I., Boon, W., Fumagalli, A., Schwenck, N., Scotti, A., Stefansson, I., & Tatomir, A. (2018). Benchmarks for single-phase flow in fractured porous media. *Advances in Water Resources*, 111, 239–258.
- Ford, D. C., & Williams, P. W. (1989). *Karst geomorphology and hydrology* (Vol. 601). Unwin Hyman London.
- Fossen, H. (2016). *Structural geology*. Cambridge university press.
- Gabrovšek, F., & Dreybrodt, W. (2001). A model of the early evolution of karst aquifers in limestone in the dimensions of length and depth. *Journal of Hydrology*, 240(3-4), 206–224.
- Gale, J. F., Laubach, S. E., Marrett, R. A., Olson, J. E., Holder, J., & Reed, R. M. (2004). Predicting and characterizing fractures in dolostone reservoirs: Using the link between diagenesis and fracturing. *Geological Society, London, Special Publications*, 235(1), 177–192.

- Gale, J. F., Reed, R. M., & Holder, J. (2007). Natural fractures in the barnett shale and their importance for hydraulic fracture treatments. *AAPG bulletin*, 91(4), 603–622.
- Gallyamov, E., Garipov, T., Voskov, D., & Van den Hoek, P. (2018). Discrete fracture model for simulating waterflooding processes under fracturing conditions. *International Journal for Numerical and Analytical Methods in Geomechanics*, 42(13), 1445–1470.
- Garipov, T., Karimi-Fard, M., & Tchelepi, H. (2016). Discrete fracture model for coupled flow and geomechanics. *Computational Geosciences*, 20(1), 149–160.
- Geiger, S., & Matthäi, S. (2014). What can we learn from high-resolution numerical simulations of single-and multi-phase fluid flow in fractured outcrop analogues? *Geological Society, London, Special Publications*, 374(1), 125–144.
- Geuzaine, C., & Remacle, J.-F. (2009). Gmsh: A 3-d finite element mesh generator with built-in pre-and post-processing facilities. *International journal for numerical methods in engineering*, 79(11), 1309–1331.
- Girardeau-Montaut, D. (2016). Cloudcompare. *France: EDF R&D Telecom ParisTech*.
- Golfier, F., Zarcone, C., Bazin, B., Lenormand, R., Lasseux, D., & QUINTARD, M. (2002). On the ability of a darcy-scale model to capture wormhole formation during the dissolution of a porous medium. *Journal of fluid Mechanics*, 457, 213–254.
- Gong, B., Karimi-Fard, M., & Durlofsky, L. J. (2008). Upscaling discrete fracture characterizations to dual-porosity, dual-permeability models for efficient simulation of flow with strong gravitational effects. *SPE Journal*, 13(01), 58–67.
- Greiserman, M., Hasson, D., Semiat, R., & Shemer, H. (2016). Kinetics of dolomite dissolution in a packed bed by acidified desalinated water. *Desalination*, 396, 39–47.
- Gureghian, A. B. (1975). A study by the finite-element method of the influence of fractures in confined aquifers. *Society of Petroleum Engineers Journal*, 15(02), 181–191.
- Hajibeygi, H., Karvounis, D., & Jenny, P. (2011). A hierarchical fracture model for the iterative multiscale finite volume method. *Journal of Computational Physics*, 230(24), 8729–8743.
- Hammersley, J. (2013). *Monte carlo methods*. Springer Science & Business Media.
- Harris, C. R., Millman, K. J., van der Walt, S. J., Gommers, R., Virtanen, P., Cournapeau, D., Wieser, E., Taylor, J., Berg, S., Smith, N. J., Kern, R., Picus, M., Hoyer, S., van Kerkwijk, M. H., Brett, M., Haldane, A., del Río, J. F., Wiebe, M., Peterson, P., ... Oliphant, T. E. (2020). Array programming with NumPy. *Nature*, 585(7825), 357–362. <https://doi.org/10.1038/s41586-020-2649-2>
- He, S., & Morse, J. W. (1993). The carbonic acid system and calcite solubility in aqueous na-k-ca-mg-cl-so4 solutions from 0 to 90 c. *Geochimica et Cosmochimica Acta*, 57(15), 3533–3554.
- Helmig, R. et al. (1997). *Multiphase flow and transport processes in the subsurface: A contribution to the modeling of hydrosystems*. Springer-Verlag.
- Hiller, T., Kaufmann, G., & Romanov, D. (2011). Karstification beneath dam-sites: From conceptual models to realistic scenarios. *Journal of Hydrology*, 398(3-4), 202–211.

- HosseiniMehr, M., Piguave Tomala, J., Vuik, C., & Hajibeygi, H. Projection-based embedded discrete fracture model (pedfm) on corner-point grid geometry for subsurface flow and geothermal modeling. In: 2020. <https://doi.org/10.3997/2214-4609.202035245>.
- Houben, M., Hardebol, N., Barnhoorn, A., Boersma, Q., Carone, A., Liu, Y., de Winter, D., Peach, C., & Drury, M. (2017). Fluid flow from matrix to fractures in early jurassic shales. *International Journal of Coal Geology*, 175, 26–39.
- House, J. E. (2007). *Principles of chemical kinetics*. Academic press.
- Huang, H., Wu, S., Cohen-Or, D., Gong, M., Zhang, H., Li, G., & Chen, B. (2013). L1-medial skeleton of point cloud. *ACM Trans. Graph.*, 32(4), 65–1.
- Huang, N., Jiang, Y., Liu, R., & Li, B. (2017a). Estimation of permeability of 3-d discrete fracture networks: An alternative possibility based on trace map analysis. *Engineering Geology*, 226, 12–19.
- Huang, S., Zhang, Y., Zheng, X., Zhu, Q., Shao, G., Cao, Y., Chen, X., Yang, Z., & Bai, X. (2017b). Types and characteristics of carbonate reservoirs and their implication on hydrocarbon exploration: A case study from the eastern tarim basin, nw china. *Journal of Natural Gas Geoscience*, 2(1), 73–79.
- IEA. (2020). *World energy outlook 2020, iea, paris*. Retrieved March 4, 2022, from <https://www.iea.org/reports/world-energy-outlook-2020>
- Jaglan, H., Qayyum, F., & Hélène, H. (2015). Unconventional seismic attributes for fracture characterization. *First Break*, 33(3).
- Jenny, P., Lee, S., & Tchelepi, H. A. (2003). Multi-scale finite-volume method for elliptic problems in subsurface flow simulation. *Journal of Computational Physics*, 187(1), 47–67.
- Jouves, J., Viseur, S., Arfib, B., Baudement, C., Camus, H., Collon, P., & Guglielmi, Y. (2017). Speleogenesis, geometry, and topology of caves: A quantitative study of 3d karst conduits. *Geomorphology*, 298, 86–106.
- Joyeux, R., & Ripple, R. D. (2007). Household energy consumption versus income and relative standard of living: A panel approach. *Energy Policy*, 35(1), 50–60.
- Jung, A., Fenwick, D. H., & Caers, J. (2013). Training image-based scenario modeling of fractured reservoirs for flow uncertainty quantification. *Computational Geosciences*, 17(6), 1015–1031.
- Kala, K., & Voskov, D. (2020). Element balance formulation in reactive compositional flow and transport with parameterization technique. *Computational Geosciences*, 24(2), 609–624. <https://doi.org/10.1007/s10596-019-9828-y>
- Kang, Q., Zhang, D., & Chen, S. (2003). Simulation of dissolution and precipitation in porous media. *Journal of Geophysical Research: Solid Earth*, 108(B10).
- Karimi-Fard, M., & Durlofsky, L. J. (2014). Unstructured adaptive mesh refinement for flow in heterogeneous porous media. *ECMOR XIV-14th European conference on the mathematics of oil recovery*.
- Karimi-Fard, M., & Durlofsky, L. J. (2012). Accurate resolution of near-well effects in up-scaled models using flow-based unstructured local grid refinement. *SPE Journal*, 17(04), 1–084.

- Karimi-Fard, M., & Durlofsky, L. J. (2016). A general gridding, discretization, and coarsening methodology for modeling flow in porous formations with discrete geological features. *Advances in water resources*, 96, 354–372.
- Karimi-Fard, M., Durlofsky, L. J., & Aziz, K. (2004). An efficient discrete-fracture model applicable for general-purpose reservoir simulators. *SPE journal*, 9(02), 227–236.
- Karimi-Fard, M., Gong, B., & Durlofsky, L. J. (2006). Generation of coarse-scale continuum flow models from detailed fracture characterizations. *Water resources research*, 42(10).
- Kassa, S., Pierson, B., Chow, W. S., & Talib, J. B. A. (2012). Identifying the link between lineament and cave passage trends to comprehend fractures continuity and influence on the kinta valley karst system. *International Journal of Speleology*, 41(1), 7.
- Kaufmann, G. (2009). Modelling karst geomorphology on different time scales. *Geomorphology*, 106(1-2), 62–77.
- Kaufmann, G. (2016). Modelling karst aquifer evolution in fractured, porous rocks. *Journal of Hydrology*, 543, 796–807.
- Kaufmann, G., Romanov, D., & Hiller, T. (2010). Modeling three-dimensional karst aquifer evolution using different matrix-flow contributions. *Journal of hydrology*, 388(3-4), 241–250.
- Kaygusuz, K. (2012). Energy for sustainable development: A case of developing countries. *Renewable and Sustainable Energy Reviews*, 16(2), 1116–1126.
- Khait, M., & Voskov, D. (2018a). Adaptive parameterization for solving of thermal/compositional nonlinear flow and transport with buoyancy. *SPE Journal*, 23, 522–534. <https://doi.org/10.2118/182685-PA>
- Khait, M., & Voskov, D. (2018b). Adaptive parameterization for solving of thermal/compositional nonlinear flow and transport with buoyancy. *SPE Journal*, 23(2), 522–534. <https://doi.org/10.2118/182685-pa>
- Khait, M., & Voskov, D. (2018c). Operator-based linearization for efficient modeling of geothermal processes. *Geothermics*, 74, 7–18. <https://doi.org/10.1016/j.geothermics.2018.01.012>
- Khait, M., & Voskov, D. (2018d). Operator-based linearization for efficient modeling of geothermal processes. *Geothermics*, 74, 7–18. <https://doi.org/10.1016/j.geothermics.2018.01.012>
- Khait, M., & Voskov, D. V. (2017). Operator-based linearization for general purpose reservoir simulation. *Journal of Petroleum Science and Engineering*, 157, 990–998.
- Kirstein, J., Hellevang, H., Haile, B. G., Gleixner, G., & Gaupp, R. (2016). Experimental determination of natural carbonate rock dissolution rates with a focus on temperature dependency. *Geomorphology*, 261, 30–40.
- Klimchouk, A. (2007). Hypogene speleogenesis. *Hydrogeological and morphogenetic perspective. National*.
- Klimchouk, A. (2009). Morphogenesis of hypogenic caves. *Geomorphology*, 106(1-2), 100–117.
- Klimchouk, A. (2012). Speleogenesis, hypogenic. *Encyclopedia of caves (second edition)* (pp. 748–765). Elsevier.

- Klimchouk, A. (2015). The karst paradigm: Changes, trends and perspectives/kraska paradigma: Spremembe, trendi in perspektive. *Acta Carsologica*, 44(3), 289.
- Klimchouk, A., Auler, A. S., Bezerra, F. H., Cazarin, C. L., Balsamo, E., & Dublyansky, Y. (2016). Hypogenic origin, geologic controls and functional organization of a giant cave system in precambrian carbonates, Brazil. *Geomorphology*, 253, 385–405.
- Klimchouk, A., Palmer, A. N., De Waele, J., Auler, A. S., & Audra, P. (2017). *Hypogene karst regions and caves of the world*. Springer.
- Koehn, D., Piazzolo, S., Beaudoin, N. E., Kelka, U., Spruženiece, L., Putnis, C. V., & Toussaint, R. (2021). Relative rates of fluid advection, elemental diffusion and replacement govern reaction front patterns. *Earth and Planetary Science Letters*, 565, 116950.
- Koohbor, B., Fahs, M., Hoteit, H., Doummar, J., Younes, A., & Belfort, B. (2020). An advanced discrete fracture model for variably saturated flow in fractured porous media. *Advances in Water Resources*, 140, 103602.
- Koudina, N., Garcia, R. G., Thovert, J.-F., & Adler, P. (1998). Permeability of three-dimensional fracture networks. *Physical Review E*, 57(4), 4466.
- Laidler, K. J. (1987). *Chemical kinetics*.
- Lamarche, J., Lavenue, A. P., Gauthier, B. D., Guglielmi, Y., & Jayet, O. (2012). Relationships between fracture patterns, geodynamics and mechanical stratigraphy in carbonates (south-east basin, France). *Tectonophysics*, 581, 231–245.
- Lasaga, A. C. (1981). Transition state theory. *Rev. Mineral.;(United States)*, 8.
- Lasaga, A. C. (1984). Chemical kinetics of water-rock interactions. *Journal of geophysical research: solid earth*, 89(B6), 4009–4025.
- Laubach, S. E., Olson, J. E., & Gross, M. R. (2009). Mechanical and fracture stratigraphy. *AAPG bulletin*, 93(11), 1413–1426.
- Le Chatelier, H. L. (1884). Sur un énoncé général des lois des équilibres chimiques. *Comptes Rendus Académie des Sciences*, 99, 786–789.
- Lee, T.-C., Kashyap, R. L., & Chu, C.-N. (1994). Building skeleton models via 3-d medial surface axis thinning algorithms. *CVGIP: Graphical Models and Image Processing*, 56(6), 462–478.
- Li, J. Z., Laubach, S., Gale, J., & Marrett, R. (2018). Quantifying opening-mode fracture spatial organization in horizontal wellbore image logs, core and outcrop: Application to upper cretaceous frontier formation tight gas sandstones, USA. *Journal of Structural Geology*, 108, 137–156.
- Li, L., & Lee, S. H. (2008). Efficient field-scale simulation of black oil in a naturally fractured reservoir through discrete fracture networks and homogenized media. *SPE Reservoir evaluation & engineering*, 11(04), 750–758.
- Li, L., & Voskov, D. (2021). A novel hybrid model for multiphase flow in complex multi-scale fractured systems. *Journal of Petroleum Science and Engineering*, 203, 108657.
- Li, X., & Li, D. (2019). A numerical procedure for unsaturated seepage analysis in rock mass containing fracture networks and drainage holes. *Journal of Hydrology*, 574, 23–34.
- Lichtner, P. C. (1996). Continuum formulation of multicomponent-multiphase reactive transport. *Reviews in Mineralogy and Geochemistry*, 34(1), 1–81.

- Lim, K.-T., Schiozer, D., & Aziz, K. (1995). A new approach for residual and jacobian arrays construction in reservoir simulators. *SPE Computer Applications*, 7(04), 93–96.
- Limberger, J., Boxem, T., Pluymaekers, M., Bruhn, D., Manzella, A., Calcagno, P., Beekman, F., Cloetingh, S., & van Wees, J.-D. (2018). Geothermal energy in deep aquifers: A global assessment of the resource base for direct heat utilization. *Renewable and Sustainable Energy Reviews*, 82, 961–975.
- Liu, E., & Martinez, A. (2014). *Seismic fracture characterization* (Vol. 575). Elsevier.
- Liu, X., Zhang, C., Liu, Q., & Birkholzer, J. (2009). Multiple-point statistical prediction on fracture networks at yucca mountain. *Environmental geology*, 57(6), 1361–1370.
- Lyu, X., Khait, M., & Voskov, D. (2021a). Operator-based linearization approach for modelling of multiphase flow with buoyancy and capillarity. *SPE Journal*. <https://doi.org/10.2118/205378-PA>
- Lyu, X., Voskov, D., & Rossen, W. R. (2021b). Numerical investigations of foam-assisted CO₂ storage in saline aquifers. *International journal of greenhouse gas control*.
- Maheshwari, P., Ratnakar, R., Kalia, N., & Balakotaiah, V. (2013). 3-d simulation and analysis of reactive dissolution and wormhole formation in carbonate rocks. *Chemical Engineering Science*, 90, 258–274.
- Mallison, B. T., Hui, M.-H., & Narr, W. (2010). Practical gridding algorithms for discrete fracture modeling workflows. *ECMOR XII-12th European Conference on the Mathematics of Oil Recovery*, cp-163.
- Manzocchi, T. (2002). The connectivity of two-dimensional networks of spatially correlated fractures. *Water Resources Research*, 38(9), 1–1.
- Maryška, J., Severn, O., & Vohralik, M. (2005). Numerical simulation of fracture flow with a mixed-hybrid fem stochastic discrete fracture network model. *Computational Geosciences*, 8(3), 217–234.
- McGinnis, R. N., Ferrill, D. A., Smart, K. J., Morris, A. P., Higuera-Diaz, C., & Prawica, D. (2015). Pitfalls of using entrenched fracture relationships: Fractures in bedded carbonates of the hidden valley fault zone, canyon lake gorge, comal county, texas/pitfalls of using entrenched fracture relationships. *AAPG Bulletin*, 99(12), 2221–2245.
- Mello, M. R., Bender, A. A., De Mio, E., et al. (2011). Giant sub-salt hydrocarbon province of the greater campos basin, brazil. *OTC Brasil*.
- Menzinger, M., & Wolfgang, R. (1969). The meaning and use of the arrhenius activation energy. *Angewandte Chemie International Edition in English*, 8(6), 438–444.
- Misi, A., Kaufman, A. J., Azmy, K., Dardenne, M. A., Sial, A. N., & De Oliveira, T. F. (2011). Neoproterozoic successions of the são francisco craton, brazil: The bambuí, una, vazante and vaza barris/miaba groups and their glaciogenic deposits. *Geological Society, London, Memoirs*, 36(1), 509–522.
- Misi, A., & Kyle, J. R. (1994). Upper proterozoic carbonate stratigraphy, diagenesis, and stromatolitic phosphorite formation, irecê basin, bahia, brazil. *Journal of Sedimentary Research*, 64(2a), 299–310.
- Modak, J. M. (2002). Haber process for ammonia synthesis. *Resonance*, 7(9), 69–77.
- Moeck, I. S. (2014). Catalog of geothermal play types based on geologic controls. *Renewable and Sustainable Energy Reviews*, 37, 867–882.

- Mohammed, I., Olayiwola, T. O., Alkathim, M., Awotunde, A. A., & Alafnan, S. F. (2021). A review of pressure transient analysis in reservoirs with natural fractures, vugs and/or caves. *Petroleum Science*, 18(1), 154–172.
- Moinfar, A., Narr, W., Hui, M.-H., Mallison, B. T., & Lee, S. H. (2011). Comparison of discrete-fracture and dual-permeability models for multiphase flow in naturally fractured reservoirs. *SPE Reservoir Simulation Symposium*.
- Morel, F. M., Hering, J. G., Hering, J. G., et al. (1993). *Principles and applications of aquatic chemistry*. John Wiley & Sons.
- Morse, J. W., Arvidson, R. S., & Lüttge, A. (2007). Calcium carbonate formation and dissolution. *Chemical reviews*, 107(2), 342–381.
- Moutte, J., Michel, A., Battaia, G., Parra, T., Garcia, D., & Wolf, S. (2010). Arxim, a library for thermodynamic modeling of reactive heterogeneous systems, with applications to the simulation of fluid-rock system. *21st Congress of IUPAC*.
- Murad, M., Lopes, T., Pereira, P., Bezerra, F., & Rocha, A. (2020). A three-scale index for flow in karst conduits in carbonate rocks. *Advances in Water Resources*, 141. <https://doi.org/10.1016/j.advwatres.2020.103613>
- Mustapha, H., & Dimitrakopoulos, R. (2011). Discretizing two-dimensional complex fractured fields for incompressible two-phase flow. *International Journal for Numerical Methods in Fluids*, 65(7), 764–780.
- Mustapha, H., & Mustapha, K. (2007). A new approach to simulating flow in discrete fracture networks with an optimized mesh. *SIAM Journal on Scientific Computing*, 29(4), 1439–1459.
- Nejadi, S., Trivedi, J. J., & Leung, J. (2017). History matching and uncertainty quantification of discrete fracture network models in fractured reservoirs. *Journal of Petroleum Science and Engineering*, 152, 21–32.
- Nelson, R. (2001). *Geologic analysis of naturally fractured reservoirs*. Elsevier.
- Novikov, A., Voskov, D., Khait, M., Hajibeygi, H., & Jansen, J. A collocated finite volume scheme for high-performance simulation of induced seismicity in geo-energy applications. In: 2021. <https://doi.org/10.2118/203903-MS>.
- Olson, J. E., Laubach, S. E., & Lander, R. H. (2009). Natural fracture characterization in tight gas sandstones: Integrating mechanics and diagenesis. *AAPG bulletin*, 93(11), 1535–1549.
- Palmer, A. N. (1991). Origin and morphology of limestone caves. *Geological Society of America Bulletin*, 103(1), 1–21.
- Palmer, A. N. (2011). Distinction between epigenic and hypogenic maze caves. *Geomorphology*, 134(1-2), 9–22.
- Palmer, A. N., & Palmer, M. V. (2000). Hydrochemical interpretation of cave patterns in the guadalupe mountains, new mexico. *Journal of Cave and Karst Studies*, 62(2), 91–108.
- Pau, G. S. H., Bell, J. B., Almgren, A. S., Fagnan, K. M., & Lijewski, M. J. (2012). An adaptive mesh refinement algorithm for compressible two-phase flow in porous media. *Computational Geosciences*, 16(3), 577–592.
- Peng, C., Crawshaw, J. P., Maitland, G. C., & Trusler, J. M. (2015). Kinetics of calcite dissolution in co₂-saturated water at temperatures between (323 and 373) k and pressures up to 13.8 mpa. *Chemical Geology*, 403, 74–85.

- Plummer, L. N., & Wigley, T. (1976). The dissolution of calcite in co₂-saturated solutions at 25 c and 1 atmosphere total pressure. *Geochimica et Cosmochimica Acta*, 40(2), 191–202.
- Plummer, L., Parkhurst, D., & Wigley, T. (1979). Critical review of the kinetics of calcite dissolution and precipitation. ACS Publications.
- Plummer, L., Wigley, T., & Parkhurst, D. (1978). The kinetics of calcite dissolution in co₂-water systems at 5 degrees to 60 degrees c and 0.0 to 1.0 atm co₂. *American journal of science*, 278(2), 179–216.
- Pontes, C., Bezerra, F., Bertotti, G., Balsamo, F., La Bruna, V., & de Hoop, S. (2020). Karst conduits formed along fracture corridors in anticline hinges of carbonate units: Implications for reservoir quality. *Fourth Naturally Fractured Reservoir Workshop*, 2020(1), 1–6.
- Popov, P., Quin, G., Bi, L., Efendiev, Y., Ewing, R., Kang, Z., & Li, J. (2007). Multi-scale methods for modeling fluid flow through naturally fractured carbonate karsts reservoirs, spe 110778. *SPE Annual Technical Conference and Exhibition*.
- Prabhakaran, R., Bruna, P.-O., Bertotti, G., & Smeulders, D. (2019). An automated fracture trace detection technique using the complex shearlet transform. *Solid Earth*, 10(6), 2137–2166.
- Prabhakaran, R., Urai, J. L., Bertotti, G., Weismüller, C., & Smeulders, D. M. (2021). Large-scale natural fracture network patterns: Insights from automated mapping in the lilstock (bristol channel) limestone outcrops. *Journal of Structural Geology*, 150, 104405.
- Pruess, K., & Narasimhan, T. (1982). On fluid reserves and the production of superheated steam from fractured, vapor-dominated geothermal reservoirs. *Journal of Geophysical Research: Solid Earth*, 87(B11), 9329–9339.
- Rajaram, H., Cheung, W., & Chaudhuri, A. (2009). Natural analogs for improved understanding of coupled processes in engineered earth systems: Examples from karst system evolution. *Current Science*, 1162–1176.
- Ramamurthy, B., Doonan, J., Zhou, J., Han, J., & Liu, Y. (2015). Skeletonization of 3d point cloud using a voxel based thinning algorithm. *Proceedings of the 23rd European Signal Processing Conference (EUSIPCO), Nice, France*, 31.
- Rehrl, C., Birk, S., & Klimchouk, A. (2010). Influence of initial aperture variability on conduit development in hypogene settings. *Zeitschrift für Geomorphologie, Supplementary Issues*, 54(2), 237–258.
- Rehrl, C., Birk, S., & Klimchouk, A. (2008). Conduit evolution in deep-seated settings: Conceptual and numerical models based on field observations. *Water Resources Research*, 44(11).
- Reichenberger, V., Jakobs, H., Bastian, P., & Helmig, R. (2006). A mixed-dimensional finite volume method for two-phase flow in fractured porous media. *Advances in water resources*, 29(7), 1020–1036.
- Reijmer, J. J., Johan, H., Jaarsma, B., & Boots, R. (2017). Seismic stratigraphy of dinantian carbonates in the southern netherlands and northern belgium. *Netherlands Journal of Geosciences*, 96(4), 353–379.
- Rijken, M. C. M. (2005). *Modeling naturally fractured reservoirs: From experimental rock mechanics to flow simulation*. The University of Texas at Austin.

- Rossetto, C. (2020). Dimensional and mechanical stability analysis of caves in bahia, brazil.
- Saldi, G. D., Voltolini, M., & Knauss, K. G. (2017). Effects of surface orientation, fluid chemistry and mechanical polishing on the variability of dolomite dissolution rates. *Geochimica et Cosmochimica Acta*, 206, 94–111.
- Sammon, P. H. et al. (2003). Dynamic grid refinement and amalgamation for compositional simulation. *SPE reservoir simulation symposium*.
- Sanderson, D. J., & Nixon, C. W. (2015). The use of topology in fracture network characterization. *Journal of Structural Geology*, 72, 55–66.
- Sanderson, D. J., Peacock, D. C., Nixon, C. W., & Rotevatn, A. (2019). Graph theory and the analysis of fracture networks. *Journal of Structural Geology*, 125, 155–165.
- Sartori Suarez, A. (2018). *Uncertainty quantification based on hierarchical representation of fractured reservoirs* (Master's thesis). Delft University of Technology. the Netherlands.
- Sauter, M. (1992). Quantification and forecasting of regional groundwater flow and transport in a karst aquifer (gallusquelle, malm, sw. germany).
- Scheidt, C., & Caers, J. (2009). Representing spatial uncertainty using distances and kernels. *Mathematical Geosciences*, 41(4), 397.
- Scheidt, C., Caers, J. et al. (2009). Uncertainty quantification in reservoir performance using distances and kernel methods—application to a west africa deepwater turbidite reservoir. *SPE Journal*, 14(04), 680–692.
- Scheidt, C., Caers, J., Chen, Y., & Durlofsky, L. J. (2011). A multi-resolution workflow to generate high-resolution models constrained to dynamic data. *Computational Geosciences*, 15(3), 545–563.
- Shaik, A., Tomlin, P., & Voskov, D. (2018). Modeling of near-well matrix acidization. *43rd Workshop on Geothermal Reservoir Engineering*.
- Shaik, R., TOMIN, P., VOSKOV, D., & DELFT, A. (2017). *Modelling of near-well acidisation* (Doctoral dissertation). Master's thesis, TU Delft.
- Shetty, S., Voskov, D., & Bruhn, D. F. (2018). Numerical strategy for uncertainty quantification in low enthalpy geothermal projects. *Workshop on Geothermal Reservoir Engineering*.
- Singurindy, O., & Berkowitz, B. (2003). Flow, dissolution, and precipitation in dolomite. *Water resources research*, 39(6).
- Spielman, D. A. (2010). Algorithms, graph theory, and linear equations in laplacian matrices. *Proceedings of the International Congress of Mathematicians 2010 (ICM 2010) (In 4 Volumes) Vol. I: Plenary Lectures and Ceremonies Vols. II–IV: Invited Lectures*, 2698–2722.
- Spooner, V., Geiger, S., & Arnold, D. (2021). Dual-porosity flow diagnostics for spontaneous imbibition in naturally fractured reservoirs. *Water Resources Research*, e2020WR027775.
- Spooner, V., Geiger, S., & Arnold, D. (2019). Ranking fractured reservoir models using flow diagnostics. *SPE Reservoir Simulation Conference*.
- Sriyanong, P. (2013). *Element-based formulations for coupled flow, transport, and chemical reactions* (Doctoral dissertation). Stanford University.

- Steeffel, C., Appelo, C., Arora, B., Jacques, D., Kalbacher, T., Kolditz, O., Lagneau, V., Lichtner, P., Mayer, K. U., Meeussen, J., et al. (2015). Reactive transport codes for subsurface environmental simulation. *Computational Geosciences*, 19(3), 445–478.
- Stumm, W., Morgan, J. J. et al. (1970). *Aquatic chemistry; an introduction emphasizing chemical equilibria in natural waters*.
- Stumm, W., & Morgan, J. J. (2012). *Aquatic chemistry: Chemical equilibria and rates in natural waters* (Vol. 126). John Wiley & Sons.
- Svensson, U., & Dreybrodt, W. (1992). Dissolution kinetics of natural calcite minerals in co₂-water systems approaching calcite equilibrium. *Chemical Geology*, 100(1-2), 129–145.
- Tagliasacchi, A., Zhang, H., & Cohen-Or, D. (2009). Curve skeleton extraction from incomplete point cloud. *Acm siggraph 2009 papers* (pp. 1–9).
- Teşene, M., Bosma, S. B., Al Kobaisi, M. S., & Hajibeygi, H. (2017). Projection-based embedded discrete fracture model (pedfm). *Advances in Water Resources*, 105, 205–216.
- Trangenstein, J. A. (2002). Multi-scale iterative techniques and adaptive mesh refinement for flow in porous media. *Advances in Water Resources*, 25(8-12), 1175–1213.
- Vallance, C. (2017). Reaction kinetics.
- Van Batenburg, D. W., De Zwart, A., Boerrigter, P. M., Bosch, M., & Vink, J. C. (2011). Application of dynamic gridding techniques to IOR/EOR processes. *IOR 2011-16th European Symposium on Improved Oil Recovery*.
- Van't Hoff, J. H. (1884). *Etudes de dynamique chimique* (Vol. 1). Muller.
- Vasuki, Y., Holden, E.-J., Kovesi, P., & Micklethwaite, S. (2014). Semi-automatic mapping of geological structures using uav-based photogrammetric data: An image analysis approach. *Computers & Geosciences*, 69, 22–32.
- Vaughan, P. J. (1987). Analysis of permeability reduction during flow of heated, aqueous fluid through westerly granite. *Coupled processes associated with nuclear waste repositories* (pp. 529–539). Elsevier.
- Verma, A., & Pruess, K. (1988). Thermohydrological conditions and silica redistribution near high-level nuclear wastes emplaced in saturated geological formations. *Journal of Geophysical Research: Solid Earth*, 93(B2), 1159–1173.
- Vidal, J., & Genter, A. (2018). Overview of naturally permeable fractured reservoirs in the central and southern upper rhine graben: Insights from geothermal wells. *Geothermics*, 74, 57–73.
- Virtanen, P., Gommers, R., Oliphant, T. E., Haberland, M., Reddy, T., Cournapeau, D., Burovski, E., Peterson, P., Weckesser, W., Bright, J., van der Walt, S. J., Brett, M., Wilson, J., Millman, K. J., Mayorov, N., Nelson, A. R. J., Jones, E., Kern, R., Larson, E., ... SciPy 1.0 Contributors. (2020). SciPy 1.0: Fundamental Algorithms for Scientific Computing in Python. *Nature Methods*, 17, 261–272. <https://doi.org/10.1038/s41592-019-0686-2>
- Vohralik, M., & Wheeler, M. F. (2013). A posteriori error estimates, stopping criteria, and adaptivity for two-phase flows. *Computational Geosciences*, 17(5), 789–812.
- Vohralik, M., & Yousef, S. (2018). A simple a posteriori estimate on general polytopal meshes with applications to complex porous media flows. *Computer Methods in Applied Mechanics and Engineering*, 331, 728–760.

- Voskov, D. V. (2017). Operator-based linearization approach for modeling of multiphase multi-component flow in porous media. *Journal of Computational Physics*, 337, 275–288.
- Waage, P., & Gulberg, C. M. (1986). Studies concerning affinity. *Journal of chemical education*, 63(12), 1044.
- Wagner, W., & Kretzschmar, H.-J. (2008). *International steam tables: Properties of water and steam based on the industrial formulation iapws-97*. Springer-Verlag Berlin Heidelberg. <https://doi.org/10.1007/978-3-540-74234-0>
- Wang, M., Kulatilake, P., Um, J., & Narvaiz, J. (2002). Estimation of rev size and three-dimensional hydraulic conductivity tensor for a fractured rock mass through a single well packer test and discrete fracture fluid flow modeling. *International Journal of Rock Mechanics and Mining Sciences*, 39(7), 887–904.
- Wang, Y., Hill, A., & Schechter, R. (1993). The optimum injection rate for matrix acidizing of carbonate formations. *SPE Annual Technical Conference and Exhibition*.
- Wang, Y., de Hoop, S., Voskov, D., Bruhn, D., & Bertotti, G. (2021). Modeling of multiphase mass and heat transfer in fractured high-enthalpy geothermal systems with advanced discrete fracture methodology. *Advances in Water Resources*, 154, 103985.
- Wang, Y., & Voskov, D. (2019). High-enthalpy geothermal simulation with continuous localization in physics. *44th Workshop on Geothermal Reservoir Engineering, Stanford, California*. <https://doi.org/https://pangea.stanford.edu/ERE/pdf/IGAsstandard/SGW/2019/Wang4.pdf>
- Wang, Y., Voskov, D., Khait, M., & Bruhn, D. (2020). An efficient numerical simulator for geothermal simulation: A benchmark study. *Applied Energy*, 264, 114693.
- Wang, Y., Hajibeygi, H., & Tchelepi, H. A. (2014). Algebraic multiscale solver for flow in heterogeneous porous media. *Journal of Computational Physics*, 259, 284–303.
- Warren, J., & Root, P. J. (1963). The behavior of naturally fractured reservoirs. *Society of Petroleum Engineers Journal*, 3(03), 245–255.
- Wellman, T. P., Shapiro, A. M., & Hill, M. C. (2009). Effects of simplifying fracture network representation on inert chemical migration in fracture-controlled aquifers. *Water Resources Research*, 45(1).
- West, D. B. et al. (2001). *Introduction to graph theory* (Vol. 2). Prentice hall Upper Saddle River.
- Willems, C. (2017). *Doublet deployment strategies for geothermal hot sedimentary aquifer exploitation: application to the Lower Cretaceous Nieuwerkerk Formation in the West Netherlands Basin* (Doctoral dissertation). Delft University of Technology.
- Willems, C., & Nick, H. (2019). Towards optimisation of geothermal heat recovery: An example from the west netherlands basin. *Applied energy*, 247, 582–593.
- Witter, J. B., Trainor-Guitton, W. J., & Siler, D. L. (2019). Uncertainty and risk evaluation during the exploration stage of geothermal development: A review. *Geothermics*, 78, 233–242.
- Wong, D. L. Y., Doster, F., Geiger, S., Francot, E., & Gouth, F. (2020). Fluid flow characterization framework for naturally fractured reservoirs using small-scale fully explicit models. *Transport in Porous Media*, 134(2), 399–434.
- Wright, M. R. (2005). *Introduction to chemical kinetics*. John Wiley & Sons.

- Wu, H., & Pollard, D. D. (2002). Imaging 3-d fracture networks around boreholes. *AAPG bulletin*, 86(4), 593–604.
- Wu, Y.-S., Di, Y., Kang, Z., & Fakcharoenphol, P. (2011). A multiple-continuum model for simulating single-phase and multiphase flow in naturally fractured vuggy reservoirs. *Journal of Petroleum Science and Engineering*, 78(1), 13–22.
- Yang, L., Oyen, D., & Wohlberg, B. (2019). A novel algorithm for skeleton extraction from images using topological graph analysis. *Proceedings of the IEEE/CVF Conference on Computer Vision and Pattern Recognition Workshops*, 0–0.
- Zeeb, C., Gomez-Rivas, E., Bons, P. D., & Blum, P. (2013). Evaluation of sampling methods for fracture network characterization using outcrops. *AAPG bulletin*, 97(9), 1545–1566.
- Zhang, J., Zhou, J., Fu, L., Li, H., & Lou, D. (2020). Karstification of ordovician carbonate reservoirs in huanghua depression and its control factors. *Carbonates and Evaporites*, 35(2), 1–16.
- Zhao, X., & Paul Young, R. (2011). Numerical modeling of seismicity induced by fluid injection in naturally fractured reservoirs. *Geophysics*, 76(6), WC167–WC180.
- Zhiwen, D., Rujun, W., Fangfang, C., Jianping, Y., Zhongqian, Z., Zhimin, Y., Xiaohui, S., Bo, X., Erpeng, L., Tao, S., et al. (2020). Origin, hydrocarbon accumulation and oil-gas enrichment of fault-karst carbonate reservoirs: A case study of ordovician carbonate reservoirs in south tahe area of halahatang oilfield, tarim basin. *Petroleum Exploration and Development*, 47(2), 306–317.
- Zlot, R., & Bosse, M. (2014a). Efficient large-scale three-dimensional mobile mapping for underground mines. *Journal of Field Robotics*, 31(5), 758–779.
- Zlot, R., & Bosse, M. (2014b). Three-dimensional mobile mapping of caves. *Journal of Cave & Karst Studies*, 76(3).



MULTI-PHASE REACTIVE TRANSPORT BENCHMARK

A.1. INTRODUCTION AND CONTEXT OF THE PROPOSAL

This document presents a proposal for a benchmark on reactive multiphase flow. The proposal was put together as a followup of the first SITRAM meeting <https://sitram19.sciencesconf.org/>, which took place in Pau in December 2019. The topic is increasingly important for modern energy applications.

The content of the benchmark was initially written by SdH and DV, and the current version is the result of discussions between the five authors. The proposal is still work in progress. Preliminary results were reported by several teams in two sessions of a minisymposium at the upcoming SIAM Conference on Mathematical and Computational Issues in the Geosciences, and it is the organizers' hope that input from the participants will enable the model to be extended towards more realistic geometries as well as physical and chemical phenomena.

A second workshop SITRAM21 <https://sitram21.sciencesconf.org/> was organized in December 2022 at the Inria Center in Paris, where participants showed further results. A special issue of the journal "Computational Geosciences" is planned, where participants will be able to present and compare their work.

The proposal was written to address several challenges commonly met in applications:

1. Robust coupling of chemical reactions with multiphase flow in porous media,
2. Phase behaviour coupling with equilibrium reactions,
3. Conservative treatment of solid phase dissolution and precipitation,
4. Effective coupling of equations in the case of multiple (concurrent) reactions.

Parts of this chapter have been published as a preprint on HAL open archive, fhal-03635080 (2022) de Hoop et al., 2022.

The general structure of the physical and chemical model is described in Sections 2 to 5, while the specific data for the proposed cases are given in Section 6, and requested output is specified in Section 7.

A.2. BENCHMARK SCENARIOS

A.2.1. 1D HOMOGENEOUS DOMAIN

The first case is a basic 1D model. The rock and fluid properties are shown in Table A.1.

Property	Value	Units
Permeability, $k_{x,y,z}$	[100, 100, 100]	[mD]
Total porosity, ϕ^T	1	[-]
Porosity, ϕ	0.3	[-]
Control volume dimension, $\Delta x, y, z$	[1, 1, 1]	[m]
Number of control volumes, N_x	1000	[-]
Phase density at p_0 , $\rho_{w,g,s}$	[1000, 100, 2000]	[kg/m ³]
Phase compressibility, $C_{w,g,s}$	[10 ⁻⁶ , 10 ⁻⁴ , 10 ⁻⁷]	[1/bar]
Phase viscosity, $\mu_{w,g}$	[1, 0.1]	[cP]
End-point relative permeability, $k_{rw,rg}^e$	[1, 1]	[-]
Corey exponents, $n_{w,g}$	[2, 2]	[-]
Residual saturation, $s_{rw,rg}$	[0, 0]	[-]
Phase partition coefficients, K_{H_2O,CO_2}	[0.1, 10]	[-]
Diffusion coefficients, $d_{cj} = d$	10 ⁻⁹	[m ² /s]
Activity coefficients, $\gamma_{cw} = \gamma$	1	[-]
Porosity-permeability dependence factor, A	3	[-]

Table A.1 Values for all the relevant fluid and rock properties.

The model is setup with an injection well (i.e., source term) in the first block and a production well in the last block, no flow boundary conditions from left and right (i.e., $\frac{\partial p}{\partial x}|_{x=0} = 0$ and $\frac{\partial p}{\partial x}|_{x=\Delta x N_x} = 0$). These are typical boundary conditions for reservoir simulation. It is possible to replace the wells and no-flow boundary condition with a Neumann boundary condition at $x = 0$ and a Dirichlet at $x = \Delta x N_x$. Table A.2 summarizes the initial, injection and production conditions and simulation time.

Note that the injection and initial compositions are given in terms of the overall mole fractions z_i , $i = 1, \dots, C$, defined as

$$z_i = \sum_{j=1}^P x_{ij} v_j, \quad i = 1, \dots, C,$$

with

$$v_j = \frac{\rho_j S_j}{\sum_{k=1}^P \rho_k S_k}, \quad j = 1, \dots, P,$$

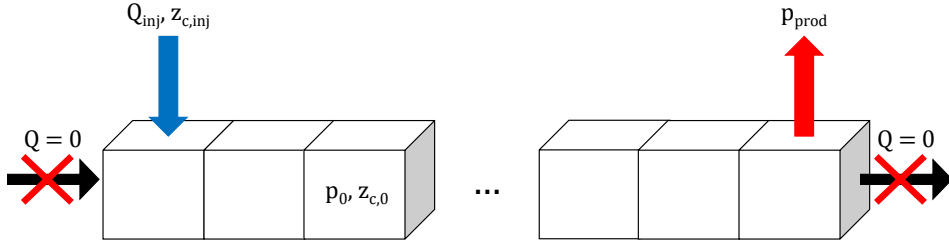


Figure A.1 One dimensional domain setup. Injection on the left is constrained with rate and composition Q_{inj} and $z_{c,inj}$ respectively. Production on the right is constrained with pressure p_{prod} . Initial condition for pressure and composition is defined as p_0 and $z_{c,0}$ respectively. No flow boundary condition is imposed on both the left and right boundary.

Property	Value	Units
Injection rate, Q_{inj}	0.2	[m ³ /day]
Injection composition, $z_{c,inj}$, $c = 1, \dots, C-1$,	[0, 1, 0, 0]	[-]
Initial pressure, P_{ini}	95	[bar]
Initial composition, $z_{c,ini}$, $c = 1, \dots, C-1$,	[0.15, 0, 0.075, 0.075]	[-]
Production pressure, P_{prod}	95	[bar]
Simulation time, T	1000	[day]

Table A.2 Boundary conditions and other simulation parameters.

We refer to Kala and Voskov, 2020 for more details. Note that composition for the C -th component can be obtained by $z_C = 1 - \sum_{j=1}^{C-1} z_j$ and is not a primary unknown (hence the initial and injection composition doesn't contain the composition of z_C), and the primary unknowns in this system are $X = [p, z_1, \dots, z_{C-1}]$. The initial and injection composition expressed in terms of molar fraction of individual species and saturation of each phases are given at the end of this Appendix A.3.2.

We now describe the chemical reaction used for this first case. It consists of a single chemical reaction (i.e., we cannot reduce the global system of nonlinear equation using the element reduction). The system consists of the following components: $z_c = [H_2O, CO_2, Ca^{+2}, CO_3^{-2}, CaCO_3]$. The kinetic reaction equation consists of



We distinguish two cases according to whether the reaction is modelled as kinetic or at equilibrium.

TWO-PHASE FLOW WITH KINETIC CHEMISTRY

Here we assume that the chemical reaction (A.1) is kinetic. The kinetic rate (i.e., the right-hand-side of equation (2.6)) is written as

$$r_k = AK_k \left(1 - \frac{Q}{K_{sp}} \right) \quad (A.2)$$

where A is the reactive surface area, which is a linear function of the solid saturation ($A = A_0 \hat{s}_s = (1 - \phi_0) \hat{s}_s$), K_k is the kinetic reaction constant, Q is the activity product (to simplify $Q = x_{ca,w} \times x_{co3,w}$) and K_{sp} is the equilibrium constant.

The values of the reaction constants are given in Table A.3. K_{sp} is equal to $0.25 \times 0.25 = 0.0625$ to ensure that the initial state is in equilibrium and no dissolution occurs.

Property	Value	Units
Kinetic constant, K_k	1	[kmol / m ³ / day]
Solubility constant, K_{sp}	0.0625	[-]

Table A.3 Kinetic and equilibrium constants.

TWO-PHASE FLOW WITH EQUILIBRIUM CHEMISTRY

The second test case is similar to the first one, except that now the reaction is treated as an equilibrium reaction. Mathematically, this adds an additional constraint equation of the form

$$Q - K_{sp} = 0, \quad (\text{A.3})$$

where Q is the activity product of the equilibrium reaction as defined in equation (2.16) (which is taken here to have the same form as in Section A.2.1) and K_{sp} is the solubility constant, with the value given in Table A.2. All the other parameters, fluid/rock/boundary condition/simulation parameters (as specified in table A.1 and A.2), are the same as for the previous case (including of course the stoichiometry of the reaction).

A.2.2. 2D HETEROGENEOUS DOMAIN

The third test case consists of a two-dimensional heterogeneous domain. In the model, a zone of high porosity (and permeability) is embedded within a lower porosity (and permeability) zone. The domain extends for 10[m] in the y -direction (all the other measures are mentioned in Figure A.2). The boundary conditions are constant injection rate on the left (bottom half of the domain pure CO₂, top half pure H₂O) and constant pressure on the right boundary (outflow) with no-flow on top and bottom.

Kinetic chemistry is used to model the dissolution of CaCO₃. See Tables A.4 and A.5 for all the parameters used in this model. Note that we have provided the initial values both in terms of the overall mole fractions and in terms of the individual mole fractions (computed with the same python code listed above), and also that the concentration of the calcite can be directly computed as a function of the porosity (see equation 2.17). All fluid and chemical parameters (e.g., kinetic constants, reference mass density, etc.) are the same as in test case A.2.1.

In addition to the two chemical systems described later, this test case can be executed with or without gravity (i.e. $g = 0$). We note that when gravity is included, it would have been more natural for the initial pressure to follow a hydrostatic law. However, the effect is quite small, and the simpler constant initial pressure was retained.

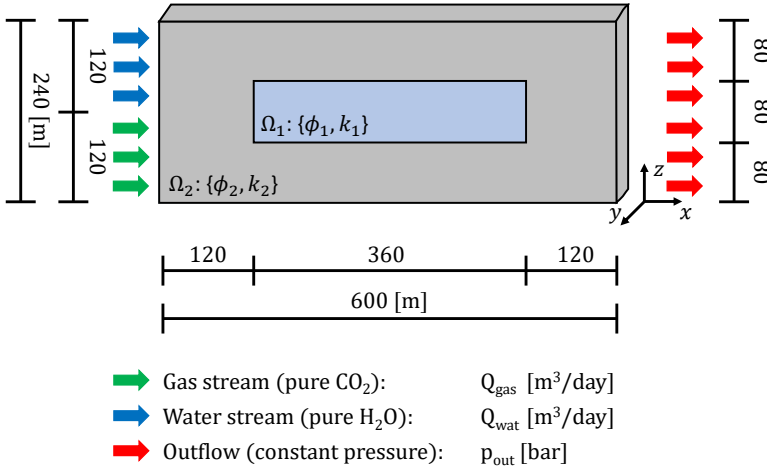


Figure A.2 Configuration of the 2D test case (Section A.2.2). Constant injection rate on the left boundary (Neumann) and constant pressure (Dirichlet) on the right. The domain extends 10[m] in the y -direction.

Property	Value	Units
Gas injection rate, Q_{inj}	1000	[m ³ /day]
Water injection rate, Q_{inj}	200	[m ³ /day]
Gas injection composition, $z_{c,\text{inj}}$, $c = 1, \dots, C - 1$,	[0, 1, 0, 0]	[-]
Gas injection composition in molar fractions, $x_{cg,\text{inj}}$, $c = 1, \dots, C - 1$,	[0, 1, 0, 0]	[-]
Water injection composition, $z_{c,\text{inj}}$, $c = 1, \dots, C - 1$,	[1, 0, 0, 0]	[-]
Water injection composition in molar fractions, $x_{cw,\text{inj}}$, $c = 1, \dots, C - 1$,	[1, 0, 0, 0]	[-]
Initial pressure on $\Omega_1 \cup \Omega_2$, P_{ini}	95	[bar]
Initial composition on Ω_1 , $z_{c,\text{ini}}$, $c = 1, \dots, C - 1$,	[0.4, 0, 0.20, 0.20]	[-]
Initial composition on Ω_2 , $z_{c,\text{ini}}$, $c = 1, \dots, C - 1$,	[0.15, 0, 0.075, 0.075]	[-]
Initial fluid composition on $\Omega_1 \cup \Omega_2$ in molar fractions, $x_{cw,\text{ini}}$, $c = 1, \dots, C - 1$,	[0.5, 0, 0.25, 0.25]	[-]
Production pressure, P_{prod}	95	[bar]
Simulation time, T	1000	[days]

Table A.4 Boundary conditions and other simulation parameters.

SIMPLE CHEMICAL MODEL

In that case, only one chemical reaction is included, and the chemical model is the same as in Section A.2.1.

However, one further simplification may be necessary: one may encounter convergence problems when running the system as described previously. If that is the case, it

Property	Value	Units
Porosity on Ω_1 , ϕ	0.8	[-]
Permeability on Ω_1 , $k_{x,y,z}$	[1896, 1896, 1896]	[mD]
Porosity on Ω_2 , ϕ	0.3	[-]
Permeability on Ω_2 , $k_{x,y,z}$	[100, 100, 100]	[mD]
Total porosity on $\Omega_1 \cup \Omega_2$, ϕ^T	1	[-]
Control volume dimension, $\Delta x, y, z$	[10, 10, 10]	[m]
Number of control volumes, $N_x \times N_y \times N_z$	$60 \times 1 \times 24$	[-]
Diffusion coefficients, $d_{c,j} = d$	10^{-9}	[m ² /s]
Gravitational acceleration, g	9.8	[m/s ²]

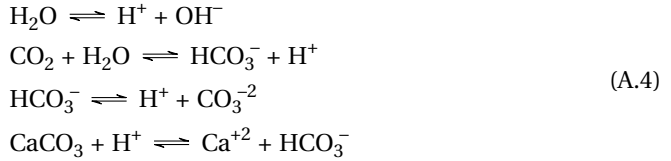
Table A.5 Values for all the relevant fluid and rock properties.

may be helpful to consider a single "meta-ion" $\text{Ca}^{2+} + \text{CO}_3^{2-}$ in the liquid phase.

EXTENDED CHEMICAL MODEL

We consider a somewhat more realistic (albeit still quite small) chemical system, including dissociation of water and of carbonic dioxide, as this makes it possible to take into account the influence of pH.

The system is composed of 4 reactions:



Note that this increases the total number of species by three, particularly to $z_c = [\text{H}_2\text{O}, \text{CO}_2, \text{Ca}^{2+}, \text{CO}_3^{2-}, \text{H}^+, \text{OH}^-, \text{HCO}_3^-, \text{CaCO}_3]$. However, this allows to represent the CaCO_3 reaction (last equation in (A.4)) with an explicit dependency on the pH of the solution.

The first three reactions are at equilibrium, the logarithms of the equilibrium constants are given in Table A.6, while the fourth reaction is kinetic, and the rate for the last reaction is given by equation (A.2), with Q now defined by:

$$Q = \frac{a_{\text{Ca},w} a_{\text{HCO}_3,w}}{a_{\text{H},w}}. \tag{A.5}$$

K_1	K_2	K_3	K_{sp}
-13.95	-6.293	-10.279	-1.899

Table A.6 Log_{10} of the equilibrium constants for extended chemical system (A.4).

For this last case, the mass actions laws are expressed in activities:

$$\begin{aligned}
 K_1 a_{\text{H}_2\text{O},w} &= a_{\text{H}^+,w} a_{\text{OH}^-,w}, \\
 K_2 a_{\text{CO}_2,w} a_{\text{H}_2\text{O},w} &= a_{\text{HCO}_3^-,w} a_{\text{H}^+,w}, \\
 K_3 a_{\text{HCO}_3^-,w} &= a_{\text{H}^+,w} a_{\text{CO}_3^{2-},w}.
 \end{aligned}
 \tag{A.6}$$

Initial conditions computed using Arxim Moutte et al., 2010 are given in table A.7. All other physical are the same as in test A.2.2.

Property	Value	Units
$x_{\text{CO}_2,w}$	3.9624×10^{-10}	[-]
$x_{\text{Ca}^{2+},w}$	2.1703×10^{-6}	[-]
$x_{\text{H}^+,w}$	2.3507×10^{-12}	[-]
$x_{\text{OH}^-,w}$	1.5475×10^{-6}	[-]
$x_{\text{HCO}_3^-,w}$	1.5467×10^{-6}	[-]
$x_{\text{CO}_3^{2-},w}$	6.2315×10^{-7}	[-]

Table A.7 Initial molar fractions for the extended chemical model

A.3. EXPECTED OUTPUT

Participants are expected to provide the following output, in the form of a CSV file for 1D output and a figure for 2D output. To make it easier to organize the results from different participants we ask that the submitted files follow a specific naming scheme, as detailed below. Each filename name has four parts: GROUP_CASE_LOC_VAR, where

GROUP is a (4 to 6 character) unique identifier, selected by each group;

CASE is a 2 character identifier for the specific benchmark case, as follows

- 11** for 1D, kinetic chemistry;
- 12** for 1D, equilibrium chemistry;
- 21** for 2D, simple chemistry;
- 22** for 1D, extended chemistry.

LOC is the location of the variables in the file (such as t1000 or x25);

VAR gives additional information, such as grav or nograv depending on whether or not gravity has been included.

A.3.1. 1D HOMOGENEOUS DOMAIN

- Text output of all variables as a function of space at time 1000 days in a CSV file named (with case = "11" or "12") GROUP_CASE_t1000.csv, containing (x , S_g , P_g , ϕ , $x_{\text{H}_2\text{O},w}$, $x_{\text{CO}_2,w}$, $x_{\text{Ca}^{2+},w}$ + $x_{\text{HCO}_3^-,w}$);

- Text output of all variables as a function of time at $x = 25$ in a CSV file named `GROUP_CASE_x25.csv`, containing $(t, S_g, P_g, \phi, x_{\text{H}_2\text{O},w}, x_{\text{CO}_2,w}, x_{\text{Ca}^{2+},w} + x_{\text{HCO}_3^-,w})$;
- It is suggested to include a numerical convergence study.

A.3.2. 2D HETEROGENEOUS DOMAIN

SIMPLE CHEMICAL MODEL

- Plot CO_2 fraction, ion mole fractions, gas saturation and porosity as a space maps at time 1000 days;
- Write the same variables as in 1D on a cross-section along the vertical line at $x = 40\text{m}$ in a CSV file named `GROUP_21_x40_VAR.csv`, containing $(y, S_g, P_g, \phi, x_{\text{H}_2\text{O},w}, x_{\text{CO}_2,w}, x_{\text{Ca}^{2+},w} + x_{\text{HCO}_3^-,w})$;
- Write the same variables as in 1D on a cross-section along the horizontal line at $y = 50\text{m}$ in a CSV file named `GROUP_21_y50_VAR.csv`, containing $(x, S_g, P_g, \phi, x_{\text{H}_2\text{O},w}, x_{\text{CO}_2,w}, x_{\text{Ca}^{2+},w} + x_{\text{HCO}_3^-,w})$.

EXTENDED CHEMICAL MODEL

Same output as for the simple chemical model, with the addition of all chemical species:

- Plot CO_2 fraction, ion mole fractions, gas saturation and porosity as a space maps at time 1000 days;
- Text output of the same variables as 1D cross-section along vertical line at $x = 40\text{m}$ in a CSV file named `GROUP_22_x40.csv`, containing $(y, S_g, P_g, x_{\text{H}_2\text{O},w}, x_{\text{CO}_2,w}, x_{\text{Ca}^{2+},w}, x_{\text{H}^+,w}, x_{\text{HCO}_3^-,w}, x_{\text{CO}_3^{2-},w}, \phi)$;
- Write the same variables as in 1D on a cross-section along the horizontal line at $(y = 50\text{m})$ in a CSV file named `GROUP_22_y50.csv`, containing $(x, S_g, P_g, x_{\text{H}_2\text{O},w}, x_{\text{CO}_2,w}, x_{\text{Ca}^{2+},w}, x_{\text{H}^+,w}, x_{\text{HCO}_3^-,w}, x_{\text{CO}_3^{2-},w}, \phi)$.

ACKNOWLEDGEMENTS

The authors are grateful to Eric Flauraud (IFPEN) for providing the initial values for the "Extended chemical model" in Section A.2.2, as well as for a careful reading of the paper.

INITIAL AND INJECTION CONDITIONS

1D injection

Properties based on injection state: `state = [P, z_h2o, z_co2, z_ca, z_co3]`
 Injection state = `[1.65e+02 1.00e-12 1.00e+00 1.00e-12 1.00e-12]`

	H2O	CO2	Ca+2	CO3-2	CaCO3
Composition, z_c	1.00e-12	1.00e+00	1.00e-12	1.00e-12	1.00e-12
Liquid MoleFrac	1.00e-11	1.00e-02	4.94e-01	4.94e-01	0.00e+00
Vapor MoleFrac	1.00e-12	1.00e+00	4.94e-13	4.94e-13	0.00e+00

Solid MoleFrac	0.00e+00	0.00e+00	0.00e+00	0.00e+00	1.00e+00
----------------	----------	----------	----------	----------	----------

	Liquid	Vapor	Solid
Phase MoleFrac	1.02e-12	1.00e+00	1.00e-12
Mass Density	1.00e+03	1.01e+02	2.00e+03
Viscosity	1.00e+00	1.00e-01	0.00e+00
Sat. phi_tot	1.17e-13	1.00e+00	1.00e-12
Sat. phi_fluid	1.17e-13	1.00e+00	0.00e+00

1D initial

Properties based on initial state: state = [P, z_h2o, z_co2, z_ca, z_co3]

Initial state = [9.5e+01 1.5e-01 1.0e-12 7.5e-02 7.5e-02]

	H2O	CO2	Ca+2	CO3-2	CaCO3
Composition, z_c	1.50e-01	1.00e-12	7.50e-02	7.50e-02	7.00e-01
Liquid MoleFrac	5.00e-01	3.33e-12	2.50e-01	2.50e-01	0.00e+00
Vapor MoleFrac	5.00e-01	3.33e-12	2.50e-01	2.50e-01	0.00e+00
Solid MoleFrac	0.00e+00	0.00e+00	0.00e+00	0.00e+00	1.00e+00

	Liquid	Vapor	Solid
Phase MoleFrac	3.00e-01	0.00e+00	7.00e-01
Mass Density	1.00e+03	1.00e+02	2.00e+03
Viscosity	1.00e+00	1.00e-01	0.00e+00
Sat. phi_tot	3.00e-01	0.00e+00	7.00e-01
Sat. phi_fluid	1.00e+00	0.00e+00	0.00e+00

CURRICULUM VITÆ

Stephan DE HOOP

27-10-1991 Born in Apeldoorn, the Netherlands.

EDUCATION

2004–2009 Koninklijke Scholengemeenschap Apeldoorn

2009–2013 Bachelor Civil Engineering
Saxion University of Applied Sciences, Enschede

2014–2015 Pre-master Geosciences
Technische Universiteit Delft

2015–2017 Master Petroleum Engineering and Geosciences
Technische Universiteit Delft

2017–2022 PhD. Applied Earth Sciences
Technische Universiteit Delft
Thesis: Towards the Uncertainty Quantification of Fractured
Karst Systems
Promotor: dr. D. V. Voskov

LIST OF PUBLICATIONS

9. **de Hoop, S.**, Voskov, D., Bertotti, G., & Barnhoorn, A., *An Advanced Discrete Fracture Methodology for Fast, Robust, and Accurate Simulation of Energy Production from Complex Fracture Networks*, [Water Resources Research](#), **58-5**, e2021WR030743 (2022).
8. **de Hoop, S.** & Voskov, D., *Fast And Robust Scheme For Uncertainty Quantification In Naturally Fractured Reservoirs*, [SPE Reservoir Simulation Conference](#), **OnePetro** (2021b).
7. **de Hoop, S.**, Jones, E., & Voskov, D., *Accurate geothermal and chemical dissolution simulation using adaptive mesh refinement on generic unstructured grids*, [Advances in Water Resources](#) **154**, 103977 (2021a).
6. Wang, Y., **de Hoop, S.**, Voskov, D., Bruhn, D., & Bertotti, G., *Modeling of multiphase mass and heat transfer in fractured high-enthalpy geothermal systems with advanced discrete fracture methodology*, [Advances in Water Resources](#) **154**, 103985 (2021).
5. Pontes, C., Bezerra, F.H., Bertotti, G., La Bruna, V., Audra, P., De Waele, J., Auler, A., Balsamo, F., **de Hoop, S.**, & Pisani, L., *Flow pathways in multiple-direction fold hinges: Implications for fractured and karstified carbonate reservoirs*, [Journal of Structural Geology](#), **146**, 104324 (2021).
4. Boersma, Q. D., Bruna, P. O., **de Hoop, S.**, Vinci, F., Tehrani, A. M., & Bertotti, G., *The impact of natural fractures on heat extraction from tight Triassic sandstones in the West Netherlands Basin: a case study combining well, seismic and numerical data*, [Netherlands Journal of Geosciences](#), **100** (2021).
3. **de Hoop, S.**, Voskov, D., & Bertotti, G., *Studying the Effects of Heterogeneity on Dissolution Processes Using Operator Based Linearization and High-Resolution LiDAR Data*, [ECMOR XVII \(Vol. 2020, No. 1, pp. 1-13\)](#). European Association of Geoscientists & Engineers. (2020a).
2. Bertotti, G., Audra, P., Auler, A., Bezerra, F.H., **de Hoop, S.**, Cayo, P., Prabhakaran, R., & Lima, R., *The Morro Vermelho hypogenic karst system (Brazil): Stratigraphy, fractures, and flow in a carbonate strike-slip fault zone with implications for carbonate reservoirs*, [AAPG Bulletin](#) **104.10**: 2029-2050 (2020).
1. **de Hoop, S.**, Voskov, V., Vossepoel, F., & Jung, A., *Quantification Of Coarsening Effect On Response Uncertainty In Reservoir Simulation*, [ECMOR XVI \(Vol. 2018, No. 1, pp. 1-16\)](#). European Association of Geoscientists & Engineers. (2018).



ISBN NUMMER 978-94-6469-044-6